Granitic melt transport and emplacement along transcurrent shear zones: Case study of the Pofadder Shear Zone in South Africa and Namibia

by
Christopher William Lambert

Thesis presented in fulfilment of the requirements for the degree of Master of Science in the Faculty of Science at Stellenbosch University

Supervisor: Prof Alexander. F.M. Kisters

December 2013

Declaration

By submitting this thesis electronically, I declare that the entirety of the work contained therein is my own, original work, that I am the sole author thereof (save to the extent explicitly otherwise stated), that reproduction and publication thereof by Stellenbosch University will not infringe any third party rights and that I have not previously in its entirety or in part submitted it for obtaining any qualification.

Date: March 2013

Abstract

The close spatial and temporal relationship of shear-zones and magmas is commonly interpreted to indicate positive feedback between magma migration, granitic emplacement and shear-zone-associated deformation. Emplacement geometries and structural fabrics are however rarely preserved, hampering the study of shear-zones and granitic magmas interactions. This study focuses on an area around the Pofadder Shear Zone (PSZ) in Namibia and South Africa as a case study for granitic bodies, mainly as pegmatite sills and dykes, and their spatial and temporal relationships to a crustal-scale shear-zone.

The PSZ is a NW-SE trending, dextral, Mesoproterozoic-Neoproterozoic transpressional shear-zone in Namaqualand, interpreted to have accommodated late-stage lateral escape of the Namaqua Metamorphic Complex in response to southward indentation of the Kaapvaal Craton around 1030 – 1080 Ma. In this study it is shown that the shear-core records an asymmetrical strain variation across the PSZ. This is indicated by pervasively banded ultramylonites, mylonites and the significant development of pervasive phyllonites at the southern margin, defining the internal ductile to brittle-ductile fabrics of the shear, during a progressive deformational evolution. Mapping of the PSZ fabrics and associated pegmatites documents how pegmatites are emplaced in structurally distinctive sites within, and adjacent to the PSZ. New U-Pb monazite ages derived from this study, show how pegmatite emplacement has occurred at different times of shear-zone development. The pegmatites are emplaced into earlier ductile to later brittle-retrograde fabrics that accompanied the ca. 45 Ma shear-zone exhumation. Pegmatites concentrated along the northern PSZ-margin are interpreted to be controlled by anisotropies developed axial planar to large km-scale and parasitic folds during the initial, predominately strike-slip stages of shear-zone deformation that occurred as early as 1005 ± 5 Ma. Within the PSZ core, pegmatite emplacement is controlled by the syn-kinematic development of (a) subvertical, mylonitic and phyllonitic foliations and (b) fracture permeabilities created by synthetic Riedel shears and dextral dilatant jogs. The most significant pegmatite development around the PSZ is the Skimmelberg Pegmatite Stockwork (SPS) which forms an extensive interconnecting network of concurrent, foliation-parallel sills and thick (> 50 m) discordant dykes within the southern footwall of the PSZ. The dykes intrude as late as 958 ± 5 Ma into feather-shaped N-S extensional fractures (mode I) that developed due to episodic stick-slip at the boundary between the PSZ core and footwall rocks during periods of late-stage transpression. The SPS forms a steeply dipping fracture network that not only creates space needed for emplacement but effectively acts as a conduit for magma transport along the margin of the PSZ. The large extensional fractures of SPS create the necessary hydraulic gradients to tap the magma source of a regional trending pegmatite belt and form a sheeted complex adjacent to the PSZ. Therefore, this study documents how, during the progressive exhumation of a large-scale transcurrent shear-zone, magma emplacement is not only concentrated within the highly permeable, high-strain domains (cores) of shear-zones but may be concentrated in diachronous, structurally controlled sites along the shear-zone margins.

Uittreksel

Die noue ruimte-tydsverband tussen skuifskeure en magmas word algemeen geïnterpreteer as 'n aanduiding van positiewe terugkoppeling tussen magma migrasie, graniet-inplasing en skuifskeur-geassosieerde vervorming. Geometrie en struktuurmaaksels van inplasings word egter selde bewaar en belemmer die studie van interaksies tussen skuifskeure en graniet-magmas. Die studie fokus op 'n area rondom die Pofadder Skuifskeur (PSS) in Namibië en Suid-Afrika as 'n gevallestudie vir graniet-liggame, hoofsaaklik as pegmatiet plate en gange, asook voorafgenoemde se ruimte-tydsverband met 'n grootskaalse skuifskeur.

Die PSS is 'n NW-SO-waarts strekkende, regs-laterale, Mesoproterosoïse-Neoproterosoïse transpressie-skuifskeur in Namakwaland, wat geïnterpreteer word om die latere-stadium laterale ontsnapping van die Namakwa Metamorfiese Kompleks te akkomodeer in reaksie op die suidwaartse indrukking van die Kaapvaal Kraton omstreeks 1030-1080 Ma. In hierdie studie word getoon dat asimmetriese vervormingsvariasie deur die skuifskeurkern aangeteken word. Hierdie word aangetoon deur gebande ultramilioniete, milioniete en die noemenswaardige ontwikkeling van filoniete wat die suidelike rand deurtrek en definiëer die interne plastiese- tot bros-plastiese maaksels van die skuifskeur gedurende 'n progressiewe vervormingsevolusie. Kartering van die PSS maaksels en geassosieerde pegmatiete dokumenteer hoe pegmatiete, aangrensend en binne die PSS, in eiesoortige strukturele terreine binnedring. Nuwe U-Pb monasiet ouderdomme, afgelei vanuit hierdie studie, toon aan hoe inplasing plaasgevind het gedurende verskillende tye van skuifskeurontwikkeling. Pegmatiete het vroeëre plastiese- tot latere bros-retrogressiewe maaksels binnegedring wat die herontbloting van die ca. 45 Ma skuifskeur meegaan. Pegmatiete, gekonsentreerd langs die noordelike rand van die PSS, word geïnterpreteer as beheer deur anisotrope wat parallel aan die asvlak van groot km-skaalse en ondergeskikte plooie ontwikkel gedurende die aanvanklike, hoofsaaklik strekkingwaarste, stadiums van skuifskeurontwikkeling wat so vroeg as 1005 ±5 Ma plaasgevind het. Binne die kern van die PSS word die inplasing van pegmatiete beheer deur die sinkenimatiese ontwikkeling van (a) subvertikale, milionitiese- en filonitiese foliasies en (b) breuk-deurdringbaarheid wat gevorm is deur sintetiese riedelskuifskeure en regslaterale uitsettende "*jogs*". Die mees noemenswaardige pegmatiet ontwikkeling rondom die PSS is die Skimmelberg Pegmatiet Stokwerk (SPS) wat 'n intensiewe netwerk vorm van intergekonnekteerde konkurrente plate, parallel aan die foliasie, en dik (>50m) diskordante gange binne die suidelike vloer van die PSS. Die gange dring in so laat as 958 ± 5 Ma binne-in veervormige N-S uitbreidende breuke (modus1) wat ontwikkel het as gevolg van die episodiese hak-en-glip op die grens tussen die PSS kern- en vloergesteentes gedurende periodes van laat-stadium transpressie. Die SPS vorm 'n styl hellende breuk-netwerk wat nie net spasie maak vir indringing nie, maar dien ook effektief as 'n geleidingsweg vir die vervoer van magma langs die rand van die PSS. Die groot uitbreidende breuke van die SPS skep die nodige hidroliese gradiënt om die magma bron van 'n regionale pegmatiet gordel te tap en vorm 'n bladvormige kompleks aangrensend tot die PSS.

Gevolglik dokumenteer die studie hoe, gedurende die progressiewe ontbloting van 'n grootskaalse torsieskuifskeur, magma inplasing nie net gekonsentreer is binne die hoogs deurdringbare, hoogsvervormde areas (kerne) van skuifskeure nie, maar ook hoe magma kan konsentreer in diachroniese, struktuur beheerde gebiede teen die rande van skuifskeure.

Acknowledgements

First and foremost I would like to thank my promoter, Prof. A. Kisters (University of Stellenbosch) for supervising this project. I cannot extend my appreciation enough for all your help and patience over a difficult few years. I would like to thank Dr. Luc Chevallier at the Council for Geoscience for motivating for the funding of the project and allowing me to spend extended time writing up the final product. To my college Dr. Paul Macey (Specialist Geologist), also at the Council, all your encouragement and constant help is greatly appreciated, what I have learnt from working with is invaluable and will never be forgotten. Without the three of you this project would never have happened.

I would also like to extend my appreciation to Mr. Conrad Groenewald, a colleague and field companion, not to mention a good friend, during much of this project. Your insight and ideas of the geology in the study area is greatly valued. To Dr. Frei and Prof. Buick at the University of Stellenbosch for the all help with the geochronology, specifically the laser ablation and data reduction for the monazite and zircon samples. Thanks are also due to Mr. Nkosi (Council for Geoscience) and Mr. Nkumenge (University of Stellenbosch) for aiding in the geochronology sample preparation and separation processes. Also thanks are due to Dr. Musekiwa and Mr. Grobbelaar (GIS Specialists at Council for Geoscience) for digitising my polygon/line maps on such short notice and always providing great results and to Mr. Coenie de Beer for help with the final edits.

Lastly I would like to thank my family for all their love and support during the last few trying weeks of the final write-up.

Again, thank you Alex, Paul and Luc.

Table of Contents

1. Introduction

1.1 Background and rationale

Granitic plutons and shear-zones show a close spatial and temporal relationship commonly interpreted to indicate the positive feedback between melt migration and/or granite emplacement and deformation (e.g. Guineberteau et al., 1987; Hutton, 1988a, 1992, 1997; Hutton and Reavy, 1992; Brown, 1994, 2007; Brown et al., 1995; Brown and Rushmer, 1997; Vauchez et al., 1997; Brown and Solar, 1998a, 1998b; Petford and Koenders, 1998; Weinberg et al., 2004). Strain localisation and shear-zone formation may be triggered by or around rheologically weaker magma bodies (e.g. Davidson et al., 1992, 1994; Grujic and Mancktelow, 1998; Tommasi et al., 1994; Neves and Vauchez, 1995; Neves et al., 1996; Neves and Mariano, 1999; Vigneresse and Tikoff, 1999) or aided in response to strain softening effects associated with the successive emplacement of melts during deformation (e.g. Hollister and Crawford, 1986; Pe-Piper et al., 1998; Vauchez et al., 1997). Alternatively, shear-zones are also interpreted to control melt migration and granite emplacement. In this case, deformation may provide (a) permeabilities, either on a grain-scale or fracture permeabilities that allow for the transfer of melts (e.g. Castro, 1987; Clemens and Mawer, 1992; Hutton, 1992; Petford et al., 1993, 1994; Davidson et al., 1994 ; Aranguren et al., 1997; Clemens et al., 1997; Petford and Koenders, 1998; Brown and Solar, 1998b; Brown and Solar 1999; Mancktelow, 2006; Blenkinsop, 2008; Weinberg and Regenauer-Lieb, 2010), (b) localised temperature highs (e.g. Clemens and Vielzeuf, 1987; Fleitout and Froidevaux, 1980; Leloup et al., 1999), or (c) variations in local and regional pressures through dilatancy along and adjacent to shear-zones, effectively creating pressure gradients (e.g. Hutton et al., 1990; D'Lemos et al., 1992; Bouillin et al., 1993; Hutton, 1996; Tobisch and Cruden, 1995; Brown and Solar 1999; Brown, 2007; Weinberg et al., 2009) that drive melt transfer in addition to the buoyancy of the granitic melts. The latter point, in particular, is commonly invoked to not only provide a magmastatic head, but also the space needed for magma emplacement within (e.g. Castro, 1986; Guineberteau et al., 1987; McCaffery, 1992; Tikoff and Teyssier, 1992; McNaulty, 1995; Hutton, 1996, 1997; Brown and Solar 1998b; Tikoff et al., 1999; Westraat et al., 2005) or along the margins of shear-zones (e.g. Hutton, 1988b; Vigneresse, 1995; Weinberg et al., 2004, 2009).

Two of the main problems in analysing the actual spatial and temporal relationships between shear-zones and granite plutons is (a) the sheer volume of granite plutons that may obscure original structural relationships (e.g. Paterson and Schmidt, 1999; Schmidt and Paterson, 2000), and (b) the obliteration of many primary intrusive features by progressive deformation in the shear-zones. When granitic intrusions show spatial relationships with shear-zones and host structures are relatively well preserved despite continued deformation, an opportunity is presented to study both the structural controls of magma transport and emplacement as well as their temporal relationships to large-scale crustal shear-zones.

However, magma emplacement in and along shear-zones may also take the form of dyke swarms or stockwork complexes showing multiple intrusive relationships and the emplacement of magma batches over a protracted period of time during progressive deformation along the shear-zone (e.g. Tobisch and Paterson, 1990; Northrup and Mawer, 1991; Hutton, 1992, 1996; Arthaud and Caby, 1993; Petford et al., 1993, 1994 ; Carreras and Druguet, 1994; Lindross et al., 1996; Vauchez et al., 1997; Druguet and Hutton, 1998; Araújo et al., 2001; Hanmer et al., 2002; Henderson and Ihlen, 2004; Stalfords and Ehlders, 2006; Liotta et al., 2008; Demartis et al., 2011; Reichardt and Weinberg, 2012). Stockworks, specifically, may record the progressive assembly of granitic bodies through repeated sheeting (e.g. Miller and Paterson, 2001), while preserving primary intrusive features, geometries and wall-rock relationships with respect to the bounding shear-zone (e.g. Archanjo and Fetter 2004; McCaffrey, 1992).

1.2 Aims of the study and introduction to study area

The Pofadder Shear-zone (PSZ) is the largest and, for the most part, best exposed of the late-tectonic shear-zones in the Mesoproterozoic Namaqua Metamorphic Complex (NMC) in southern Africa (e.g. Beukes, 1973; Toogood, 1976; Beukes and Both, 1978; Figs. 1.1a,b). Granitic intrusives and, in particular, sheet- and pod-like pegmatite bodies display a close spatial and temporal relationships with the PSZ. This, together with the rugged and arid terrain, makes the shear-zone an ideal place to study the relationships between shear-zone deformation and controls on the migration and emplacement of granitic magmas. The presence, intrusive relationships and controls of syn-kinematic intrusives along and within the shear-zone have only briefly been described and noted in regional studies (e.g. Toogood, 1976, Becker et al., 2006; Miller, 2008). To date the only studies that focused on granitic intrusives in the PSZ were those by Moore (1975, 1981) who described the emplacement of pegmatite bodies controlled by large gabbroic to ultramafic complexes caught up in the PSZ and enveloped by the mylonitic foliation.

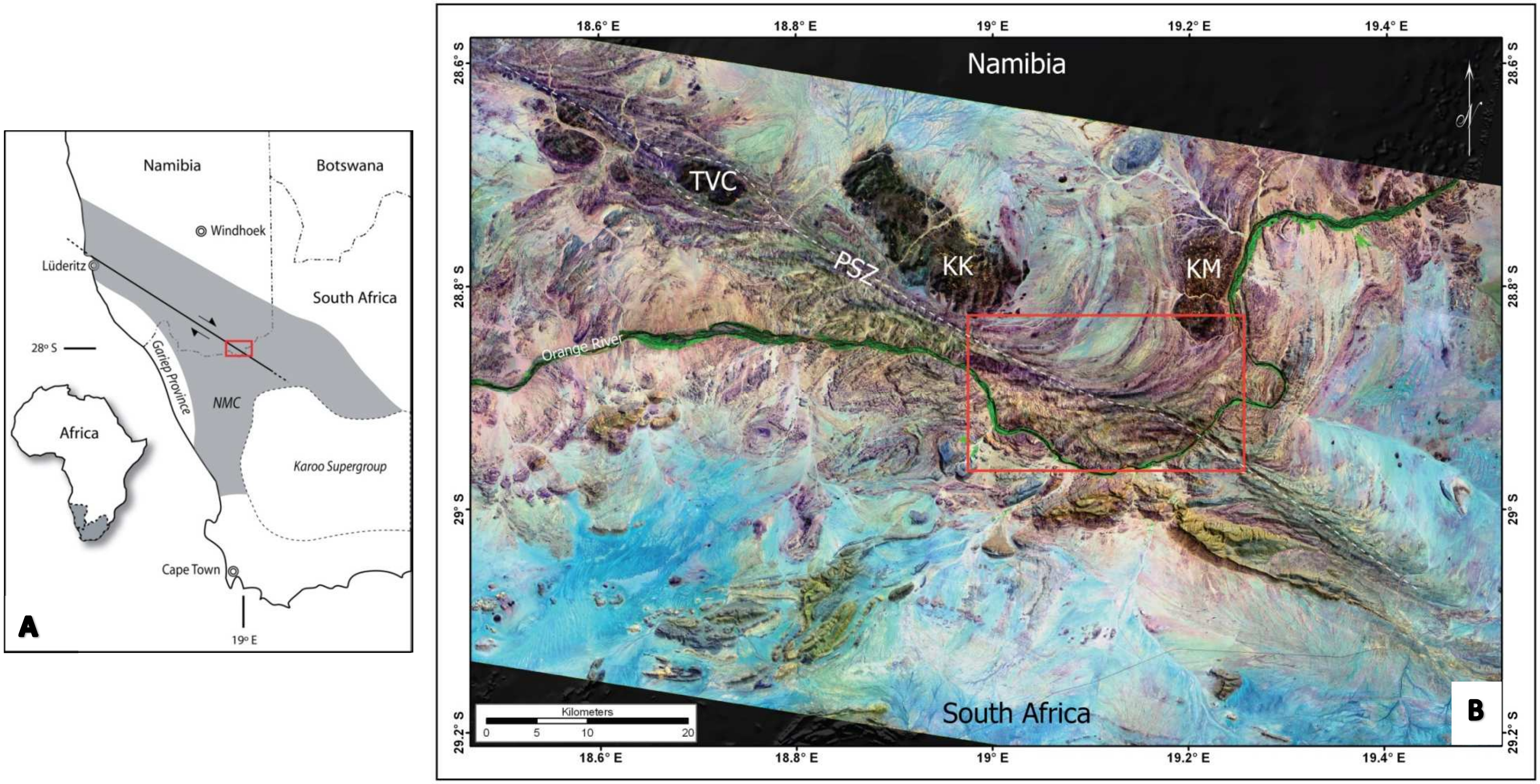

Figure. 1.1 (A). Locality map of study area (red rectangle) within the greater Namaqualand Metamorphic Province (grey) in South Africa and Namibia, indicating the extent of the Pofadder Shear-zone in Namibia and South Africa where it extends into the Atlantic Ocean and is covered by younger Karoo-aged strata respectively. (B) ASTER image (RGB = 1,3,5) of the PSZ in the vicinity of the greater study region (subset; Fig. 1.2). The image shows the rotation of the gneissic wallrocks into parallelism with the PSZ (stippled white line). Three gabbroic complexes; the TVC: Tantalite Valley Complex; KK: Kum Kum Norite; KM: Keimasmond Norite, collectively known as the Tantalite Valley Line, are pre-PSZ mafic complexes of the Gordonia Subprovince that are largely enveloped in rocks deformed by the PSZ.

Even at first glance different granite and pegmatite geometries and occurrences are apparent within and adjacent to the PSZ. The most obvious is the Skimmelberg Pegmatite Stockwork (SPS), an extensively developed pegmatite complex along the southern margin of the PSZ. The SPS is by far the largest exposed pegmatite complex in the Namaqua Metamorphic Complex and is located just north of the Orange River in the region of the Skimmelberg Mountains of the Karas Province in southern Namibia (Figs. 1.1-2). Here, intrusive and wall-rock relationships of the pegmatites that occur both within and outside the PSZ are preserved. Therefore for this study, a deeply-incised dry river section that forms a tributary to the Orange River was studied in detail. The river bed provides a ca. 4 km (28.873° S, 19.064° E to 28.901° S, 19.042°E) long traverse (Fig. 1.2), with up to 150 m topographic relief, providing a near-complete 3-D exposure through the 900 m wide core of the PSZ and wallrocks on either side. In addition to the SPS, granites and pegmatites occur within the high-strain PSZ core as well as the northern wallrocks. In each of these three locations pegmatite geometries and structural controls differ in addition to the PSZ structural fabrics. Therefore, for the purpose of this study, the traverse is divided into three structural domains, namely the (1) Northern Domain (ND) which, including the Waterfalls Locality (WL), forms the northern wallrocks of the (2) PSZ core, and (3) the Southern Domain (SD) that encompasses the SPS (Fig. 1.2).

This study aims to:

- Characterise fabric elements and the structural evolution of the PSZ in the study area.
- Describe the types and geometries of magma bodies in and around the PSZ.
- Illustrate spatial and temporal relationships of the various granitic and pegmatite bodies relative to the PSZ.
- Deduce the nature of structural controls for magma emplacement in the respective domains.
- Conclude on the magma emplacement history and different structural controls on melt migration and emplacement in the PSZ.

The structural inventory within each domain is presented in Chapter 4, the granite and pegmatite geometries and structural controls within each domain are presented in Chapter 5. Chapter 6 presents geochronological data that constrains the timing of granite and pegmatite emplacement in and around the PSZ. The control of magma emplacement in and around the PSZ is subsequently discussed in Chapter 7.

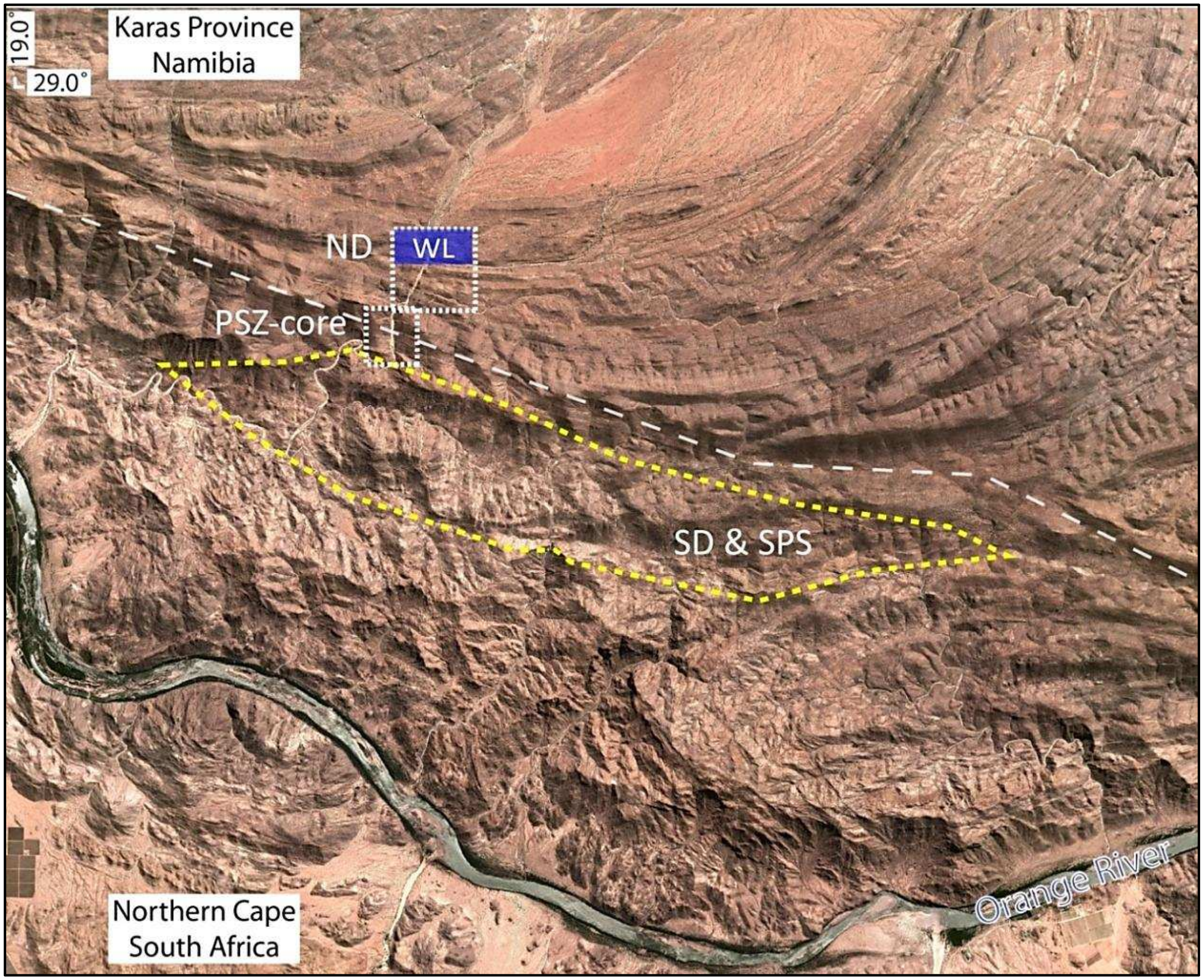

Figure. 1.2. Google Earth image of the greater study area illustrating the location of the SPS (yellow area) and the relative structural domains, namely the Northern Domain (ND); PSZ core; Southern Domain (SD). The blue rectangle represents the Waterfalls Locality (WL) within the ND.

1.3 Methodology

Field work for this study comprised altogether 3 months, spread over 5 shorter field visits between April 2009 and July 2011. Access to the remote river section is only possible via 4WD and the southernmost areas, north of the Orange River, could only be reached on foot.

Geo-referenced Google Earth imagery was used to create base-maps at varying scales, dependant on the variation in scene resolution and complexity of the exposure in the field. As part of this study, a regional geological map was produced through the detailed field mapping and remote sensing (Appendix A). Due to the extensive distribution of granites and pegmatites in the study area, both Google Earth (1-5 m resolution) and ASTER (15-90 m resolution) imagery were used as remote sensing datasets to delineate previously unmapped granitic bodies and lithological boundaries in and around the PSZ. In total, some 5168 granitic (*sensu lato*) bodies have been mapped in this study.

All locality readings were recorded using a handheld Garmin GPS 60s using a WGS84 datum. All structural readings were recorded using a Freiberg structural compass with a magnetic declination of 23^{o} west. Planar structural readings are represented by dip azimuth and dip angle whereas all linear readings are depicted as plunge azimuth and plunge angle.

Structural data represented in stereoplots are plotted as Schmidt equal area projections onto the lower hemisphere in Spheristat for Windows ® (2.2) by Pangaea Scientific (1990-1998). In the stereoplots, linear fabrics are illustrated using density distribution plots while planar fabrics are illustrated using great-circles. Additional software used for this study includes ERDAS Imagine (9.1) for remote sensing, ArcMap (9.3) for creation of all geological maps and Adobe Illustrator (CS6) is used for line drawings.

Samples of specific rock types were collected for petrographic, microstructural and geochronological analysis. A list of samples and short description is given in Appendix B.

2. Regional Geology

2.1 Regional Setting

The Namaqua Metamorphic Complex (NMC) in South Africa and Namibia forms the western sector of the 100-400 km wide Namaqua-Natal metamorphic belt (Fig. 2.1) that spans southern Africa (De Beer and Meyer, 1984; Jacobs et al., 1993; Thomas et al., 1993a,b 1994a,b). It forms a small, but significant segment of the global network of Grenville-aged orogenic belts that were created during the assembly of the supercontinent Rodinia in the late (ca. 1350-1050 Ma) Mesoproterozoic (Hoffman, 1991, 1992).

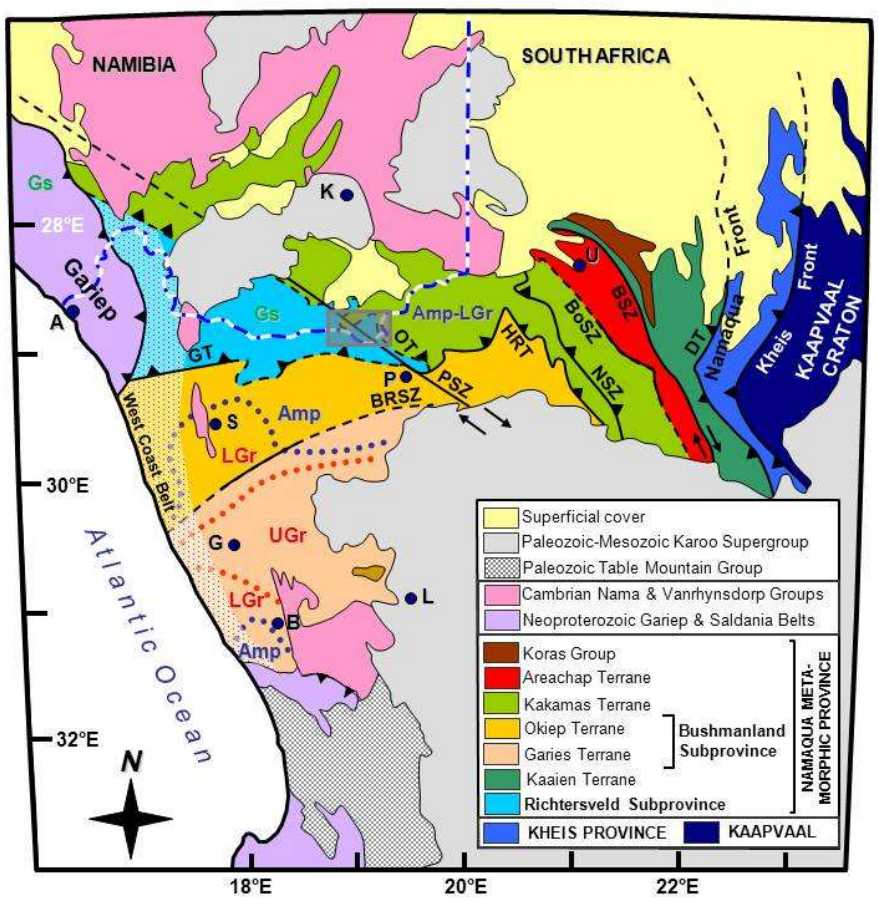

Figure. 2.1. Tectonostratigraphic and metamorphic subdivision of the NMC. Major crustal features and terrane boundaries of the NMC: GT= Groothoek Thrust; OT = Onseepkans Thrust; PSZ = Pofadder Shear-zone; HRT = Hartbees River Thrust; BRSZ = Buffels River Shear-zone; NSZ = Neusberg Shear-zone; BoSZ = Boven Rugzeer Shear-zone; BSZ = Brakbos Shear-zone; DT= Dabeep Thrust. Place Names are indicated as: A = Alexander Bay; B= Bitterfontein; G = Garies; K = Karasburg; L = Loeriesfontein; P = Pofadder; S = Springbok; U = Upington; Metamorphic isograds after Waters (1986): UGr = upper granulite facies; LGr = lower granulite facies; Amp = Amphibolite Facies; Gs = Greenschist Facies; The stippled region along the coast represent the West Coast Belt, a zone of tectonic reworking of the NMC during the Neoproterozoic Pan African Orogeny. Rectangle shows greater study area. Figure modified after Hartnady et al., (1985); Thomas et al., (1994a); Moen and Toogood (2007) and Macey et al., (2011).

The NMC records the accretion of juvenile Mesoproterozoic (1600-1200 Ma) supracrustal and plutonic rocks and the reworking of existing Kheisian age (ca. 2000 Ma) continental crust along the SW edge of the Archaean (>2500 Ma) Kaapvaal Craton (Hartnady et al., 1985). The amalgamation has traditionally been interpreted to be the result of continent – continent and/or arc-continent-continent (e.g. De Beer and Meyer, 1983) collisional tectonics that culminated between ca. 1200 and 1100 Ma (Hartnady et al., 1985; Joubert, 1971, 1986; Stowe, 1986; Thomas, 1989; Jacobs et al., 1993, 2008; Geringer et al., 1994; Thomas et al., 1989, 1993a,b, 1994a,b; Jacobs and Thomas, 1994; Moen, 1999; Moen and Armstrong 2008). The final convergent/collisional stages are referred to as the Namaqua Orogeny (*sensu stricto*; e.g. Tack et al., 1993; Cornell, 2006; Moen and Toogood, 2007; Miller, 2008) and is thought to be dominated by early north-vergent folding and thrusting (Thomas et al., 1994a) followed by oblique transcurrent shearing as a consequence of SW-directed indentor tectonics (Jacobs et al., 1993). Subsequent deformation during the Neoproterozoic Pan African orogenic event is believed to have only affected the West Coast Belt (Fig. 2.1).

Recent geochronological studies have highlighted a more complex and polyphase evolution of the Namaqua Orogeny in which at least two distinct tectono-metamorphic episodes at ca. 1200 and 1030 Ma can be distinguished (Armstrong et al., 1988; Gibson et al., 1996; Reid, 1987; Raith and Harley, 1998; Robb et al., 1999; Eglington and Armstrong, 2000, 2003; Bailie and Reid, 2000; Grantham et al., 2000; Raith and Cornell, 2000; Raith et al., 2003; Clifford et al., 2004, 2012; Pettersson et al., 2004, 2007; Eglington, 2006; Cornell et al., 2007, 2009; Bailie et al., 2011; de Beer, 2010; Macey et al., 2011; Clifford and Barton, 2012). The regional significance of these tectonic phases is not well understood and controversially discussed, but both events are associated with voluminous granite plutonism (e.g. Gibson et al., 1996; Robb et al., 1999; Macey et al., 2001, 2011; Clifford et al., 2004; Duchesne et al., 2007; de Beer, 2010) and high-grade metamorphism (amphibolite-facies and higher; Waters, 1986, 1988, 1989, 1990; Robb et al., 1999; Andreoli et al., 2006; Moen and Toogood, 2007), particularly in the central-western parts of the orogen (e.g. Raith and Cornell, 2000; Raith et al., 2003; Andreoli et al., 2006; Macey et al., 2011). The second high-temperature metamorphic event is considered as the peak metamorphic event and commonly considered to be the result of the mafic underplating of the Namaquan crust that also finds its expression in the intrusion of mafic bodies such as those of the Koperberg Suite between 1060-1020 Ma (e.g. Kisters et al., 1994; Gibson et al., 1996; Robb et al., 1999; Clifford et al., 2004). Figure. 2.2 summarises the geochronological history of Namaqualand. Comprehensive reviews on the evolution of the NMC can be found in Cornell et al., (2006), Eglington (2006), Macey et al., (2011) and references therein.

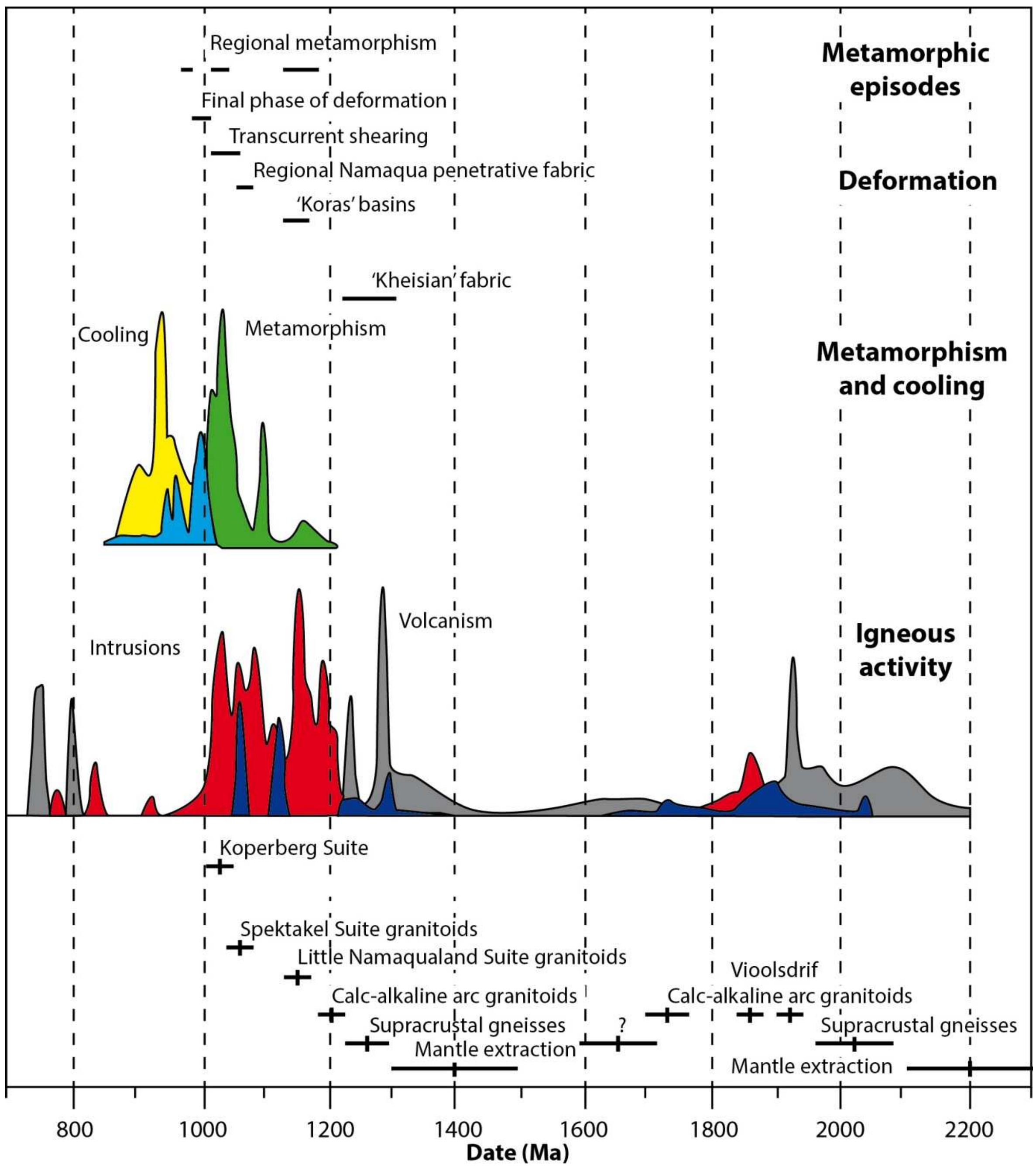

Figure. 2.2. Geochronology and correlation to deformation, metamorphic and igneous activity in the Namaqua Metamorphic Complex. Modified after Eglington (2006).

2.2 NMC

Based on variations in depositional environments and metamorphic grade, the NMC has been subdivided into various terranes and subprovinces (Fig. 2.1), separated by major structural breaks (Cornell et al., 2006; Miller, 2008). The ages of structures of the purported terranes are, however, similar and both the presence and the significance of supposedly terrane-bounding faults remains controversial (e.g. Jacobs et al., 2008). The presently accepted subdivision of the NMC includes, from west to east, the Richtersveld Subprovince, Bushmanland Subprovince, Kakamas, Areachap and Kaaien Terranes (Hartnady et al., 1985; Thomas et al., 1993a,b, 1994a,b). The study area falls exclusively in the Richtersveld Subprovince (Fig. 2.1). A more detailed lithological description for the Richtersveld Subprovince is provided below, but the remaining terranes/subprovinces are only briefly described in order to place the study area into a broader geological framework. The subdivision adopted in this study follows that of Thomas et al. (1994a).

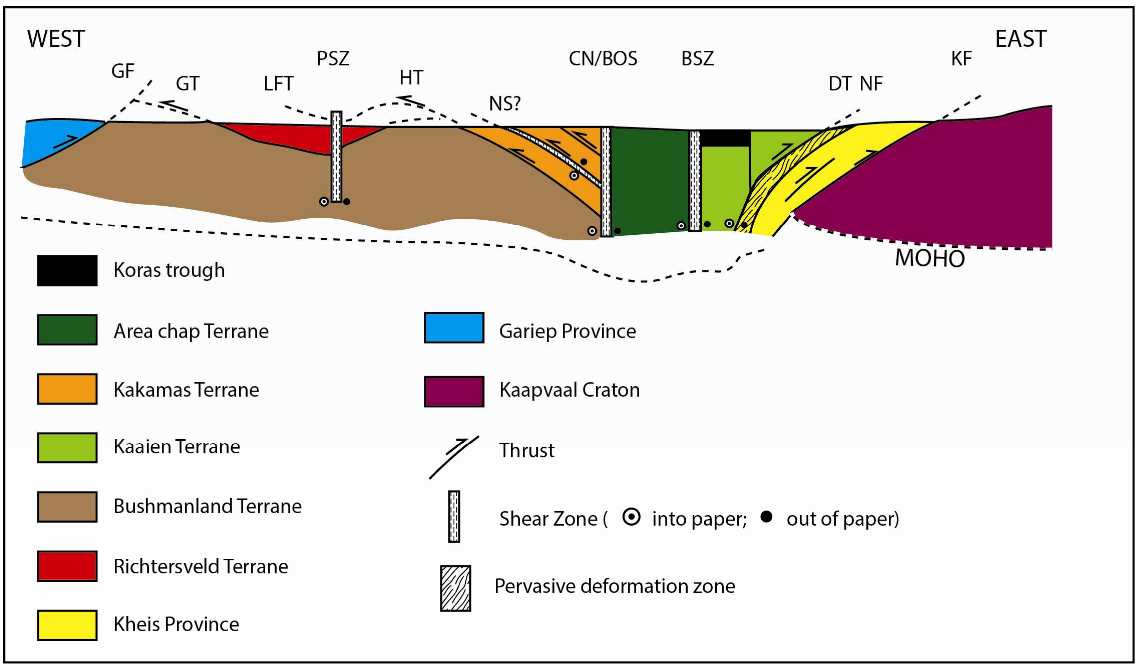

Figure. 2.3. Idealised cross section through the NMC illustrating the largely accepted subdivision of the NMC and the respective terrane boundaries and late-stage shears; GF = Gariep Front; GT = Groothoek Thrust; LFT= Lower Fish River Thrust; PSZ = Pofadder Shear-zone; HT= Hartbees River Thrust; NS=Neusberg Thrust; CN/BOS = Cnydas Shear/Boven Rugzeer Shear-zone; BSZ = Brakbosch Shear-zone; DT/NF = Dabeep Thrust/Namaqua Front; KF=Kheis Front. Modified after Thomas et al. (1994a).

2.2.1 Richtersveld Subprovince

The Richtersveld Subprovince represents a Palaeoproterozoic (1700-2000 Ma) block within the NMC that largely escaped Mesoproterozoic reworking, experiencing only low- to medium-grade (greenschist-facies) metamorphism (Barr and Reid, 1993, Cornell et al., 2006) in its centre. Metamorphic grades and the extent of the Namaquan overprint increase eastwards (Fig. 2.4) to reach amphibolite-facies grades (Joubert 1986; Thomas et al., 1994b) that were attained at ca. 1200 Ma (Welke et al., 1979). The Richtersveld Subprovince is made up of ca. 2000 Ma volcano-sedimentary successions that were intruded by voluminous granite and granodiorite between 1730 Ma – 1900 Ma (Reid, 1979; Reid and Barton, 1983) interpreted to represent the relics of a Palaeoproterozoic island arc (Reid, 1987, Cornell et al., 2006). The stratigraphic subdivision of the Richtersveld Subprovince is highly contended with models largely based on age correlations of units across shears and the contentious existence of bounding shear-zones separating the Richtersveld Subprovince from the other terranes (e.g. Beukes, 1973; Joubert, 1986; Thomas et al., 1993b). The structural ambiguity has led to further subdivision of the Richtersveld Subprovince into smaller lithostratigraphic terranes (e.g. Colliston et al., 1989 Colliston and Schoch, 1998, 2000a, 2000b, 2006) and/or incorporation of the Richtersveld Subprovince into the Bushmanland Subprovince (e.g. Moen and Toogood, 2007).

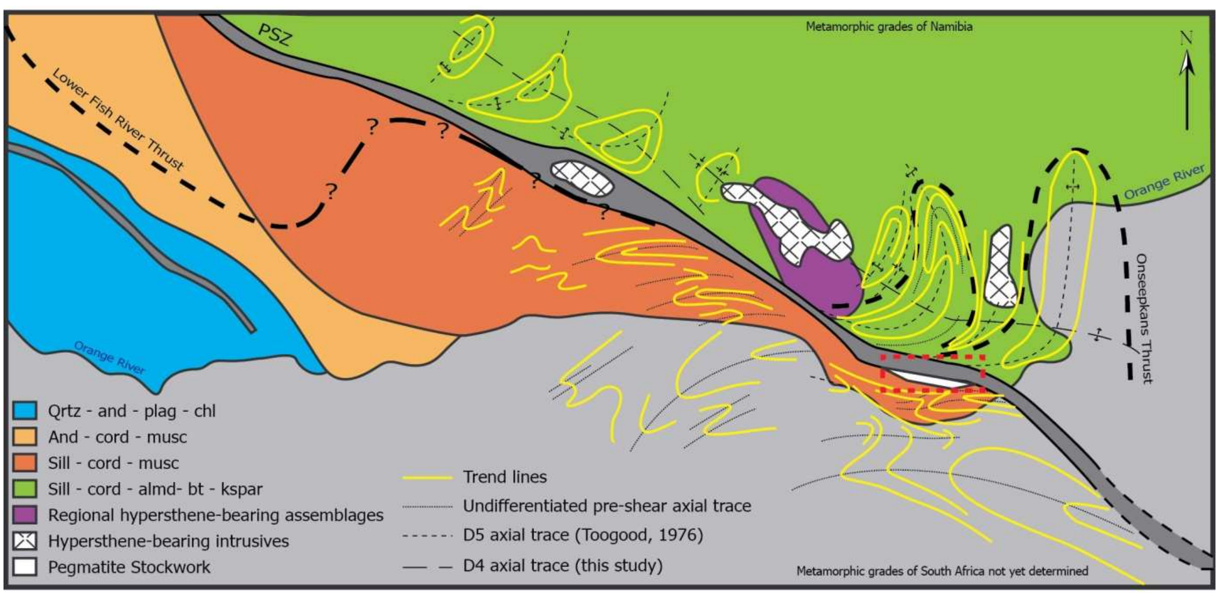

Figure. 2.4. Structural and metamorphic map of the eastern parts of the Richtersveld Subprovince in the vicinity of the PSZ, illustrating the progressive increase in regional metamorphic grade from west to east and the axial traces and form lines of pre-D_4 folds. The study area (red box) falls south of the Onseepkans Thrust, placing it exclusively within the Richtersveld Subprovince. Modified after Beukes (1973) and Toogood (1976).

The Richtersveld Subprovince is bounded in the west by the Gariep Front (e.g. Frimmel et al., 1996, 2011; Gresse et al., 2006), while in the south, it is proposed to be separated from the higher grade Bushmanland Subprovince by the Groothoek Thrust (Blignault et al., 1983). Recently, however, numerous authors question the existence of the Groothoek Thrust as a terrane boundary (e.g. Moen, 2001; Agenbacht, 2007; Moen and Toogood, 2007) and rather suggest the change in metamorphic grade from the Bushmanland Subprovince into the Richtersveld Subprovince as being gradational. To the east, the Richtersveld Subprovince is bound by the Onseepkans Thrust (Moen and Toogood, 2007), synonymous with the Hartebees River Thrust (Harris, 1988, 1992; Thomas et al., 1994a), dividing the Richtersveld Subprovince from the Kakamas Terrane. This division is proposed to extend northwards and form the continuation of the Lower Fish River Thrust (Colliston et al., 1989, 1991), synonymous with the Tantalite Valley Line (Becker et al., 2006; Miller, 2008), where the actual contacts are obscured by the later Pofadder Shear-zone (Fig. 2.4). Figure. 2.4 illustrates how the PSZ parallels metamorphic isograds separating two distinctly different metamorphic domains of upper-amphibolite to lower-granulite facies rocks in the north from mid- to lower amphibolite-facies rocks in the south (Beukes, 1973; Blignault, 1977; Toogood, 1976; Miller, 2008).

2.2.2 Bushmanland, Gordonia and Kheis Subprovinces

The Bushmanland Subprovince, bounded in the east by the Hartebees River Thrust against the Kakamas Terrane (Harris 1988, 1992; Thomas et al., 1994a), forms the largest terrane within the NMC and is further subdivided into two tectono-metamorphic terranes (Fig. 2.1), namely the Okiep Terrane in the north and the Garies Terrane in the south. The Bushmanland Subprovince is composed of limited Kheisian granitic gneiss basement and volcano-sedimentary successions deposited between (1900 Ma – 1200 Ma), being dominated by voluminous suites of syn- and late-tectonic Namaqua intrusive rocks (e.g. Macey et al., 2001). These include the ca. 1200 Little Namaqua Suite (Robb et al., 1999; Clifford et al., 2004; De Beer, 2010; Macey et al., 2011), the ca. 1060 Spektakel Suite (Robb et al., 1999; Clifford et al., 2004) and the mafic 1060-1030 Ma Koperberg Suite (McIver et al., 1983; Cawthorn and Meyer, 1993; Kisters et al., 1994).

Recent work, specifically in Namibia, has incorporated the Kakamas and Areachap Terranes into the Gordonia Subprovince (e.g. Eglington, 2006; Moen and Toogood, 2007; Miller, 2008). The Gordonia Subprovince is separated from the Kaaien Terrane by the Brakbos Shear (Coward and Potgieter, 1983; Stowe, 1983, 1986; Thomas et al., 1994a). The Boven Rugzeer Shear is proposed to separate the Kakamas from the Areachap Terrane (Harris, 1992). The Kakamas Terrane is generally considered to be composed of high-grade supracrustal gneisses, charnokites and granites with the late stage NNW- trending Neusberg Shear-zone separating an arenite and calc-arenite supracrustal succession in the east from high-grade metapelite and biotite-garnet paragneisses in the west (e.g. Van Bever Donker, 1980; Moen, 1988; Botha et al., 1976, Thomas et al., 1994a). The Areachap Terrane represents a narrow, NNW-trending terrane comprised of 1300 Ma amphibolite-grade metabasic and intermediate supracrustal gneisses (Geringer et al., 1986, 1994, Cornell et al., 1990). The Areachap Terrane contains juvenile Mesoproterozoic crust, showing clear subduction-related signatures (Geringer et al., 1986, 1994; Cornell et al., 1992; Jacobs et al., 2008) that are interpreted to indicate a series of volcanic arcs (Geringer and Ludick, 1990).

The Kaaien Terrane, recently incorporated into the Kheis Subprovince (e.g. Eglington, 2006), represents a transition from the high-grade Areachap Terrane to the Kheis-Kaapvaal Craton and is marked by older Sm-Nd model ages from the Areachap Terrane into the Kaaien Terrane across the Brakbos Shear-zone (Cornell et al., 1986; Thomas et al., 1994a). To the east, the boundary between the Kaaien Terrane and the Kheis Subprovince is the Dabeep Thrust (Hartnady et al., 1985, Cornell et al., 2006), although this remains contentious as geophysical data suggests the boundary to be the Namaqua Front (Thomas et al., 1994a, Hoal et al., 1993), a prominent suture zone dominated by dextral shearing (De Beer and Meyer, 1983; Stowe, 1983). The Kaaien Terrane is composed of Kheisian-aged metasediments and Namaqua-deformed to undeformed-unmetamorphosed volcanics (e.g. Botha et al., 1979; Moen, 1988), which are interpreted to have formed as an extensional back-arc basin to the Areachap Terrane (Thomas et al., 1994b) between 1290 Ma (Moen et al., unpublished data) and 1171 Ma (Gutzmer et al., 2000).

2.3 Late stage evolution of the NMC

Following the burial and late-stage high-T metamorphism, unroofing of the Namaqua orogen led to the cooling of the NMC rocks to temperatures below ca. 350^{o}C by 950-980 Ma (Barton and Burger, 1983; Cornell et al., 1990, 1992; Grantham et al., 1993; Eglington, 2006). During the exhumation and cooling, deformation was characterised by the development and/or reactivation of a series of ductile, dextral NW-SE trending shears (Fig. 2.5). Shearing is interpreted to have occurred due to lateral escape tectonics in response to the sustained southward indentation of the rigid Kaapvaal Craton into the newly accreted NMC (Humphreys and Van Bever Donker, 1987; De Beer and Meyer, 1984; Van Bever Donker, 1991; Jacobs et al., 1993; Jacobs and Thomas, 1994). The PSZ, also referred to as the Pofadder-Marshal Rocks Lineament (e.g. Miller, 2008) or the Tantalite Valley mylonite belt (e.g. Joubert, 1975), is the largest and best exposed example of these late-tectonic shear-zones. The PSZ, along with the other late-stage dextral shears throughout the NMC, exhibits retrograde deformation fabrics and mineral assemblages that indicate formation under broadly greenschist-facies conditions (Toogood, 1976; Van Bever Donker, 1980; Stowe, 1983; Humphreys and Van Bever Donker, 1990; Geringer et al., 1994). Shear-zone kinematics are commonly dominated by wrench faulting with localised dip-slip components in response to northerly directed principal stresses at the later stages of indentation tectonics (e.g. Toogood, 1976; Van Bever Donker, 1991; Jacobs et al., 1993; Thomas et al., 1994a). Work on shears from this late-stage cluster has largely been economically motivated and centred around the copper district of the Areachap Terrane (e.g. Geringer et al., 1986, 1988, 1994; Stowe, 1983, Moen, 1988, Cornell et al., 1992; Bailie, 2011, 2012) with little focus on the PSZ and, significantly, its relationship to the pegmatites of the regional pegmatite belt (discussed below).

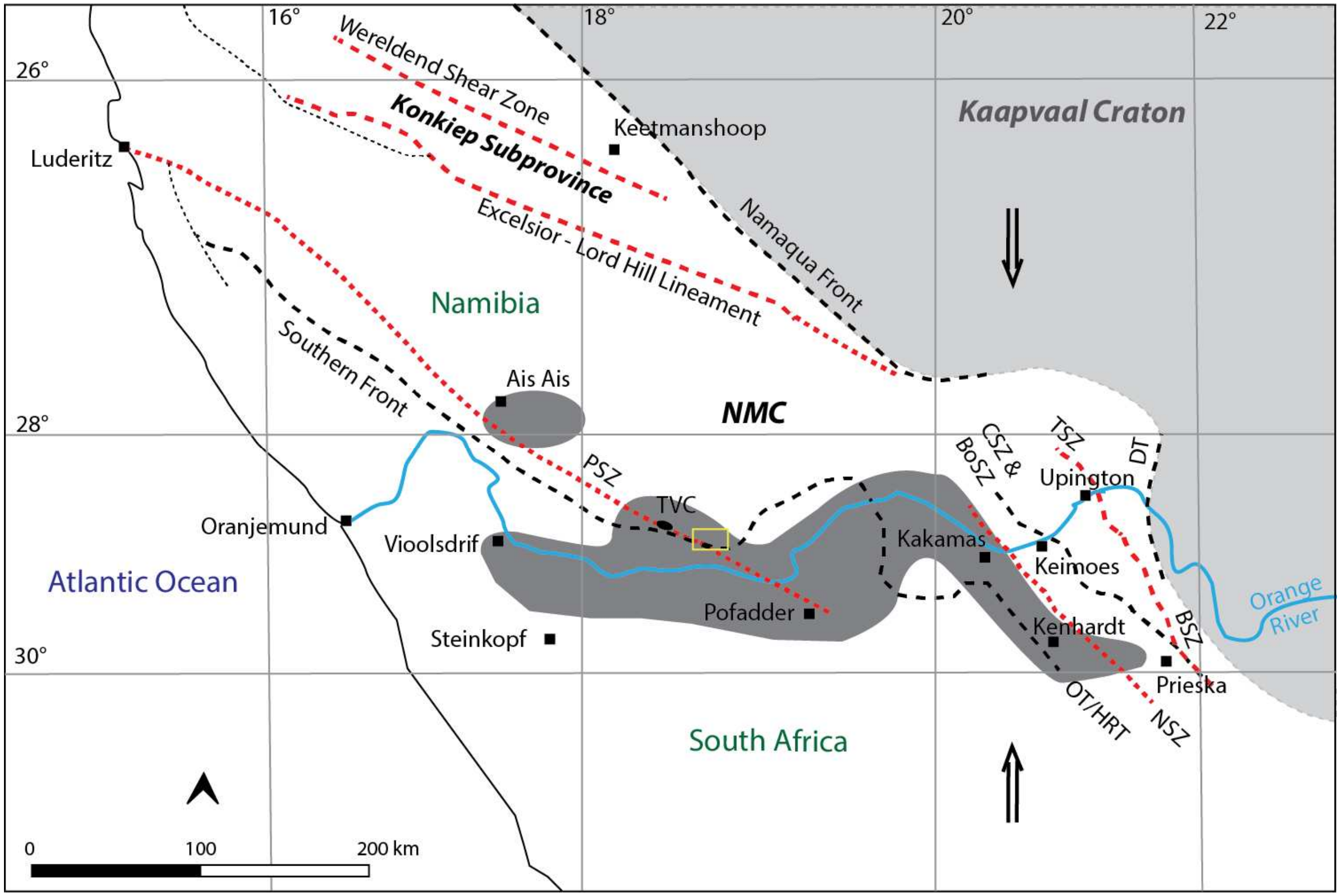

Figure. 2.5. Diagram illustrating the position of NW-SE trending structural features within the NMC formed due to a prolonged period of indentor tectonics of the Kaapvaal Craton and the NMC. Not all shears developed as late-stage dextral shears but some, particularly those around Upington, are interpreted to have been reactivated during the cooling of the NMC between 1080-965 Ma (Cornell et al., 1992). Shears highlighted in red are those described to have recorded late-stage dextral movement. The dark-grey colour represents the outline of the Northern Cape pegmatite belt (e.g. Gevers et al., 1937; Martin, 1965; Schutte, 1972; Hugo, 1970; Beukes, 1973 and Blignault, 1977). The yellow box indicates the study area. Abbreviated structures; OT = Onseepkans Thrust; PSZ = Pofadder Shear-zone; HRT = Hartbees River Thrust; CSZ = Cnydas Shear-zone; BoSZ = Boven Rugzeer Shear-zone; NSZ = Neusberg Shear-zone; TSZ = Trooilapspan Shear-zone; BSZ = Brakbos Shear-zone; DT= Dabeep Thrust. Modified after Toogood (1976), Blignault (1977) and Joubert, (1986).

2.4 Pegmatite belt

The mainly transcurrent late-stage shearing and unroofing of the NMC is accompanied by the emplacement of late-stage granites (e.g. Stowe et al., 1983; Bailie, 2011) and the development of regionally widespread pegmatites throughout the NMC and across terrane boundaries (e.g. Stowe, 1983; Cornell et al., 1992; Cornell and Pettersson, 2007; Miller, 2008). An important aspect central to this study is the close association of the PSZ with the pegmatite belt. The north-westerly trending PSZ intersects the broadly undulating, easterly trending belt in its southern portion.

In the Northern Cape Province of South Africa and the southern Karas region of Namibia, the pegmatites form an extensive 16 km wide, ca. 450 km long, continuous W-E trending belt extending from Vioolsdrif to Kenhardt in South Africa (Gevers, 1936; Gevers et al., 1937; Schutte 1972; Hugo, 1970; Blignault, 1977, Cornell et al., 2006; Cornell and Pettersson, 2007; Appendix A; Fig. 2.5). The extent of the belt in Namibia is not well documented, but is proposed to extend as far as Ais-Ais (e.g. Blignault, 1977; Miller, 2008). The pegmatites mainly occur as several hundred meter long and up to 20 m wide, lenticular to sheet-like bodies with the majority occurring concordant to the regional fabric and a few as smaller discordant bodies (Hugo, 1970). The pegmatites vary in composition and internal structure, ranging from simple, homogeneous and unzoned quartz-feldspar-muscovite-bearing assemblages to complexly zoned, heterogeneous bodies containing more exotic minerals such as beryl, lepidolite, columbite-tantalite, sillimanite, together with U- and REE-bearing minerals, which were sporadically mined (Gevers, 1936; Gevers et al., 1937; Hugo, 1970, Minnaar and Theart, 2006). The distribution and compositional variation across the pegmatite belt is currently under investigation (Minnaar, in prep). The structural setting of the belt is not yet well constrained and the belt has previously been correlated with tectonostratigraphic boundaries such as the Groothoek thrust (e.g. Cornell et al., 2006) and the Southern Front (Blignault, 1977). The emplacement of the pegmatite belt is considered to have occurred between ca. 1025 Ma and 945 Ma (Holmes, 1950; Jahns, 1955; Nicolaysen, 1962; Nicolaysen and Burger, 1965). Older generations of pegmatites have, however, been dated at 1104 Ma in the Prieska region but are related to earlier metamorphic phases (Cornell et al., 1992). Detailed studies on pegmatites within the belt have been focused on their economic potential in South Africa (e.g. Hugo, 1970; Minnaar and Theart, 2006) and Namibia (e.g. Moore, 1975). The SPS has only been documented on regional maps (e.g. Cameron, 1936, Toogood, 1976), but the controls of pegmatite emplacement have not been described or discussed in any detail.

2.5 Structural geology and correlation of regional deformation episodes

Regional fabrics and structures surrounding the PSZ are described by Toogood (1976) who distinguishes six (D_1 – D_6) different phases of deformation. The D5 and D6 episodes relate to deformation along the PSZ. In this study, only four stages of deformation (D_1-D_4) are distinguished. Differences in the nomenclature between the terminology devised by Toogood (1976) and this study mainly relate to the recognition of the progressive nature of deformation events, particularly shearing associated with the PSZ. Deformation stages D_1 – D_3 are associated with regional deformation events in the Bushmanland and Gordonia Subprovinces, whereas the D_4 deformation is related to deformation along the PSZ and exclusively to the structures associated with the PSZ.

A brief synopsis of the structural nomenclature adapted in this study follows and can be used in conjunction with Appendix C.

D_1: This early deformation phase is not recognised within this study, but is reportedly characterised by rootless, isoclinal folds within older (ca. 1800 Ma) supracrustal rocks occurring in other parts of the NMC (e.g. Joubert, 1971, 1974; Cornell et al., 2006; Miller, 2008).

D_2: This deformation phase is considered the principal deformation phase of the Namaqua orogeny with associated amphibolite-grade metamorphism (650-700^o C at 4kbar; Waters 1986, 1989) in the southern parts of the Bushmanland Subprovince. D_2 fabrics are characterised by large-scale, east-west trending, isoclinal folds (F_2) and an associated, regionally consistent, E-W trending penetrative, subhorizontal foliation (S_2), with an E- or NE- plunging L_2 mineral stretching lineation (Joubert, 1971, 1986). The stretching lineation is thought to be parallel to the regional top-to-the SW kinematics and transport direction during the Namaqua orogeny (e.g. Colliston and Schoch, 1998, 2000a; Moen and Toogood, 2007; Macey et al., 2011). S_2 is largely defined by the alignment of biotite, muscovite and sillimanite in metapelites and quartzo-feldspathic rocks, whereas hornblende aggregates define the foliation in mafic schists and gneisses (Moen and Toogood, 2007).

Within the study area, the gneissic foliation is expressed by the compositional variation in and/or across various lithological units. Gneisses are mainly banded hornblende-biotite gneisses or quartzo-feldspathic gneisses (Fig. 2.6a). The S_2 foliation is further defined by the alignment of porphyroclasts and the formation of quartzo-feldspathic augen gneisses and hornblende-biotite augen gneisses where quartz and biotite and/or hornblende mineral aggregates anastomose around large (1 cm – 5 cm) K-feldspar augen respectively (Fig. 2.6b).

Figure. 2.6. (A) D_2 fabrics in hornblende-biotite bearing orthogneiss with large K-feldspar phenocrysts forming augen-gneiss textures. (B) Mafic, banded hornblende-biotite gneisses typical of S_2 within the wallrocks of the PSZ.

This phase of deformation (D_2) ended between ca. 1120 Ma, bracketed by the age of the youngest deformed gneisses of the Little Namaqualand Suite (Rob et al., 1999; Raith and Cornell, 2000; Raith et al., 2003; Cornell et al., 2006, 2008; Clifford et al., 2004; de Beer et al., 2002; Eglington, 2006; de Beer, 2010; Macey et al., 2011) and 1086 ± 16 (SHRIMP) from rocks of the weakly deformed Spektakel Suite (Rob et al., 1999; Grantham et al., 2000; Clifford et al., 2004; Cornell et al., 2006, 2009; Eglington, 2006).

D_3: The D_3 deformation event is characterised by kilometre-scale, originally E-W-trending, upright- to inclined, shallow-plunging, open F_3 folds (Joubert, 1971, 1975; Macey et al., 2011). These large-scale F_3 folds rotate existing F_2 folds and earlier (D_1-D_2) fabrics (Fig. 2.4). The formation of these folds is closely linked to the formation of steep structures containing syn-deformation intrusions and melt breccias (e.g. Kisters et al., 1996a,b, 1998). Rocks of the 1060-1030 Ma Koperberg Suite in the Okiep Copper District intruded during D_3, thereby constraining the late-Namaquan timing of F_3 folding. This timing is coeval with the peak of high-T metamorphism in the NMC and granulite-facies conditions in the highest-grade parts of the Bushmanland Subprovince (T = ca. 830 ^{O}C, P = 5-7 kbar; Zelt, 1980; Schmitz and Bowring, 2003; Eglington, 2006). Within the study area F_3 fold geometries are not well defined as they are deformed due to subsequent deformation (D_4) and transposed and/or truncated by the high-strain core of the PSZ or refolded by F_4 folds to form doubly plunging folds (Fig. 2.4).

D_4: This deformation phase relates to the deformation within and adjacent to the PSZ**.** Due to the superimposition and transposition of earlier fabrics into D_4 shear-zones, a clear distinction of fabrics in the regional-scale shear-zones is often difficult, particularly in the high-strain core of the PSZ. Fabrics associated with the PSZ (D_4) are defined by both amphibolite- and greenschist-facies mineral assemblages and show a range from pervasive ductile (continuous) via brittle-ductile fabrics to essentially brittle (discontinuous) fabrics (e.g. Toogood, 1976; Mclaren, 1988; this study). There are clear overprinting relationships from earlier amphibolite-grade and ductile to greenschist-facies and more brittle fabrics, indicating that deformation occurred under progressively lower-grade conditions during a prolonged period of exhumation (discussed in Chapter 4). Hence, D_4 fabrics and structures are treated in this study to describe a polyphase deformation history related to progressive shearing along the PSZ. The largely co-axial nature of high- and lower-grade planar and linear fabrics indicates the progressive nature of the deformation. Based on overprinting relationships, mineral assemblages and deformation textures of the D4 event have been subdivided in this study into separate stages ($D_{4a\text{-}b}$), representing the progressive evolution of the shear-zone and related fabrics. The structural characteristics for individual deformation stages ($D_{4a\text{-}b}$) that occur within the study area are described in detail in Chapter 4.2.

3. Rocks of the field area

3.1 Lithostratigraphy of host rocks

The stratigraphy devised for the study area (Appendix A) is largely derived from the comprehensive fieldwork of Moen and Toogood (2007). The volcano-sedimentary successions in the study area are therefore interpreted to include those of the Orange River (see also Droëboom Group) and Bushmanland Groups (Moen and Toogood, 2007). The nomenclature and subdivision of the intrusive rocks is again problematic, but, based on regional distributions, can broadly be divided into two suites, namely those of the Vioolsdrif Suite (Moen and Toogood, 2007) and those of undifferentiated pink gneisses, previously grouped as the Hoogoor Suite (SACS, 1980). The Vioolsdrif Suite is composed of calc-alkaline granodiorites, mafic and felsic intrusives (Thomas et al., 1996; Moen and Toogood, 2007). The undifferentiated gneisses have recently been defined by Moen and Toogood (2007) and are composed of quartzo-feldspathic augen gneisses, hornblende-biotite augen gneisses and lesser deformed granitic and mafic intrusives.

The ND is dominated by tectonically interleaved successions of the quartzo-feldspathic paragneisses and metavolcanic rock from the greater volcano-sedimentary groups as well as tonalitic-granodioritic (i.e. Noudap Gneiss) and granitic orthogneisses (i.e. Coboop Gneiss). The PSZ core, although largely structurally overprinted, is lithologically similar to the ND but has an increased volume of amphibolitic successions. South of the PSZ amphibolites and supracrustals are rare and the orthogneisses are typically interlayered displaying lit-par-lit like intrusive relationships. In the SD, along the boundary with PSZ core, granodiorite form the dominant lithology and is intruded by more felsic quartzo-feldspathic granites and gneissic equivalents. Further south, outside the study area, the quartzo-feldspathic gneisses are more prominent grading into muscovite-rich, sillimanite-bearing quartzo-feldspathic gneisses and sillimanite-biotite schists of the Onseepkans Formation (Moen and Toogood, 2007).

3.2 Pegmatites

Most of the intrusive granitoids dealt with in this study are pegmatites and not granites (*sensu stricto*). The following chapter provides a brief overview of the characteristics of the complex crystal-melt-H_2O system that pegmatites represent and its bearing on our understanding of melt migration and emplacement.

Pegmatites are very coarse grained (> 20 mm) igneous rocks commonly composed of granitic minerals (quartz + feldspar ± muscovite ± biotite), usually forming massive vein like bodies (London, 2003). Although intermediate and mafic pegmatites occur, they are less common. Traditionally, the term 'pegmatitic' is used purely for the textural classification of any rocks with abnormally large grain sizes (Gillespie and Styles, 1999). Pegmatite classification is complex and not without controversy with the most widely accepted terminology having been devised by Černý (1991a, 1991b, 1992, 2000) and Černý and Ercit (2005). Pegmatites can generally be classified based on their geological setting and/or the identification of enriched trace elements, specifically of the REE elements (e.g. Černý and Ercit 2005). Table. 3.1 summarises the most commonly accepted classification scheme for granitic pegmatites. Accurate classification of pegmatites therefore requires detailed geochemical analysis, a process that falls outside the scope of this study. Field descriptions of pegmatites are broadly based on their shape (e.g. lenticular, tabular, irregular, bulbous, etc.), the complexity of their mineralogy and the internal distribution of the mineral aggregates and/or structures (homogeneous or heterogeneous, zones, etc.; e.g. Cameron, 1936). The internal composition of granitic pegmatites varies and can consist of concentric zones, usually crystallizing from the walls inwards from multiphase mineral assemblages at the onset of crystallization to singly saturated units in the centre (e.g. Cameron et al., 1949; London, 2005, London and Kontak, 2012).

Class	Petrogenetic Family	Typical Minor Elements	Metamorphic Environment	Relation to Granites	Structural Features
Abyssal	-	U, Th, Zr, Nb, Ti, Y, REE, Mo	(upper amphibolite to) low- to high-P granulite facies; (~4-9 kb; ~700-800°C)	none (segregations of anatectic leucosomes)	conformable to mobilized cross-cutting veins
Muscovite	-	Li, Be, Y, REE, Ti, U, Th, Nb>Ta	high-P, Barrovian amphibolite facies (kyanite-sillimante); (~5-8 ; ~650-580°C)	none (anatectic bodies) to marginal and exterior	quasi-conformable to cross-cutting
Rare-element	**LCT**	**L**i, **C**s, Nb>**T**a, Rb, Be, Ga, Sn, Hf, B, P, F	low-P, amphibolite to upper greenschist facies (andalusite-sillimanite); (~2-4kb, ~650-500°C)	(interior to marginal to) exterior	quasi-conformable to cross-cutting
	NYF	**N**b>Ta, **Y**, **F**, REE, Ti, U, Th, Zr	Variable	interior to marginal	interior pods, conformable to cross-cutting exterior bodies
Miarolitic	**NYF**	Nb>**T**a, **Y**, **F**, Be, REE, Ti, U, Th, Zr,	Shallow to sub volcanic; (~1-2 kb)	interior to marginal	interior pods and cross-cutting dykes

Table. 3.1. The Four classes of granitic pegmatites (Černý, 1991a).

At present, there are two main models for the origin of granitic pegmatites (London, 2005; Simmons et al., 1995, 1996, 2008; Černý et al., 2012; London and Morgan, 2012). One school of thought relates pegmatite formation to late-stage fractional crystallization processes of granitic plutons, largely based on their proximal spatial associations and close trace element resemblance to the granitic plutons (e.g. O'Connor et al., 1991). The processes for pegmatites forming through late-stage fractional crystallization was first described by Jahns and Burnham (1969) and was later comprehensively reviewed by other authors

(London, 2005; Simmons 2008; London and Morgan, 2012; London and Kontak, 2012). The recent reviews highlight the importance and role of fluxing agents such as B, H_2O, F, P, and Li in the melts in lowering melt viscosity (Simmons et al., 2008), the crystallization of the volatile-melt-crystal mixtures away from the equilibrium liquidus boundary with or without the presence of aqueous fluid phases (London, 2005), the effects of undercooling and quick cooling rates and the low nucleation rates, which give rise to the characteristically large crystals (Simmons et al., 2008; London, 2005). Pegmatites derived through fractional crystallization are largely grouped into the Muscovite-REE, Rare-element and Miarolitic classes, which occur under granulite to lower-pressure amphibolite facies conditions and are also found intruded in greenschist facies conditions respectively (e.g. Černý and Ercit, 2005).

A second school of thought relates the formation of pegmatites to the partial melting of high-grade rocks. This is largely due to the common similarity between pegmatites and host-rock major element geochemistry (e.g. Novák et al., 1999), the isolation of pegmatite dykes from any known sources (e.g. Simmons et al., 1995), the identification of leucosomes with pegmatitic textures in metamorphic terranes (Martin and De Vito, 2005) and the difficulty in relating highly evolved magma compositions to the comparatively primitive chemistry of likely sources (e.g. Norton and Redden, 1990). Pegmatites formed through anatexis are commonly interpreted to belong to the Abyssal and Muscovite classes occurring in low- to high pressure (4-9 kbar; 700 - 800 ^{o}C) and high pressure (5-8 kbar; 580 - 650 ^{o}C) metamorphic environments respectively (e.g. Černý and Ercit, 2005). These pegmatites are expected to be mineralogically simple and usually devoid of substantial zonation, commonly composed of quartz + sodic plagioclase + K-feldspar ± muscovite ± garnet ± biotite ± apatite ± beryl ± tourmaline (Barr, 1985). The formation of pegmatites as products of partial melting has been studied in less detail but has been supported by various authors (e.g. Norton and Redden, 1990; Hutton and Revy, 1992; Simmons et al., 1995, 1996; Druguet and Hutton, 1998; Novák et al., 1999; Martin and De Vito, 2005) and have been documented in areas of deformation such as shear-zones (e.g. Northrup and Mawer, 1991; Carreras and Druguet, 1994; Schärer et al., 1996; Zegers et al., 1998; Hanmer et al., 2002).

In both genetic models, pegmatites represent felsic hydrous granitic liquids that largely mimic the behaviour of viscous felsic magmas (e.g. London, 2005). The magmas are therefore similarly transported from their sources through one or a combination of transport mechanisms. Emplacement geometries may be highly complex and controlled by the interplay of (a) pegmatite fluid pressures, (b) rheological states of the host rocks, (c) regional and local stresses, (d) pore-water pressures, (e) presence of anisotropies, and (f) creation of dilatational sites (Brisbin, 1986). These factors are largely controlled by the relative depth and deformation of the system at a specific time during shear-zone formation and/or exhumation (e.g. Brisbin, 1986). Therefore, understanding pegmatite geometries and their relative modes of transport/emplacement, both inside and outside the PSZ, aids in the generic understanding of this interplay of magmas and shear-zones.

4. Structure of the PSZ

The PSZ extends for over 500 km from the Atlantic seaboard in Namibia to ca. 30 km SE of Pofadder in the Northern Cape of South Africa (e.g. Moen and Toogood, 2007; Miller, 2008;). The trace of the shear-zone is defined by a steep NE dipping, 2-7 km wide core of mainly amphibolite-facies mylonites (Toogood, 1976), describing a gently undulating, but regionally consistent WNW trend of around 300°. The core is bordered on both sides by polyphase deformed (D_2-D_3) orthogneisses and minor supracrustals that are rotated over a width of up to 30 km into the core of the PSZ (Figs. 1.1-2; Appendix A). This clockwise rotation of the wallrocks and earlier fabrics and structures underlines the dextral strike-slip kinematics along the PSZ (Toogood, 1976; Moen and Toogood, 2006; Miller 2008).

4.1 Previous work

Previous work on the PSZ has largely been on a regional scale (e.g. Beukes, 1973, 1978; Joubert, 1974, 1975; Jackson, 1976; Mclaren, 1988), or has focused around the copper-nickel deposits of the Tantalite Valley Complex (Fig. 1.1b), an ultramafic body that is enveloped by the PSZ (Moore, 1981). Toogood (1976) focuses on the structural and metamorphic evolution of the surrounding gneissic terrain and describes textures and kinematics within the core (Appendix C) of the PSZ, describing it as a "….*zone of anomalously high non-coaxially accumulating finite strain… (Toogood, 1976, p99.)"*, defined by mylonites and interfingering gneissic units. Toogood (1976) also highlights the heterogeneous strain in the PSZ and distinguishes non-coaxial from co-axial strain domains. The non-coaxial strike-slip component was mainly deduced from the pronounced sigmoidal drag of the wall-rocks on either side of the PSZ and the resulting fold interference patterns with earlier fold generations and preservation of asymmetric fabric elements. He concludes that the PSZ has experienced up to 40% pure shear shortening during predominately dextral strike-slip kinematics with a simple shear direction of 107^{o}.

4.2 Fabrics and structural evolution of the PSZ in the study area

Based on (1) overprinting relationships, and (2) distinctly different mineral assemblages and microstructural development, fabrics in the PSZ can be seen to describe a progressive evolution that was already hinted at by Toogood (1976). In this study, only two main fabric-forming phases ($D_{4a\text{-}b}$) related to the PSZ are distinguished. A clear distinction between inherited, older and actual shear-zone fabrics (D_4) is often problematic and is primarily based on strain intensity. Fabrics in the mainly medium- to coarse-grained gneiss units bordering the PSZ are mainly re-orientated D_2 fabrics, commonly with lower fabric intensities compared to those in the PSZ. In general, the occurrence of protomylonites and mylonites is taken as an indication of D_4 fabrics and mylonitic textures (*sensu stricto*) seem restricted to the shear-zone. Fabric intensities and, thus, strain is heterogeneous across the PSZ. This has a profound effect on the geometry and contact relationships between granite and pegmatite sheets and the PSZ, so that a brief characterisation of fabric development in the PSZ is given below and discussed in more detail within the sections dealing with each of the study domains (Figs. 1.2; 4.1).

D_{4a}

Deformation during D_{4a} includes the rotation and ductile folding of the gneissic wallrocks and formation of mylonitic fabrics in and adjacent to the PSZ. D_{4a} fabrics may therefore include (1) merely passively rotated, composite fabrics (S_2/S_4, L_2/L_4) inherited from the wall-rocks outside the shear-zone, together with (2) newly formed fabrics (S_{4a}, L_{4a}) related to deformation in the PSZ. The boundary of the PSZ is, therefore, not always sharp, particularly along the northern contacts. The pervasive recrystallization of all mineral components, including feldspar and hornblende, and the amphibolite-facies parageneses defining the fabrics indicate deformation under at least mid-amphibolite-facies conditions

D_{4b}

D_{4b} fabrics (S_{4b}, L_{4b}) and structures are largely parallel to those of D_{4a}, but are characterised by retrograde, broadly greenschist-facies mineral assemblages and a brittle-ductile overprint of earlier high-T (D_{4a}) structures. Importantly, pervasive D_{4b} fabrics and structures are largely confined to the PSZ core, with only localised D_{4b} reactivation of older D_{4a} structures outside the shear. This is clearly the result of the localisation of later, retrograde strain increments into the shear-zone.

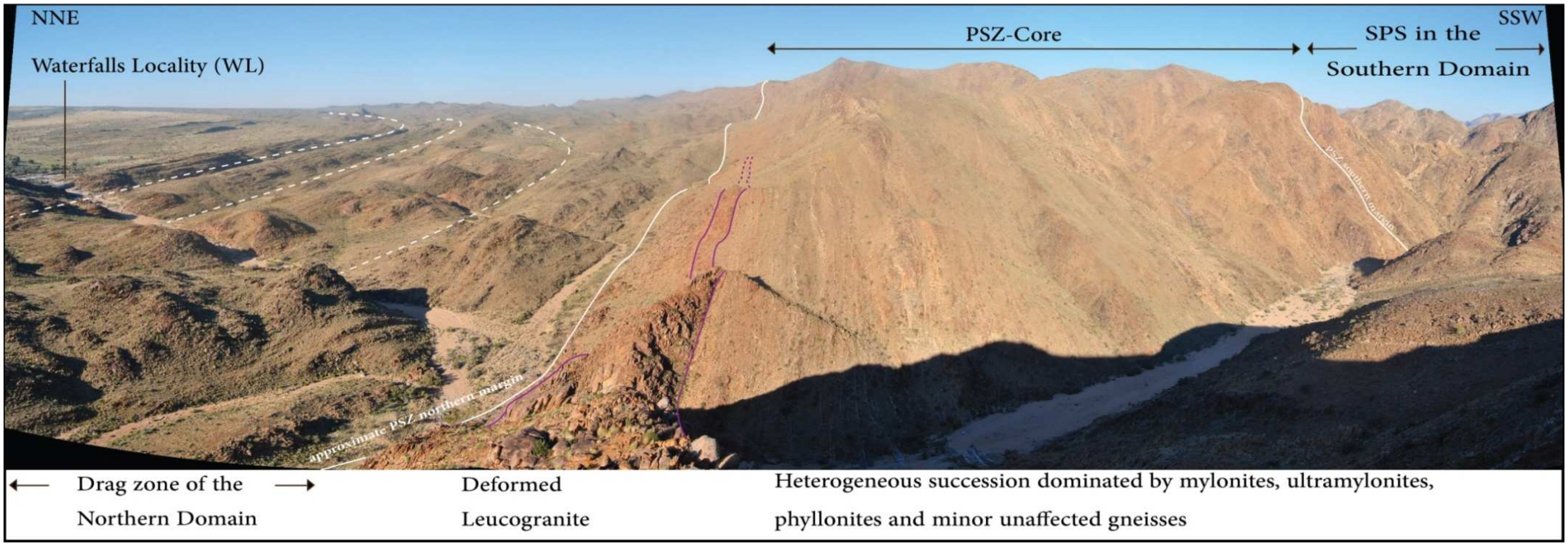

Figure. 4.1 Panoramic, along-strike view (to the SE) across the PSZ and adjacent wallrocks showing the respective study domains (ND, PSZ core, SD). Field of view is approximately 2 km wide in the middle ground of the photo. High-grade gneisses along the northern margin of the shear-zone show a pronounced drag from regionally northerly trends into the northwest-southeast trend of the PSZ (lithological layering annotated by white dashed lines). The actual shear-zone boundaries are not always well defined, but the core of the shear-zone, defined by northwest-trending mylonitic fabrics, is indicated by solid white lines in the photo. The pink lines annotate the strike of a ca. 1230 Ma deformed leucogranite that is transposed by the PSZ.

Folding F_4

For this study, D_4 related folding is considered to include the transposition of the earlier (F_2-F_3) folds into parallelism with the shear-zone fabric (Fig. 2.4) and/or the formation of similarly orientated F_4 folds (Fig. 4.1b) in and adjacent to the shear. In the ND, F_4 folds refold existing planar fabrics (S_2) and contain a D_4 planar fabric (S_{4a}; Fig. 4.2b). In the wall-rock gneisses, F_4 folds vary in size, displaying amplitudes between 10 and 500 cm. The folds form upright, WNW plunging, closed- to isoclinal folds.

Due to high-strain intensities F_4 folds in the core of the PSZ are rarely seen but where preserved are isoclinal with an axial planar fabric (S_{4a}). In places, the folds are truncated by small-scale shear-zones (Fig. 4.2b). The shears are axial planar to F_4 folds and, thus, parallel to the S_{4a} fabric, but clearly retrograde with chlorite-epidote mineral assemblages and ductile-brittle fabrics along them indicate a later age than formation of the PSZ. These later and retrograde planar fabrics are denoted as S_{4b} (discussed below). The parallelism of S_{4a} and S_{4b} fabrics having formed at different metamorphic conditions indicates the progressive nature of deformation in the PSZ (D_{4a} to D_{4b}). This progressive development of D_4 fabrics and the high-strain intensities in the PSZ makes correlation of F_4 folds with specific D_4 deformation phases (i.e. $D_{4a,b}$) problematic. F_4 folds are therefore interpreted to have formed during the progressive development of the PSZ. They are therefore distinguished based on their location with respect to the various study domains and therefore will be discussed for each domain.

Foliation (S_{4a})

S_{4a} is a neo-formed amphibolite-facies foliation occurring axial planar to F_4 folds, and is expressed as mylonitic fabrics of various intensities. It is the earliest D_4 fabric recognized in the PSZ, and post-dates inherited fabrics preserved in low-strain domains (Fig. 4.2b). S_{4a} is defined by the alignment of hornblende and/or biotite aggregates in mafic rocks (Figs. 4.3a,e). In quartz-feldspar dominated assemblages the preferred lattice orientation of dynamically recrystallised feldspar and statically and dynamically recrystallised quartz that make up the groundmass defines the foliation along with formation of quartz ribbons and the grain-preferred orientation of larger quartz grains and feldspar augen (Fig. 4.3f). The formation of S_{4a} mylonites and ultramylonites (discussed in Chapter 4.2.1) is defined by much finer grain sizes as a result of the pervasive dynamic recrystallisation of all mineral components leading to the development of core and mantle structures, dynamically recrystallised and mantled quartz and feldspar porphyroclasts with recrystallised tails and/or subgrain development. Mafic mylonites show strain partitioning, with neo-formed hornblende and biotite that wrap around lozenges of undeformed domains and/or grains (Fig. 4.3f).

Figure. 4.2. F_4-fold geometries and associated fabrics. (A) Folding within the ND, oblique cross sectional view, facing WNW. F_4 fold, folding of the gneissic foliation (S2, yellow) and the formation of a PSZ related axial planar foliation (S_{4a}, blue). Here S_{4a} is a spaced to penetrative foliation largely defined by the alignment of hornblende indicating D_{4a}, occurred at least, at amphibolite-facies conditions. (B) Folding in the PSZ core, oblique plan view facing NNW. Folded granitic melt forms a F_4 fold with an axial planar mylonitic foliation (S_{4a}, stippled white lines). The fold is truncated along both limbs by a later, lower grade mylonitic fabric where epidote and chlorite are developed along the contacts (S_{4b} is constrained within the stippled yellow line).

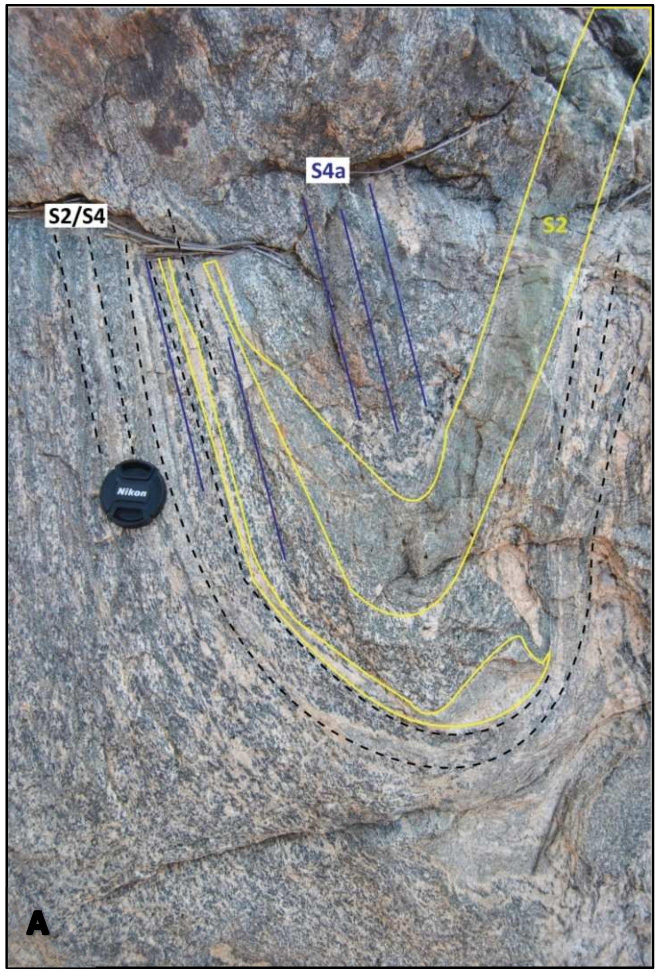

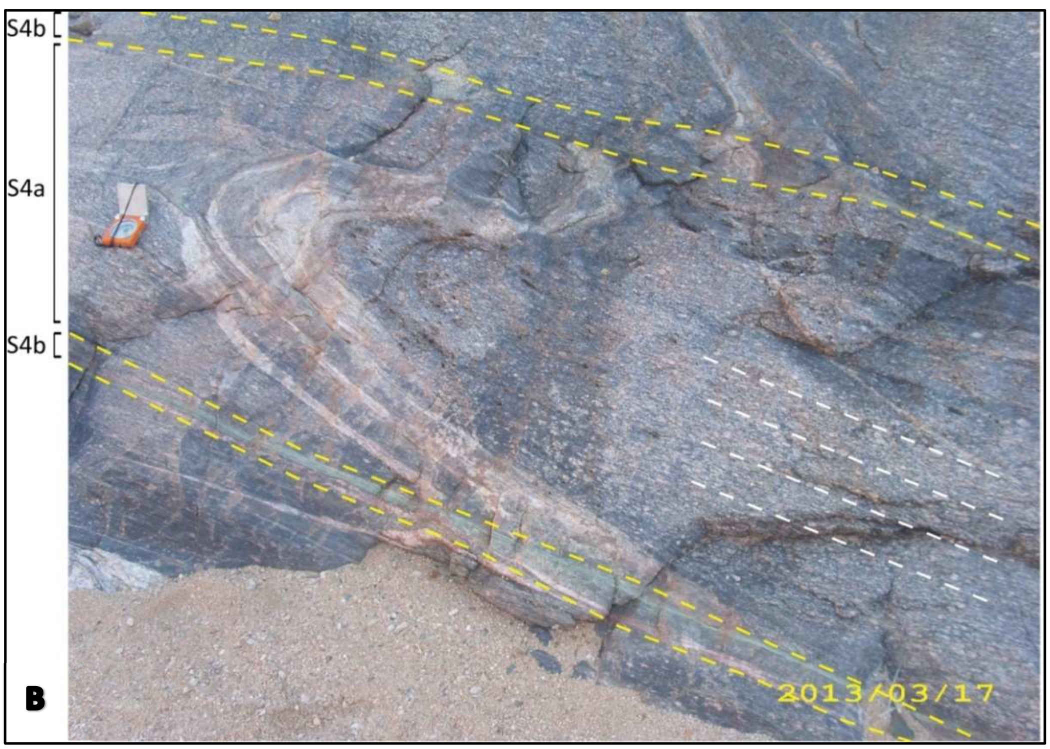

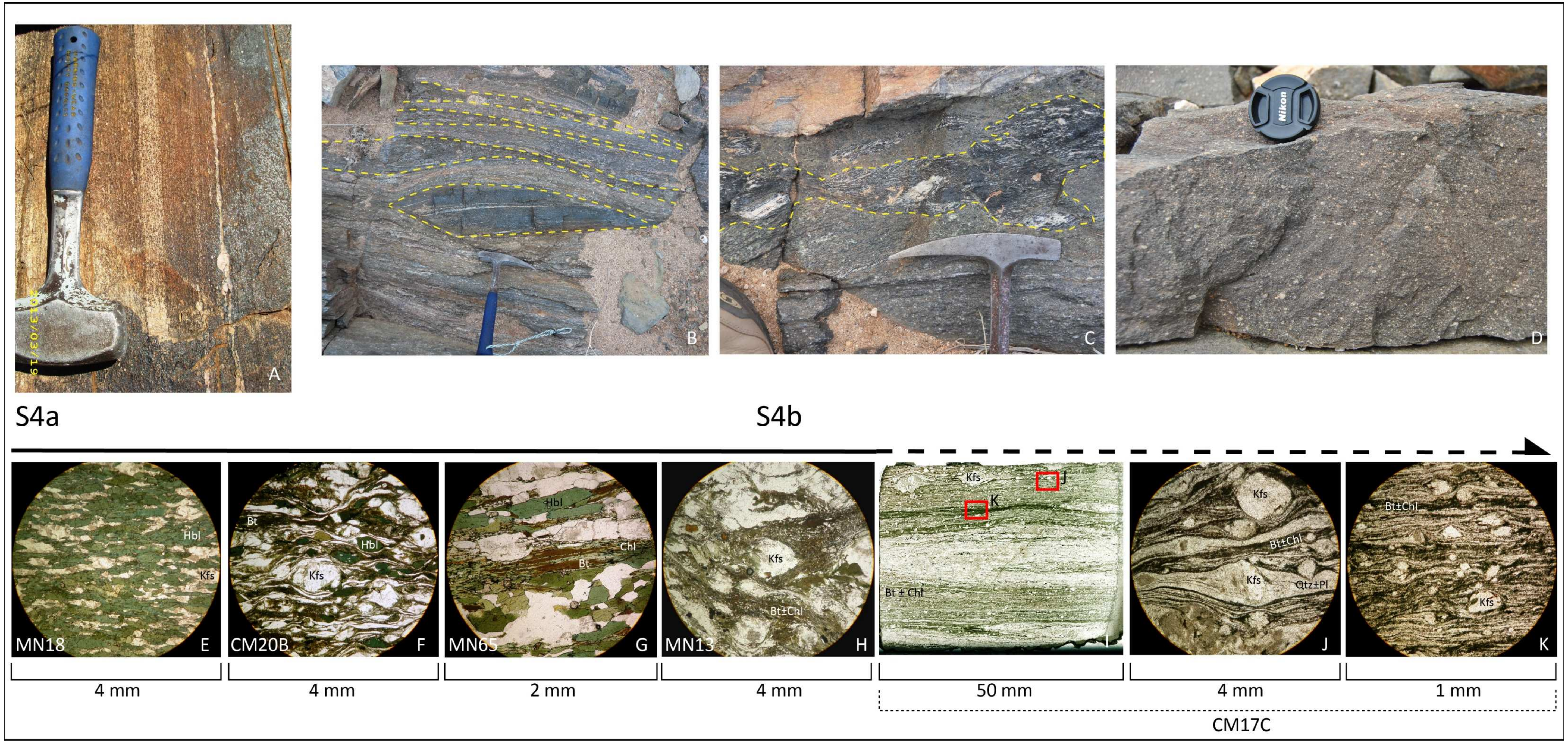

Figure. 4.3. Photomicrographs (E-K) in PPL and oblique plan views of the D_4 foliation in outcrop (A-D) illustrate the progressive development (from left to right respectively) of S_4 within the ND and PSZ core. Deformed but largely preserved S_{4a} amphibolites (A, E, F) are progressively replaced by biotite-chlorite fabrics (S_{4b}), initially (G) along the margins where amphibolite facies domains (yellow stippled domains) are (B) enveloped by a younger retrogressed S_{4b}-fabric. Further dominance/development of S_{4b}, particularly within the PSZ leads to significantly overprinted S_{4a}-domains (C, H) and ultimately the formation of S_{4b} mylonites (J) and phyllonitic fabrics (D, K). The section slide (I) indicates the variation in strain heterogeneity and degree of grain refinement within S_{4b} fabric in a single sample (CM17C). Mineral abbreviations after Kretz (1983).

Foliation (S_{4b})

S_{4b} is defined by the retrograde replacement of the amphibolite-facies S_{4a} fabric to lower-grade greenschist-facies fabrics characterised by the replacement of hornblende by biotite, initially along the grain margins, but progressively completely replacing the hornblende grains. In places biotite is further retrogressed to chlorite (Fig. 4.3g). In mafic assemblages the foliation is defined by the development of anastomosing biotite and chlorite beards around D_{4a} domains such as S_{4a}-porphyroclasts of hornblende (Figs. 4.3h,i) and the formation of dynamically recrystallised quartz ribbons (Fig. 4.3j). In homogeneous quartzo-feldspathic and pegmatite successions, S_{4b} is defined by dynamically recrystallised quartz ribbons and the preferred alignment of dynamically recrystallised quartz-matrix grains that surround blocky-subrounded fractured/fragmented feldspar porphyroclasts that are commonly fractured (Fig. 4.4), rotated and mantled with recrystallised tails. Notably D_{4a} and D_{4b} fabrics are largely co-axial and the pervasive nature of S_{4b} is commonly well developed and in places so pronounced that sometimes limited evidence of higher-T S_{4a} fabrics is preserved (Fig. 4.3d).

Figure. 4.4. Photomicrograph (CM21C) from PSZ core, XPL, FOV = 4 mm across. Feldspar porphyroclasts (yellow domain) are commonly internally fractured to a point where original porphyroclast geometries are no longer visible. Dynamically recrystallised quartz and biotite blades wrap around the original feldspar grain. Biotite is commonly developed within the internal fractures, along the subgrain margins.

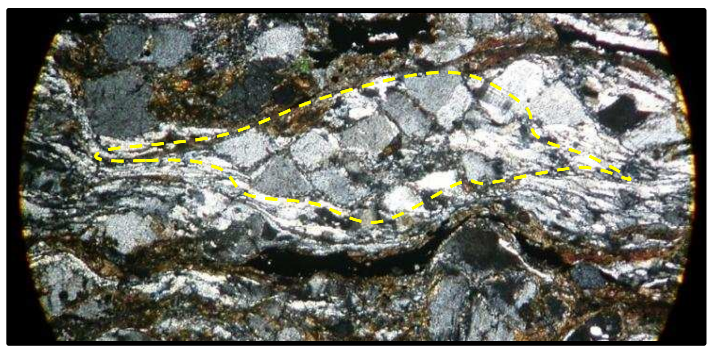

The most notable manifestation of S_{4b} is the development of pervasive phyllonites (i.e. mica-rich mylonites and ultramylonites; e.g., Brodie et al., 2007). In outcrop or hand specimen, phyllonites appear, at first glance, as cataclasites (Fig. 4.3d), characterised by angular, broken, cm-sized feldspar fragments set in a fine-grained biotite and/or biotite-chlorite matrix. In thin section, however, phyllonites show ductile-brittle deformation textures in which the anastomosing S_{4b} foliation is defined by biotite, wrapping around rounded, but internally fractured feldspar clusters (Figs. 4.3i-k). The cm-sized feldspar fragments (Fig. 4.5a) suggest that phyllonites are largely derived from pegmatites (e.g. Wenk and Pannetier, 1990; Goodwin and Wenk, 1995; Jefferies et al., 2006) in the PSZ and the presence of pegmatite pods preserved in low strain zones in phyllonites seems to confirm this interpretation (Figs. 4.5a,b).

The stability of biotite as the main fabric-forming mineral in phyllonites indicates that deformation has probably occurred under mid- to upper greenschist-facies conditions, which agrees with the brittle-ductile behaviour displayed by feldspar. The locally observed retrogression of biotite to chlorite, both defining the S_{4b} fabric, again indicates that D_{4b} probably occurred at variable conditions and, in general, during the retrogression, cooling and exhumation of the shear-zone rocks. S_{4b} fabrics may also take the form of discrete, cm-wide shear-zones superimposed on wider S_{4a} mylonites (Fig. 4.2b). In this case, the S_{4b} shears are evident as zones of bright-greenish epidote and chlorite and brittle-ductile textures along which the high-T S_{4a} fabrics are replaced. K-feldspar is often reddish in these zones, indicating alteration of the otherwise whitish feldspars during retrograde shearing.

Figure. 4.5. Evidence of phyllonites derived from pegmatites from plan view field photos within the PSZ core. (A) Angular feldspar fragments within a matrix of biotite and chlorite provide indicators for brittle-ductile deformation and development of phyllonites from pegmatite precursors. (B) The preservation of pegmatite pods within the phyllonites occurring in low strain domains suggest the angular fragments seen in A are derived from the alteration of pegmatites.

Lineations L_{4a}

L_{4a} lineations (Fig. 4.6a) take the form of a subhorizontal mineral stretching lineation developed on S_{4a} surfaces. The stretching lineation is defined by stretched quartz and/or aligned biotite aggregates in granitic gneisses and rodded hornblende in amphibolite units, or by well-developed fold-rodded surfaces in the hinge zones of F_4 folds. Except for where L_{4a} is developed on S_{4a} mylonites, distinguishing L_{4a} from older linear fabrics (L_2) is problematic, especially those within ca. 20 km of the PSZ, where they are re-orientate parallel to/or overprinted by D_4 fabrics. L_{4a} is therefore regarded for this study as the high-T, subhorizontal, stretching lineation parallel to the PSZ within the gneissic wallrocks of the ND, SD and the high-strain PSZ core.

Lineations L_{4b}

L_{4b} (Fig. 4.6b) is similarly a stretching lineation defined by stretched quartz-feldspar and/or aligned biotite aggregates in granitic gneisses and rodded biotite and/or chlorite in mafic units and phyllonites. L_{4b} is developed on S_{4b} surfaces and distinctly defined by steep, subvertical plunges (discussed in Chapter 4.2.2). L_{4b} lineations are concentrated within the PSZ and are rarely observed outside the high-strain core.

Figure 4.6. D_4 Lineations within the study area. (A). Oblique cross sectional view of the S_{4a}-foliation plane, taken in PSZ core illustrating the subhorizontal L_{4a} stretching lineation. (B) View perpendicular and (C) oblique view of the S_{4b} foliation plane illustrating the subvertical L_{4b} stretching lineation.

Shear-sense indicators

Shear sense indicators in the PSZ include rotated porphyroclasts with delta and sigma geometries in both D_{4a} (Figs. 4.7a,b) and D_{4b} fabrics (Figs. 4.7c,d). S-C and S-C' (Fig. 4.8b) are prevalent within the PSZ core with S-C' dominant over S-C. The drag (D_{4a}) of the gneissic wallrocks (Figs. 1.1b,2; 4.1; Appendix A) and majority of the shear sense indicators within and adjacent to the PSZ core indicate a dextral sense of shear for both D_{4a} and D_{4b}. There are, however, numerous symmetrical structures within the study area, particularly within the PSZ core. Infrequent sinistral shear-sense indictors, particularly in the northern wallrocks adjacent to the PSZ, are characterised by m-scale S-C' fabrics (Fig. 4.8a) and the deflection of marker units across discrete shears that obliquely cross cut S_{4a} at ca. 30^{o} in the vicinity of the WL. Here, small dextral shears form their conjugates (bearing 120^{o} -130^{o}) similarly deflecting younger marker units. The inferred dextral strike-slip kinematics agrees with the shallow plunge of mineral stretching lineations.

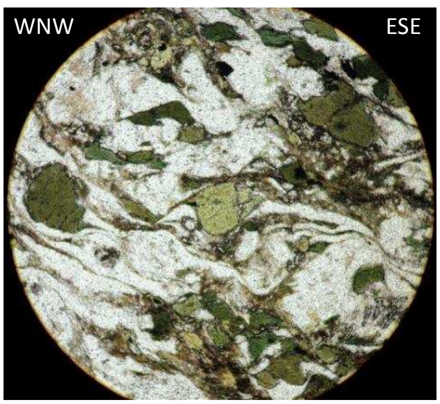

Figure. 4.7. (A). Photomicrograph (MN11) from PSZ core, PPL, FOV = 2 mm. Rotation of an amphibole grain part of the S_{4a} foliation, forms a delta clast indicating a dextral sense of shear.

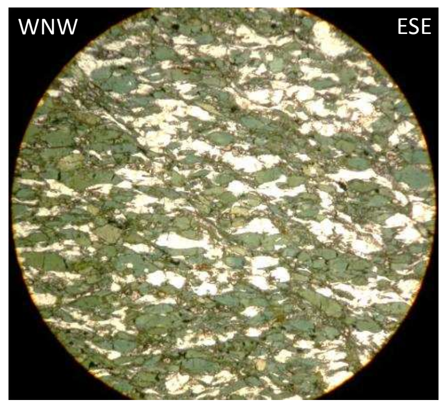

(B). Photomicrograph (MN54) from PSZ core, PPL, FOV = 4 mm. S-C' fabrics indicate a dextral sense of shear and define the S_{4a} foliation.

(C). Plan view with top WNW, taken in PSZ core. A rotated feldspar porphyroclast within a biotite dominated matrix (S_{4b}) forms a sigma clast indicating a dextral sense of shear.

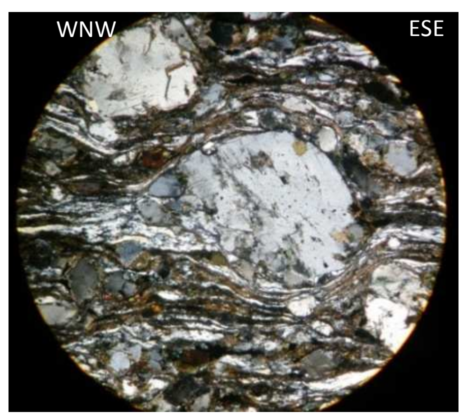

(D). Photomicrograph (CM21C) from PSZ core, XPL, FOV = 4 mm. Dextrally rotated (delta) and mantled feldspar porphyroclast (centre view) within the S_{4b} domain.

Figure 4.8. (A) Cross section along the southern edge of the ND, facing WNW. Discrete shears (stippled yellow lines) represent C'-shears in a sinistral S-C' fabric that deflects S_{4a} (stippled white lines). (B) Plan view with top to NNE. Large sigmoidal shaped remnants of an earlier S_{4a} indicate a dextral sense of shear during D_{4b}. The pervasive S_{4b} (stippled yellow) shows a well-developed S-C' fabric which again indicates a dextral shear sense.

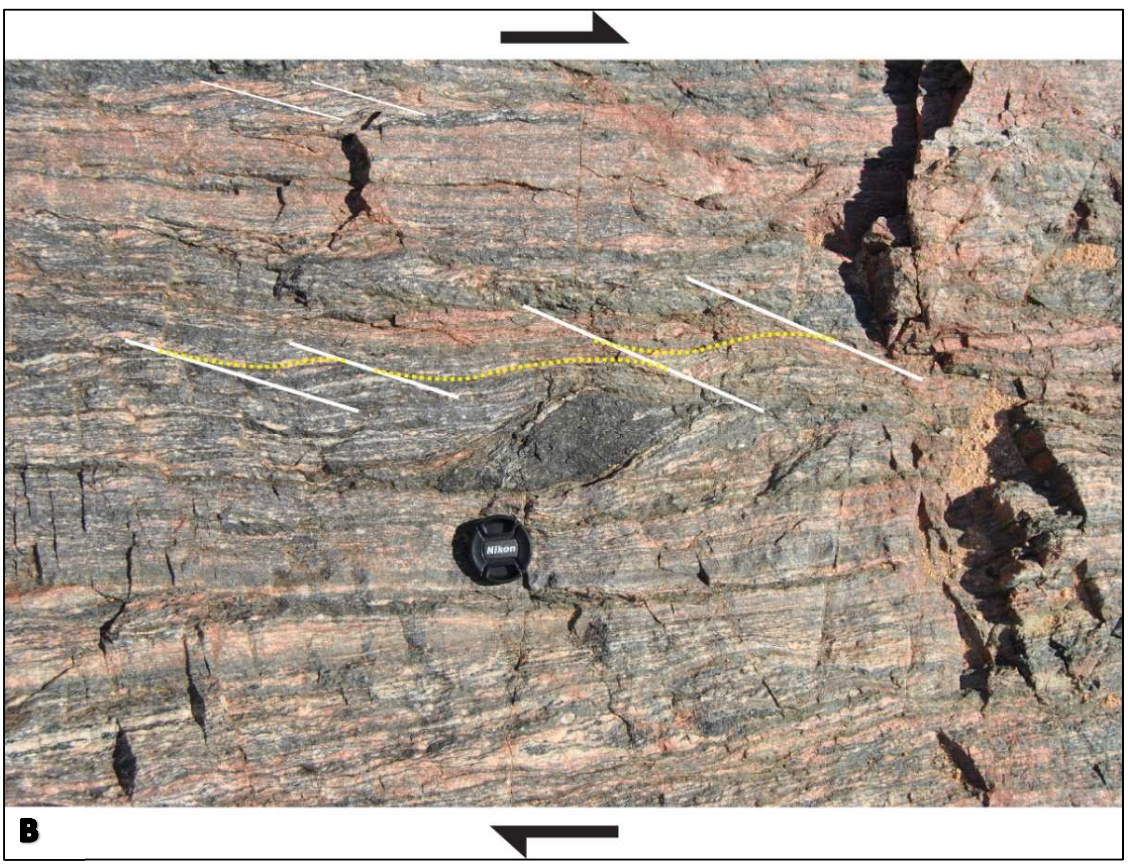

4.2.1 Northern Domain (ND)

Structurally, this domain is characterised by the drag and folding of wallrocks adjacent to the shear and progressive intensification of D_{4a} fabrics towards the PSZ core. Within ca. 20 km north of the PSZ the regional, shallowly dipping S_2 foliation steepens to subvertical attitudes during its gradual rotation into the ND and PSZ-fabric (S_4; Fig. 4.9). In the ND, the effects of the PSZ and D_4 fabric development are particularly pronounced within 1-2 km from the core, evidenced by (1) the rotation of rocks into parallelism with the D_4 shear-zone (Fig. 4.9), (2) the formation of S_{4a}-parallel mylonite zones (S_{4a}-mylonites), between which earlier fabrics are folded (F_4), and (3) the development of a lower strain fabric (S_{4a}) axial planar to the F_4 folded successions (Fig. 4.10).

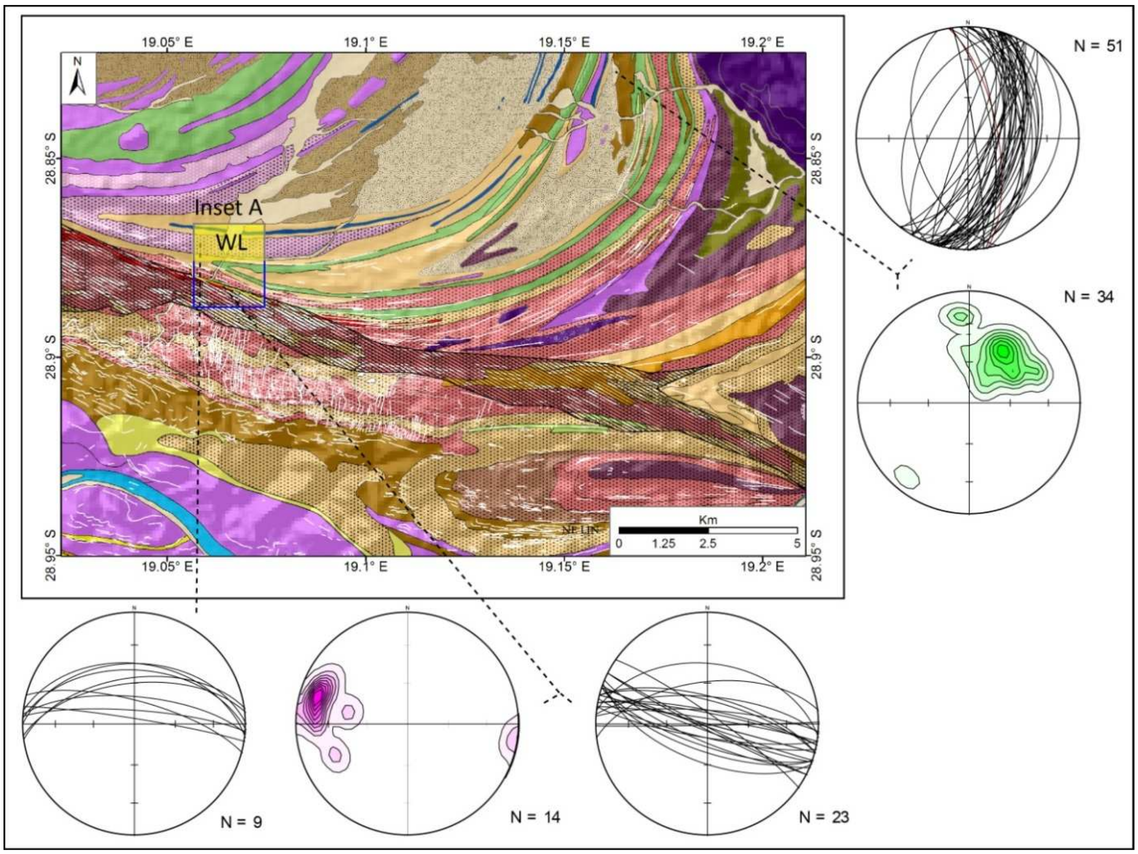

Figure 4.9. The geological map illustrates the rotation of the structural fabrics into the ND (blue box, inset A). Stereoplots show that the planar fabric foliation to the NE of the study area is dextrally rotated into parallelism with the PSZ, whereas in the ND the composite fabric (S_2/S_4) is parallel to the shear-zone fabric (S_4). In the ND, the planar fabric progressively steepens towards the PSZ, changing from a moderate dip around the WL to a subvertical fabric adjacent to the PSZ boundary. The linear fabrics show a similar rotation into the PSZ from moderate NE plunging lineations to subhorizontal WNW plunging lineations respectively. Inset A is illustrated in Fig. 4.10 (below). The legend for the geological map is found in Appendix A.

Figure. 4.10. Cross section of an approximately 1 km wide, N-S traverse across the ND. The geological map represents inset A from Fig. 4.9. The cross section illustrates the progressive development of D_4 fabrics towards the PSZ core. The cross-section is schematic, drawn and without a vertical scale but illustrates the dominant structural fabrics (S_2/S_4; $S_{4a,b}$; F_4) developed at their respective locations within the ND.

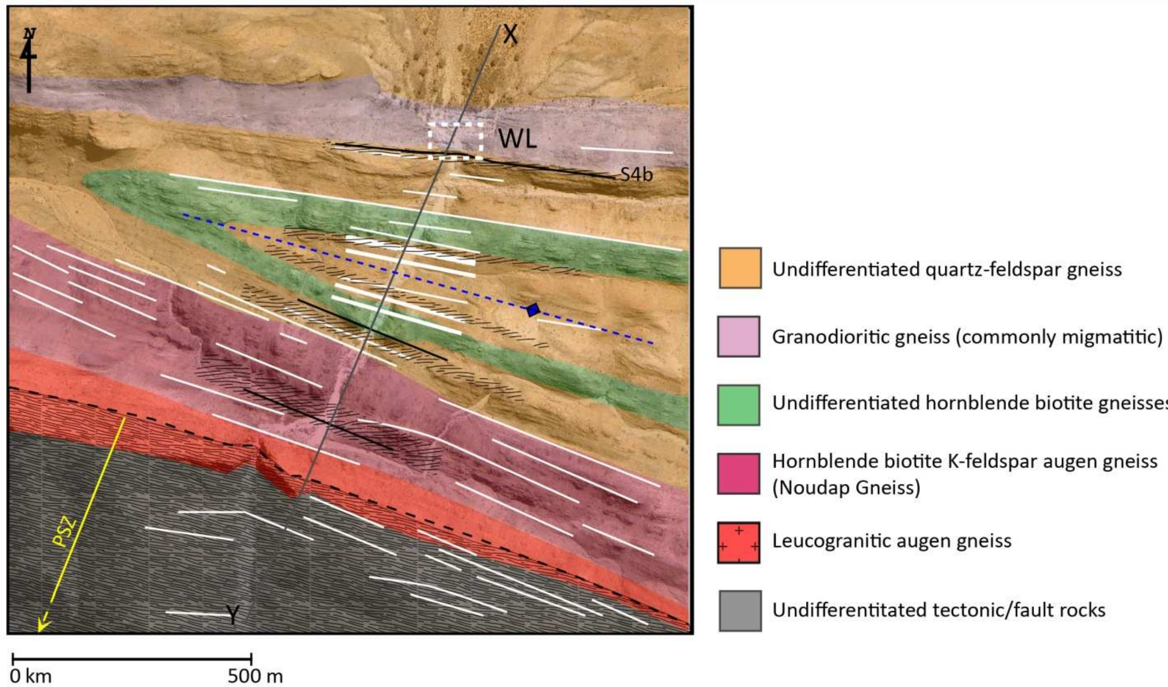

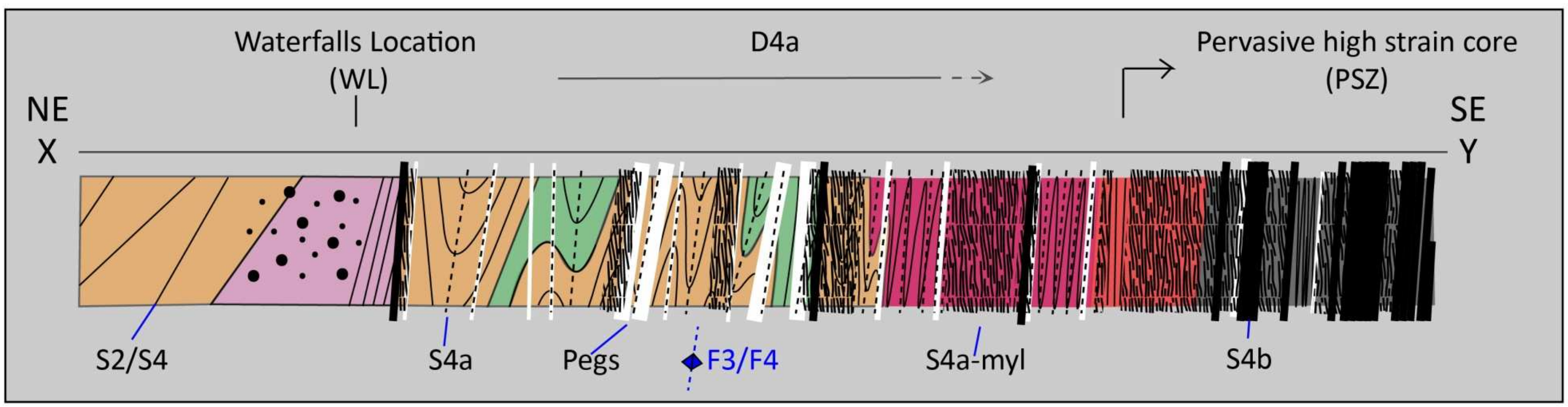

A progression in the D_{4a} fabric intensity is observed from the wallrocks towards the core where, from the Waterfalls Locality (WL) to the PSZ core the dominant fabric passively changes from (1) prolate at the WL, to a (2) moderate – steeply dipping (S_{4a}) S>L fabric, to (3) a steeply-dipping, mylonitic-S_{4a} fabric close to the PSZ core (Figs. 4.10,11a). The increase in fabric intensity and development of S_{4a}-mylonites is, thus, gradual towards the core of the PSZ, and marked by initially widely spaced (100-200m) S_{4a}-mylonites that, closer to the core of the PSZ, form a closely-spaced anastomosing network of mylonitic shear-zones. This transition is accompanied by the progressive widening of these mylonitic zones, enveloping domains with lower fabric intensities (S_2/S_4, S_{4a}) up to the northern PSZ core boundary, where mylonitic fabrics overprint nearly all pre-existing fabrics (Fig. 4.10).

Much of the ND is underlain by the hinge of an earlier (F_3), south verging-upright WNW plunging antiform with a wavelength of 130 m (Figs. 4.9-10; Appendix A). From spatial datasets (e.g. ASTER and Google Earth) the limbs of this fold can be traced ca. 10 km to the northeast where they are orientated perpendicular to the shear (Fig. 4.9, Appendix A). The half-wavelength of the fold shows a dramatic decrease into the ND where it tightens from a width of over 1 km in the northeast and outside the PSZ to less than 300 m within the ND. Parasitic F_4 folds developed within the ND appear to be preserved as high-grade (amphibolite facies) parasitic, similar folds developed co-axial to the PSZ core with a well developed subvertical S_{4a} fabric (Figs. 4.2a, 2.11b) or as small (cm-scale) disharmonic folds in deformed pegmatites (discussed in Chapter 5.3). The fold geometries show a similar tightening and increased intensity towards the PSZ, marked by the transition from upright, open to tight geometries (Fig. 4.2) in the north to isoclinally folded and transposed folds along the northern PSZ margin (Figs. 4.9,11c).

In summary, the ND shows a gradual increase in fabric intensity (S_{4a}) towards the PSZ marked by (a) the change from relatively unaffected wall-rock gneisses to tightly folded and transposed successions towards the PSZ, and (b) the change from regionally developed and rotated gneissic fabrics (S_2/S_4) to mylonitic fabrics (S_{4a}) adjacent to the PSZ. This change is noted over a distance of ca. 1 km from the core of the PSZ and defines the strain gradient into the PSZ core. The progressive increase in S_{4a} fabric intensity towards the core suggests a gradual strain gradient from the wallrocks into the PSZ, defining a diffuse northern PSZ margin. The northern boundary of the PSZ is therefore relatively indistinct compared to the southern margin (discussed later) and here defined by the position where the mylonitic foliation (S_{4a}) becomes overwhelmingly dominant.

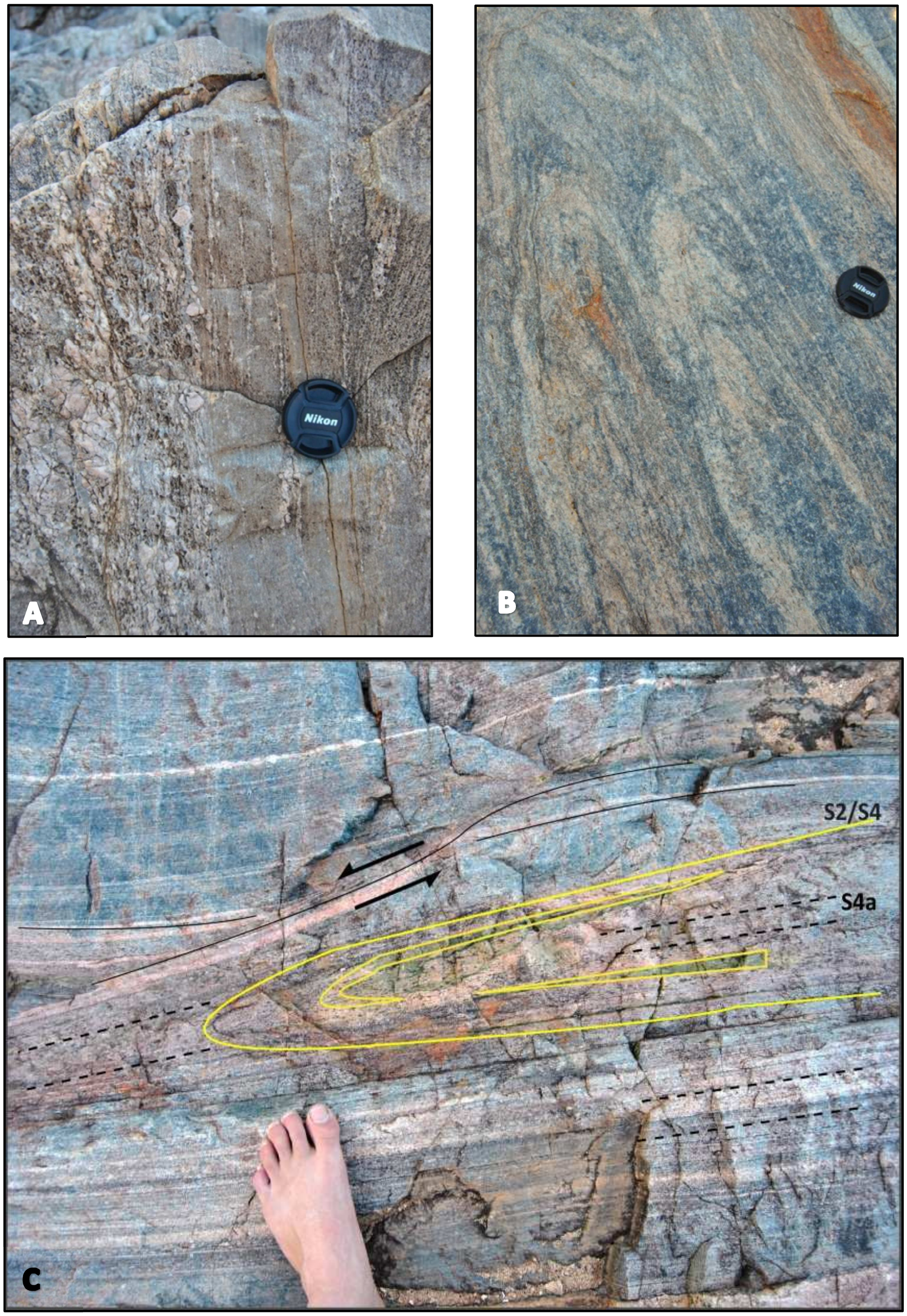

Figure. 4.11. (A) Cross sectional view facing WNW, of the S_{4a}-mylonitic fabric within the ND. Mylonitic and ultramylonite fabrics within the mylonite zone highlight the strain heterogeneity within the high-strain domains. (B) Oblique cross sectional view facing NW showing high grade similar – multilayer folds preserved ca. 500m from the PSZ core in the ND. (C) Plan view with to south, isoclinal fold geometries preserved adjacent to PSZ core. The isoclinal fold is defined by the composite S2/S4 fabric has a well-developed penetrative axial planar foliation (S_{4a}).

4.2.2 PSZ core

The PSZ core forms a 900 m wide, structurally heterogeneous zone defined by the extensive, although heterogeneous development of mylonitic fabrics ($S_{4a,b}$). In addition, it has a lithological heterogeneity and banding related to the transposition of original compositional variations into $S_{4a,b}$ and the emplacement of granites and pegmatites into the shear-zone. In contrast to the rather gradual northern boundary of the PSZ, the southern boundary of the PSZ core against the SD is sharp. The latter contact is best exposed at the coordinates 28.8928 ^{o} S, 19.0692^{o} E and defined by an abrupt change in fabric intensity from mylonitic rocks (S_{4b}-phyllonites) of the PSZ into only weakly foliated granites and granite gneisses that constitute the southern wallrocks of the SD. Regionally the mylonitic fabrics ($S_{4a,b}$) that define the PSZ core trend NW-SE (Figs. 1.1b; 2.4; Appendix A) but rotate to WNW-ESE trends within this section of the study area (Figs. 2.4; 4.12).

Three main subdomains can be distinguished from north to south across the mylonitic core of the PSZ. The northern margin of the core (Fig. 4.12-purple zone) is largely dominated by amphibolite-facies S_{4a} fabrics in leucocratic orthogneisses and/or pegmatite hosts and S_{4b} fabrics are only locally developed. Some 100 m into the core of the PSZ, amphibolitic rocks with a well-developed, anastomosing, S_{4a} mylonitic fabric defined by the grain-shape preferred orientation of amphibole and plagioclase (Fig. 4.12-MN71) dominate. In low-strain pods, the interlayered leucogranite gneisses can be shown to be intrusive into the amphibolites by the preservation of intrusive breccias in which cm-sized angular to slightly elongated pods of leucogranite intrude foliated (S_2) amphibolites. Discrete (< 1 cm thick) S_{4b} fabrics, commonly developed as thin phyllonites, locally overprint the higher-T fabrics. The phyllonite development seems preferentially localised along the margins of pegmatite sheets against amphibolites where the coarse-grained quartzo-feldspathic pegmatites are progressively transformed into phyllonitic rocks. Along the northern margin the mylonitic fabric is subvertical, dipping to the NNE and SSW (Fig. 4.12-purple great circles). Here L_{4a} is predominately developed, significantly more so than L_{4b}, and the shallow to subhorizontal L_{4a} plunges to both the WNW and ESE (Fig. 4.12-purple density plot).

Figure 4.12. (next page). Panoramic, along-strike views of the PSZ core indicating the passive change in fabrics across the shear from a ductile D_{4a} dominated northern zone to a brittle-ductile D_{4b} southern zone respectively. Scale is 1 km across in foreground. Stereoplots (mylonitic fabrics) illustrated with great-circle plots; lineations are illustrated with density distribution plots), photographs and photomicrographs illustrate the nature of the outcrop within the PSZ core from north to south and are colour coded with respect to the three dominant structural zones with the PSZ core.

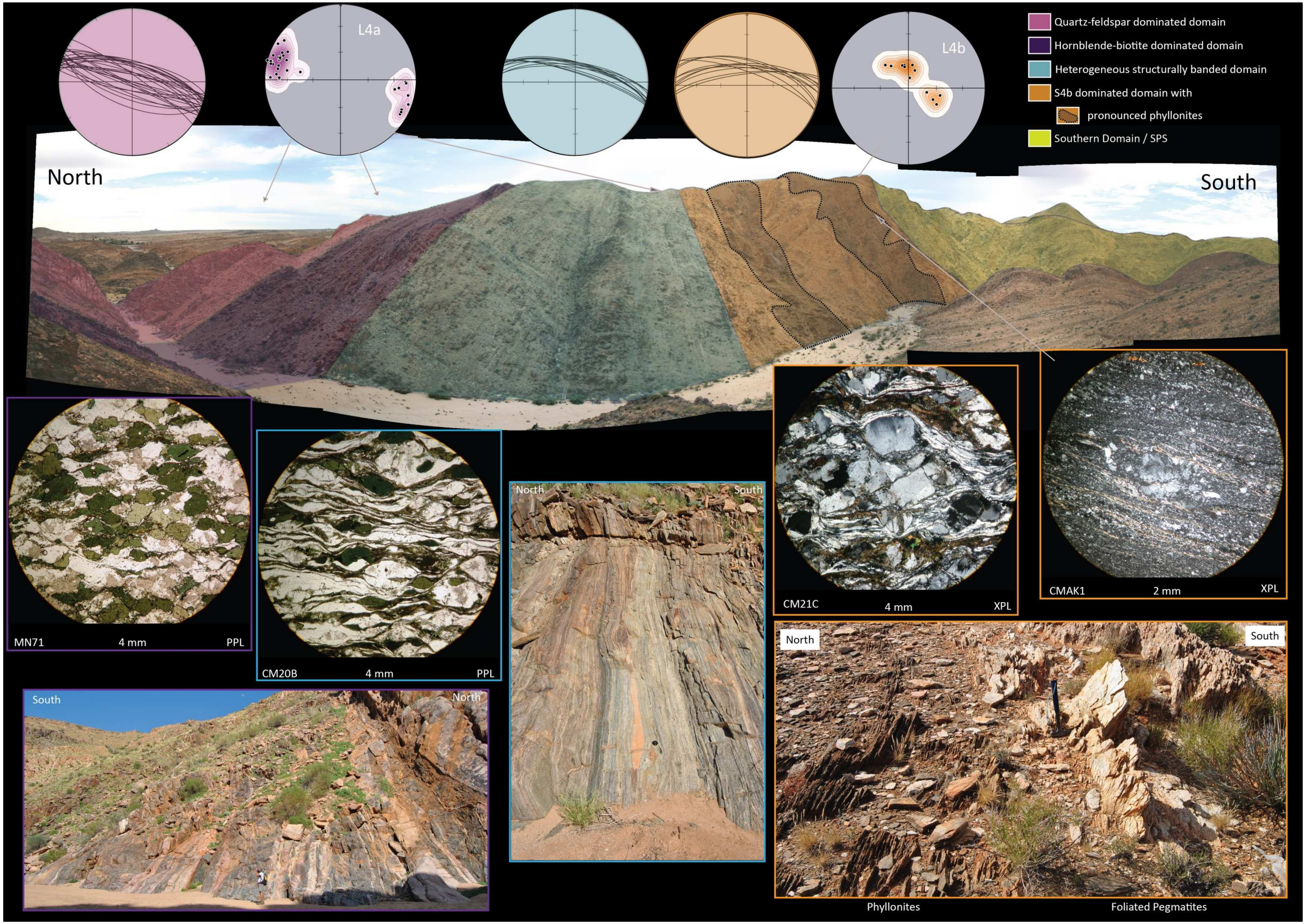

L4a
L4b
Quartz-feldspar dominated domain
Hornblende-biotite dominated domain
Heterogeneous structurally banded domain
S4b dominated domain with
pronounced phyllonites
Southern Domain / SPS
North
South
MN71
4 mm
PPL
CM20B
4 mm
PPL
North
South
CM21C
4 mm
XPL
CMAK1
2 mm
XPL
North
South
South
North
Phyllonites
Foliated Pegmatites

About 450 – 700 m into the core (Fig. 4.12-blue zone), S_{4b} fabrics and phyllonite formation become prominent and obliterate original lithological relationships and variations. S_{4a} fabrics are only preserved in boudin-like structures enveloped by S_{4b} (Figs. 4.3b,c). The mylonitic fabric shows less orientational variation and becomes increasingly pervasive, overprints S_{4a} (Fig. 4.12-CM20B) and dips exclusively to the NE (Fig. 4.12-blue stereoplot). L_{4a} lineations are similarly dominant over L_{4b}, and parallel those along the northern domain.

The southernmost exposures of the core are dominated by S_{4b} phyllonites and mylonitic fabrics (Figs. 4.12-CM21C, CMAK1) over a width of ca. 200m. An increased volume of pegmatites towards the southern margin coincides with the progressively dominant phyllonite successions, suggesting the occurrences of the two rock lithologies are implicitly related. Original pegmatitic precursors of the biotite phyllonites are preserved in low-strain lenses (Fig. 4.12-orange zone). The mylonitic/phyllonite foliation shows a slight rotation towards the north, but retains consistently steep dips to the NNW (Fig. 4.12 - orange zone). The L_{4b} mineral stretching lineations dominate and are very prominent on S_{4b} phyllonite surfaces (Fig. 4.6c) and in mylonitised pegmatites, where they are defined by stretched quartz and feldspar (Fig. 4.6b). Notably, the lineation is progressively rotated to steeper and subvertical plunges in this southern section, plunging both to the NNW and ESE along the southern boundary (Fig. 4.12-orange stereo plots).

From north to south the overall progression of D_4 structural fabrics across the core is characterised the transition of ductile, high-temperature S_{4a} fabrics to lower temperature brittle-ductile conditions dominated by D_{4b} fabrics. The progression gradually extends to the southern margin of the PSZ to the contact, where the boundary is defined by an abrupt change in fabric intensity into the southern footwall rocks (SD). The strain gradient across the southern contact is accentuated by the juxtaposition of high-strain fabrics, expressed as phyllonites, ultramylonites and ultracataclasites (Fig. 4.12-CMAK1) of the PSZ against weakly foliated gneisses of the SD.

4.2.3 Southern Domain (SD)

The southern domain (SD) covers the Skimmelberg Mountains immediately south of the PSZ core (Fig 1.2). One of the most notable features of gneisses in the SD is the lack of high-strain fabrics, the abrupt appearance of shear-zone fabrics and apparent high-strain gradient into the PSZ and its core. This strain contrast is illustrated by (a) the lack of a mylonitic foliation in rocks of the SD (Fig. 4.13a-e), (b) the undeformed nature of large, cross-cutting magma sheets (discussed in Chapter 5), and (c) the preservation of pre-D_4 features, where the low fabric intensities preserve original magmatic structures and textures such as euhedral feldspar megacrysts, intrusive contact relationships (Fig. 4.13b) and elongate, magmatic dioritic enclaves (Fig. 4.13d).

The effects of the PSZ (D_4) on the gneissic wallrocks quickly become less apparent south of the PSZ-SD boundary. For this reason, where the planar fabrics in the SD are adjacent to the PSZ, subvertical and parallel to those within the core, they are considered to represent lower strain intensities of S_4. In the S_4 is rarely seen as axial planar to F_4 folds (Fig. 4.13e). The (re-orientated) regional S_2-fabric (annotated as S_2/S_4) shows shallower dips away from the PSZ core to ca. 45^o at the southern, eastern and western limits of the domain (Fig. 4.14). Notably, S_2/S_4 is commonly defined by the alignment of muscovite and/or chlorite retrogressed from biotite. This emphasizes the lower-metamorphic grades of rocks south of the PSZ (Fig. 2.4) and the metamorphic break across the PSZ (Beukes, 1973; Toogood, 1976; Miller, 2008). S_{4b} is only locally developed within the SD as PSZ-parallel, discrete (1 - 5 cm) shears that dextrally displace marker units (Fig. 4.13c). Due to the nature of the outcrop (e.g. large pavements and steep cliffs) in the SD the exposure of linear fabrics is less prominent but sporadically shows moderate plunges of 30 - 40^o away from the centre of the SD (Fig. 4.14). The significance of the orientation and its relation to the SPS is discussed in Chapter 7.

Figure. 4.13. (Next page). Various structural features within the SD illustrating a significantly lower strain regime compared to the ND and PSZ core. (A) Photomicrograph, (CM38B), XPL, FOV = 4 mm. A weak pre-D_4 foliation, defined by the alignment of biotite minerals while the euhedral nature of the interstitial grains indicates a largely preserved igneous texture. (B) Oblique plan views, with top to NE, taken in the SD. Primary intrusive contacts are preserved between the grey hornblende-biotite augen gneiss (i.e. Noudap) and cream-pink quartzo-feldspar gneiss (i.e. Coboop). (C) Oblique plan view onto cliff face, facing north, discrete (< 1 cm) S_{4b} shears (stippled yellow) displace a small N-S pegmatite dyke with a dextral sense of movement. (D) Along strike-plan view, with top east Elongated (but not D_{4a}-deformed) dioritic enclaves (ca. 30 cm long) in the Noudap Gneiss indicate the preservation of an earlier, pre-D_4 magmatic fabrics that have largely been unaffected by D_4 in the southern domain. (D) Longitudinal view along S_2/S_4. The preservation of elongated (30 cm long) dioritic enclaves (yellow oval) highlight primary igneous textures in the SD which are not observed in the PSZ core and ND. (E) Oblique plan view, taken facing SE. Rarely observed fold geometry within the aiding in the otherwise difficult distinction of planar fabrics in the SD. Here S_2 (yellow lines) has been folded (F_4) forming a composite S_2/S_4 fabric (black lines), both of which occur parallel to the axially planar S_{4a} fabric (blue lines).

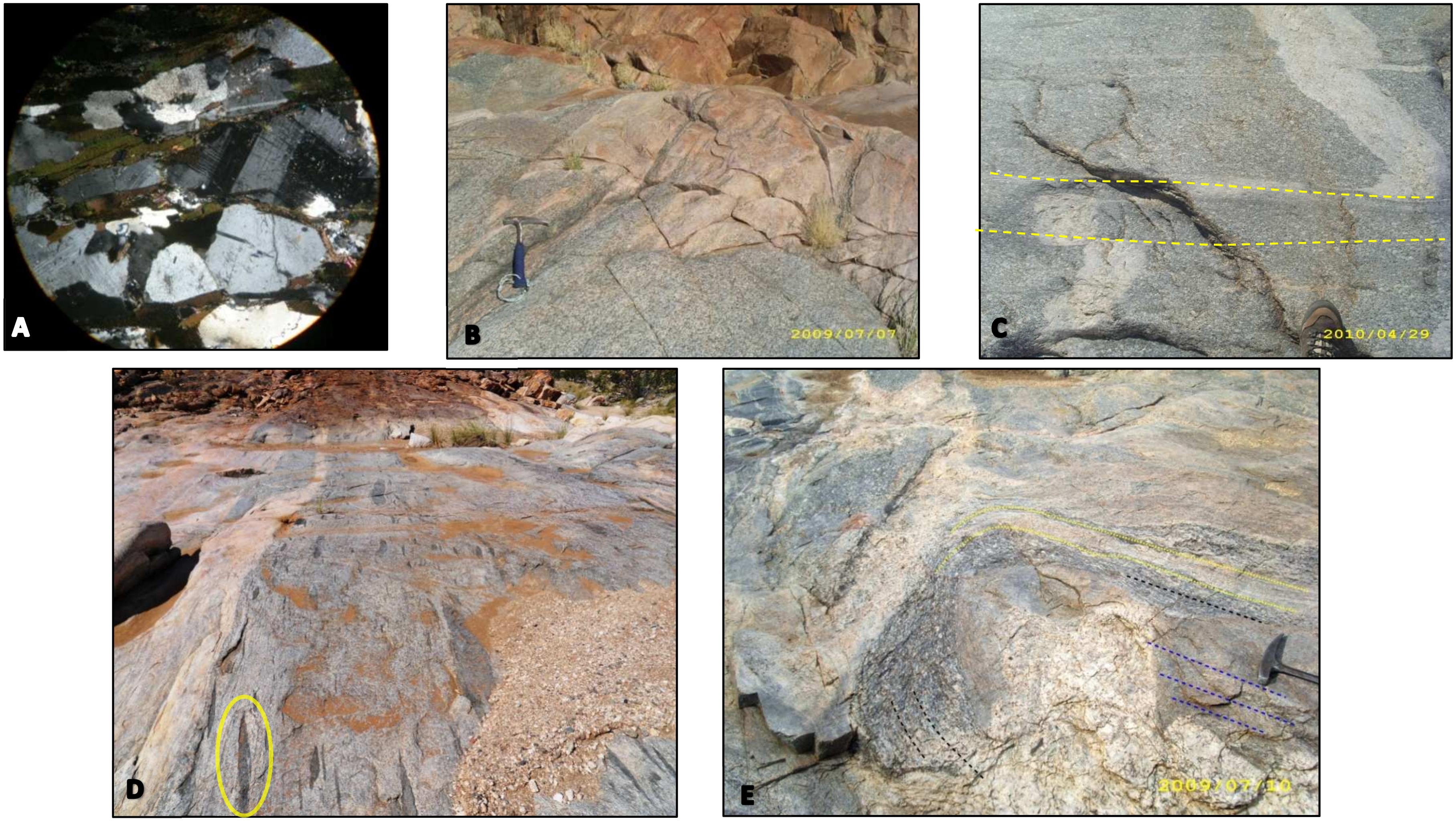
A
B
2009/07/07
C
2010/04/29
D
E
2009/07/10

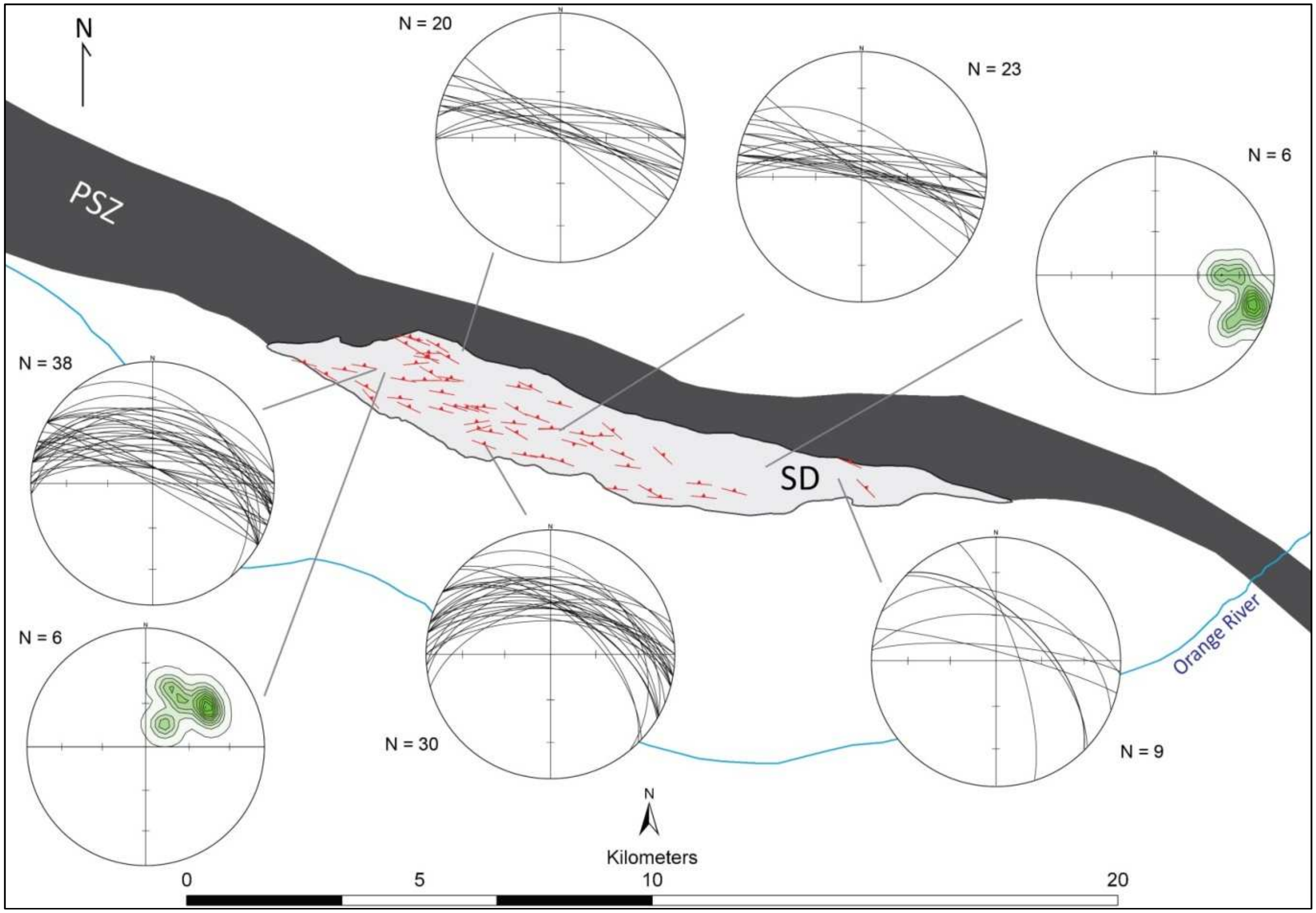

Figure 4.14. Diagram illustrating the distribution of structural fabrics within the southern domain. Foliations (red) with corresponding great-circle stereoplots illustrate the variation in S2/S4 and/or S2 within the southern domain where the planar fabric shallows progressively away from the northern boundary and bends to the NE towards the east. The lineations in the SD (green) change from a moderate NE plunge in the west to an ESE plunge in the east from east to west.

5. Granites and pegmatites

Granitoids intrusive into the PSZ are predominately pegmatites and minor leucogranites. The pegmatites are mainly sheet-like, but may also display more irregular, pod-like geometries as well as composite geometries assembled from more than one distinct intrusive pulse. Intrusive relationships, as well as the geometry and deformation of pegmatites vary within each of the three domains defined for the PSZ in Chapter 1.2. This not only illustrates variable emplacement controls, but also a different timing of pegmatite emplacement along the PSZ. The present chapter documents pegmatite geometries with respect to structural fabrics and highlights the structural controls on pegmatite emplacement within each of the domains.

5.1 PSZ core domain

Pegmatites in the core occur mainly as simple, homogeneous bodies consisting almost exclusively of quartz, perthitic K-feldspar, plagioclase and biotite, with variable amounts of garnet that commonly occur as drawn out, foliation-parallel aggregates. Although commonly homogenous and unzoned, pegmatites may also show a weak zonation defined by quartz ± feldspar ± biotite- rich margins and predominately quartz ± feldspar cores. Granitic and pegmatitic intrusive rocks in the core occur as (1) sheet-like, foliation ($S_{4a,b}$) parallel bodies, (2) isoclinally folded and variably transposed sheets, (3) pegmatites cross-cutting the foliation at shallow angles, or (4) in pod- or jog-like geometries that seem connected to sheet-like and foliation-parallel pegmatites. The characteristics of each type are discussed below.

5.1.1 Foliation-parallel pegmatites

The majority of pegmatite bodies within the core occur parallel to the gneissic (S_2/S_4) and mylonitic ($S_{4a,b}$) foliation (Figs. 5.1-3). These pegmatites are laterally continuous, up to 15 or 20 m wide sheet-like bodies confined between S_{4a}-foliation planes, and can be traced for more than 1 km along strike within the PSZ core (Appendix A). The pegmatites show evidence of multiple sheeting where amalgamated sheets are indicated by multiple quartz-rich cores separated by feldspar-dominated zones (Fig. 5.2). In the northern and central portions of the PSZ core, early granitic magma phases that define the compositional layering (Fig. 4.12-purple zone) dominate while relatively few large (> 2 m) pegmatite bodies are present. In addition to the pegmatites along the northern boundary of the PSZ, a leucocratic, creamy pink leucogranite occurs ca. 20 m into the PSZ core. The leucogranite contains ductile fabrics that are parallel to S_{4a} fabrics of the enveloping PSZ. The timing of emplacement of this granite sheet is discussed in Chapter 6.

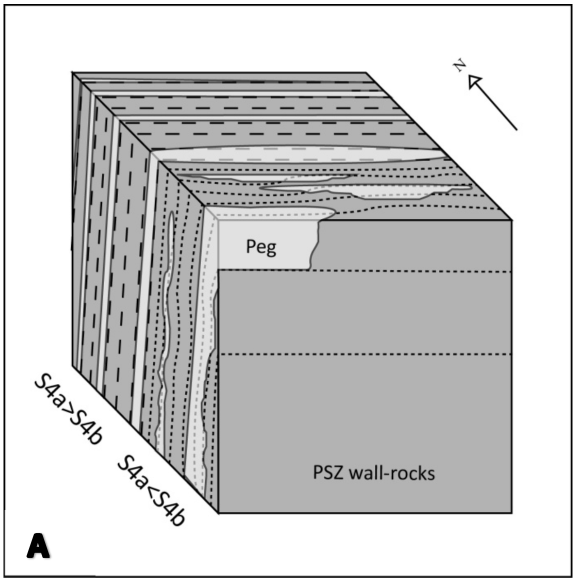

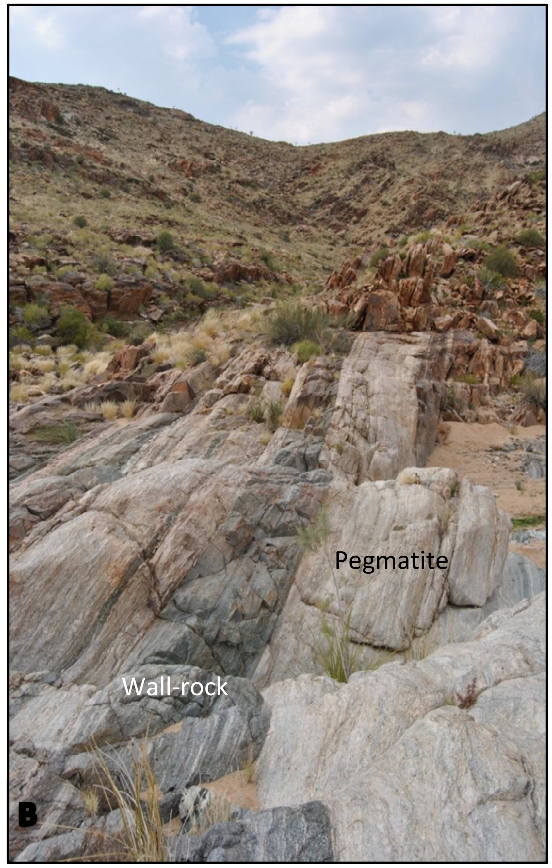

Figure. 5.1. (A) Schematic 3D block diagram illustrating the emplacement geometries of the foliation ($S_{4a,b}$) parallel pegmatites within the core from north to south respectively. (B) Along strike view towards the southeast, showing steeply-dipping, sheeted and highly foliated pegmatites parallel to the mylonitic foliation.

Figure 5.2. Cross sectional view towards ESE. Compositional layering and multiple quartz-rich cores within a pegmatite sheet in the PSZ core suggests assembly of pegmatite sheets through multiple melt batches/pulses.

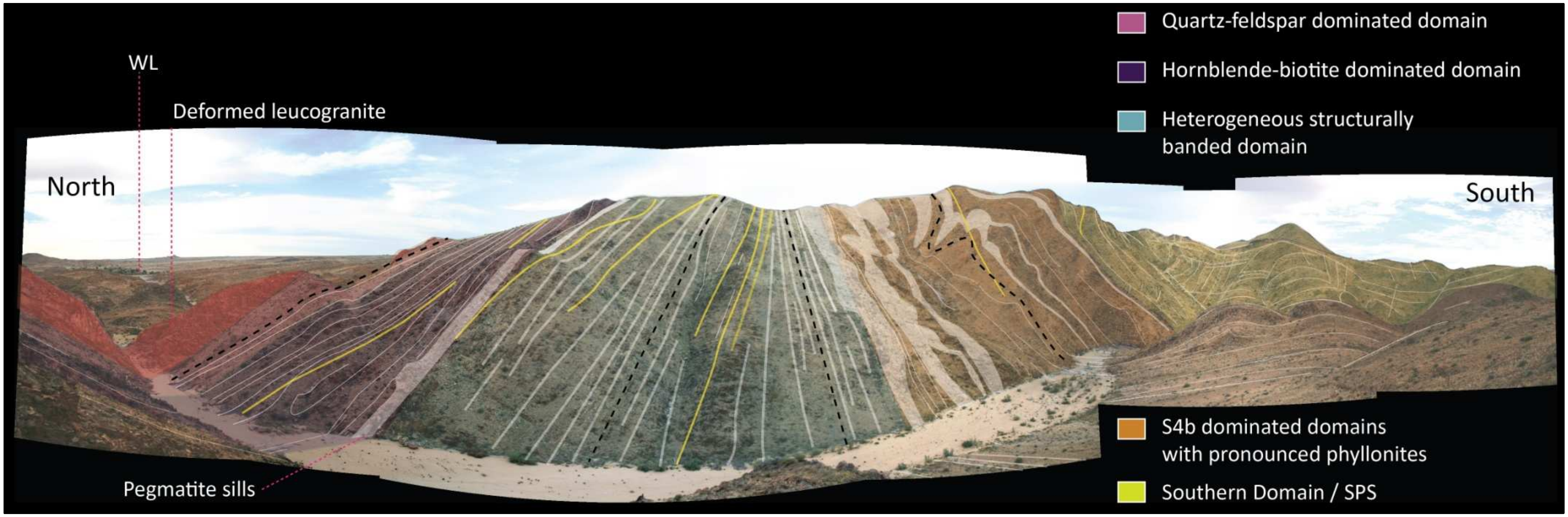

Figure. 5.3. Panoramic, along-strike view of the PSZ core (facing east in the foreground) indicating the distribution and thicknesses of the granitic bodies across the core. Scale is ca. 1 km across in foreground. Pegmatites (white) within the purple domain are relatively thin (1 m - 2 m) compared to the remainder of the core where pegmatite density increases and bodies reach over 20 m in thickness. Pegmatite geometries across the core occur predominately as sheet like bodies parallel to the mylonitic ($S_{4a,b}$) foliation (stippled black). Notably fewer pegmatites occur as sheeted bodies that cross cut the foliation at a shallow angle (yellow lines). The orientations of the pegmatites suggest they may have intruded along synthetic Riedel shears within the (dextral) shear-zone. Rarely observed folded pegmatites (purple zone) are preserved in low-strain domains and contain an axial planar mylonitic foliation (S_{4a}).

The abundance and thicknesses of pegmatites increase towards the southern boundary of the PSZ (Figs. 5.3-4), where individual pegmatite sheets may be up to 15 - 20 m thick (Fig. 5.4b). Here pegmatite geometries appear largely altered by the pervasive development of the S_{4b}-phyllonites and occur as lensoid to sheeted and laterally discontinuous bodies (Fig. 5.1a). The discontinuity of the pegmatites and sharp lateral terminations, coupled with the pervasive nature of S_{4b} makes their tracing along strike problematical. Pegmatite contacts with the wall-rocks remain relativity sharp, defined by compositional and textural discontinuity across the contacts but dissimilar to those at the northern margin, are slightly irregularly shaped, locally stepping across the foliation planes before continuing parallel to the mylonitic foliation ($S_{4b} \geq S_{4a}$; Fig. 5.1a,4). The increased occurrence of pegmatites towards the southern margin of the core corresponds to the increased dominance of the D_{4b}-phyllonite successions in this region of PSZ core.

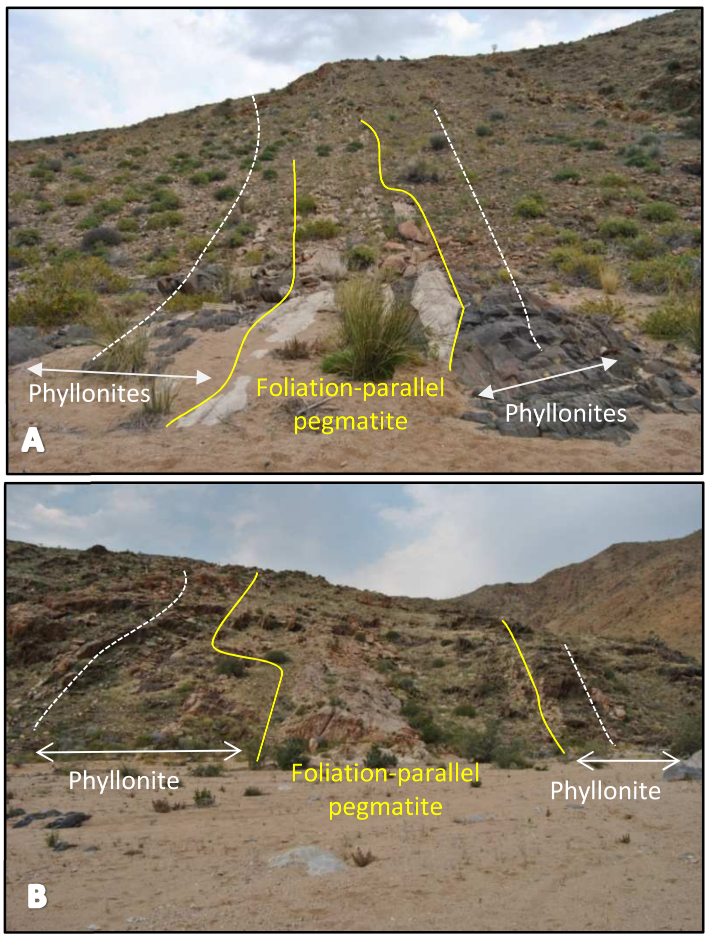

Figure 5.4 Photographs taken in the PSZ core of pegmatites parallel to the phyllonitic foliation (S_{4b}; stippled white). (A) Centrally (ca. 120 m from the northern boundary) into the PSZ core, facing west. Phyllonite successions (2 m thick) adjacent to pegmatites are developed. GPS serves as scale. (B) At the southern limit of the PSZ core, outcrop succession ca. 80 m across in foreground, facing ESE. Notably the thickness of the phyllonites towards the southern boundary increase and pegmatites (up to 15 m thick) are, in places preserved as remnants within the pervasive phyllonite successions.

The foliation-parallel pegmatites are almost invariably deformed (Figs. 5.5a-d), but strain intensities and the degree of later deformation differ according to the location of granite and pegmatite sheets in proximity to high-strain zones ($S_{4a,b}$) within the PSZ and their relative timing of emplacement. Relatively unstrained pegmatites still display pristine igneous textures (Fig. 5.5a), and macroscopic fabrics are only evidenced by the grain-shape preferred orientation of quartz or the marginal recrystallization of feldspar. High-strain equivalents have experienced a near-complete D_4 overprint to form either foliated phyllonites (Fig. 4.5) or quartz-feldspar ultramylonites and ultracataclasites (Figs. 4.12-orange zone; 5.5d). In the latter case, pegmatites have undergone a near-pervasive grain refinement to form granular to banded quartzo-feldpathic gneisses and mylonites (Fig. 5.5b). The variable degrees to which the pegmatites are deformed within the core indicate that they were largely emplaced as syn-kinematic intrusions during the development of the PSZ.

The pegmatite geometries and their alignment parallel to shear-zone fabrics within the PSZ core suggests emplacement of the sheets to have been mainly controlled by subvertical lithological and structural (D_4) anisotropies induced during transposition and PSZ-deformation. The preferentially orientated anisotropies decrease the tensile rock strength and create zones of high permeability along which granitic magma preferentially migrates (e.g. Brown and Solar, 1999; Weinberg, 1999; Brown, 1994, 2007, 2010).

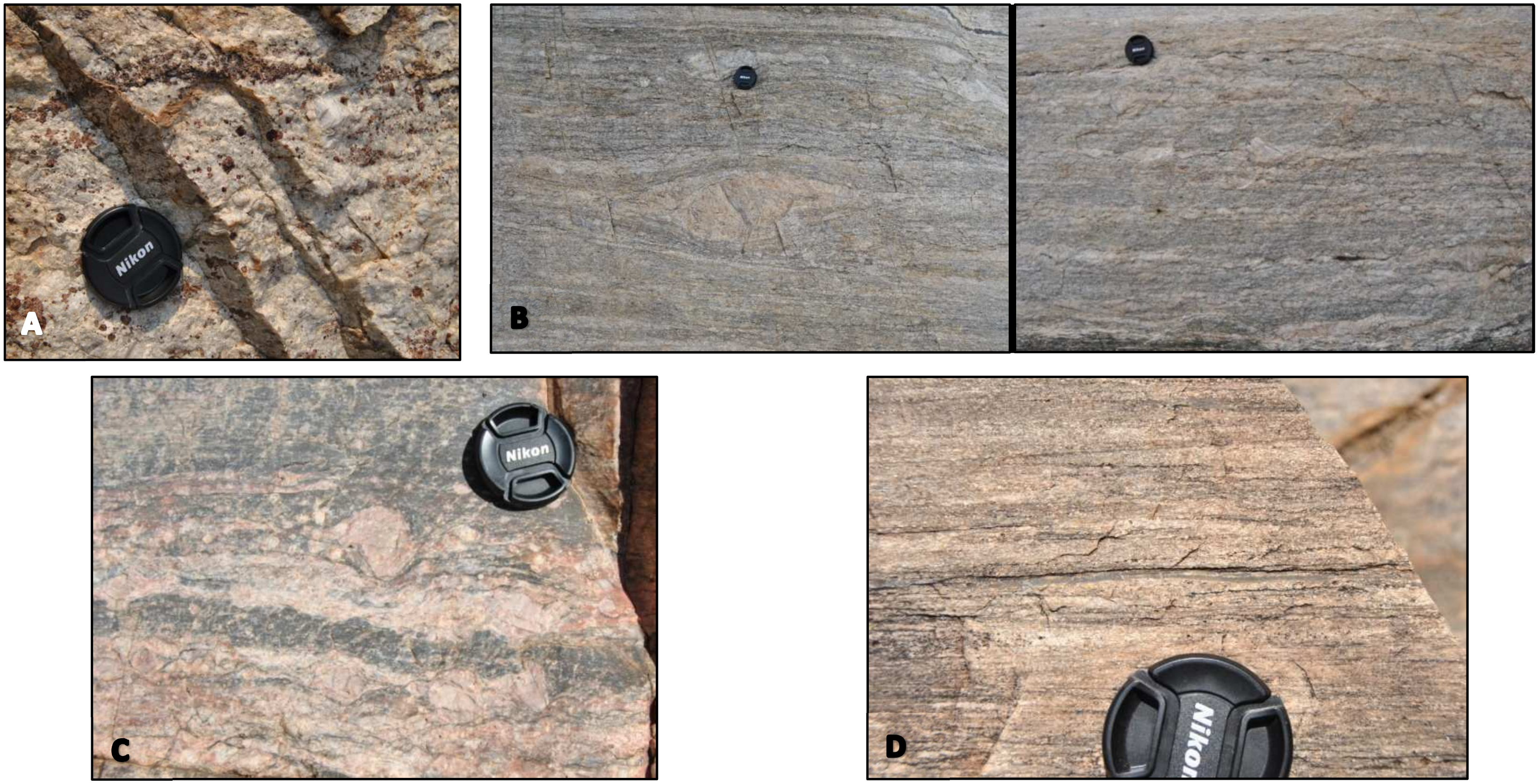

Figure. 5.5. (A). Oblique plan view with top to north, showing relatively pristine pegmatitic textures, the lack of a strong fabric and garnet cumulates within foliation parallel pegmatites. (B). Plan views with top to north, of deformed pegmatite sheets centrally within the PSZ core. Despite the ductile overprint, pegmatites still retain their primary fabrics in lower-strain pods as seen in the large (80 cm) feldspar phenocrysts amidst quartz ribbons and a recrystallised quartzo-feldspathic matrix and the formation of a gneissic compositional banding within the pegmatite. (C) Plan view with top to north of protomylonitic textures in deformed pegmatites within the PSZ core. The feldspar phenocryst (centre view) is rotated dextrally forming a weakly defined delta clast but internally the phenocryst is fractured by brittle deformation mechanics (D_{4b}). (D) Plan view with top to north. Substantial grain refinement of the pegmatites forming very fine grained, banded quartz-feldspar ultramylonite defined almost exclusively by quartz ribbons. A photomicrograph of this ultracataclasite is found in Fig. 4.12 (CMAK1).

5.1.2 Pegmatites oblique to the foliation

Pegmatites that cross-cut the foliation can be straight or are folded into open to isoclinal folds, which suggests syn to late- and post-tectonic emplacement.

The folded pegmatites largely retain their coarse-grained primary textures, but tight to isoclinal folding has partly transposed the intrusive sheets into the mylonitic S_{4a} foliation. In places, late-stage, retrograde S_{4b} shears dismember and displace individual pegmatite sheets (Figs. 4.2b; 5.6). These folded pegmatites are interpreted to trace F_4 folds as their axial planes are commonly parallel to the mylonitic foliation. The lack of high-strain fabrics within the pegmatites but relative deformation by D_{4a} and D_{4b} suggest that emplacement occurred syn-kinematic to D_4 and was initially controlled by original anisotropies across the lithological boundaries (S_2/S_4) and subsequently by the high-strain fabric (S_{4a}).

Figure. 5.6. Oblique longitudinal view facing E of a folded and subsequently transposed and truncated pegmatite within the PSZ core. S_{4a} is axial planar to these folds and transposed dextrally by chlorite-epidote rich brittle-ductile domain (stippled green). This pegmatite within the PSZ core is therefore inferred to be emplaced between S_{4a} and S_{4b}.

The laterally continuous oblique pegmatites (Figs. 5.7a-c) cross-cut the mylonitic foliation at consistently shallow angles (ca. 20^o - 30^o) and with a consistent clockwise sense of rotation with respect to the shear-zone foliation. These pegmatites have similarly well defined, relatively straight contacts with the wallrocks. This is consistent with emplacement of the sheets into synthetic Riedel shears (e.g. Davies et al., 2000; Katz et al., 2004) related to the dextral shear along the PSZ. In numerous cases, the low-angle cross-cutting sheets can be seen to be connected to foliation-parallel pegmatites.

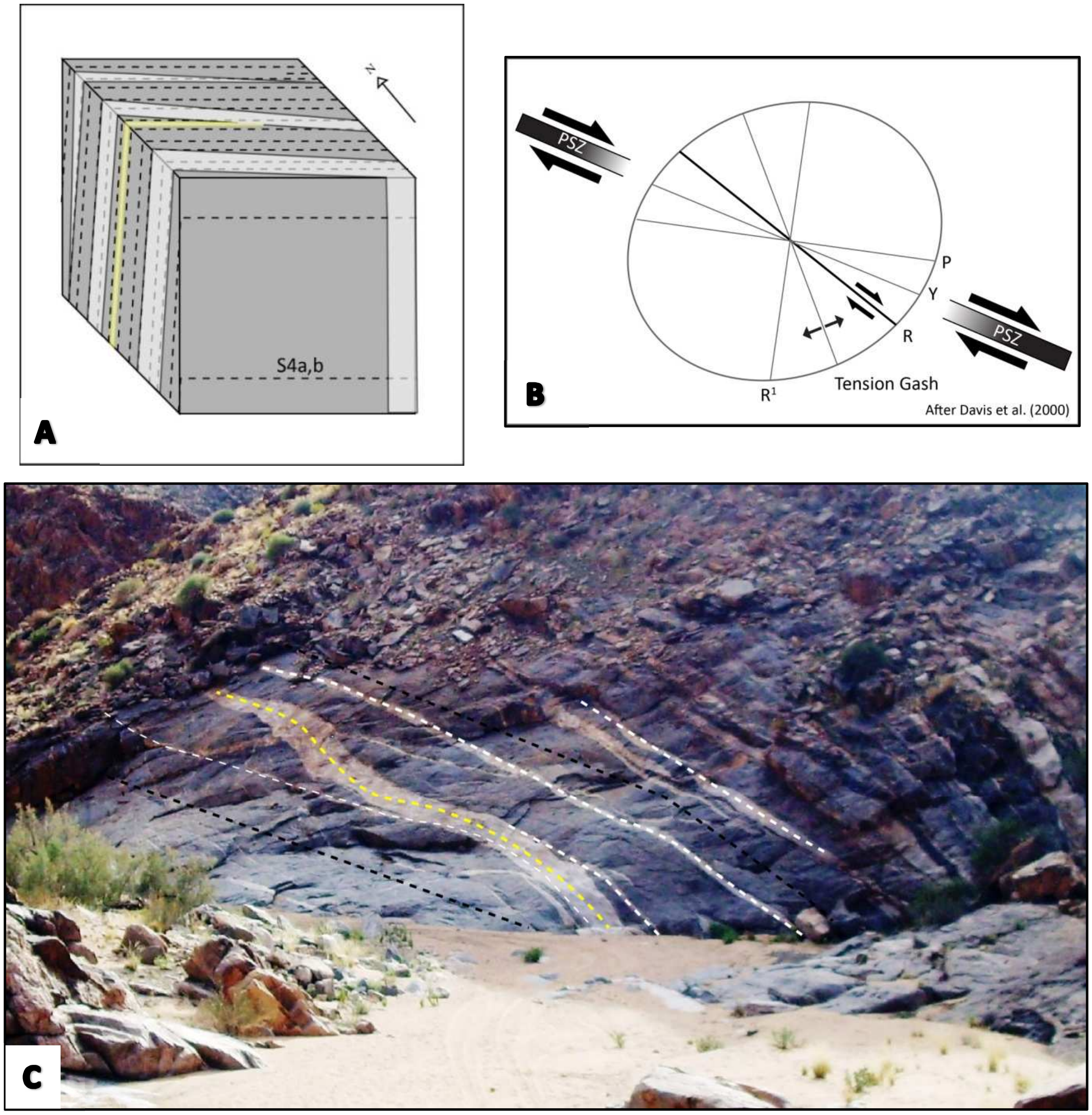

Figure. 5.7. (A). Schematic 3D block diagram illustrating the emplacement geometry of pegmatites that cross cut the foliation ($S_{4a,b}$) within the PSZ core. Foliation parallel pegmatites (yellow) commonly feed into the obliquely orientated pegmatites. In places (northern margin) pegmatites transposed into the mylonitic ($S_{4a,b}$) foliation make their distinction from those parallel to the foliation problematic. (B) Strain ellipse orientated in the direction of the regional PSZ trend. The strain ellipse indicates the orientations of various structures formed within predominately dextral simple shear domains such as the northern PSZ margin. The obliquely cutting pegmatites are emplaced in those correlating to the orientation of synthetic Riedel shears (R) (C). Oblique along-strike view towards west showing two distinct pegmatite orientations. Foliation- ($S_{4a,b}$; stippled black) parallel pegmatites (stippled white) are connected by cross-cutting pegmatite (stippled yellow).

5.1.3 Jog-like pegmatite geometries

High-angle cross-cutting pegmatites in the PSZ core form in jog-like pod geometries that appear to be confined to the S_{4b}-dominated southern margin of the PSZ. The central, highly discordant parts of the z-like jogs are orientated at high angles (80^o - 90^o) to the inferred stretching direction in the PSZ core. This discordant central part is bounded at the ends by two prominent foliation-parallel pegmatite sheets (Fig. 5.8). These jogs range in size but do not exceed more than 10 m in length and 5 m in width (Fig. 5.9, localities e.g. A, B, C). Smaller, foliation-parallel pegmatites connect with the discordant parts of the jogs and textural and mineralogical continuity (Fig. 5.9d) between pegmatites in the high-angle jogs and the concordant pegmatites suggest that they formed contemporaneously. Importantly, foliation-parallel pegmatites typically widen towards the high-angle jogs, resulting in funnel- or wedge shaped geometries with the widest parts located at the intersection between the two geometries (Fig. 5.9, localities e.g. D, D', D''). This also results in the highly irregular boundaries of the high-angle jogs against wallrocks. The widening of the concordant pegmatites within 1-2 m of the high-angle jog also suggests connectivity between the two geometries. Dyke intersections with the thinner, intersecting sills exhibit inconsistent cross-cutting relationships, commonly with the dykes cutting across the concordant thinner sills (Fig. 5.9, localities e.g. E). The implications of numerous feeders into the jogs and their inconsistent cross-cutting relationships is discussed in Chapter 7.

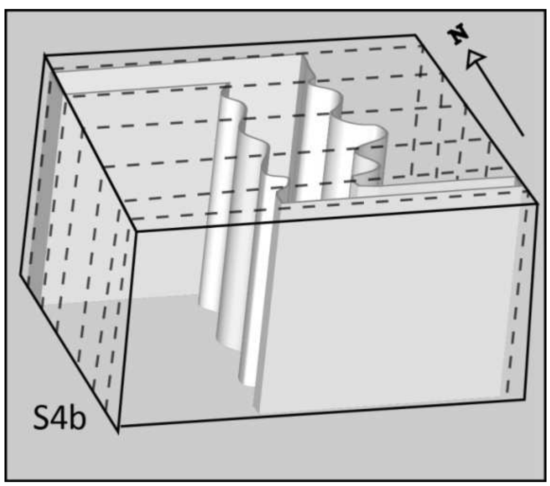

Figure. 5.8. Schematic 3D block diagram of the z-like jog geometries observed within the PSZ core. The jog is defined by a short stubby, commonly deformed (showing cuspate-lobate fold geometries) dyke connecting two or more foliation parallel pegmatites to form a z-like jog forming in a dextral shear regime.

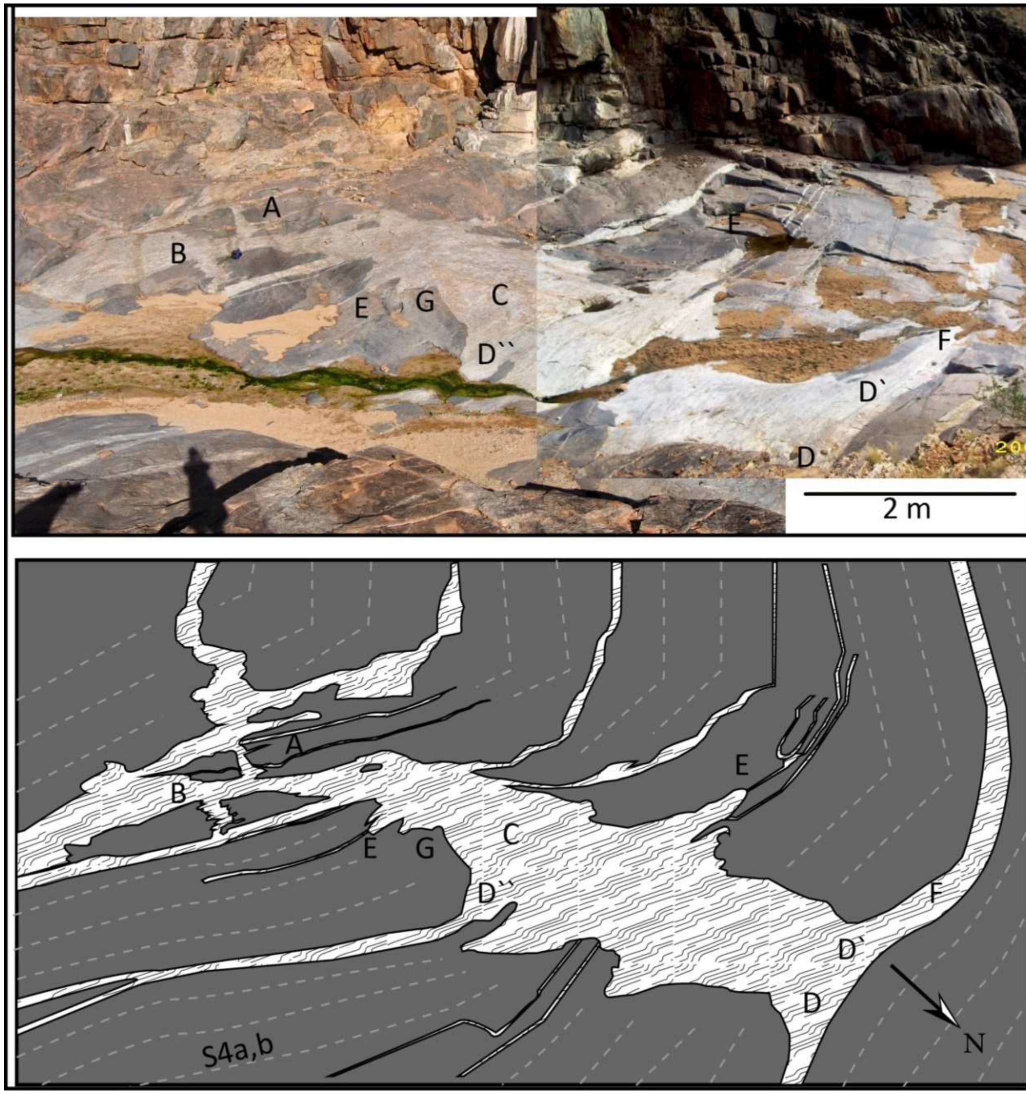

Figure. 5.9. Diagram of interconnected jog-like pegmatite geometries at the southern margin of the PSZ core. Digitised oblique plan view, facing SSW, of different-sized, stubby pegmatite dykes (A, B, C) connecting a series of foliation parallel sills (D) and subsequently cutting across others (E). Note sills are deformed to quartzo-feldspathic mylonites (F) while deformation of the dykes forms cuspate-lobate folds along their margins (G) and protomylonites within their centres (C). The schematic line diagram above illustrates the formation of a dilatant site during the development of a dextral jog during dextral shearing characterising D_{4a}.

The dykes and connecting sills are deformed under ductile conditions and develop a mylonitic-S4 fabric throughout the pegmatite bodies (Fig. 5.9f). Depending on the thickness of the dykes they are variably deformed in their centres (Fig. 5.9c) but typically show cuspate to lobate deformation folds (Fig. 5.9g) along their margins, developed in response to the competency difference between the host rocks and the dykes during D_4. The deformation features within the pegmatites and the relative preservation of the original jog-like geometry suggests the jogs developed syn-kinematic to PSZ deformation.

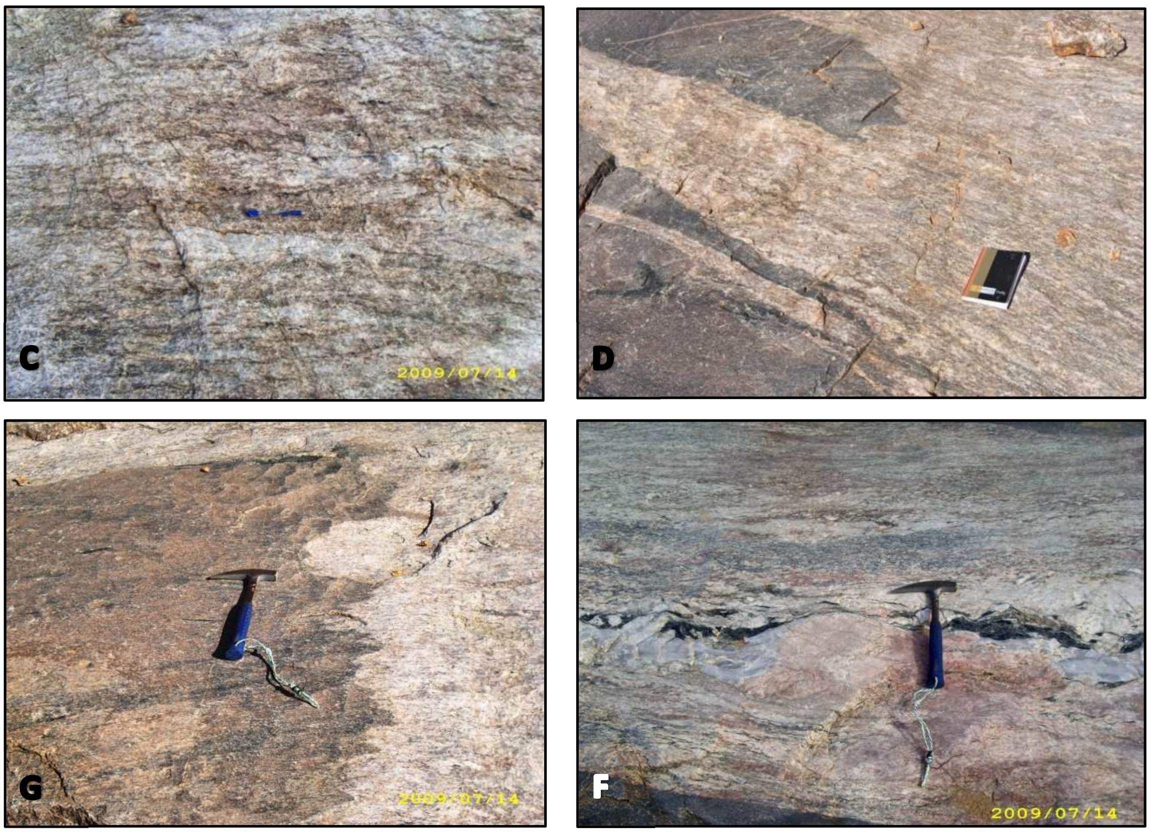

Figure 5.9 cont. Localities from the above diagram. (C) Oblique plan view, top to south. Deformation within the centre of a thick (3 m) discordant pegmatite to mylonites and protomylonites. (D) Oblique plan view, facing SE of the contact between a concordant and discordant pegmatites where mineral and textural continuity suggest contemporaneous emplacement. (G) Plan view with top to south. Cuspate and lobate folding along the margins of the pegmatite dyke. (F) Oblique plan view of the concordant pegmatite dyke where deformed is characterised by the formation of quartz ribbons and preferred alignment of biotite booklets.

5.2 Skimmelberg Pegmatite Stockwork in the SD

The SPS is an extensively developed pegmatite complex within the southern footwall of the PSZ, the extent of which defines the SD (Fig. 5.10-orange domain). The SPS is characterized by a stockwork of intersecting concordant pegmatite sills (Fig. 5.10-blue vectors) and discordant, northerly-trending dykes (Fig. 5.10-red vectors) in which pegmatites may make up 60-70 volume % of the outcrop. The extent of the SPS is defined exclusively by the occurrence of sharply discordant dykes and broadly forms a lensoid area with the centre of this region, located at ca. 28.902°S, 19.068°E. The SPS trends WNW-ESE, parallel to the adjacent PSZ, covering an area of ca. 12 km by 2 km. The northern boundary of the SD is very sharp and defined by the contact of the SPS against the high-strain PSZ core (discussed in Chapter 4.2.2). The western and eastern boundaries are less well defined and are taken as the lateral limit of pegmatite dyke occurrences. The southern boundary of the SD is equally gradual and taken as the southernmost occurrences of pegmatite dykes and their terminations. This rather transitional southern boundary coincides with the first occurrence of the muscovite-sillimanite-bearing units of the Onseepkans Formation (Appendix A).

5.2.1 Pegmatite Sills

Within the SPS, ca. 350 concordant pegmatite bodies have been mapped. The pegmatites occur almost exclusively subparallel or parallel to the wall-rock foliation (S_2/S_4, S_{4a}) and are therefore regarded as sills (*sensu stricto*). The vast majority of sills are compositionally and texturally homogeneous and composed predominantly of variable proportions of coarse-grained quartz and large (up to 15 cm) feldspar (microcline and oligoclase) crystals that together constitute more than 90 volume % of the pegmatites. Muscovite, garnet and magnetite are present, but subordinate. Zoning is not always evident within the sills but, in places, subtle compositional variations from quartz-feldspar assemblages to quartz-dominated cores are observed. The sills appear compositionally similar to those of the regional pegmatite belt that occur proximal to the study area (see Chapter 2.4). Therefore, for the purposes of this study, concordant pegmatites confined to the SD are considered to be part of the SPS.

Figure. 5.10. (see next page). Map of pegmatites within the SPS (orange) and surrounding areas. Stereoplots are poles to planes for the N-S pegmatite dykes (red), NW-SE trending sills (blue) within the SPS and sills to the south of the SPS (grey) are indicated. Note that anomalous orientation data in the respective stereoplots correlate with specific domains within the SPS and is indicated by the stippled-black lines.

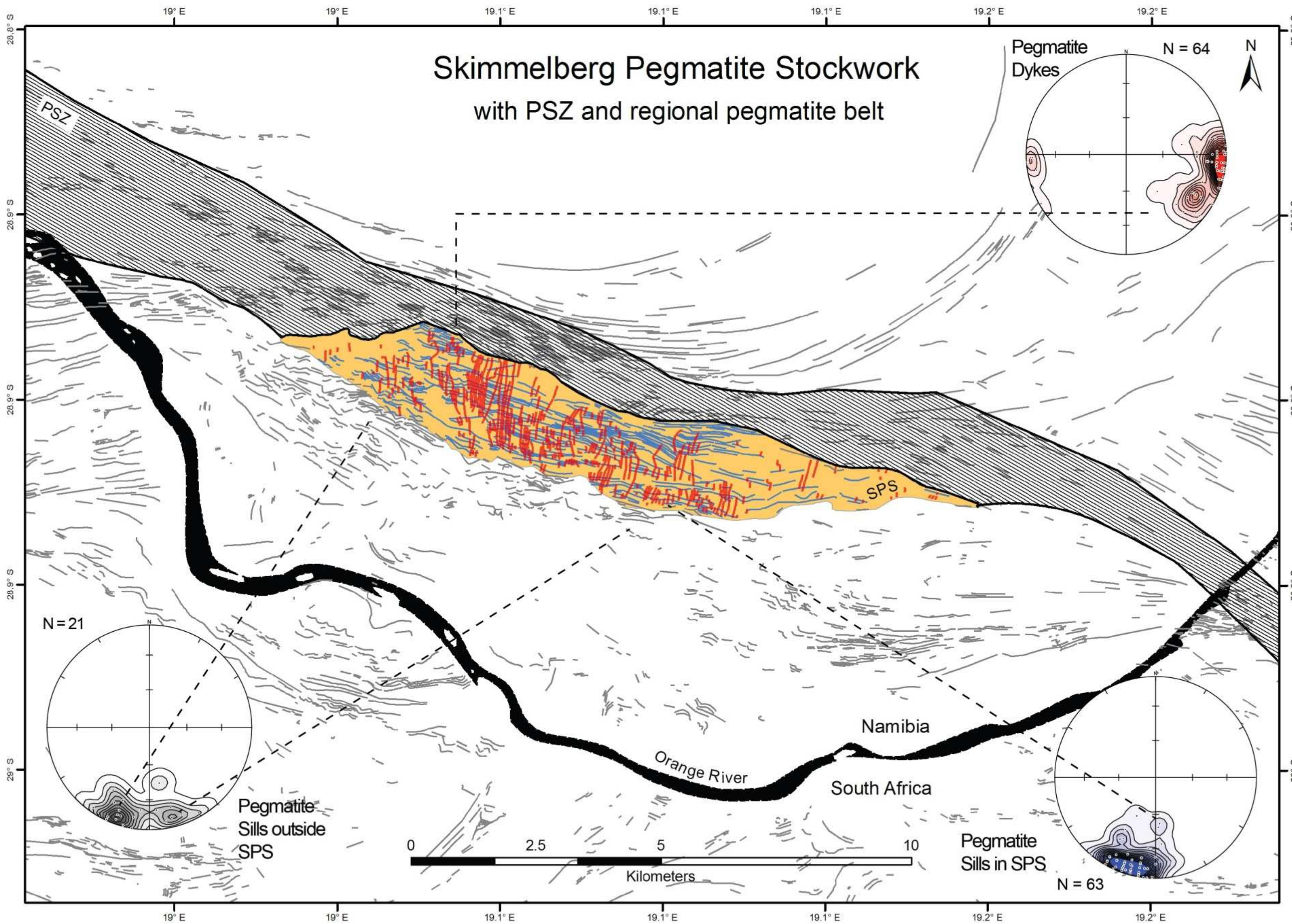

Skimmelberg Pegmatite Stockwork
with PSZ and regional pegmatite belt
Pegmatite
Dykes
N = 64
N
PSZ
SPS
N = 21
Pegmatite
Sills outside
SPS
Namibia
Orange River
South Africa
0
2.5
5
10
Kilometers
Pegmatite
Sills in SPS
N = 63
19° E
19.1° E
19.2° E
28.8° S
28.9° S
29° S

The majority of the sills within the SPS occur as uniformly tabular bodies (Fig. 5.11a) with length-to-width ratios between 10:1 and 100:1. Individual sills are typically between 3 m and 7 m thick. Rare, invariably sheeted pegmatites made from multiple, smaller bodies can reach up to 18 m in total thickness. The sills commonly have sharp wall-rock contacts and can commonly be traced over 2 km along strike before laterally tapering (Figs. 5.11b,c) and terminating into the wallrocks or against high-angle dykes (discussed below). In cross-section, vertical terminations are not observed and due to topographic variation within the SD, the sills are seen to extend more than 300 m along their Y-axes. The lateral tips of the pegmatites are texturally and mineralogically similar to the pegmatite centres and form thin (cm-scale) vein-like geometries that widen towards the centre of the body, commonly over distances of less than 2 m (Figs. 5.11b,c), defining the tapering to disc-shaped geometries at the terminations. The relative continuity in sill thickness along the X and Y-axes of the bodies, however, defines the overall tabular geometry of the sills. There is little to no evidence of brecciation at sill terminations and the foliation planes appear to be cleanly parted with the pegmatite sills intruded in between them. The sills are variably distributed across the SD, with negligible notable variation in the physical dimensions between pegmatites occurring centrally within and at the margins of the SD. Similarly, with the exception of the effects of deformation (discussed below), there is little variation in the mineralogical and textural properties between sills across the SD. Adjacent to the PSZ the sills attain sub-vertical dips towards NNE but are progressively shallower-dipping towards the southern margin (Fig. 5.10). This correlates directly with a progressive decrease in the D_4 fabric intensity away from the PSZ.

Deformation of the sills within the SPS is significantly lower than those within the PSZ core, with the majority of the sills relatively undeformed. Note that deformation in the sills is most prominent along the northern margin of the SD and becomes less evident away from the margin. Along the margin with the PSZ core the sills may display mylonitic textures (discussed in Chapter 5.1.1) but away from the margin, deformation of the sills results in partial segregation into wallrocks or weakly foliated to boundinaged and folded pegmatites. The foliated pegmatites exhibit a weak PSZ-parallel fabric (S_{4a}) defined by the alignment of muscovite booklets. The thinner (< 5 m) sills typically exhibit boudinage or are folded, forming monoclinal-open fold geometries and/or upright south-verging isoclinal folds. The latter fold geometry contains an axial planar S_{4a} fabric suggesting these pegmatites were folded during D_{4a}. The thicker sills commonly only display deformation along their margins, typified by the weak deflection of host rock foliations. In the centre of the SPS deformation textures are relatively rare and sills are commonly devoid of deformation textures (Figs. 5.11a,b). These sills typically have sharper contacts with the host rocks, showing little to no evidence for deflection of the host rock foliation along/around the contacts. Therefore, in addition to the overall thickness of the sills and competency contrast with the host rocks, the degree of deformation in the sills depends on the relative timing of emplacement and the distance from the PSZ core. Thus, the varying degrees of deformation of sills in the SPS present field evidence for the emplacement of the sills as multiple intrusive phases during D_4. This observation is pertinent to the interpretation of geochronological data derived from the SPS pegmatite sills (discussed in Chapter 7).

Emplacement of the sills in the SPS, particularly along the northern margin, therefore appears to be controlled by the development of a subvertical low-strain-S_{4a} in the wallrocks, similar to those that parallel the mylonitic foliation within the PSZ core. Away from the margin, where the effects of D_4 are less palpable, the controlling factor for sill emplacement is deemed to be anisotropies derived from the (re-orientated) gneissic fabrics (S_2/S_4).

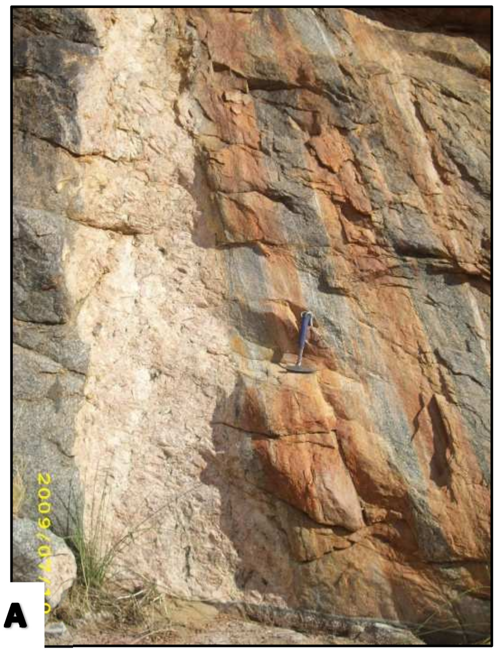

A

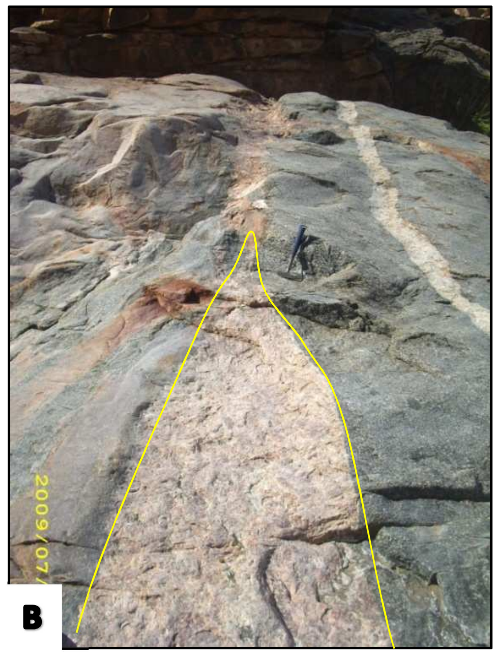

B

C

Figure. 5.11. (A) Cross-sectional view (facing west) of a tabular SPS pegmatite sill parallel to the wall-rock foliation (defined by compositional and gneissic layering - S_2/S_4). (B) Oblique plan view, facing east of two SPS pegmatite sills that are parallel to the wall-rock foliation (S_2/S_4). Here the larger pegmatite (centre view) tapers from ca. 1 m thick to < 10 cm over a distance of less than 2 m. The adjoining pegmatite sill to the south is considerably thinner but is laterally continuous, traced over 20 m along strike. (C) Oblique view (facing NNW) of a pegmatite sill that pinches from ca. 1 m wide to ca. 30 cm over a distance of less than 3 m. The sills in A, B, C are largely undeformed, preserving primary igneous textures and although the contacts are slightly irregular, they generally have sharp contacts with the wallrocks.

5.2.2 Pegmatite Dykes

Some 330 discordant pegmatite dykes have been mapped in the SPS (Fig. 5.10). The dykes mostly have simple mineral assemblages, but some dykes also show internal heterogeneities and zonation patterns. The cores of the dykes are composed predominately of large (up to 50 cm) quartz and feldspar (microcline and oligoclase) crystals, whereas the marginal zones (20 cm – 5m wide) contain substantially higher amounts of muscovite, garnet and magnetite. Generally the dykes are compositionally similar to sills within the SPS.

The majority of the dykes occur as N- to NNE-trending, steep to subvertical tabular bodies (Figs. 5.12-14) cross-cutting the wall-rock foliation (S_{4a}, S_2/S_4) at oblique to high angles (Fig. 5.14). Although contacts with the wallrocks are sometimes uneven and some of the smaller dykes are irregular in shape, the majority of the dykes, especially thicker examples (> 5 m width), show knife-sharp contacts (Fig. 5.14a). Individual dykes are commonly sheeted and can be seen to be made up of compositionally and texturally distinct, multiple phases. Dykes are notably more abundant and larger in the western to central parts of SPS (Fig. 5.10), where pegmatites may constitute up to 80 volume % of the exposures. Dyke abundances gradually decrease towards the southern and eastern margins (Figs. 5.9). The thickest and longest dykes can span up to 2 km, from the northern PSZ-SD boundary (Figs. 5.9-13) across to the southern margin where they appear to taper, pinching towards the south, defining wedge-shaped geometries (X-axis > Z-axis; Figs. 5.12,14b). The extension of the dyke-wedge along its Y-axis is unknown due to the lack of vertical terminations. However from exposures along steep cliffs they may be considered to be greater than 400 m long. Some of the dykes reach over 50 m in thickness (Z-axis) at the northern margin but pinch to less than 5 m before terminating or connecting to pegmatite sills (discussed below in Chapter 5.2.3). The dykes have length-to-width ratios between 5:1 and 40:1. The thickest and longest dykes are, however, invariably sheeted and aspect ratios may not be representative of individual pegmatite bodies. At the western and eastern margins of the SPS, the frequency of dykes within the wallrocks is ca. 20 volume % pegmatite to wall-rock ratio and dykes range in thickness from 7 to 15 m and has strike lengths of commonly less than 100 m (Fig. 5.9). Along the northern margin of the SD, the dykes are consistently orientated at high angles to the high-strain PSZ core fabric ($S_{4a,b}$). Centrally within the SPS, the sheets dip steeply to the WNW but towards the western margin, dykes trend NE-SW and dip between 55^{o} -75^{o} to the WNW (Fig. 5.12).

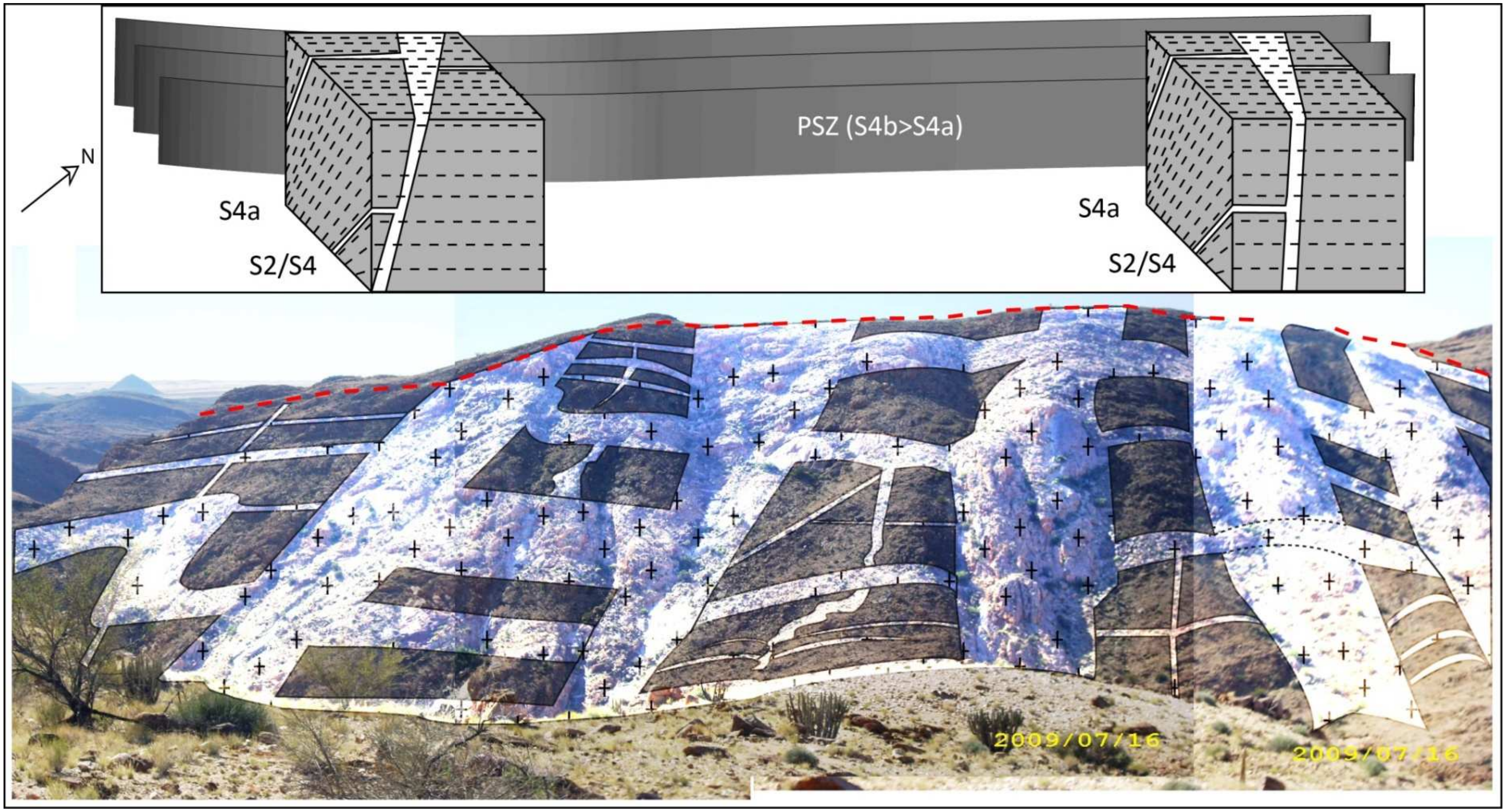

Figure. 5.12. Panoramic view of southward facing cliffs along the northern boundary of the SPS, adjacent to the PSZ core (stippled red). The cliff section is ca. 800 m wide. Interconnecting pegmatite sills and dykes (digitized in white) form part of the extensively developed pegmatite stockwork in the footwall of the PSZ. The schematic block diagrams illustrate the wedge-shape geometry and orientation of the dyke sheets with regard to the D_4 fabrics (S_{4a} along the PSZ, S2/S4 southwards).

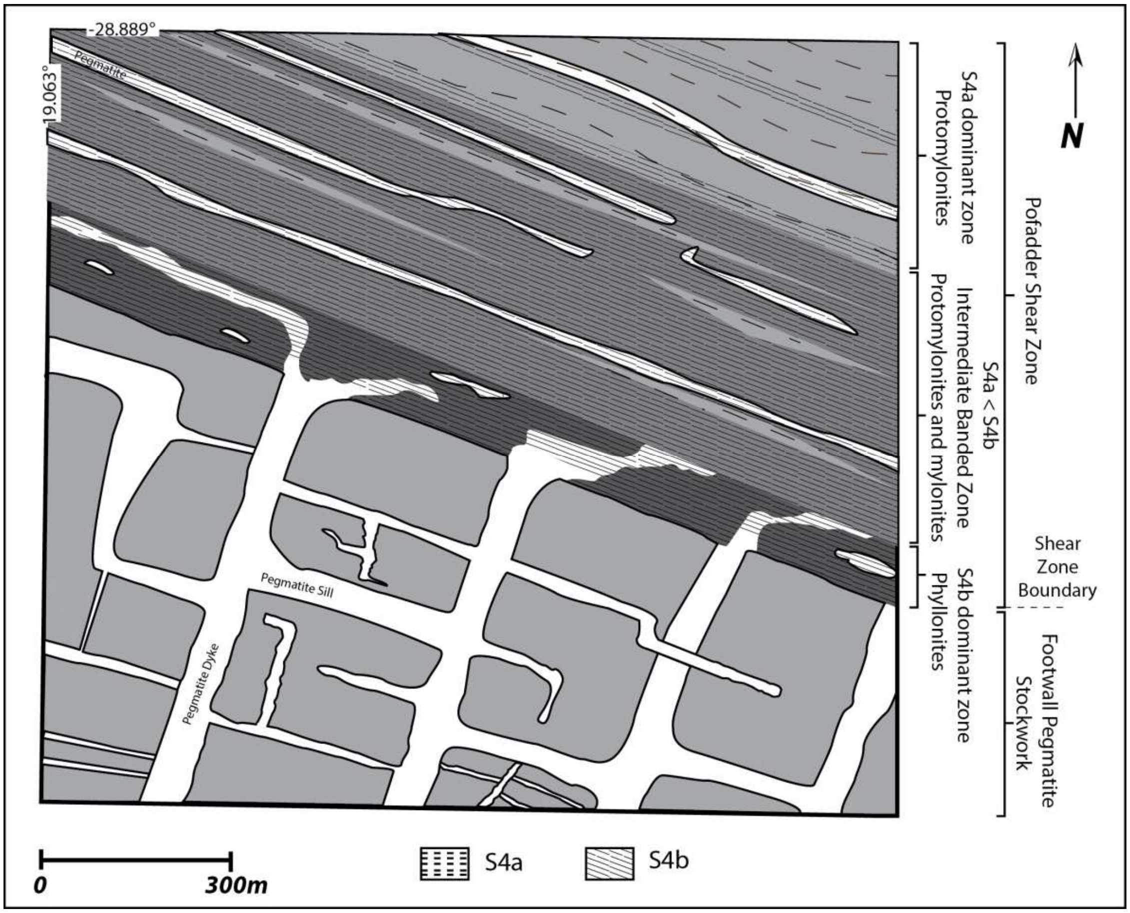

Figure. 5.13. Geological map of southern margin of the PSZ core, illustrating the limit of the core and S_{4b} fabric development, as well as the transposition of N-S trending pegmatite dykes into the PSZ core. Note the tapering z-like geometry formed by the dykes and inconsistent cross-cutting relationships of the dykes and sills.

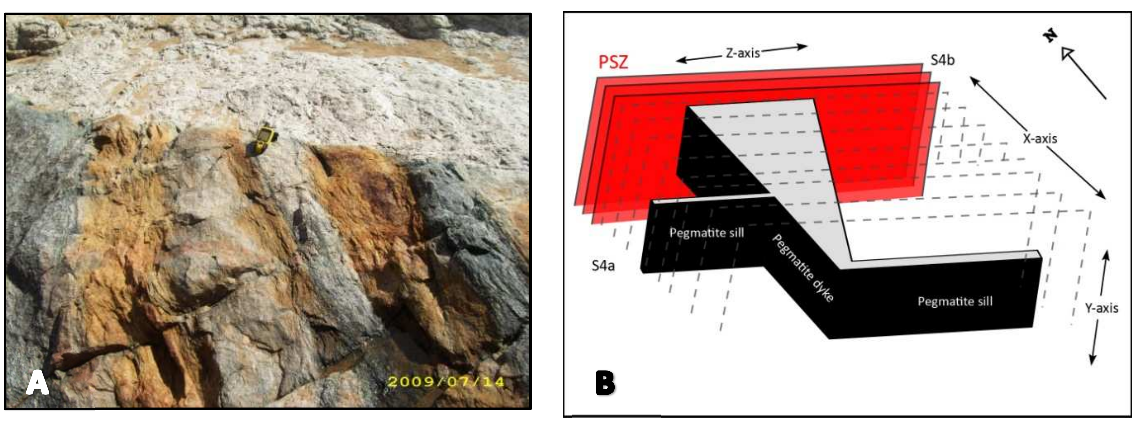

Figure. 5.14. (A) Oblique plan view, facing west. Pegmatite dykes within the SPS strike perpendicular to the foliation (S2/S4), here defined by interlayered granodiorite and quartzo-feldspathic orthogneisses. The dykes occur as tabular sheet-like bodies and typically show sharp contacts with the wallrocks. (B) Schematic illustration of the pegmatite dyke geometry forming a wedge shaped body that tapers (pinches) southwards away from the PSZ–core.

The majority of the dykes retain a weak fabric parallel to the main shear fabric (S_4) defined by muscovite booklets and rarely by the preferred orientation of quartz and feldspar crystals (Fig. 5.15a). The foliation is commonly observed within the cores of the thinner (2 m - 5 m thick) dykes but, in wider (> 20 m) dykes, the planar fabric is only developed along the marginal zones (Fig. 5.15b) and not evident in the core zones, which display macroscopically undeformed pegmatitic textures.

Figure 5.15. Plan views of pegmatite dykes of the SPS, views with tops to north. (A) The foliation defined by muscovite booklets is developed in core zones of thinner (< 5 m) pegmatite dykes while (B) only in the rim zones of thicker the pegmatite dykes of the SPS. In the marginal zones the foliation is additionally defined by the preferred alignment of quartz and feldspar crystals.

As with the deformation of the SPS sills, evidence of PSZ deformation (D_4) in the dykes is largely dependent on the thickness of the pegmatite bodies and host-rock lithology and, in general, deformation is similarly less apparent away from the northern margin of the SD. Dykes thinner than ca. 2 m can show F_4 fold geometries with axial traces that parallel both the wall-rock foliation (S4a) and the foliation that is commonly retained in the marginal zones of the thicker dykes (Fig. 5.16a). In dykes between ca. 2 m – 5 m, thick cuspate-lobate fold geometries (Fig. 5.16b) are commonly developed due to the competency contrasts between the dykes and host rocks during deformation (D_4).

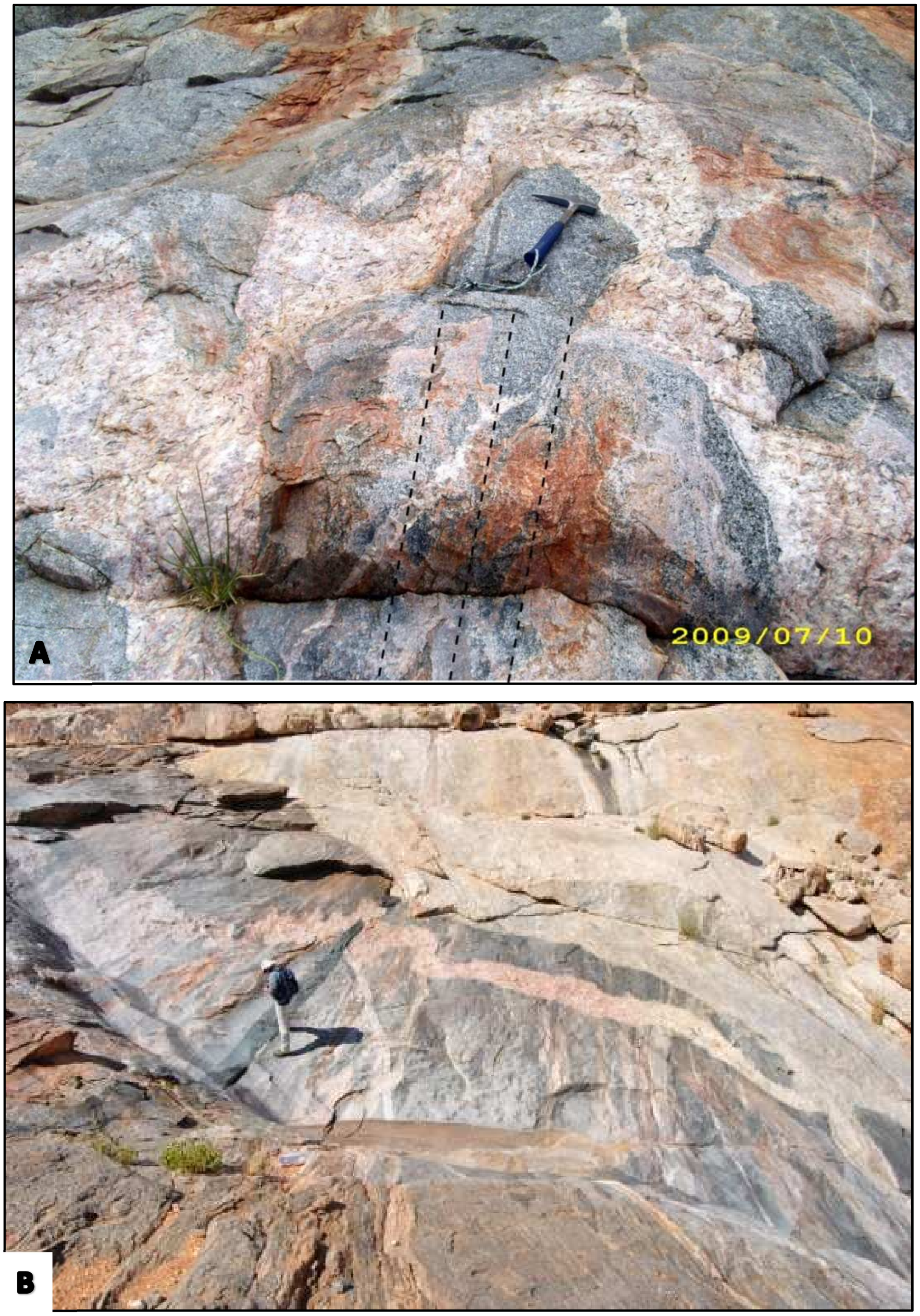

Figure. 5.16. Fold geometries within the dykes of the SPS. (A) Plan view with top to NNE. A thin N-S dyke is folded with an axial plane parallel to the wall-rock foliation (stippled black and indicated by the elongated dioritic enclave to the left of the geological hammer). (B) Oblique plan view with top to east. A thin pegmatite dyke extends northwards from a pegmatite sill. The dyke is relatively undeformed in the south but is deformed towards its northern termination, showing cuspate-lobate fold geometries largely due to compositional contrasts with the fine grained quartzo-feldspathic host rocks when both are subjected to deformation that occurred subsequent to dyke emplacement.

In contrast to the rather ill-defined southern, western and northern margins of the SPS, pegmatite dykes terminate abruptly in the north against the mylonites (phyllonites) of the PSZ (Fig. 5.13). Even wide (> 50 m) and laterally extensive pegmatites terminate within less than 10 m against this contact. Terminations display S-like geometries through numerous N-S dykes being rotated clockwise into the PSZ before ultimately being dragged and transposed into the mylonitic fabric (S_{4b}) of the PSZ core (Fig. 5.13). The initially coarse-grained pegmatite dykes undergo a pervasive grain refinement and are deformed into banded quartz-feldspar ultramylonites and ultracataclasites with no visible porphyroclasts amid the quartz and feldspar ribbons (Fig. 4.12-CMAK1). The sense of drag and clockwise rotation of pegmatites along this contact is consistent with the dextral shear along the PSZ. Within the SD, some smaller (> 1 m thick) dykes are truncated and/or displaced by locally developed D_4 shears (Fig. 5.17).

The general lack of displacement of marker units or lithological contacts in the wallrocks and their laterally extensive nature suggests that the dykes of the SPS occupy extensional (mode I opening) fractures. These fractures appear to be uniquely developed adjacent to the PSZ core in the southern footwall rocks. The thicker dimensions (Z-axes) of the dykes along the PSZ margin suggest opening of the fractures during dextral shear in the PSZ. This, coupled with the development of a shear-parallel foliation (S_{4a}) within the dykes, suggests, at least from field observations that these fractures developed during PSZ-deformation (D_4). The varying degrees of D_4 deformation of the dykes suggests that magma emplacement along these fractures occurred in multiple pulses over this period of deformation.

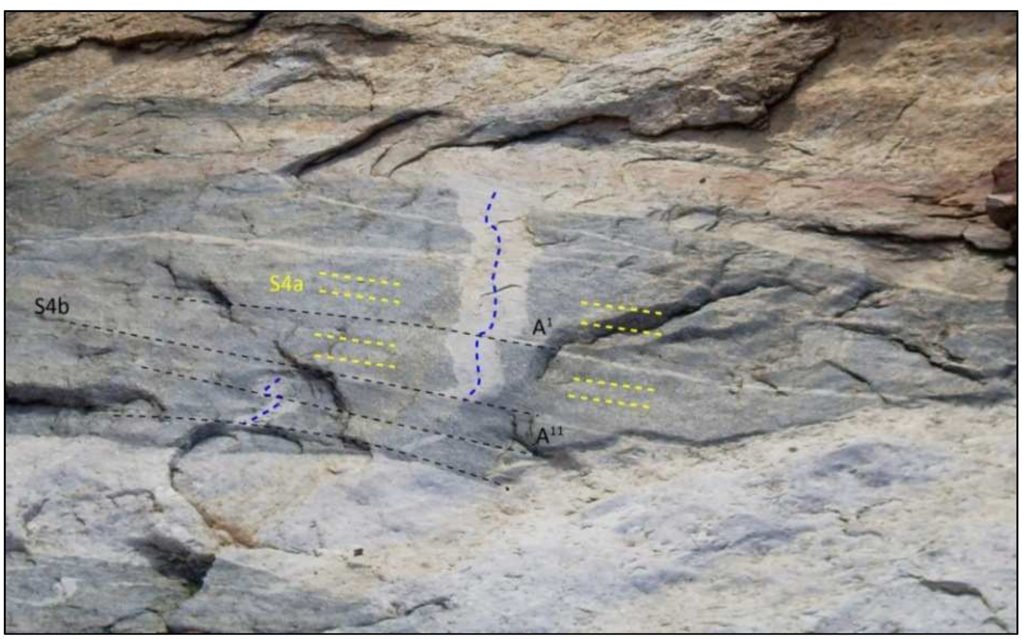

Figure. 5.17. Oblique plan view of a small scale (50 cm wide) pegmatite dyke extending down from a thick (8 m) pegmatite sill. The dyke shows multiple dextral and a rare sinistral truncation by S_{4b} (stippled black). Notably thin pegmatite sills extend along the S_{4b} plane (A', A'') and connect with the dyke.

5.2.3 Intrusive relationships between sills and dykes in the SPS

The majority of dykes in the SPS are perpendicular to the sills, forming a network of pegmatite sheets (Figs. 5.12-13,17). This network typically displays a 'tree-like' (Fig. 5.18) pattern. The 'tree-like' geometry of the stockwork is observed on all scales, from cm- and m-thick sheets to cliff sections and pegmatite widths > 50 m (Fig. 5.12, 5.18). Contact and cross-cutting relationships between sills and dykes are similar to those described for the jog geometries along the PSZ-margin (Chapter 5.1.3). They show similar inconsistent cross cutting relationships (Fig.5.19a), displaying evidence of relatively younger pegmatite sills cross-cutting pegmatite dykes (Fig. 5.18,19b) and/or dykes cross-cutting older pegmatite sills (Fig. 5.19c). Commonly an individual will cut across one dyke but be truncated by a second adjoining dyke. Most contacts display co-genetic relationships seen by (1) the development of quartz and mica crystals across the contact boundaries (Fig. 5.18,19d) or (2) where sills feed into the larger dykes they are diagnostically wider at the contact (Fig. 5.18,19a,b, localities e.g. X, X', Y, Z, Z'). Small dykes are commonly deformed, show z-like geometries (Fig. 5.19a) and support the formation of thicker discordant bodies from multiple, thinner concordant pegmatite sills. These inconsistent relationships between the sills and dykes provide field evidence for relatively synchronous emplacement of the sills and dykes within the SPS. Geochronological data for sills and dykes are presented in Chapter 6.

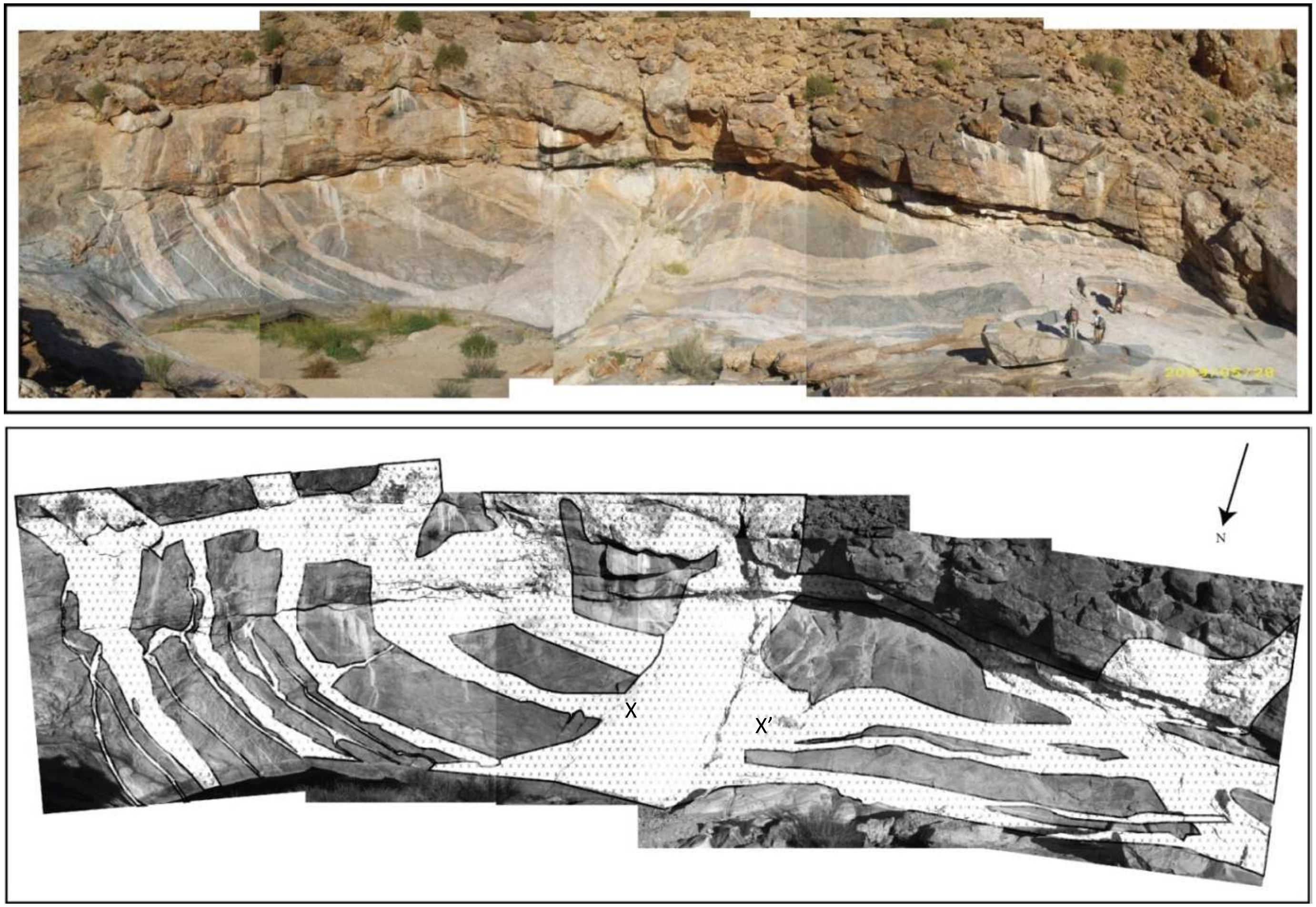

Figure. 5.18. Composite of a panoramic plan view of the typical pegmatite network in the SPS, facing south. The connective network of pegmatite sills and dykes within the SPS forms a tree-like mesh with thicker dykes connected to thinner sills at a variety of scales. The digitised photo (bottom) illustrates the cross cutting relationships between the sills and dykes, where the dykes are truncated by, and truncate their respective sill counterparts. Where sills and dykes show co-genetic relationships, the sills are typically wider at the contacts (e.g. localities X, X’).

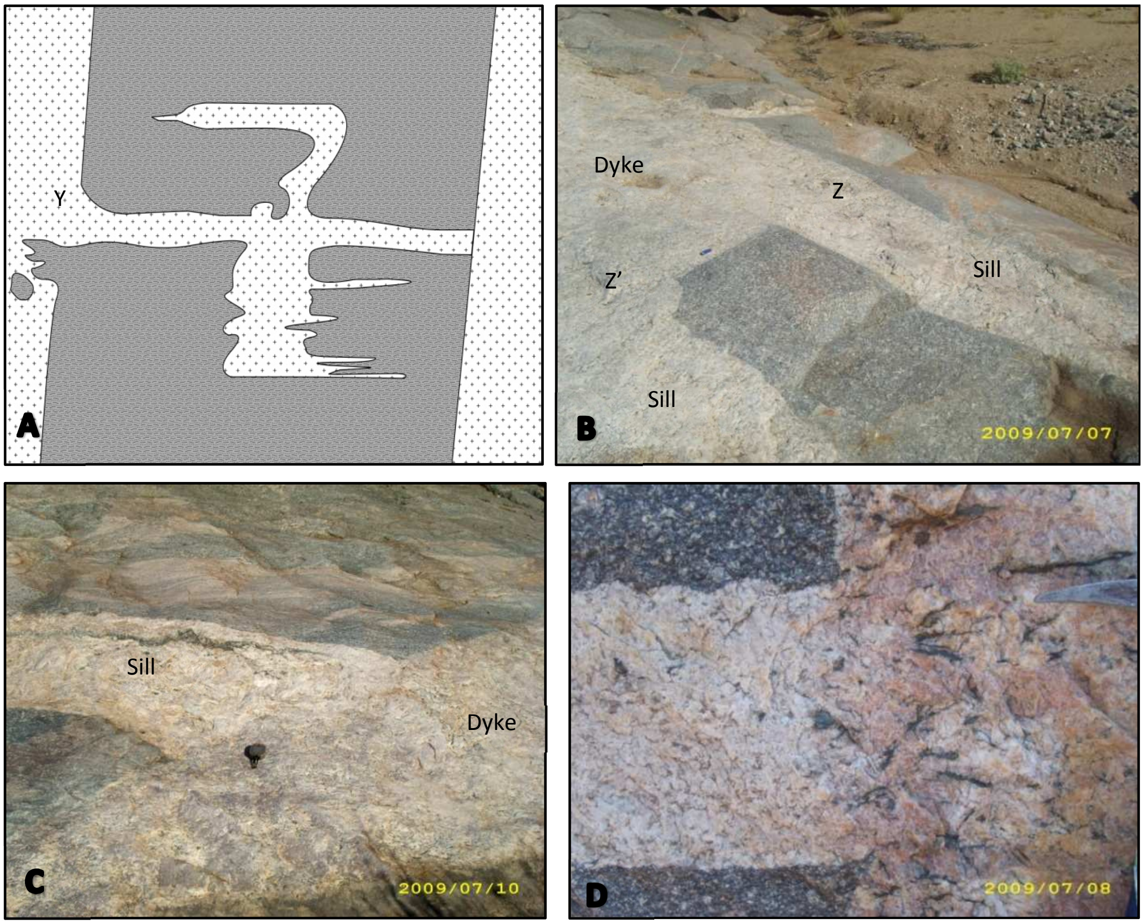

Figure. 5.19 (A) Schematic diagram illustrating the geometry of a smaller, irregular shaped dyke (40 cm thick) formed between two relatively larger, tabular dyke sheets (pegmatites are stippled, solid line along the contact indicates truncation of the pegmatite, open pattern indicates compositional and textural continuity and connectivity between sill and dyke and diagnostic funnel shape (Y). (B) Oblique plan view of dyke and sill intersections in SPS, top to NW. Inconsistent overprinting relationships between the sills and dykes is indicated where (Z) the sill cross cuts the dyke and at (Z') they shows co-genetic relationships and notably an inflated, funnel shaped contact. A 5cm long lighter serves as scale. (C) Oblique plan view of dyke and sill intersections in SPS, top to NW. A pegmatite dyke within the SPS truncates a pegmatite sill. (D) Plan view of dyke and sill contact in SPS, top to north. A perpendicular intersection of a pegmatite dyke (right) and sill (left) where an overgrowth of quartz, feldspar and muscovite occur across the contact between the pegmatites, suggesting co-genetic growth of both sills and dykes in the SPS. Point of geological hammer serves as scale.

5.3 The ND

Magmatic bodies in the ND range from (1) older (D_2-D_3), deformed and folded, thin (0.5 – 40 cm) quartz-feldspar veins that are cross-cut by later D_4 fabrics, to (2) thicker more prominent pegmatite sills or low-angle sheets and lenses contained within pre-syn D_4 fabrics, an (3) younger (post-D_4) undeformed quartz veins and granitic leucosomes within collapsed boudin necks. This study focuses on the pegmatites contained within D_4 fabrics.

The D_4-pegmatites occur principally as coarse grained, leucocratic white to pink, unzoned and homogenous pegmatites consisting almost exclusively of quartz, perthitic K-feldspar, plagioclase with minor amounts of biotite, with little to no garnet. There is, however, a significant change in geometry towards the PSZ core, showing an overall transition from pod-like and irregular bodies to more lenticular and tabular sills (Figs. 5.20-23). At the WL, where the D_4 fabrics are prolate (Fig. 4.10), pegmatites occur as discontinuous decimetre-sized patches enveloped by the wall-rock fabrics (Fig. 5.21a). The pegmatite patches are commonly lenticular, elongated and strongly boundinaged. The prolate fabrics are replaced by S>L fabrics towards the south and the PSZ core where (1) S_{4a} mylonitic fabrics and (2) F_4 fold generations are progressively developed (Fig. 4.10). Figure. 5.20 illustrates how the change in strain corresponds to the change in pegmatite geometry to form larger, interconnected, subvertical sheet-like bodies.

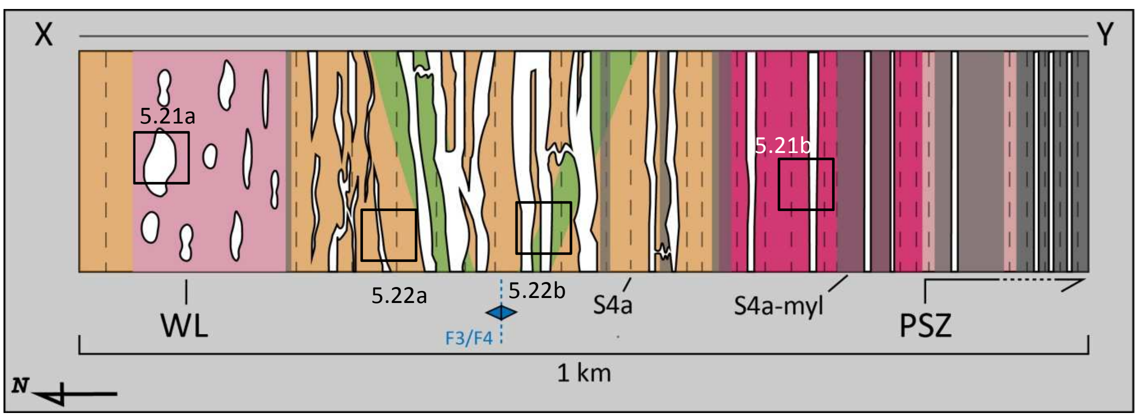

Figure. 5.20. Schematic plan view section (from X-Y, Fig. 4.10) across the ND illustrating the systematic change in pegmatite geometries and progressive development of S_{4a} towards the PSZ core. The wall-rock lithologies depict those of Figure 4.10 and the geological map (Appendix A). Note locations of Figs. 5.21a,b and 5.22a,b.

Figure. 5.21. (A) Oblique plan view, top to NE at the WL in the ND. Here pegmatites occur as irregular pod-like bodies enveloped in the foliation (S_2/S_4). (B) Cross-sectional view (facing east) of the pegmatites adjacent to the PSZ core. Here pegmatites typically occur as smaller individual sheets parallel to the wall-rock foliation and axial planar to the parasitic F_4 folds (see F_4 fold at bottom left of the photo).

One of the most notable features of the sheeted pegmatites within the ND is their association with F_3/F_4 and F_4 fold geometries (Fig. 5.22). This is documented by pegmatites (a) concentrated within the hinge of a large re-orientated (F_3/F_4) antiform that broadly defines the structure of the domain (Figs. 4.10; 5.20,22b) and (b) their axially planar emplacement to high-grade, parasitic F_4 folds (Figs. 5.21b,22b). Towards the hinge zone of the antiform, the pegmatites are increasingly sheeted and pervasive, occurring as closely spaced sets of three to four individual subvertical sills that trend WNW-ESE, parallel to the axial plane of the F_3/F_4 antiform (Fig. 5.22a). Notably this is in the L_{4a} stretching lineation direction. The individual sheets vary in thickness from 0.5 - 5 m and, in the hinge zone of the antiform, show the formation of composite, amalgamated sets that can reach ca. 20 m in thickness (Fig. 5.22a) and can be traced over 500 m along strike. Separate pegmatite sets are commonly connected by a series of thinner (< 40 cm) disharmonically folded pegmatites that are co-axial with the wall-rock fabrics (Figs. 5.22a, e.g. locality X; 5.23). These sheeted pegmatites have relatively irregular contacts with the wallrocks and are commonly boundinaged (Figs. 5.22a, e.g. locality Y; 5.23). Due to the lack of topographic variation vertical terminations are rarely observed.

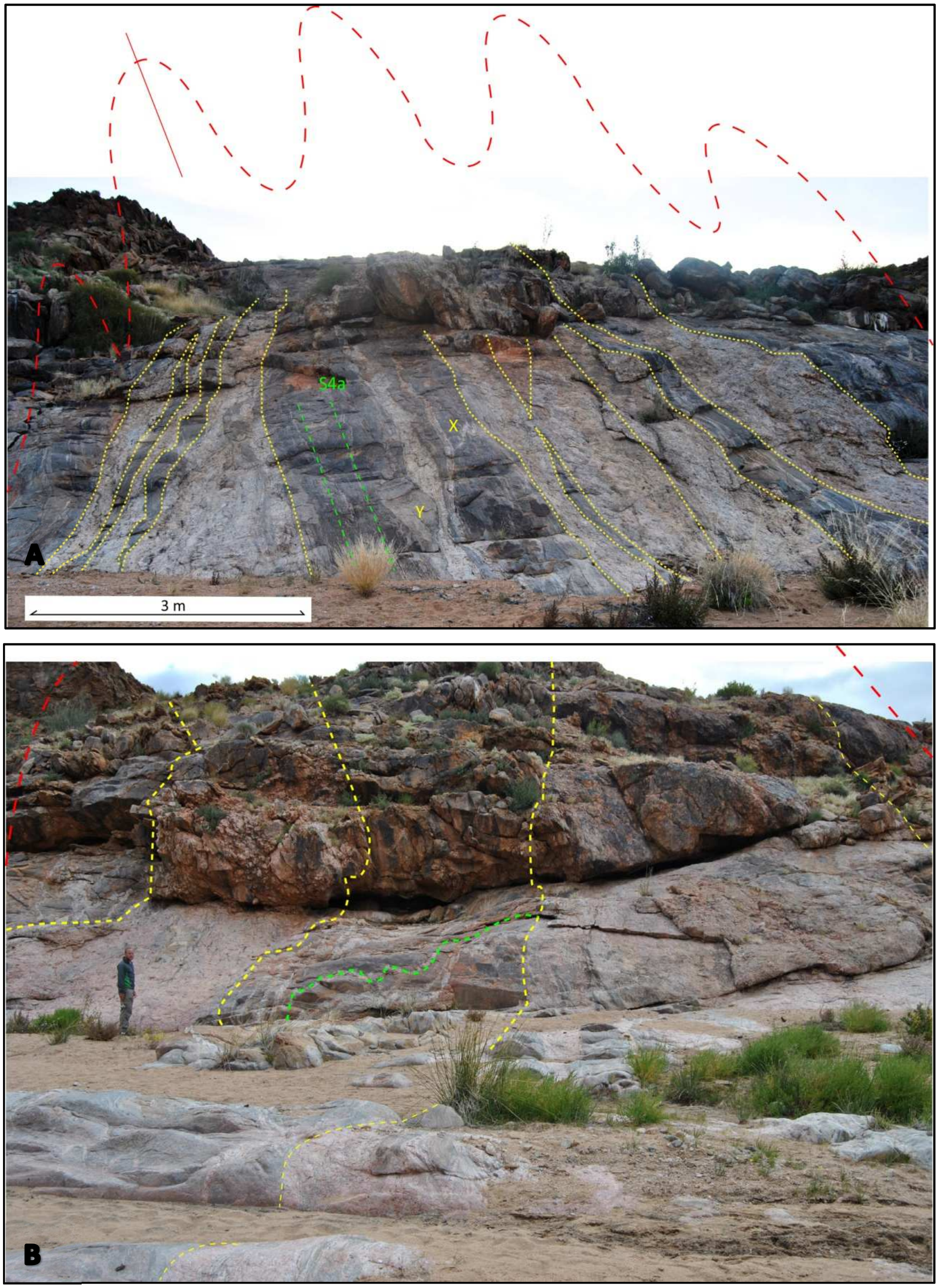

Figure. 5.22. Cross sectional views towards the west illustrating the axial planar relationship between pegmatite sheets and fold geometries (stippled red) within the ND. The sheets are emplaced (A) axially planar to parasitic F_4 folds or (B) significantly developed within the hinge of a large F_3/F_4 antiform. Note the disharmonically interconnecting folds at X (also stippled green) and pegmatite boudinage (at Y).

Outside the hinge zone, pegmatites do not exhibit the same density or pervasive nature and the connectivity of closely-spaced pegmatites is no longer evident (Fig. 5.20). These pegmatites do, however, still exhibit a close spatial association with F_4 folds. South of the hinge zone, towards the PSZ core pegmatite geometries are largely subvertical, tabular shaped bodies emplaced axially planar to the parasitic F_4 folds (Figs. 5.21b,23). Lateral terminations are similar to those within the PSZ core and defined by tapered tips, which can extend several meters before pinching out. These tabular pegmatites have length to width ratios between 10:1 and 20:1 and rarely exceed more than 3 m in thickness (Z-axis). Here pegmatites contacts are notably less irregular and are defined by relatively sharp, straight boundaries parallel to the planes of the subvertical, mylonitic-S_{4a}.

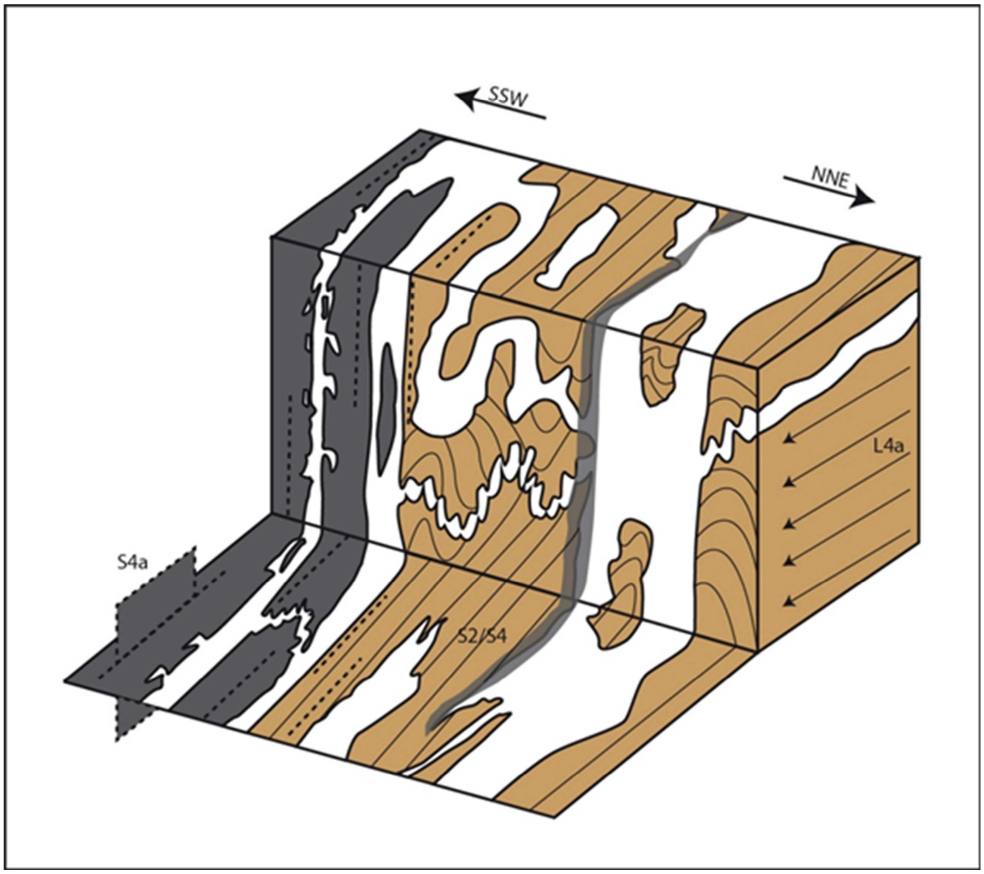

Figure. 5.23. A schematic 3D-cross sectional diagram of pegmatite bodies that occur axially planar to F_4-folds The sheeted bodies are connected by thinner disharmonically folded pegmatites that cross- cut the foliation but are co-axial with the sheets, elongated in the L_{4a} direction. Close to the southern margin of the ND, where associated with $S_{4a,}$ the thinner pegmatites are almost completely overprinted by the mylonitic fabric, while those thicker than 2 m only show deformation along the margins.

The pegmatites in the ND are invariably deformed, the extent of which depends on their emplacement within S_{4a} mylonitic domains and the thickness of the particular pegmatite body. Strain is commonly partitioned into the pegmatite bodies while the hosts exhibit extensive sericite development along the intrusive margins. The ductile overprint of S_{4a} completely transformed thinner sheets (< 1 m) and changed them into protomylonites, mylonites (Fig. 4.11a) and ultramylonites, whereas thicker sheets are only deformed along their margins, having been transformed into protomylonites, whereas the cores remain relatively unaffected and preserve the original pegmatitic textures.

The pegmatite emplacement in the ND appears to be directly related to F_3/F_4 and F_4 folds. At the WL, where folding is absent and S_{4a} is underdeveloped, pegmatite geometries are pod-like and irregular. As fold geometries and subsequently S_{4a} becomes progressively more prominent, the occurrence of coalesced and laterally continuous tabular pegmatite sheets similarly increases and these become concentrated within the hinge zone of a large F_3/F_4 antiform or consistently emplaced axial planar to high grade fold geometries. The variable boudinaging of the sheeted bodies in the F_3/F_4 hinge zone indicates intrusion parallel to the direction of finite shortening during D_4. The controls of emplacement of the pegmatites within the ND are thus inferred to be axial planar anisotropies of F_4 folds (e.g. Vernon and Paterson, 2001; Weinberg and Geordie, 2008), that developed during the folding and transposition that characterised the early stages of shear-zone deformation (D_{4a}).

5.4 Pegmatite Controls: Synopsis

The following section aims to synthesize the controls on pegmatite emplacement within each domain around the PSZ and can be used in conjunction with Figure. 5.24.

- The ND: The pegmatite geometries show a transition from patchy and pod-like shapes outside the PSZ to (1) sheet-like pegmatites that are axial planar to F_4 folds and or cross-cut S_4 mylonites, and (2) subordinate, shallowly dipping and commonly tightly folded sheets that connect with the S_{4a} - parallel sheets.
- The PSZ core: Within the core, three main pegmatite geometries are developed, namely pegmatites (1) parallel to the high-strain mylonitic (S_{4a}, S_{4b}) fabric, (2) orientated as synthetic Riedel shears and (3) short, stubby dykes forming jog-like geometries, connected by foliation-parallel sheets.
- The SD: This domain is defined by the development of an extensive pegmatite stockwork (SPS) of foliation-parallel (S2/S4, S_{4a}) sills and subvertical, northerly trending, commonly wedge-shaped dykes. The interconnectivity and inconsistent cross-cutting relationships suggest contemporaneous emplacement of sills and dykes, and the extent of deformation indicates this occurred during the later stages of PSZ deformation (D_{4b}).

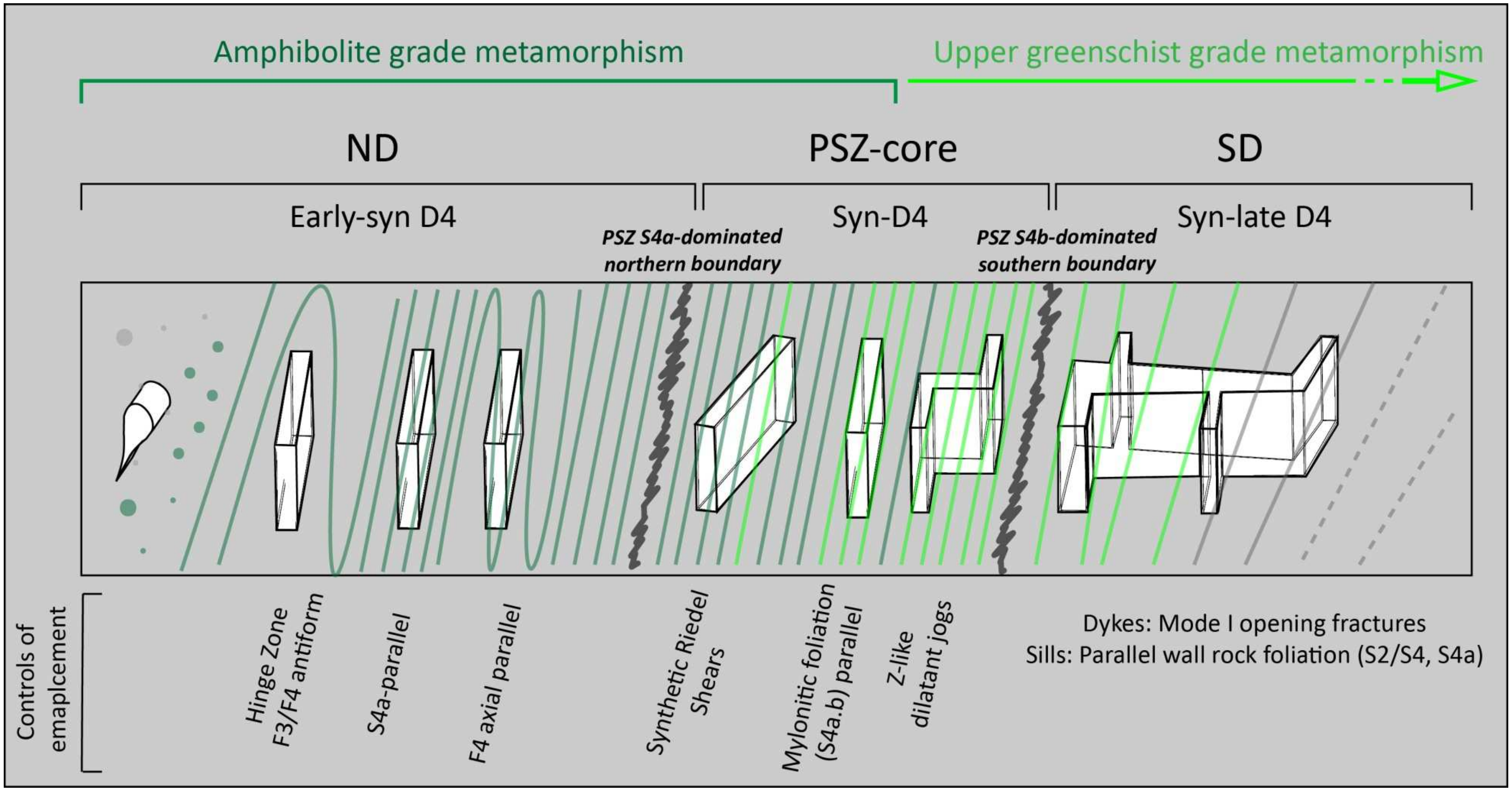

Figure. 5.24. Schematic cross-section of the PSZ illustrating the various pegmatite geometries within the three study domains. The diagram highlights the transition in structural and metamorphic fabrics across the shear.

6. Geochronology

6.1 Analytical procedures

Zircons and monazites were extracted from whole-rock samples by Elijah Nkosi at the laboratories of the Council for Geoscience in Pretoria following standard separation techniques making use of sieves, the Wilfley percussion table, the Frantz magnetic separator and heavy liquids (e.g. Macey, 2005). The sample concentrates were examined under a binocular microscope and suitable grains from both zircon and monazite sample concentrates were mounted in separate epoxy sets. Photomicrographs in transmitted and reflected light were taken of all of the grains and these, together with back-scatter electron (BSE) and cathodoluminescence (CL) images, were used to determine the internal structures of the mounted monazite and zircon grains respectively and to target specific areas (e.g. core and rim) within the samples. The BSE imaging of the monazite grains was done using a ZEISS EVO MA15VP SEM housed in the Central Analytical Facility (CAF) electron micro-beam unit in the Department of Earth Sciences, Stellenbosch University. Zircons were imaged in CL mode using the CAF LEO 1450 VP SEM. During SEM analysis the selection of suitable grains, specifically monazites from the respective samples was additionally aided by identification through energy dispersive X-ray spectroscopy (EDS-SEM) to ensure that the chemical characterization (signature) of the mounted grains corresponds to those of zircon and monazite respectively. Numerous grains, with similar physical characteristics to monazite seen under the binocular and scanning electron microscopes returned chemical signatures contradictory to those of monazite, with an anomalously high-Th content and are therefore were excluded from further analytical procedures. Zircon grains, specifically from pegmatites occurring in the PSZ core and SD were largely metamict and experienced substantial Pb-loss and are therefore similarly excluded from the analysis.

Zircon and monazite analysis was conducted over three sessions by Dr. Frei by laser ablation-inductively-coupled-mass spectrometry (LA-ICP-MS) in the ICP-MS unit of CAF using an Agilent 7500ce quadrupole ICP-MS coupled to a 213 nm New Wave laser. The number of spots varies across each grain dependant on grain size and sample abundance. The operating conditions, largely defined in Kisters et al. (2012) were optimised to provide the maximum sensitivity for the high masses (Pb-U) while inhibiting oxide formation (ThO+/Th+<0.5%). Ablations of the respective samples, standards and secondary standards occurred in a custom-built small-volume sample cell **(**cf. Horstwood et al., 2003**)** in Hg carrier gas. The resulting aerosol was mixed with Ar prior to introduction into the ICP-MS via a signal-smoothing manifold. Initial data reduction was conducted in-house using the Glitter software package (van Achterbergh et al.,2001) to calculate the relevant isotopic ratios (^{207}Pb/^{206}Pb, ^{208}Pb/^{206}Pb, ^{208}Pb/^{232}Th, ^{206}Pb/^{238}U and ^{207P}b/^{235}U). ^{235}U was calculated from ^{238}U counts via the natural abundance ratio ^{235}U = ^{238}U/137.88 (Jackson et al., 2004). Individual isotopic ratios were displayed in time-resolved mode. Isotopic ratios generated during the first 5 to 10s of each analysis were discarded. Ablation depth-dependent elemental fractionation was corrected for by tying the integration window for the unknown monazite to the identical integration window of the standard (Jackson et al., 2004). Instrumental drift was corrected against the monazite standard using linear interpolative fits. ^{204}Pb-based common Pb corrections were applied were necessary (cPb: indicated in the isotope tables) according to the well-known contamination of the carrier gases by ^{204}Hg (e.g. Jackson et al., 2004). The U-Pb data for the respective samples (Appendix D1-6) were plotted on Wetherill concordia diagrams using the Excel macro software Isoplot (Ludwig, 2000) and reported based on the agreement between ^{207}Pb/^{235}U, ^{206}Pb/^{238}U and ^{207}Pb/^{206}Pb. Uncertainties given for individual analyses (ratios and ages) in the tables are at the 2σ level; weighted mean or concordia ages are given at the 2σ or 98% confidence levels. The analysis commonly yielded age uncertainties of less than 1 % which is considered to be unrealistically precise for LA-ICP-MS analysis. These age uncertainties are therefore considered to represent the minimum level of uncertainty within an error margin of 1 % for the acquired ages (Buick, *pers comm*.). Th and U abundances were calculated using NIST612 glass (Pearce et al., 1997) as an external standard and assuming stoichiometric Ce as an internal standard.

For zircon, the analytical runs involved repeated analysis cycles of the GJ-1 standard with an age of 608.5 ± 0.4 Ma (Jackson et al., 2004), NIST-612 glass (Pearce et al., 1997) and Plešovice secondary standard with a of 337.33 ± 0.38 Ma (Slama et al., 2008; Appendix D1), followed by 10 of the unknowns (i.e. sample CP32). Laser ablations were performed at a frequency of 10 Hz and an energy density of 3.22 J/cm^2 and produced 30 µm diameter pits. Integration times for U/Pb age determinations were 15 ms for ^{206}Pb, 40 ms for ^{207}Pb, and 10 ms for ^{29}Si, ^{208}Pb, ^{204}Pb, ^{232}Th and ^{238}U. LA-ICP-MS acquisitions consisted of a 30 second measurement of the gas blank, followed by 30 seconds of measurement of Si, U, Th and Pb signals during ablation. U and Th concentrations were extracted from the same integration windows as those used for age determinations, using NIST-612 as the external standard and stoichiometric SiO_2 as the internal standard. 11 analyses of the Plešovice zircon yielded a concordia age of 334 ± 3 Ma (Appendix D1; 96% confidence level; MSWD of concordance and equivalence = 0.17), within error of the accepted age (Slama et al., 2008).

For the monazite grains analytical protocols followed those defined by Buick et al. (2011). Integration times for U/Pb age determinations were 15 ms for ^{206}Pb, 40 ms for ^{207}Pb, and 10 ms for ^{140}Ce, ^{208}Pb, ^{204}Pb, ^{232}Th and ^{238}U. LA-ICP-MS acquisitions consisted of a 60 second measurement of the gas blank, followed by 40 seconds of measurement of Ce, U, Th and Pb signals during ablation. Laser ablations were performed at a frequency of 4 Hz and an energy density of ~4.5 to 5 J/cm^2, and produced 20 µm diameter wide pits. The low-Th USGS monazite 44609, with an ID-TIMS age of 424.9 ± 0.4 Ma (Aleinikoff et al., 2006) is used as the primary standard and the high-Th Thomson Mine monazite (TM), with a 1766 Ma age (Williams et al., 1996) as the secondary standard (Appendix D2-6). Thirty analyses of the Thomson Mine monazite yielded a weighted mean ^{207}Pb/^{206}Pb age of 1758.6 ± 3.5 Ma (95% confidence level; MSWD = 0.53) and a concordia age of 1760.8 ± 3.0 Ma (2σ, MSWD of concordance and equivalence = 0.48) which is within error of the accepted age (Williams et al., 1996). The U, Pb and Th concentrations were calculated using the U content of the USGS 44069 standard of 2167 ppm and Th/U ratio of 11.5.

6.2 Field setting, grain morphology and results

The present chapter provides the field setting, grain morphologies and a summary of the analytical results. The CL and BSE images contain spot-localities (annotated in yellow) which represent the respective ablation sites and link to the individual entries in the respective analytical tables (Appendix D1-D6). $^{206}Pb/^{238}U$ (annotated white) and rare $^{207}Pb/^{206}Pb$ (annotated red) ages (in millions of years) for the respective spot localities are presented without uncertainties (assuming at 1% error margin).

6.2.1 Sample CP32

Sample location: -28.8812, 19.0591.

This sample is from the leucogranite that occurs ca. 20 m into the PSZ core (Fig. 6.1). The granite (*stricto lato*) is deformed by D_{4a}, showing a clear ductile mylonitic-S_{4a} overprint, pervasively developed across the granitic body (Fig. 6.1). The granite forms a significant marker horizon (Fig. 5.3, Appendix A) where it can be traced ca. 8 km to the west of the study and ca. 1 km to the east where it becomes completely transposed into the PSZ-fabric. The granite is composed predominately of quartz, plagioclase and K-feldspar augen with minor amounts of biotite.

Figure. 6.1. Plan view with top to west. Ductile deformation (D_{4a}) is evident in the deformed leucogranite that is transposed along the PSZ.

Zircon morphology

The zircon grains in this sample set occur as clear-translucent, euhedral prismatic grains with maximum lengths ranging between 60 and 200 µm and have typical length-to-width ratios between 2:1 and 3:1. Locally the grains are fractured due to mechanical effects of sample preparation. CL images (Fig. 6.2a) reveal medium-broad banded and oscillatory-zoned zircons with notably common inherited cores defined by stubby subrounded to resorbed morphologies (e.g. locality nos. 7, 14, 21, 25, 33).

Results

The strong transposition of the leucogranite into the PSZ-fabric with the relative preservation of intrusive contacts initially led to this sample being analysed in an attempt to define the maximum age of the D_4. Additionally this analysis adds to the database on the distribution and genesis for syn-late tectonic plutonism within the greater NMC (Macey, in prep).

Approximately 40 spots across the cores and rims of 20 grains were analysed (Fig. 6.2a; Appendix D1) of which 4 could not be used as they are either metamict or strongly discordant (e.g. locality nos. 9, 28, 38, 40). Individual analyses on the majority of the xenocrystal zircon cores yield $^{206}Pb/^{238}U$ ages around 1300 Ma while a rare, single core (Fig. 6.2a, locality no. 14) yielded a $^{207}Pb/^{206}Pb$ age of 1824 ± 18 (2σ) Ma (Fig. 6.2). Analysis of primary cores and pristine rims yield concurrent ages of which 12 are discordant between (75% – 94%) with an upper intercept of 1236 ± 9.5 Ma and a lower intercept below the accepted Pb-loss limit. The highly concordant data (95 - 100 %) yield a concordia age of 1233 ±6 Ma (2σ, decay-const. errs ignored, MSWD of concordance and equivalence = 0.46; Fig. 6.2b) suggesting granitic magma crystallization occurred between ca. 1233 and 1236 Ma.

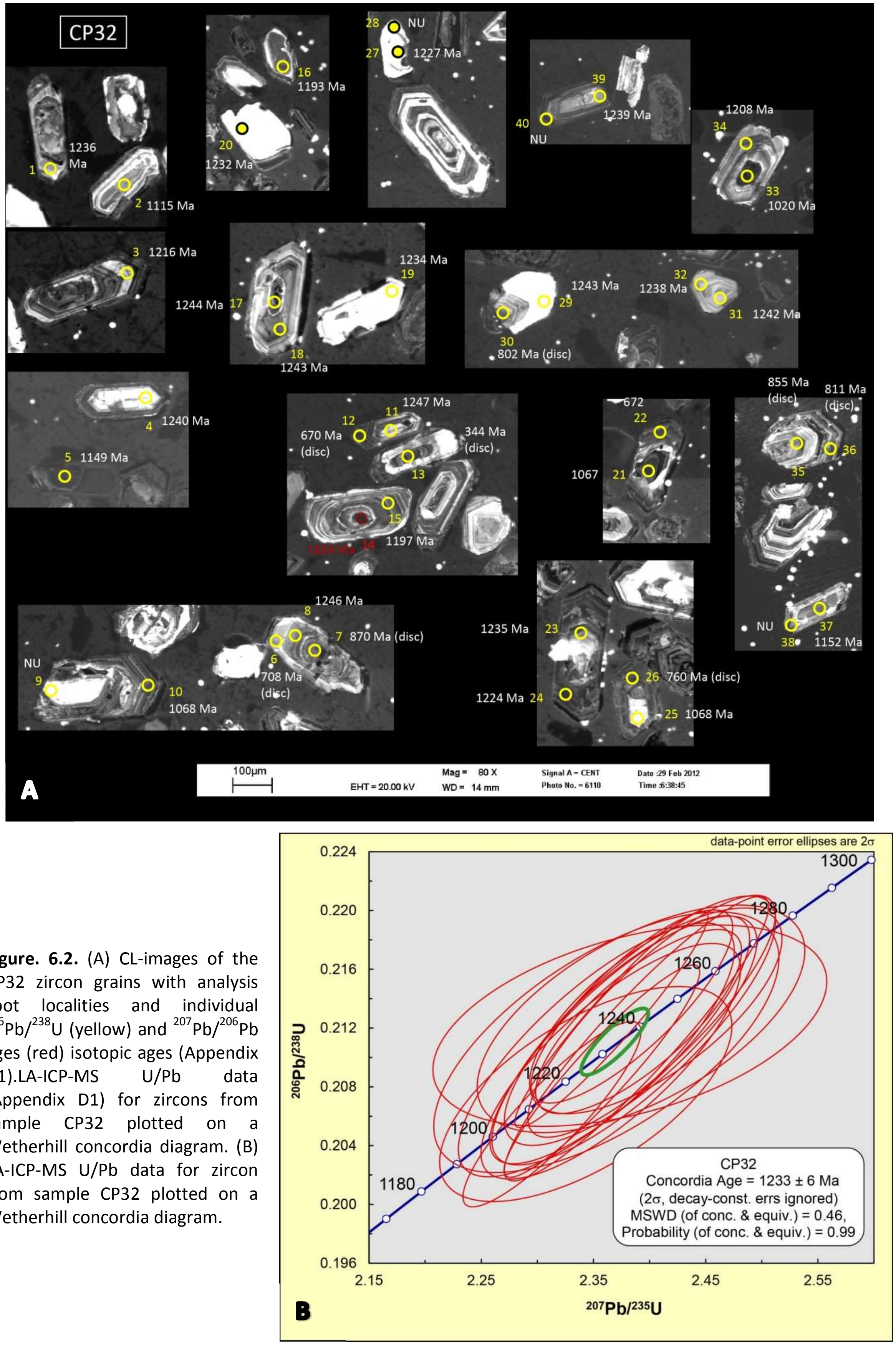

Figure. 6.2. (A) CL-images of the CP32 zircon grains with analysis spot localities and individual $^{206}Pb/^{238}U$ (yellow) and $^{207}Pb/^{206}Pb$ ages (red) isotopic ages (Appendix D1).LA-ICP-MS U/Pb data (Appendix D1) for zircons from sample CP32 plotted on a Wetherhill concordia diagram. (B) LA-ICP-MS U/Pb data for zircon from sample CP32 plotted on a Wetherhill concordia diagram.

6.2.2 Sample CM38-A

Sample location: -28.8929, 19.0489

Sample CM38A is from a coarse-grained pegmatite sill within the SPS (Fig. 6.3). The sill has sharp wall-rock contacts and is relatively undeformed, showing only a low-strain D_4 fabric along the margins. The sill is 5 m – 6 m in width and can be traced along strike for ca. 300 m. The pegmatite was sampled away from any intersections with connecting pegmatite dykes. Compositionally the pegmatite is a simple, unzoned heterogeneous body composed of quartz, perthitic K-feldspar with minor muscovite, garnet and magnetite. The pegmatite is hosted exclusively by the megacrystic biotite K-feldspar-augen gneiss (Noudap Gneiss).

Figure 6.3. View to east of the concordant pegmatite sill in the SPS sampled (CM38-A) for monazites. The sill is 5 m thick and relatively undeformed, with sharp wall-rock contacts that parallel the wall-rock foliations (S2/S4; S_{4a}).

Monazite morphology

The small to medium (100-200 µm) monazite grains occur as pale yellow to orange subrounded to subhedral grains in reflected light. Under BSE, monazite grains from this sample set are commonly faceted, forming equant to elongate euhedral grains with length-to-width ratios between 2:1 and 3:1 (Fig. 6.4a). The grains show weakly defined patchy (e.g. localities no. 1-4) and oscillatory zonation patterns (e.g. localities no. 5-9), the latter defined by concentric, light-CL rims around darker-CL centres.

Results

Age data from this sample are expected to provide emplacement ages for pegmatite sills within the SPS.

The analysis incorporated 24 spots over 9 grains (Fig. 6.4a; Appendix D2) and isotopic data are 98-101% concordant (based on agreement between $^{207}Pb/^{235}U$, $^{206}Pb/^{238}U$ and $^{207}Pb/^{206}Pb$), except for 4 analyses (locality nos. 6-9) which are significantly discordant (< 30%) and are therefore excluded from the analysis. Their discordancy is attributed either to mechanical malfunctions such as ablation-spot drifting (locality no. 7-9) or to them being analysed across zonation boundaries (locality no. 6). One analyses (locality no. 2) shows a discordant (92 %) age and yields an upper intercept of 995 ± 6.5 with a MSWD = 0.92. The remaining 19 analysis yield a concordia age of 994 ± 3 Ma (2σ, decay-const. errs ignored, MSWD of concordance and equivalence = 0.78; Fig. 6.4b) with the ages between the centres and rims of respective grains all occurring within the accepted error limits (ca. 1%) of each other.

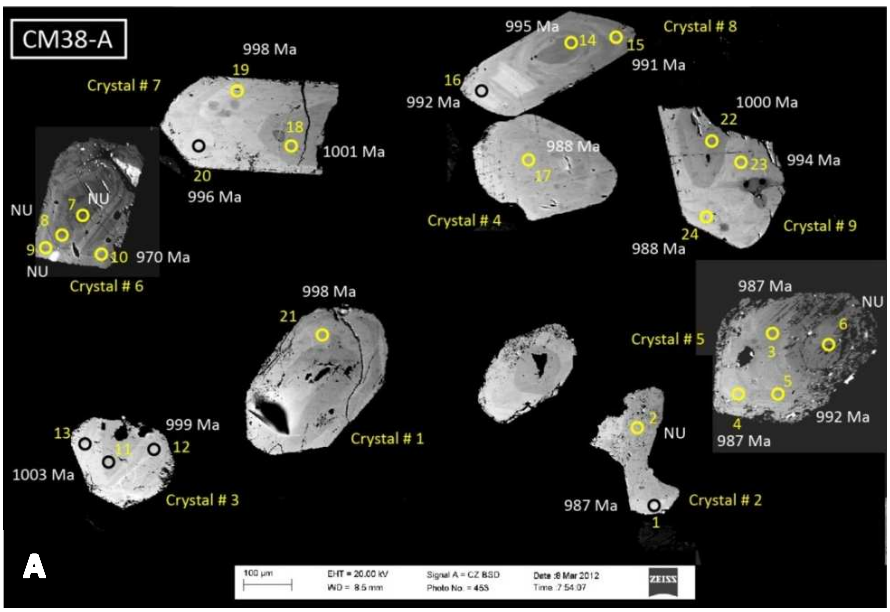

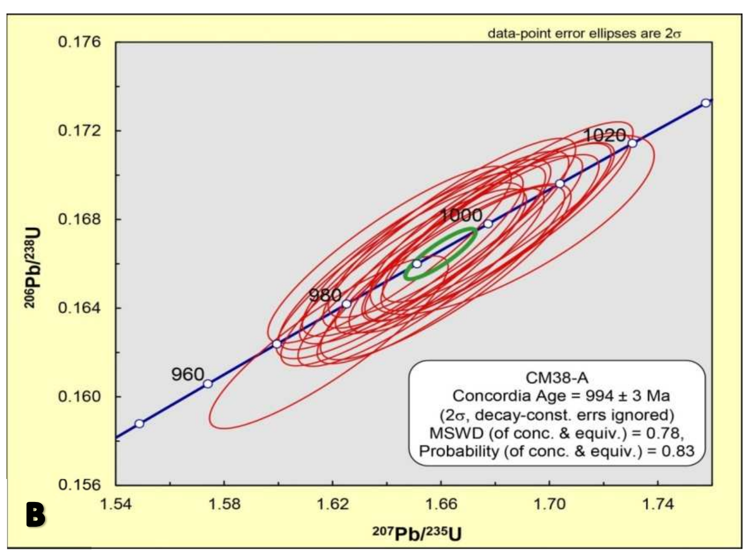

Figure. 6.4. (A) BSE images of the CM38-A monazite grains with analysis spot localities and individual $^{206}Pb/^{238}U$ isotopic ages (Appendix D2). LA-ICP-MS U/Pb data for monazite from sample CM38-A plotted on a Wetherhill concordia diagram.

6.2.3 Sample CM13-B

Sample location: -28.8947; 19.0545.

This sample is from a coarse-grained, thick (40 m) discordant pegmatite dyke from the north-western margin of the SPS (Fig. 5.12). The dyke is relatively undeformed with a weak foliation (S_{4a}) defined by the alignment of muscovite booklets. The sample was located at the centre of the N-S trending dyke away from intersecting pegmatite sills (Fig. 6.5). The dyke is composed of large quartz and perthitic K-feldspar crystals with muscovite and minor garnet and magnetite present. Along strike, to the northern limit, the dyke is truncated and transposed by the high-strain fabric (S_{4b}) of the PSZ while the southern termination is defined by a significant tapering and termination into a pegmatite sill. The pegmatite dyke cross-cuts the wall foliation and intrusive contacts (S2) between the megacrystic biotite K-feldspar augen (Noudap Gneiss) and the quartzo-feldspathic (Coboop Gneiss) orthogneisses.

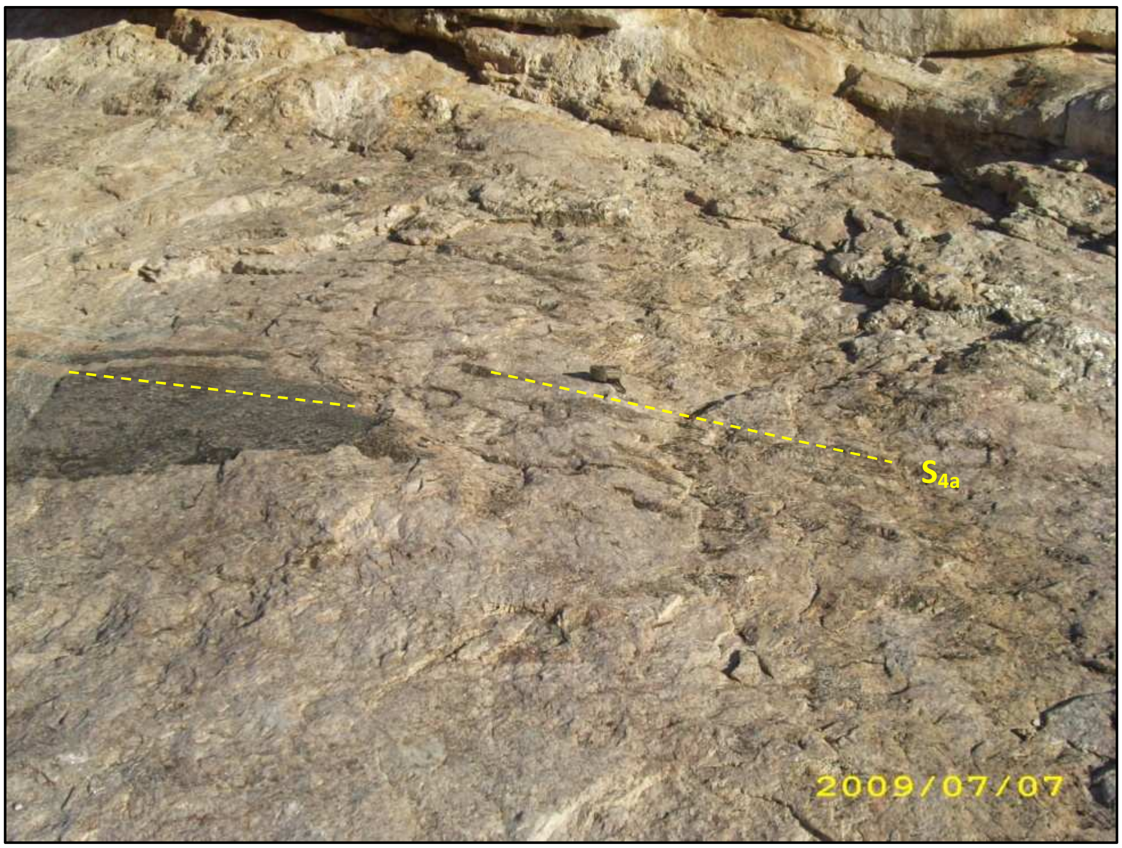

Figure 6.5. Oblique plan view with top to NE of the N-S trending pegmatite dyke in SPS sampled for monazite age analysis (CM13-B). Note the S_{4a} foliation across the core of the dyke.

Monazite morphology

The monazites from this sample range in size from small (100 µm) to large (300 - 400 µm), subangular to subrounded grains with length-to-width ratios between 3:2 and 4:1. In reflected light the grains are a pale yellow to orange colour. Under BSE (Fig. 6.6a) few zonation patterns are observed amongst the grains but, where identified, are predominately patchy (e.g. locality nos. 8-11).

Results

Age data from this sample will provide an emplacement age for this pegmatite dyke occurring along the NW margin of the SPS. The age of emplacement will additionally constrain the later D_{4b}-deformation of the PSZ.

In the mount 16 analyses were conducted on both the centres and margins of 7 different monazite grains (Fig. 6.6a; Appendix D3). 5 analyses (locality nos. 2, 4, 6, 10-11) were excluded due to mechanical drift of the laser during ablation. The remaining data yielded two analyses (localities nos. 8-9) with discordant ages, with an upper intercept of 953 ± 8 Ma (2σ; MSWD = 0.95) Ma and a lower intercept below the accepted Pb-loss limits (Fig. 6.6b). The 9 remaining concordant ages (99-101 %) yielded a concordia age of 958 ± 5 Ma (2σ, decay-constant errors ignored, MSWD of concordance and equivalence = 0.77; Fig. 6.6c). This suggests that crystallisation of this pegmatite dyke occurred between ca.950 and 960 Ma.

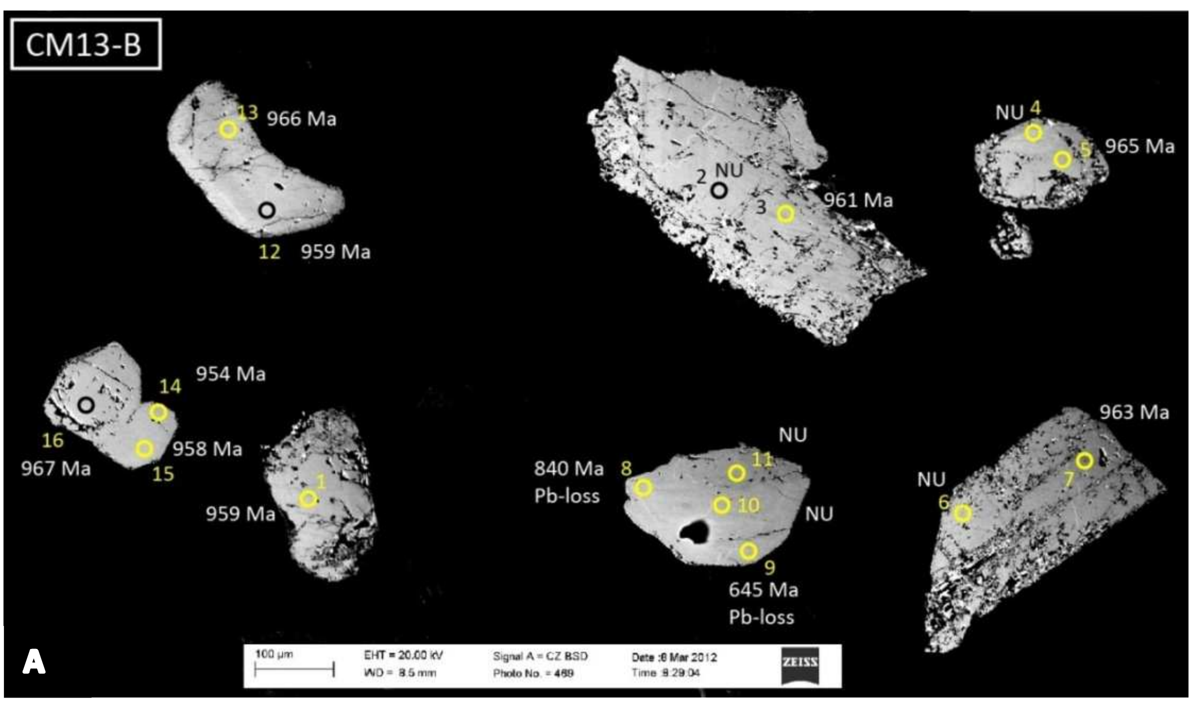

Figure. 6.6. (A) BSE images of CM13-B monazite grains with analysis spot localities and individual $^{206}Pb/^{238}U$ isotopic ages (Appendix D3).

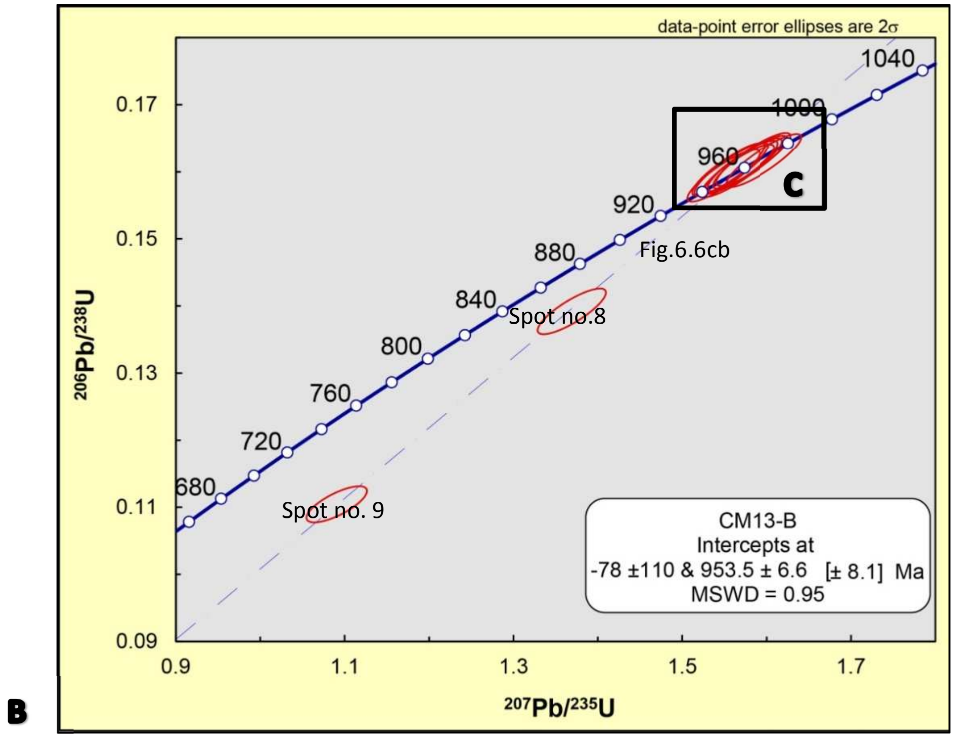

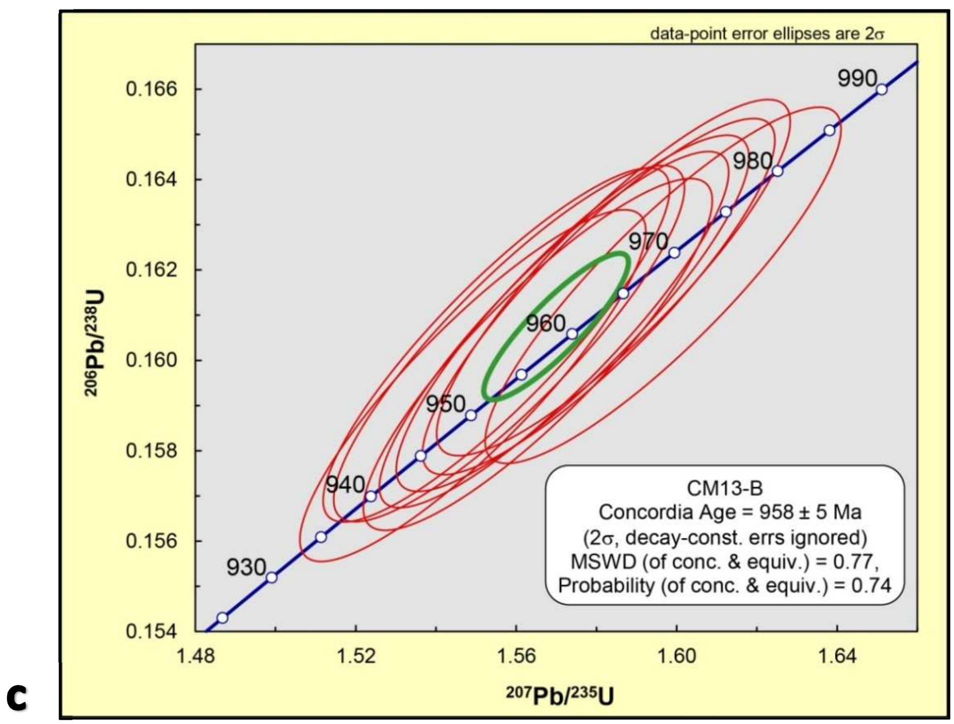

Figure. 6.6. cont. LA-ICP-MS U/Pb data (Appendix D3) for monazite from sample CM13-B plotted on Wetherhill concordia diagrams. (B) Shows plot of all the accepted data including discordant data, while (C) is an inset of the concordant data only.

6.2.4 Sample CM15-B

Sample location: -28.8959, 19.0608

This sample is a second sample from a large, N-S-trending pegmatite dyke in the SPS. The sample was taken from a dyke east of CM13B, occurring towards the centre of the SPS. Similarly, the dyke is relatively undeformed with a weak foliation (S4) defined by the alignment of muscovite booklets. CM15-B was sampled from the core domain of the ca. 40 m-thick simple, homogeneous, weakly zoned dyke (Fig. 6.7a). In the core of the pegmatite (sample location) the S_{4a} foliation is not evident and the dyke is composed of large quartz and perthitic K-feldspar crystals with muscovite and minor garnet and magnetite present. Comparable to CM13-B, the dyke is truncated and transposed by the high-strain fabric (S_{4b}) along its northern limits while southwards the dyke tapers and pinches out completely. The pegmatite similarly cuts across the earlier (S2) fabrics and intrusive contacts of the Noudap and Coboop wall-rock gneisses.

Figure. 6.7. Oblique plan view, top to NW of the sampled pegmatite dyke (CM15-B). Note the foliation normal to the dyke-wallrocks contacts.

Monazite morphology

The medium sized (100-200 µm) monazite grains occur as pale yellow to orange subangular, blocky grains in reflected light, with length-to-width ratios between 1:1 and 2:1. Under BSE (Fig. 6.8a) the grains show weakly defined patch zonation (e.g. locality nos. 17-19) and only rare oscillatory zoning with darker-BSE cores and lighter-BSE rims (e.g. locality nos. 9-12).

Results

Age data from this sample provide a secondary control on emplacement ages for pegmatite dykes in the SPS, specifically those occurring centrally within the SD. The age of emplacement provides added constraints on the later D_{4b}-deformation of the PSZ.

In the mount 20 spots were analysed on 6 different grains is which both rims and cores were distinguished and analysed (Fig. 6.8a; Appendix D_4). The majority of the analyses were strongly concordant (99%-100%) with only one analysis (locality no. 1) discordant due to a scattered ion signal during ablation and is therefore excluded. Individual $^{206}Pb/^{238}U$ ages between the rims and core zones of respective grains fall within the 2σ-error limits and therefore do not indicate significantly older inherited core ages. The resulting analysis of sample CM15-B yielded a concordia age of 962 ± 3 Ma (2σ, decay-const. errs ignored, MSWD of concordance and equivalence = 0.37; Fig. 6.8b), which is the crystallisation age of the core domain of this pegmatite dyke.

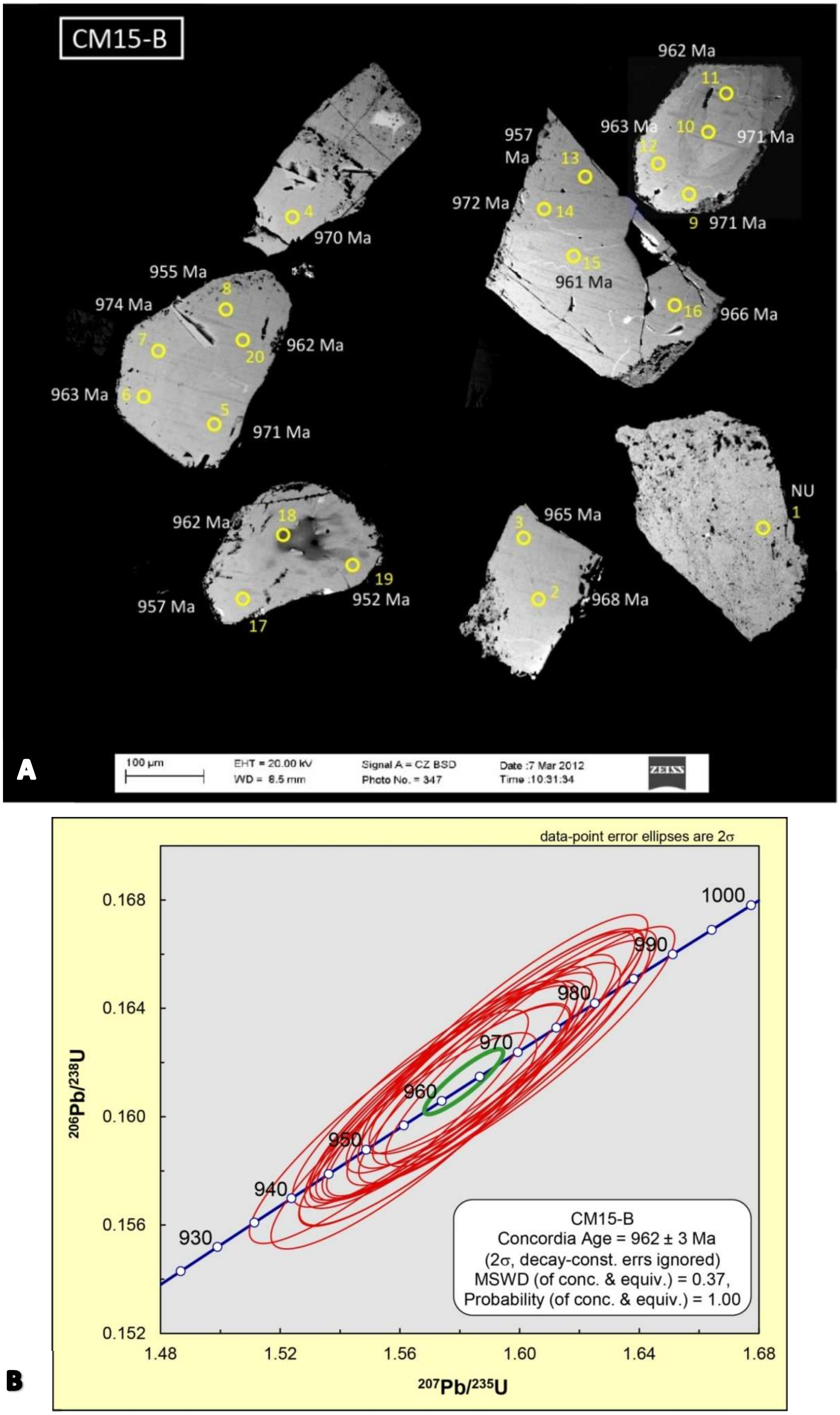

Figure 6.8. (A) BSE images of CM15-B monazite grains with analysis spot localities and individual $^{206}Pb/^{238}U$ isotopic ages (Appendix D4). (B) LA-ICP-MS U/Pb data for monazite from sample CM15-B plotted on a Wetherhill concordia diagram.

6.2.5 Sample CP31-C

Sample location: -28.8781, 19.0621

This sample is from a deformed pegmatite in the ND, located ca. 200 m north of the PSZ core within an S_{4a}-mylonitc domain. Here the pegmatite occurs parallel to the S_{4a}-mylonic foliation and axial planar to F_4 fold (Fig. 6.9). Strain is partitioned into the thin (< 50 cm), tabular pegmatite body while the equigranular quartzo-feldspathic host is only weakly deformed. The pegmatite is strongly confined between the high-strain foliation planes.

Figure. 6.9. Cross-sectional view, facing west of pegmatite sampled (CP31-C): axial planar to F_4 fold geometries and parallel to the high-strain-S_{4a}.

Monazite morphology

Few suitable monazite grains (< 15) existed within this sample and they occur predominately as relatively small (~100-150 µm) yellow to orange, subangular to subrounded grains with length-to-width ratios between 1:1 and 3:2. When observed in reflected light, the grains have a distinct pitted or honeycomb texture. Under BSE (Fig. 6.10a) the monazite grains show evidence of patchy zoning (e.g. locality nos. 3-4, 11) and are commonly fractured.

Results

The results of this analysis provide an emplacement age for a pegmatite that is axial planar to parasitic F_4 folds, defining the timing of the initial stages of D_{4a}-deformation.

From this sample, 12 spots across 6 grains were analysed (Fig. 6.10a; Appendix D5) of which 5 analyses were deemed unusable (locality no. 4-6, 7, 12) due to mechanical drift of the laser. The remaining, largely concordant data show no discernible differences between the lighter-and darker-patchy domains and yield a concordia age of 1005 ± 5 Ma (2σ, decay-const. errs ignored, MSWD of concordance and equivalence = 1.5; Fig. 6.10b). Thus, yielding an emplacement age for a pegmatite controlled by the development of amphibolite grade fabrics in the ND.

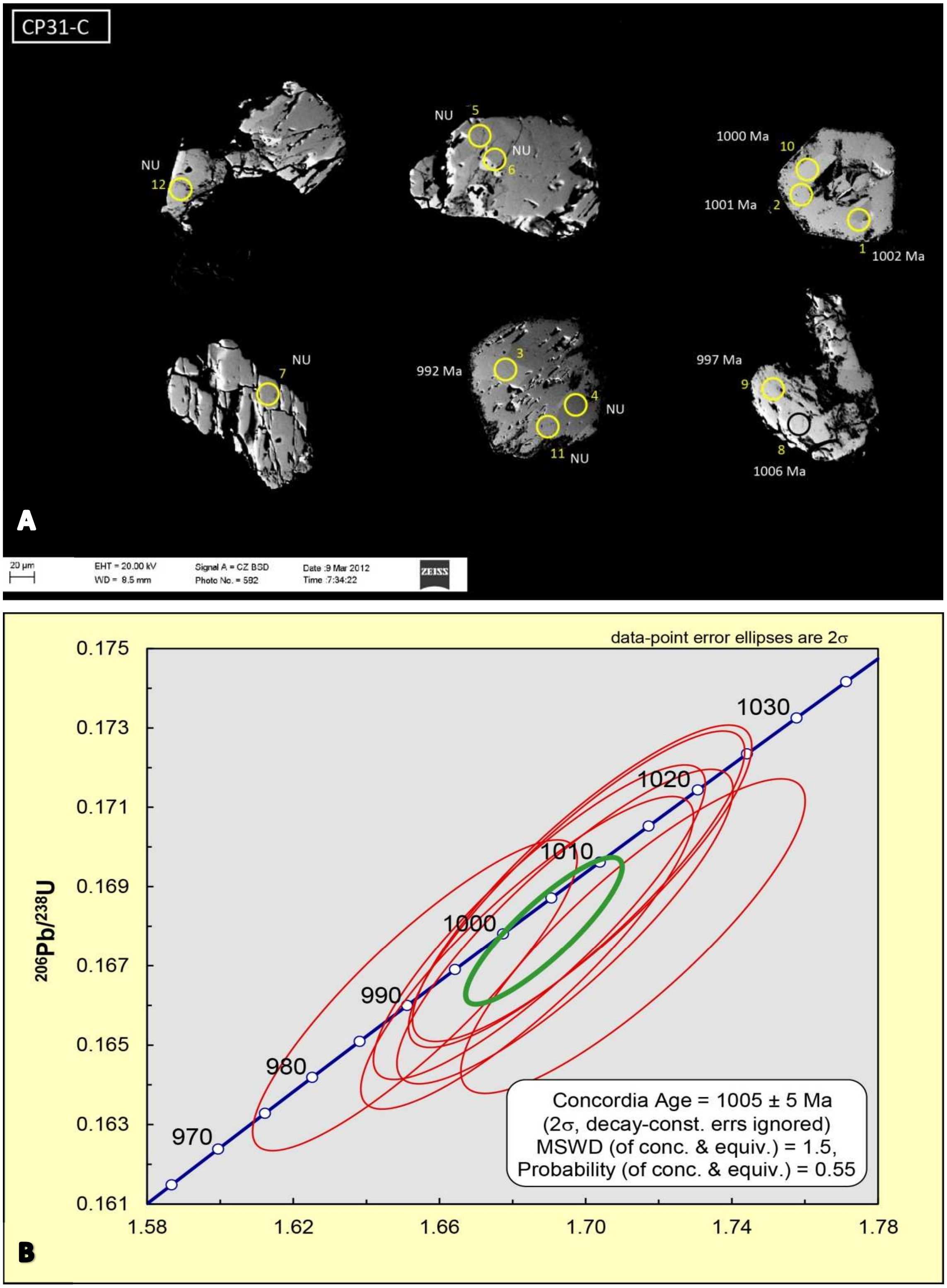

Figure. 6.10. (A) BSE images of CP31-C monazite grains with analysis spot localities and individual $^{206}Pb/^{238}U$ isotopic ages (Appendix D5). (B) LA-ICP-MS U/Pb data for monazite from sample CP31-C plotted on a Wetherhill concordia diagram.

6.2.6 Sample KG36

Sample location: -28.9090, 19.216200

This sample is from a pegmatite occurring in a large km-scale PSZ-related (F_3/F_4) fold structure that occurs southeast of the greater study area. The sample was collected on a detailed N-S traverse across the shear-zone, along its eastern extension, by Dr. Macey and Mr. Groenewald. This pegmatite therefore occurs outside the bounds of the immediate study area and has been analysed for geochronological comparison with those within the study areas and its relation to older D_4 fabrics. Similar to what is observed in the ND, this pegmatite occurs axial planar to F_4 fold geometries and cuts across a re-orientated gneissic foliation (S_2/S_4; Fig. 6.11). The pegmatite is composed predominately of quartz, perthitic K-feldspar and muscovite with minor amounts of magnetite and is hosted by a homogeneous quartzo-feldspathic orthogneiss.

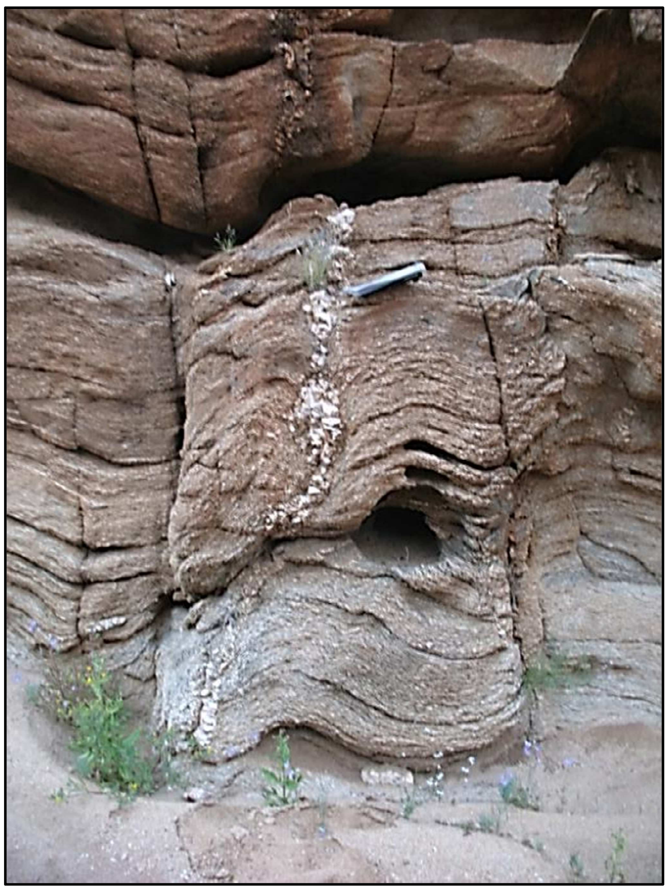

Figure. 6.11. Cross sectional view, facing NW, pegmatite dyke axial planar to a large D_4 related fold, emplaced discordant but co-axial to the re-orientated gneissic fabric (S2/S4).

Monazite morphology

Only 6 monazite grains were recovered for this sample. The grains are predominately small (60-120 µm) with length-to-with ratios between 1:1 and 3:2, defining the subangular to blocky grains. In reflected light the grains are a pale yellow to tan colour and have relatively smooth surfaces. Under BSE (@@Fig. 6.12a) the majority are free of zonation but occasionally both oscillatory (crystal no. 1) and patchy (crystal no. 4) zonation is present.

Results

Analysis of this pegmatite provides a control for the ages obtained from within the three study domains, and also provides an age for pegmatites occurring axial planar to the F_4 fold geometries.

The scarcity of monazite grains in this sample only allowed 14 spots to be analysis (Appendix D5) on 4 grains, one of which was fractured during sample preparation (crystal no. 2). Two analyses (locality nos. 11, 13) returned strongly discordant (< 60%) values due to signal-strength irregularities during ablation. Of the remaining 12 spots, individual $^{206}Pb/^{238}Pb$ ages on the rims and cores of the returned values within their 2σ limitations and collectively yield a concordia age of 990 ± 4 Ma (2σ, decay-const. errs ignored, MSWD of concordance and equivalence = 7.2; Fig. 6.12b). This therefore indicates pegmatites outside the study areas have similar ages to those within the ND and some sills within the SD.

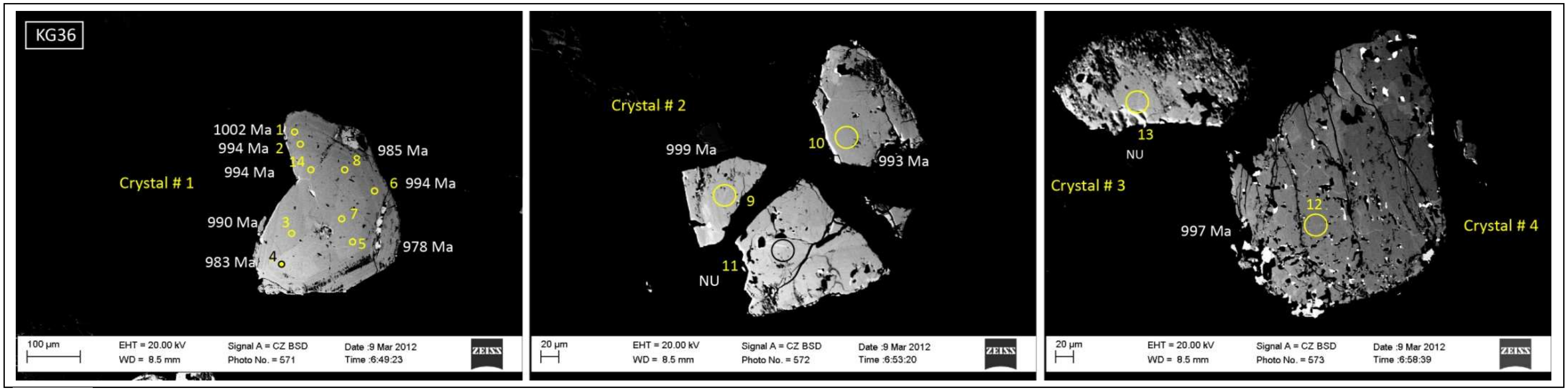

A

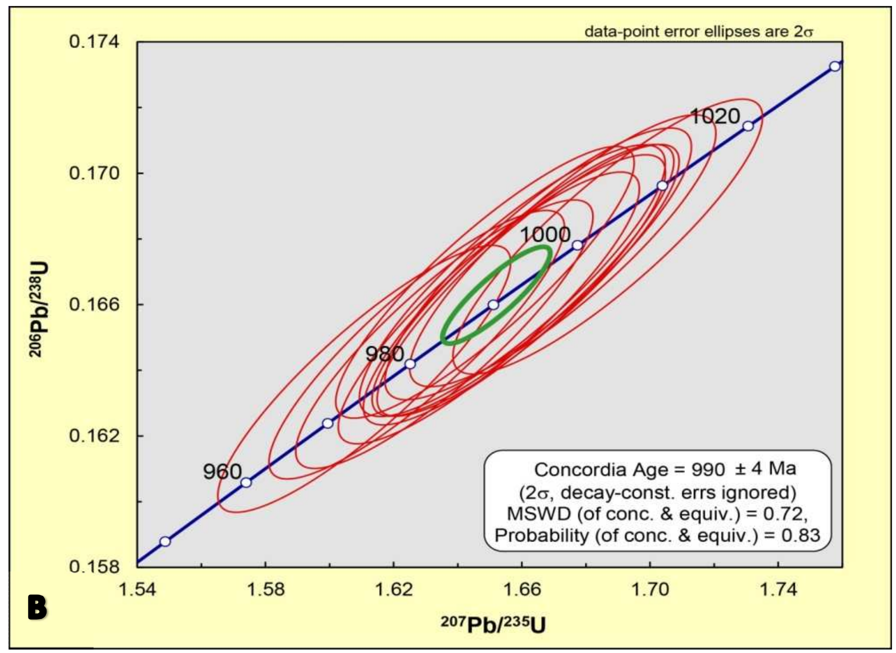

Figure. 6.12. (A) BSE images of KG36 monazite grains with analysis spot localities and individual $^{206}Pb/^{238}U$ isotopic ages (Appendix D5). (B) LA-ICP-MS U/Pb data (Appendix D5) for monazite from sample KG36 plotted on a Wetherhill concordia diagram.

6.3 Summary of results

A variety of pegmatites were sampled across the study area and analysed, a brief synopsis of the results is provided below;

- Zircons from a PSZ-deformed leucogranite loosely provide a maximum-age constraint on D_4-deformation at 1233 ± 10 Ma. The emplacement of the granite correlates with ages for syn-tectonic-Namaqua aged Little Namaqualand Suite rocks in the Bushmanland Subprovince (e.g. Eglington, 2006; Macey et al., 2011, Macey, *in prep*). The zircons typically have inherited cores with distinctly different morphologies suggesting inherited ages of ca. 1300 Ma and 1824 ± 18 Ma. These inherited ages are similar to what is described by Eglington (2006) for many of the zircons analysed from rocks of the Little Namaqualand Suite in the Bushmanland Subprovince. The ca. 1800 Ma age represents early igneous activity in the Bushmanland Subprovince (e.g. Bailie and Reid, 2000; Pettersson et al., 2004) while the ca. 1300 Ma ages are commonly related to igneous activity (e.g. Barton and Burger, 1983; Bial et al., 2013) in the Gordonia Subprovince and/or detrital zircons derived from supracrustal rocks in the Garies Terrane (Bushmanland Subprovince) and the Gordonia Subprovince (Eglington, 2006).

- The monazites from the respective samples yield single age populations with little to no evidence of inheritance or metamorphic crystal growth, suggesting that the concordant ages derived from these analyses represent the emplacement ages of the respective pegmatites.

- Monazites from pegmatite bodies occurring axial planar to F_4 related folds in the ND and outside the study area are dated at 1005 ± 5 Ma and 990 ± 4 Ma respectively.

- Monazite from a pegmatite sill from the SPS yielded ages of 994 ± 3 Ma.

- Monazites from two thick pegmatite dykes in the SPS yield concordia ages of 962 ± 3 Ma 958 ± 5 Ma respectively.

7. Discussion

7.1 Structural evolution of the PSZ in the study area

Fabrics and structures in the mapped section of the PSZ document the progressive evolution and exhumation of the shear-zone. The earliest recognised shear-zone fabrics (D_{4a}) suggest deformation under amphibolite-facies conditions. During this time, wall-rock gneisses underwent a rotation into the PSZ. This deformation and the progressive transposition of fabrics along the northern margins of the shear-zone are marked by (1) the development of shear-zone-parallel, high grade F_4 folds, (2) the gradual strain increase towards the PSZ core, and (3) the preservation of amphibolite-facies fabrics in the ND. The rotation of fabrics, subhorizontal stretching lineations and shear-sense indicators point to dextral transcurrent kinematics along the shear-zone. Much of the core of the PSZ is, however, characterised by retrograde and increasingly brittle-ductile fabrics (D_{4b}). The mafic amphibolites and felsic granitoids are not amenable to detailed P-T work but biotite- and chlorite/epidote-dominated assemblages, together with the mixed brittle-ductile behaviour of the fault rocks are consistent with broadly greenschist-facies conditions of deformation during D_{4b}. Notably, relics of higher-grade D_{4a} fabrics are present in most parts of the shear-zone, testifying to the originally higher grades of metamorphism during deformation. The steepening of stretching lineations in the southern D_{4b}-dominated domains, together with the rotation of the north-westerly trending shear-zone foliation to more WNW trends, at high angles to the maximum principal stress (Fig. 7.1), suggest a more transpressive component of deformation (e.g. Robin and Cruden, 1994; Tikoff and Teyssier, 1994; Tikoff and Greene, 1997; Neves et al., 2003). In fact, the anticlockwise rotation of the foliation by 15 - 20^{o} corresponds to a compressional bend in the PSZ at this locality (Fig. 7.1) and invokes localised high contractional stresses in the SD region (e.g. McNulty, 1995). The development of pervasive (30 to 40 m wide) domains of rheologically weaker D_{4b} phyllonites along the southern margin of the core has most likely led to the localisation of strain during D_{4b} and shearing under greenschist-facies conditions along the southern margin of the PSZ (e.g. Goodwin and Wenk, 1994; Jefferies et al., 2005; Lee et al., 2012). Notably strain partitioning into the phyllonites, during continued deformation, may promote fluid influx that enhances deformation, thereby creating a positive feedback between deformation and pegmatite intrusion (e.g. Brown and Solar, 1998a, 1998b; Petford and Koenders, 1998; Weinberg et al., 2004). Strain partitioning along the southern margin of the PSZ core results in an abrupt fabric-gradient between the shear-zone and its southern wallrocks, defining the sharp southern boundary of the PSZ core. Thus, in comparison, the southern boundary does not exhibit the same rotation and progressive transposition of regional fabrics into the PSZ as the indistinct northern margin, where higher-grade D_{4a} fabrics dominate. The fabric development thus documents a very distinct asymmetry of the PSZ that also points to a slightly diachronous evolution of fabrics across the PSZ, from earlier higher-temperature fabrics in the north to later brittle-ductile deformation in the south.

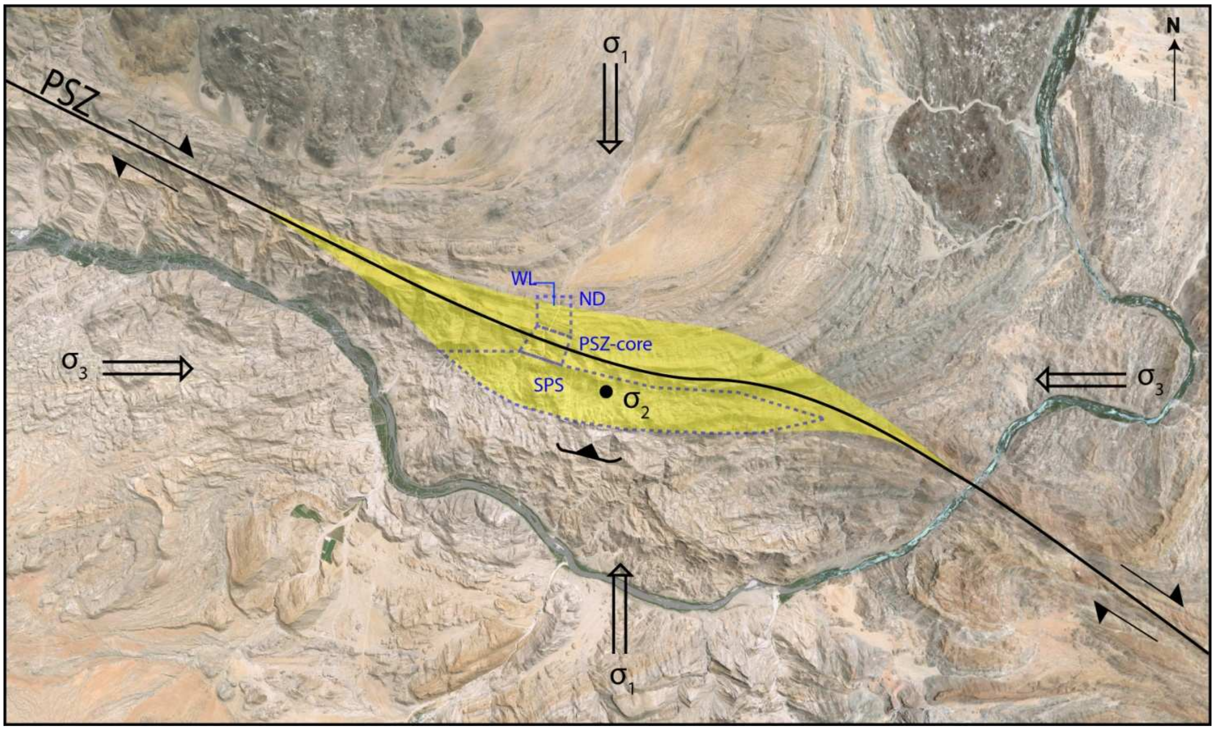

Figure. 7.1. Digitised Google Earth image illustrating the formation of a compressional bend (yellow domain) within the study area.

7.2 Pegmatite emplacement in and around the PSZ

Pegmatites in and around the PSZ show distinct spatial and temporal relationships with shear-zone-related fabrics and structures. The mapping of D_4 shear-zone fabrics and pegmatites also shows that pegmatites were emplaced in structurally distinct sites within and adjacent to the PSZ and that emplacement has occurred at different times of shear-zone development, from earlier D_{4a} fabrics to later, retrograde D_{4b} fabrics that accompanied the retrogression and exhumation. Although the source of the pegmatite magma is, at this stage unknown, the presence of the intersecting Orange River Pegmatite Belt indicates that granitic magmas are present and locally mobile. This suggests that, in this section of the PSZ, granitic melt pressures are relatively high and have the potential to flow down hydraulic gradients created during PSZ deformation. Figure 7.2 serves as a synoptic diagram for the distribution, geometry and controls of pegmatite emplacement documented here.

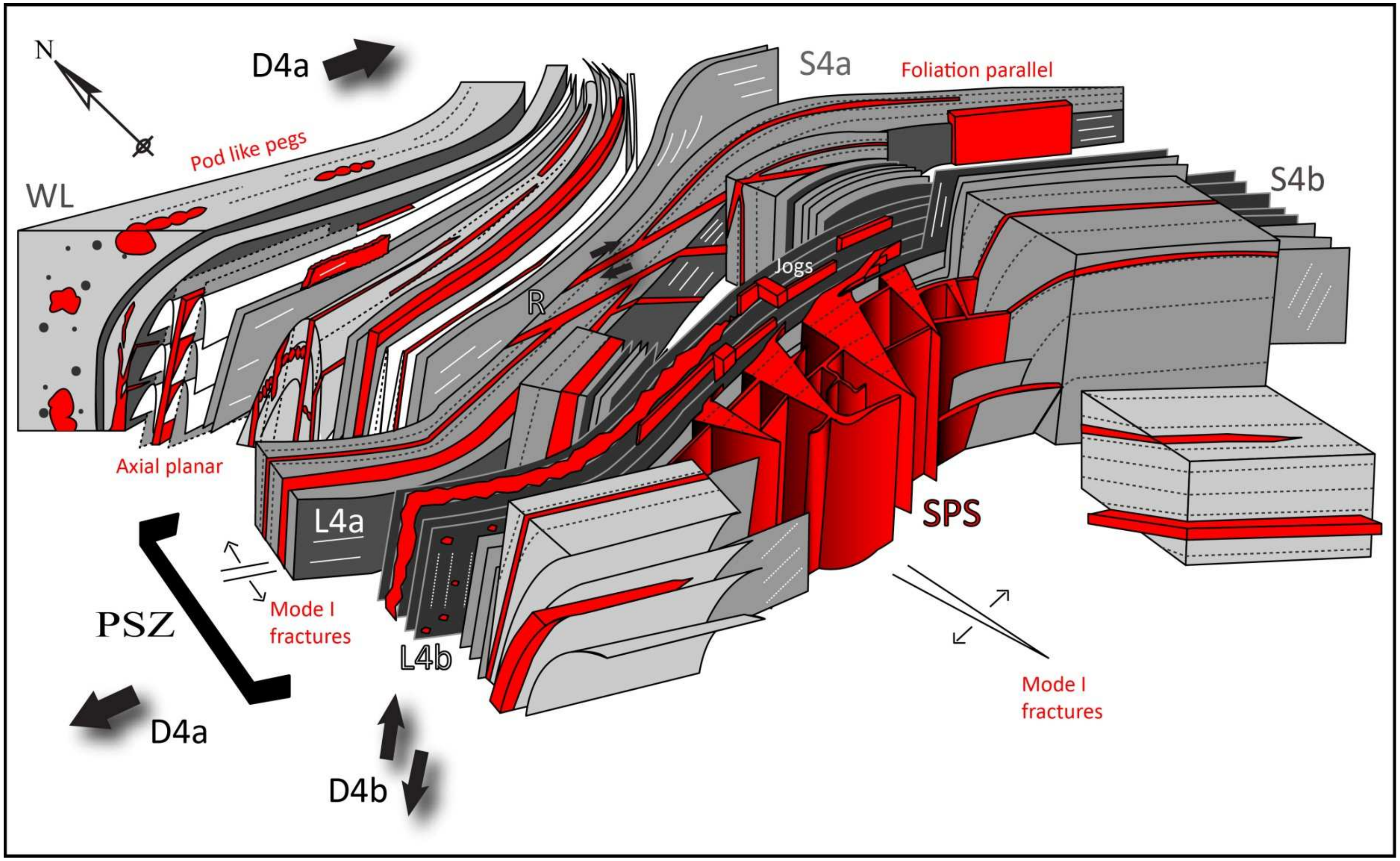

Figure. 7.2. Synoptic sketch illustrating fabric elements of the PSZ and the various controls on pegmatite emplacement created during the respective stages of deformation. Note: pegmatites are coloured red and not drawn to scale. Abbreviations: R: Synthetic Riedel shears, WL: Waterfalls Locality; SPS: Skimmelberg Pegmatite Stockwork.

7.2.1 ND

The effect of D_4 strains on pegmatite geometries in the ND is illustrated by the gradual transition of initially patchy, intrusive geometries to pegmatite sheets. Here pegmatite sheets are consistently emplaced parallel to the axial planes of F_4 folds and older fold geometries (F_3/F_4) that developed during progressive transposition of regional fabrics into the shear-zone fabrics (D_{4a}).

The emplacement of granitic dykes or hydrothermal veins, during folding and into the axial planes of folds, is only briefly documented for pegmatites, and is a common feature of many high-grade metamorphic terrains (e.g. Hand and Dirks, 1992; Collins and Sawyer, 1996; Paterson and Miller, 1998; Sawyer et al., 2000; Pawley et al., 2002; Memeti et al., 2005; Sawyer, 2008; Weinberg and Geordie, 2008; Weinberg et al., 2009), although it is also a poorly understood phenomenon. Axial planes in folds and axial-planar foliations are commonly understood to represent planes of shortening, approximating the XY-plane of the finite strain ellipsoid. Granite dyking or veining implies the formation of extensional and ideally mode I fractures in the plane of shortening. The magma or fluid pressure in the fracture may at least, temporally attain supralithostatic pressures, but this does not explain their formation in the XY plane. Numerous possible models have been suggested to account for this feature; see the comprehensive review in Vernon and Paterson (2001). The models include (1) the temporal relaxation of stresses during folding (e.g. Means, 1986), (2) the development of a pervasive axial-planar foliation (e.g. Etheridge, 1983; Lucas and St-Onge, 1995) and (3) axial-planar fractures formed due to strength contrasts during folding of multi-layered successions (e.g. Allibone and Norris, 1992). Alternatively, (4) magmatic fluids in the axial surfaces of strongly asymmetrical folds and localised shear zones are injected as transient, dilatant jog that opened during relative movement along the surfaces (e.g. Sawyer and Robin, 1986; *Fig. 6, p188*, Veron and Paterson, 2001,). All of these models create mechanical anisotropies that could be preferentially exploited. However, none of the explanations offered in the literature for the emplacement of thick (> 10 m) axial planar pegmatite sheets within the hinge zone of the large F_3/F_4 fold seems viable. For example, S_{4a} represents the axial planar foliation, but is not expressed as a prominent mechanical anisotropy in the hinge zone, and compositional layering in the banded gneisses is far better developed but is cross-cut by the pegmatites. The controls on emplacement of the pegmatite sheets, outside the hinge zone do however, appear to favour the second model (point 2). In this scenario the transition into sheeted and subsequently thin tabular geometries, largely retained between foliation planes, correlates with the increased development and pervasiveness of S_{4a} and the S_{4a}-mylonitic fabric towards the core. Figure. 7.3 provides a possible explanation for the controls on pegmatite emplacement across the ND towards the core.

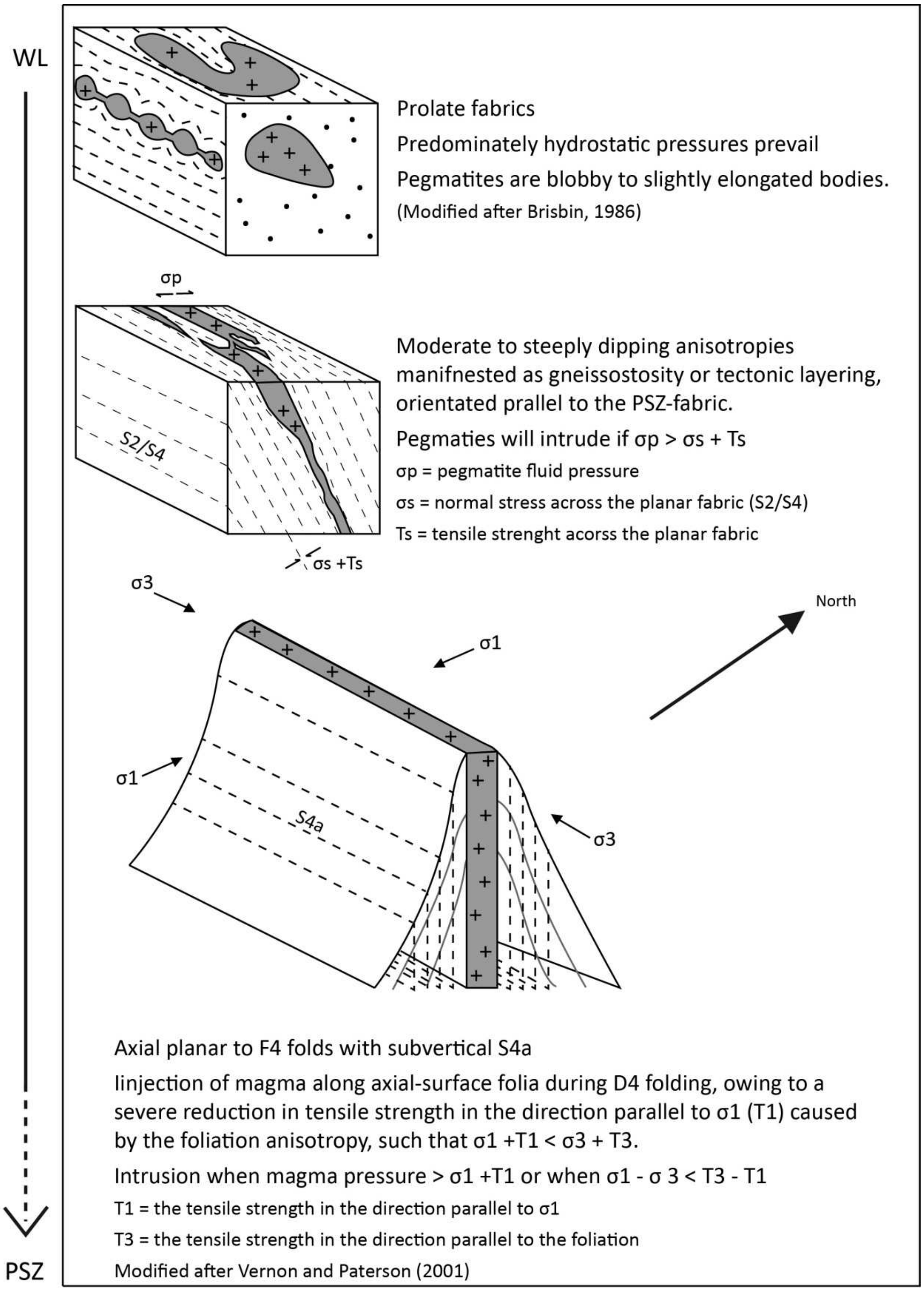

Figure. 7.3. Schematic diagram illustrating the conditions for emplacement of pegmatites across the ND, corresponding to the progressive development of D_{4a} related fabrics and notably the axial planar foliation to F_4 folds.

At the WL the lack of well-defined vertical anisotropies suggests that largely hydrostatic pressures prevailed and that magma pressures were unable to overcome the tensile rock strengths resulting in the formation of irregular bulbous bodies (e.g. Brisbin, 1986). As S_{4a} becomes progressively developed and subvertical towards the PSZ core, this axial planar fabric induces anisotropies normal to the maximum compressive stress and reduces the tensile rock strength in this direction (Gretener, 1969; Brisbin, 1986; Delaney et al., 1986), thus allowing injection of the magma along the axial-planar surface. Notably, where these axial-planar foliations become subvertical, transport/emplacement is aided by buoyancy driven forces (e.g. Lister and Kerr, 1991; Brown and Solar, 1998b; Weinberg et al., 2009; Brown, 2013).

At this stage, there is no convincing explanation for the emplacement of pegmatite sheets into and along the subvertical axial planes of F_4 folds. The pegmatite sheets of the ND do, however, illustrate the emplacement of granitoids during the earlier stages of shear-zone formation and that they are controlled by the creation amphibolite-facies grade D_{4a} structures (Fig. 7.2-3).

7.2.2 PSZ core

Evidence for controls on pegmatite emplacement within the confines of the PSZ are commonly obliterated as the intrusive relationships and pre-existing geometries are altered by the dominant high-strains, commonly folding and/or transposing pre-existing structures into parallelism with the PSZ-fabric. In lower strain domains, however, the preservation of various pegmatite geometries suggests that emplacement was controlled by multiple processes. The various controls are discussed below.

(a) Pegmatites parallel to the mylonitic foliation

Pegmatite bodies that are parallel to the mylonitic fabrics ($S_{4a,b}$) are subvertical, sheeted and tabular. They are confined between the subvertical foliation planes (S_{4b} and, to a lesser extent, S_{4a}). Subsequent deformation and also boudinage of pegmatite sheets, documents intrusion of the pegmatites at high angles to the shortening direction. This suggests that emplacement of the sheets occurred during low differential and effective stresses where the difference in tensile strength normal to and parallel to the anisotropy was greater than the differential stress. The Mohr-Griffith-Coulomb failure criterion (Brace, 1960; Sibson, 1998; Cox, 2010), represented on Mohr diagrams (Fig. 7.4), can be used to describe the relative orientations and modes of failure as a function of these principal stresses, their orientations and the mechanical properties of the rocks that undergo compressional deformation. In the PSZ the mylonitic foliation ($S_{4a,b}$) is developed as a pervasive fabric that created a pronounced mechanical anisotropy and planes of weakness (Fig. 7.4; lower failure envelope). Differences in tensile strengths normal to and parallel to the anisotropy are small, and Rutter and Neuman (1995) suggest values of < 1-5 MPa, so that the differential stresses during PSZ deformation are likely to have be even smaller (Fig. 7.4). This is particularly evident along the southern margin where biotite-rich phyllonites dominate the shear-zone rocks. The biotite-rich composition, together with the pervasive fabric in the phyllonites renders these rocks weak compared to, for example, the feldspar-dominated, massive wallrocks outside the PSZ (discussed below), and also results strain localization into the phyllonites. Deformation in the shear-zone was dominated by ductile creep and, given the weak nature of the shear-zone rocks, accommodates only low differential stresses. Hydration of the shear-zone rocks and the presence of granitic magmas also indicate low effective stresses during deformation. Figure. 7.4 illustrates how, at increasing fluid pressures and low differential stresses, rocks will experience failure along a plane of weakness (i.e. in the mylonitic foliation) before occurring across the foliation plane (i.e. by the intersection of upper failure envelope). Thus, within the highly pervasive PSZ core, it is the mylonitic-S_4 anisotropy that controls pegmatite emplacement through dilation between foliation planes (Figs. 7.2), which ultimately are sites of low hydrostatic pressures suitable for granitic magma emplacement.

Notably, the subvertical mylonitic fabrics, similar to those in the ND, provide vertical conduits through which magma may be transported to shallower crustal levels, driven primarily by magma buoyancy (Lister and Kerr, 1991; Brown and Solar, 1998b; Weinberg et al., 2009; Brown, 2013).

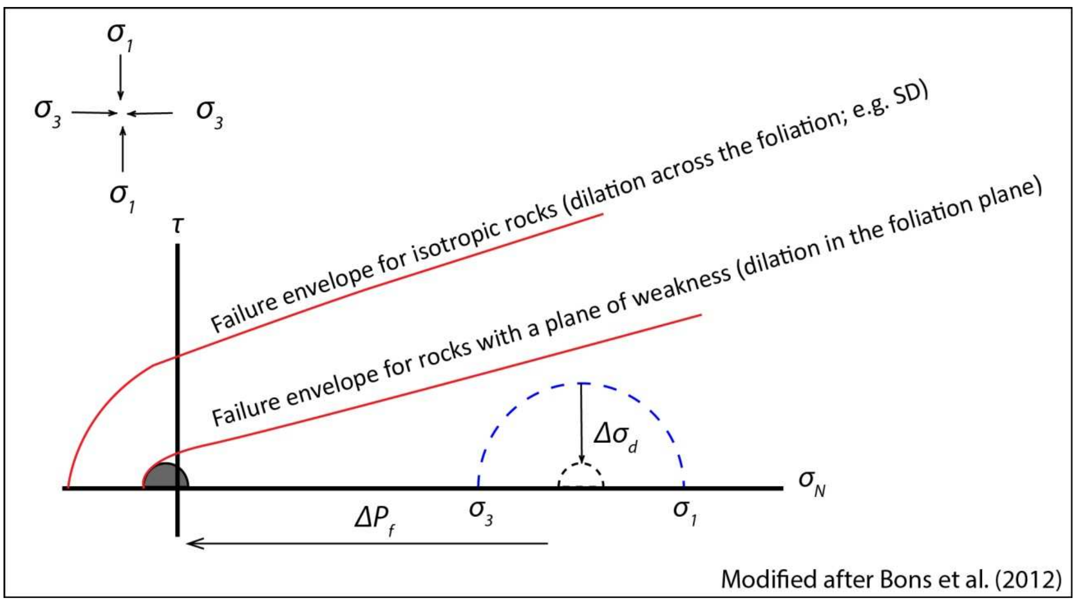

Figure 7.4. Conditions for development of opening fractures along and perpendicular to the dominant foliation can qualitatively be described through a Mohr diagram. Under ductile deformation conditions (dark grey; e.g. PSZ) differential stresses are excitedly lower than those outside the PSZ (blue circle). Reduced differential stresses ($\Delta\sigma_d$) and increasing fluid pressure (ΔP_f) in the PSZ allows for the stress-circle to intersect the failure envelope for rocks with a plane of weakness in the brittle field and fracture in the foliation plane before fracturing across the foliation plane.

(b) Pegmatites along Riedel Shears

The emplacement of lenticular to tabular pegmatite bodies in synthetic Riedel shears suggest a second control for magma emplacement with the PSZ core. The overall orientation of the shears and the dextral PSZ kinematics, support the formation of these Riedel shears, particularly in the northern domain of the PSZ.

Riedel shears are commonly invoked to represent domains of brittle fracture that develop during the early- to syn-kinematic stages of strike-slip shear-zones (e.g. Gamond, 1983; Katz et al., 2004; Ghosh and Chattopadhyay, 2008). These brittle domains may represent either subsidiary faults originating through stick-slip deformation (e.g. Byerlee and Brace, 1968) or ductile deformation bands that developed due to brittle deformation at the grain scale (e.g. Davis et al., 2000). In the case of PSZ the former conditions are favoured due to the relatively sharp, straight boundaries and general lack of displacement of markers across the pegmatite bodies. Therefore, in the early stages of PSZ deformation (D_{4a}), the development of Riedel fractures created preferentially orientated, highly permeable pathways (i.e. anisotropies) along which granitic magma fluids could intrude (e.g. Sibson, 1986, 1996; Araújo et al, 2001; Casas et al., 2001; Katz et al., 2004; Demartis et al., 2011; Xu et al., 2013), thus controlling the emplacement of the obliquely cross-cutting pegmatites.

In the lower strain domains, the preserved pegmatite geometries (Fig. 5.7c) show foliation-parallel pegmatites connecting to the larger oblique pegmatites. With the distribution of multiple synthetic Riedel shears across the core this suggests magma transport may occur at the km-scale within the PSZ, possibly as conjugate Riedel shear conduits (Fig 7.5) as described by Tchalenko (1970) and Sibson (1996).

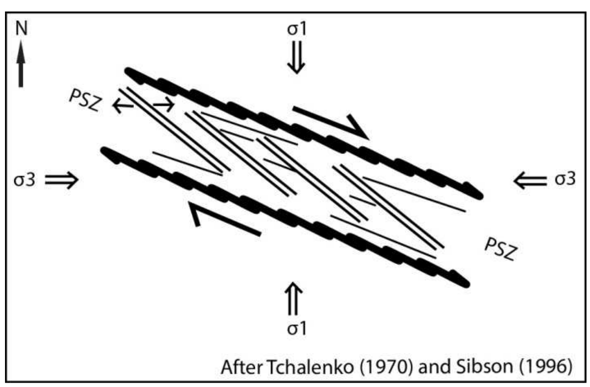

Figure. 7.5. Schematic diagram of the Riedel shear mesh that may be developed across the PSZ.

(c) Pegmatites within dilatant jogs

The intrusion of pegmatites along the southern margin of the PSZ into dilatant jogs (Fig. 5.9) documents yet another transport mechanism for magma within the high-strain PSZ (Fig. 7.2). The dominant feature of the jog geometry is the cm- to m-sized, discordant dyke that cross-cut the wall-rock foliations at high angles, parallel to the direction of shortening. In contrast to the vast majority of foliation-parallel sheets, jog formation is thus not directly controlled by the shear-zone anisotropy. The discordant pegmatites are emplaced into step-over sites that develop due to undulations in the mylonitic fabric during periods of right-lateral transcurrent shearing (Figs. 5.9, 7.6). The emplacement of felsic magma within dilatant jogs and their role as sites of magma transfer is well documented (e.g. Hutton et al., 1990, 1996; D'Lemos et al., 1992; Bouillin et al., 1993; Brown and Solar 1999; Brown, 2007; Weinberg et al., 2009). This process not only creates the necessary hydraulic gradients to support buoyancy driven transport but also creates space for emplacement within high-strain shear-zones (Castro, 1986; Guineberteau et al., 1987; McCaffery, 1992; Tikoff and Teyssier, 1992; McNaulty, 1995; Hutton, 1996, 1997; Brown and Solar 1998b; Tikoff et al., 1999; Westraat et al., 2005). The exposures within the PSZ preserve the connective relationships between discordant dykes and the commonly multiple, interconnecting concordant sills. The widening of the concordant pegmatites at the intersections with the dykes not only suggests contemporaneous emplacement but points to a transfer of melt from the concordant sheets into the jog (Fig. 7.6; e.g. Brown, 1994, 2013; Kisters et al., 2009; Hall and Kisters, 2012). The existence of numerous feeders into the jogs and their inconsistent cross-cutting relationships suggest multiple feeding events. In addition, the variation in the size of different jogs suggests progressive growth/development of the jogs (Fig. 7.6). Thus, the jogs developed over incremental dilatational events, creating lower pressures within the jogs and sucking melt towards these subvertical, extraction pathways (Fig. 7.6).

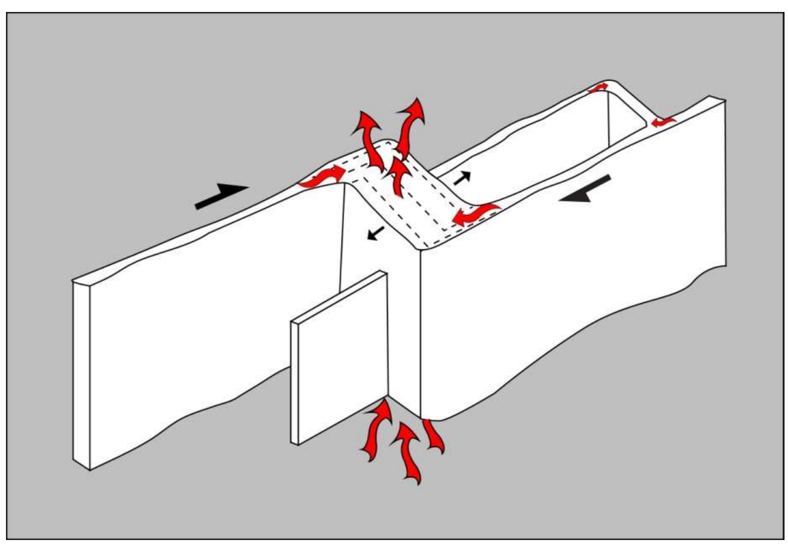

Figure. 7.6. Schematic 3-dimentional diagram illustrating how the dilatant jogs form over incremental dilatational events and drain the connective network of concordant sills. The jogs subsequently form steeply orientated transport pathways for the magma to higher crustal levels driven primarily by magma buoyancy forces.

7.2.3 SPS

The SPS is defined by the presence of northerly-to north-easterly-trending dykes in the southern footwall of the PSZ. The actual pegmatite stockwork is the result of the intersection of dykes and sills, the latter forming part of the regional Orange River Pegmatite Belt. Both dykes and sills are only weakly deformed so that original intrusive relationships are well preserved. As described in detail in Chapter 5.2.3, the intersecting and cross-cutting relationships between dykes and sills indicate a largely coeval emplacement of the two. This also points to some degree of connectivity between the two geometries. Sills show all the characteristics of the pegmatites of the regional pegmatite belt and their emplacement seems controlled mainly by regional gneissosity (S_2/S_4.) of the wall-rock sequences and/or the weakly-developed S_{4a} when emplaced adjacent to the PSZ. The conditions for rock failure along these planes of weakness are similar to that is described for those parallel to the foliation in the PSZ (Chapter 7.2.2; Fig. 7.4a).

Dykes show the following characteristics that are pertinent to understanding of their formation.

1. Dykes occur adjacent to the PSZ and along the southern margin of the shear-zone. They only project for a few meters into the mylonitic fabrics (S_{4b}) of the PSZ, but extend for up to 2 km into wallrocks of the SD. The northern terminations of dykes in the PSZ are invariably deformed and transposed into the S_{4b} fabric, consistent with the dextral shear along the PSZ.

2. The dykes are discordant to the wall-rock foliation and typically have sharp contacts, though internally they commonly exhibit PSZ-parallel fabrics.

3. Many of the dykes have, in detail, a wedge-shaped geometry. The maximum opening/width of dykes occurs next to the shear-zone-wall-rock contacts and they taper towards the south and away from the shear-zone (Fig. 7.7). The pegmatites have intruded into extensional (mode I) fractures and there is no discernible shear displacement across dykes.

4. Dyke formation is spatially confined to the ca. 12-15 km -long contractional bend in the PSZ, and they are most abundant in the western-central parts of this segment along the PSZ (Fig. 7.7). Similar dykes are not observed along the northern margins of the PSZ.

5. Dykes intrude at high-angles to S_{4b} in the contractional bend, but enclose angles of ca. 45° in the rest of the PSZ.

6. Thicker dykes are commonly fed by multiple, coeval and intersecting sills, to form dendritic (‘tree-like’) geometries on a variety of scales (up to km-scale).

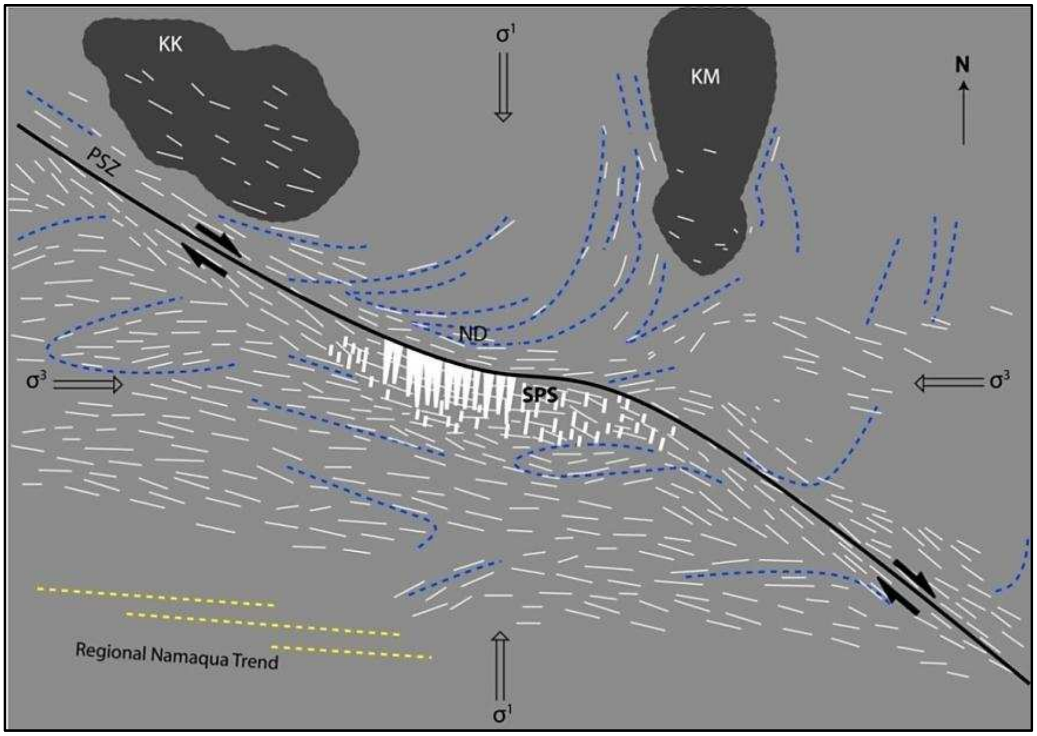

Figure. 7.7. Schematic overview of the SPS in the southern footwall of the PSZ. Regional stresses during the latter stages of southward indentation of the Kaapvaal Craton and the NMC with the maximum (σ^1) and minimum (σ^3) regional stresses are indicated. Note the location of largest dykes of the SPS, concentrated at the hinge point of the undulating PSZ and the pegmatites of the regional belt are largely parallel to the regional Namaqualand gneissic foliation (S_2). Trend lines are stippled blue while the pegmatites are solid white lines. The gabbro-norite bodies (KK) Kum Kum and (KM) Keimasmond Norite are illustrated for regional context.

Points 1 to 3 provide compelling evidence that the dykes formed as a direct result of shear displacement along the PSZ. D_4 deformation migrates towards the southern PSZ-margin with time (Chapter 4.2.2) so that during the latter stages of PSZ evolution, deformation is concentrated in the S4b-dominated successions of the core and into the footwall of the SD. These two domains do, however, display different modes of fracture that control the emplacement of pegmatites (Fig. 7.8a). The formation of extensional (mode I) fractures in the SD (point 3), intruded by pegmatite dykes, again points to dyking under low differential and, probably low effective stresses (Hancock, 1985; Etheridge, 1983; Sibson, 1998; Bons et al., 2012). The greenschist-facies conditions and mixed ductile-brittle creep recorded by fabrics in the PSZ are consistent with low differential stresses. Lowering the effective stress is likely to be driven by the high magmatic pressures (e.g. Davidson, 1994; Hall and Kisters et al., 2012) originating from the regional pegmatite belt. These conditions represent the ground preparation for dyking exclusively in the SD and can be summarised by the Mohr diagram in Figure. 7.8a.

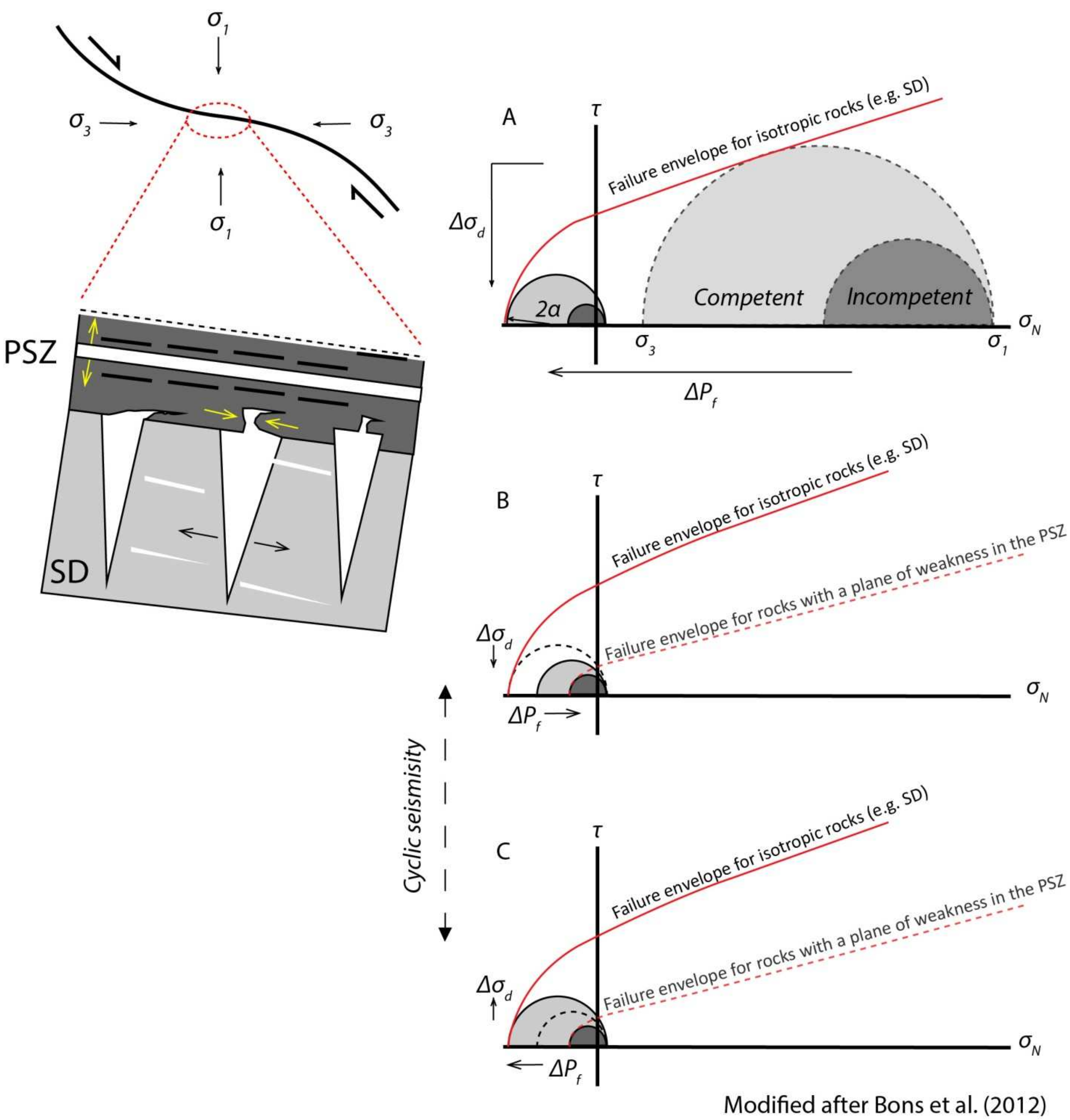

Figure. 7.8. Schematic Mohr diagrams illustrating the relative stress conditions along the southern margin of the PSZ (see text for detailed description). (A) In an anisotropic system competent rocks (SD; light grey) can experience larger differential stress and therefore intersects the failure envelope before incompetent rocks (PSZ; dark grey). When the angle 2α = 180^{o} to σ3, mode I fractures occur across the foliation in the SD but cannot be sustained within the PSZ and the fractures that propagate from the SD into the PSZ collapse. (B) After wall-rock fracture the temporary reduction of differential stress and fluid pressure shift the competent rock system away from the failure envelope and conditions promote failure in the plane of weakness in the PSZ and SD. (C) During a period of interseismicity, increasing differential stress and increasing fluid pressures move the incompetent rock system back towards the brittle failure envelope until fracturing occurs across the foliation in the SD and reverts the system back to the conditions represented in B.

Figure. 7.8a illustrates the contrasting modes of failure within the PSZ core (dark grey semi-circle) and the SD (light grey semi-circle) as the system undergoes deformation at elevated magmastatic pressures. The SD represents a more competent rock system that is documented (Chapter 4.2.3) to be relatively undeformed and only weakly affected by the PSZ. In addition, the SD occurs within a region of increased mean rock strength and can therefore experience larger differential stresses (larger semi-circle on Mohr diagram) before deforming. In contrast, the PSZ represents a rheologically weaker, incompetent system that can only experience small differential stress before fracturing (smaller semi-circle). The maximum compressive stress during the shear-zone formation is inferred to be the same in both PSZ core and SD and, as such, these domains share the same σ_1 and $\tau = 0$ points (Bons et al., 2012). Therefore, during sustained compression, the competent system will intersect the failure envelope for brittle fracture before that of the incompetent system (Fig. 7.8a; Bons et al., 2012). The mode I fractures are orientated at high angles to the least compressive stress when 2α approaches 180^{o} to σ_3. Stress relaxation after fracturing inhibits differential stress from increasing sufficiently to intersect the brittle failure envelope in the incompetent system (Bons et al., 2012). This contrast between the two systems is particularly well documented by the termination of the thick pegmatite dykes across the PSZ-boundary (Figs. 5.13, 7.8a). Differential stress is larger in the SD and this promotes fracture formation and pegmatite sheeting of the SPS. The large differential stress required for fracturing cannot be sustained within the weak PSZ core and therefore the fractures that propagate from the SPS into the PSZ cannot be kept open; collapsing a distance of less than 5 m into the PSZ core (Figs. 5.13, 7.8a).

The orientation and concentration of the larger dykes towards the western margin of the SPS (point 4; Fig. 7.5) correlates with the formation of pinnate joints in the wallrocks of contractional fault zones (e.g. Hancock, 1985). The dyke geometries are similar to the feather fractures described by Friedman and Logan (1970) and Blenkinsop (2008, see *Fig. 2d, p625*). Notably the formation of feather fractures adjacent to shear zones implies mode I fracturing perpendicular to the shear surface after a slip event (Friedman and Logan, 1970; Blenkinsop, 2008). This is analogous to what is observed at the boundary of the PSZ core and SD (point 3, 4 and 5) under largely transpressive conditions during the later stages of PSZ deformation (D_{4b}). In fact, the formation of these extensional fractures may correlate with a continuous string of discrete seismic events in the SD, with each fracture in the wall-rock forming after a period of ductile creep within the shear-zone and subsequent build-up of differential stress in the SD. Figure 7.8b-c illustrates stress-cycling conditions during a period of interseismicity in the SD. After the seismic event/fracturing (Fig 7.8b) stress conditions will temporarily change as the PSZ 'shields' the SD from the applied stress (e.g. Bons et al., 2012) and draining of the magma decreases the magmastatic pressure (Sibson, 2000), moving stress conditions away from the brittle failure envelope. Once the fracture is sealed and/or magma is emplaced, an accumulation of differential stress within the SD and the increased fluid pressure due to magma ponding would move the system back towards the failure envelope until subsequent brittle failure occurs (Fig. 7.8c).

This postulated alternation between periods of rock failure and pegmatite emplacement in the SD is similar to the cyclic fault-value model defined by Sibson (1975, 1990, 1992, 2000). The inconsistent cross-cutting relationships between the pegmatite sills and dykes similarly provides evidence for cyclic deformation processes in the SD. Therefore the controls for emplacement of the SPS are directly related to far-field regional stresses (Fig. 7.2) and the dextral transpressional kinematics along the PSZ during D_{4b} and the later stages of deformation.

Similar to what is observed for the dilatant jogs within the PSZ, the connectivity of dykes and sills and their documented geometries (Chapter 5.2.3; point 6) in the SPS suggests that the stockwork represents a km-scale, transient fracture network for the transport of magma from relatively static pathways (e.g. Hutton et al., 1990, 1996; Kisters et al., 2009; Brown and Solar 1999; Brown, 2007; Weinberg et al., 2009). In this case, the stockwork transported magma from the foliation-parallel sills into wide (> 50 m), highly permeable mode I, fracture conduits. Where sills connected with thick (ca. 30 - 50 m) dykes they have steep intersections that aided in buoyancy-driven magma ascent. On a regional scale, fracturing and fracture dilatancy that characterises this extensively developed pervasive network, facilitated in the transport of magma to higher crustal levels (e.g. Lister and Kerr, 1991; Clemens and Mawer 1992; Tobisch and Cruden, 1995; Rubin, 1998, Brown and Solar, 1999; Brown, 2013). Such efficient magma extraction would create significantly low magmastatic pressures within the SPS, thus creating a regional-scale hydrostatic gradient towards the SD. This, coupled with cyclic periods of brittle rock failure and sheeted granitic emplacement correlates with hydraulic pumping (e.g. Sibson, 1992; Weinberg et al., 2009) of magma from a local source, such as of the regional pegmatite belt, towards the PSZ. This has implications for incremental pluton growth by repeated sheeting (e.g. Miller and Paterson, 2001; Mahan et al., 2003) or dyking (e.g. Hutton, 1992; Bartley et al., 2008; Brown, 2013).

7.3 Regional implications of geochronological results

U-Pb monazite ages underline emplacement of the pegmatites around the PSZ over a protracted period of time between ca. 1005 and 960 Ma. The previous chapters outlined the specific structural controls of pegmatites related to the initial PSZ-shearing (D_{4a}) under amphibolite-facies conditions in the ND, to later greenschist-facies and brittle-ductile deformation (D_{4b}) along the PSZ and in the SD. Hence, the spread of crystallisation ages also provides an indication of the duration of shearing along the PSZ. The age of 1005 ± 5 Ma of older pegmatites controlled by the ductile D_{4a} structures in the ND is interpreted as a minimum age for the onset of D_4 shearing along the PSZ. Younger pegmatites intruded between ca. 990 and as late as 960 Ma in the case of the cross-cutting dykes of the SPS. The geochronological data indicate sills to be up to 30 Ma older than dykes in the SPS. However, inconsistent cross-cutting relationships, dyke-sill terminations and the geometry of sill-dyke intersection clearly document the connectivity and coeval emplacement of sills and dykes in the SPS (Figs. 5.19-20). Hence, the seemingly different ages of the three samples from the SPS are interpreted to represent an artefact of the sampling and, instead, the two different age populations point to dyke- and sill emplacement in the SPS over a period of up to 30 Ma. Both the variation and range of the pegmatite crystallisation ages within the SD suggests that emplacement of the pegmatites within this domain was likely to be episodic. The younger emplacement ages of pegmatites in the SPS correlate with the mixed ductile-brittle controls of intrusion that possibly reflects intrusion into cooler wallrocks accompanying the progressive exhumation of rocks along the PSZ. The deformation of most pegmatites in the SPS suggests that D_4 shearing along the PSZ likely continued after dyke emplacement and the 960 Ma age of the dykes provides a lower age bracket for deformation. Hence, deformation along the PSZ seems to have been recorded over a period of at least 45 Ma between 1005 Ma and 960 Ma. These results correspond to previous age estimates for pegmatite emplacement between ca. 1025 Ma and 945 Ma (Holmes, 1950; Jahns, 1955; Nicolaysen, 1962; Nicolaysen and Burger, 1965) and provide a tighter and more robust constraint on the timing and duration of faulting in this part of the NMC.

8. Conclusions

Detailed structural mapping of a section in and around the PSZ, aided by selected geochronological analysis, shows that pegmatites are spatially and temporally associated with the late-stage transcurrent PSZ. These results provide tighter constraints on the timing and duration of faulting in this part of the NMC. Here well-preserved relationships between pegmatite geometries and the fabrics and structures of the PSZ highlight the interaction between shear-zone deformation and its controls on the migration and emplacement of granitic magmas.

From this study the following main conclusions can be drawn for the emplacement of pegmatites during the evolution of the PSZ:

- The PSZ records an asymmetrical strain development across the core, indicated by pervasive banded ultramylonites, mylonites and significantly, the development of pervasive phyllonites at the southern margin. This defines a progressive deformational history during the exhumation of the shear-zone, from early ductile, amphibolite facies conditions (D_{4a}) along the northern margin to later, brittle-ductile, greenschist-facies conditions (D_{4b}) at the southern margin. The expression of D_4 fabrics across the PSZ further defines a transition in shear-zone dynamics from predominately wrench-dominated mechanics along the northern margin to a transpressional shear component at the southern boundary, during the evolution of the PSZ.

- Pegmatites emplaced within and along the margins of the PSZ core show distinctly different geometries and relationships to D_4 structures and fabrics developed across the PSZ. This highlights both spatial and temporal relationships of pegmatites emplaced in and around the PSZ. In the northern wallrocks the pegmatites occur as tabular to sheeted bodies, axial planar to earlier transposed folds (F_3/F_4) and parasitic F_4 folds that developed during the early stages of shear-zone evolution (D_{4a}). In the PSZ core pegmatites occur as tabular and sheeted bodies (a) parallel to (b) oblique to the mylonitic foliation and (c) as stubby discordant dykes connecting to multiple concordant sills basically define z-like jog geometries. The variable deformation of pegmatites within the core suggests syn-kinematic ($D_{4a\text{-}b}$) emplacement for these pegmatites. In the southern footwall of the PSZ the emplacement of the SPS is not only the most significant concentration of pegmatites within the study area but also one of the largest pegmatite complexes within the Orange River Pegmatite Belt. The stockwork is defined by the extensive development of thick (up to 50 m), wedge-shaped, discordant pegmatite dykes connected to laterally continuous and largely coeval, concordant and tabular pegmatite sills. The weak shear-parallel fabric within the pegmatites and the transposition of the dykes into the PSZ core suggests emplacement within the SPS occurred during the later stages of shear-zone development (D_{4b}).

- The PSZ created various structural controls for pegmatite emplacement during it evolution. In the northern wallrocks the controls are interpreted to be anisotropies along the axial planes of earlier-large scale folds (F_3/F_4) and the (S_{4a}) axial planar foliation of parasitic F_4 folds developed during the folding and transposition of the gneissic wallrocks. In the PSZ core emplacement is controlled by the development of (a) subvertical, mylonitic and phyllonitic foliation anisotropies and (b) fracture permeabilities through synthetic Riedel shears and dextral dilatant jogs. In the SPS sills are controlled by the anisotropies of the rotated gneissic foliation (S_2/S_4) and the inherited shear foliation (S_{4a}) adjacent to the PSZ core. The dykes are emplaced into feather-shaped N-S mode I fractures, possibly during episodic stick-slip events, and are therefore controlled by the far-field regional stresses and the dextral transpressional kinematics along the PSZ during D_{4b}.

- Pegmatites within the northern wallrocks yield ages of ca. 990 Ma to 1005 Ma while ages from pegmatites with the SPS indicate emplacement of the stockwork occurred between ca. 960 Ma and 990 Ma. This suggests that the controls on emplacement developed over a prolonged period of shear evolution that is constrained, at least between D_{4a} and D_{4b} in the study area, to a period of ca. 45 Ma.

- This study highlights the role of deformation in the transport and emplacement of granitic magmas in and around transcurrent shear-zones. Here magma is not only concentrated within the highly permeable core but along the margins of the PSZ. In this study, the extent of granitic magma emplacement around shear zones is exemplified by the SPS, occurring in the southern footwall of the PSZ. The SPS, as an extensive fracture network, also has implications for (1) the creation of low hydrostatic pressures towards large-scale shear-zones, (2) the extraction of melt from regional sources and (3) possibly the formation of large granitic plutons adjacent to shear-zones through repeated sheeting.

References

Agenbacht, A.L.D., 2007. *The geology of the Pofadder area. Explanation sheet 2918. Council for Geoscience, South Africa.* Pretoria, South Africa: Council for Geoscience.

Aleinikoff, J.N., Schenck, W.S., Plank, M.O., Srogi, L.A., Fanning, C.M., Kamo, S.L. and BosbyshelL, H., 2006. Deciphering igneous and metamorphic events in high-grade rocks of the Wilmington complex, Delaware: Morphology, cathodoluminescence and backscattered electron zoning, and SHRIMP U-Pb geochronology of zircon and monazite. *Bulletin of the Geological Society of America,* **118**(1-2), pp. 39-64.

Allibone, A.H. and Norris, R.J., 1992. Segregation of leucogranite microplutons during syn-anatectic deformation: an example from the Taylor Valley, Antarctica. *Journal of Metamorphic Geology,* **10**(4), pp. 589-600.

Andreoli, M.A.G., Hart, R.J., Ashwal, L.D. and Coetzee, H., 2006. Correlations between U, Th content and metamorphic grade in the Western Namaqualand belt, South Africa, with Implications for radioactive heating of the crust. *Journal of Petrology,* **47**(6), pp. 1095-1118.

Aranguren, A., Larrea, F.J., Carracedo, M., Cuevas, J. and Tubía, J.M., 1997. The Los Pedroches batholith (Southern Spain): polyphase interplay between shear-zones in transtension and setting of granites. In: BOUCHEZ, J. L, HUTTON, D.H.W. AND STEPHENS, W.E., ed, *Granite: From Segregation of Melt to Emplacement Fabrics.* Dordrecht: Kluwer Academic, pp. 215-230.

Araújo, M.N.C., Da Silva, F.C.A. and De Sá, E.F.J., 2001. Pegmatite Emplacement in the Seridó Belt, Northeastern Brazil: Late Stage Kinematics of the Brasiliano Orogen. *Gondwana Research,* **4**(1), pp. 75-85.

Archanjo, C.J. and Fetter, A.H., 2004. Emplacement setting of the granite sheeted pluton of Esperança Brasiliano orogen, Northeastern Brazil). *Precambrian Research,* **135**(3), pp. 193-215.

Arthaud, M.H. and Caby, R., 1993. Magma injection and transtension along sinuous lithospheric shear-zones: examples from the Late Proterozoic Brasiliano belt in Ceará, northeast Brazil. *Terra Abstracts,* **5**, pp. 201.

Bailie, R.H. and Reid, D.L., 2000. Towards the age and origin of the metalliferous Bushmanland Group, Northern Cape Province, South Africa. *Journal of African Earth Sciences,* **31**, pp. 5.

Bailie, R., Rajesh, H.M. and Gutzmer, J., 2012. Bimodal volcanism at the western margin of the Kaapvaal Craton in the aftermath of collisional events during the Namaqua-Natal Orogeny: The Koras Group, South Africa. *Precambrian Research,* **200-203**, pp. 163-183.

Barr, D., 1985. Migmatites in the Moines. In: J.R. Ashworth, ed, *Migmatites.* Glasgow, U.K.: Blackie.

Bartley, J.M., Coleman, D.S. and Glazner, A.F., 2006. Incremental pluton emplacement by magmatic crack-seal. *Earth and Environmental Science Transactions of the Royal Society of Edinburgh,* **97**(04), pp. 383.

Barton, E.S. and Burger, A.J., 1983. Reconnaissance isotopic investigations in the Namaqua Mobile Belt and implications for Proterozoic crustal evolution – Upington geotraverse. *Special publications of the Geological Society of South Africa,* **10**, pp. 173-191.

Becker, T., Schreiber, U., Kampunzu, A.B. and Armstrong, R., 2006. Mesoproterozoic rocks of Namibia and their plate tectonic setting. *Journal of African Earth Sciences,* **46**(1–2), pp. 112-140.

Beukes, G.J., 1973. ‘n Geologiese ondersoek van die gebied suid van Warmbad, Suidwes-Afrika, met spesiale verwysing na die metamorfmagamatiese assosiasies van die Voorkambries gesteentes*.* PhD edn. Free State: University of Orange Free State.

Beukes, G.J. and Botha, B.J.V., 1978. Die Tantalite Valley-megaskuifskeursone in die gebied suid van Warmbad, Suidwes-Afrika. *Annual Report,* Geological Survey of South Africa, **11¸**pp.247-252

BIAL, J., SCHENK, V., BÜTTNER, S., APPEL, P. 2013. Mesoproterozoic UHT metamorphism and two metamorphic events separated by retrogression in the central Namaqualand Metamorphic Complex (Kakamas Terrane), South Africa. Abstracts. 24^{th} Colloquium of Africa Geology, Addis Ababa, Ethiopia.

Blenkinsop, T.G., 2008. Relationships between faults, extension fractures and veins, and stress. *Journal of Structural Geology,* **30**(5), pp. 622-632.

Blignault, H.J., 1977. Structural-metamorphic imprint on part of the Namaqua Mobile Belt in South West Africa. 21 edn. *Bulletin Precambrian Research Unit*, 21, University of Cape Town.

Blignault, H.J., Van Aswegen, G., Van der Merwe, S.W. and Colliston, W.P., 1983. The Namaqualand geotraverse and environs: part of the Proterozoic Namaqua Belt. In: B.J.V. Botha, (Eds.) *Namaqualand Metamorphic Complex.* Pretoria: Geological Society of South Africa, pp. 1-29.

Bons, P.D., Elburg, M.A. and Gomez-Rivas, E., 2012. A review of the formation of tectonic veins and their microstructures. *Journal of Structural Geology,* **43**, pp. 33-62.

Botha, B.J.V., Grobler, N.J., Linstrom, W. and Schmit, C.A., 1979. Metamorphic zonation in the Matsap, Kheis and Namaqua domains east and west of the Kaaien Hills, Northern Cape Province. *Transactions of the Geological Society of South Africa*, **82***,* pp. 66-75*.*

Botha, B.J.V., Grobler, N.J., Linstrom, W. and Schmit, C.A., 1976. Stratigraphic correlation between and the Kheis and Matsap Formations and their relation to the Namaqua Metamorphic Complex. *Transactions of the Geological Society of South Africa*, 79*,* pp. 304-311*.*

Bouillin, J., Bouchez, J., LespinassE, P. and Peˆcher, A., 1993. Granite emplacement in an extensional setting: an AMS study of the magmatic structures of Monte Capanne (Elba, Italy). *Earth and Planetary Science Letters,* **118**(1–4), pp. 263-279.

Brace, W.F., 1960. An extension of the Griffith theory of fracture to rocks. *Journal of Geophysical Research,* **65**(10), pp. 3477-3480.

Brisbin, W.C., 1986. Mechanics of pegmatite intrusion. *American Mineralogist,* **71**(3-4), pp. 644-651.

Brodie, K., Fettes, D., Harte, B. and Schmid, R., 2007. Structural terms including fault rock terms. In: D. Fettes and J. Desmons, (Eds.), *Metamorphic Rocks: A Classification and Glossary of Terms. Recommendations by the IUGS Subcommission on the Systematics of Metamorphic Rocks.* New York: Cambridge University Press, pp. 1-14.

Brown, M. and Rushmer, T., 1997. The role of deformation in the movement of granitic melt: views from the laboratory and field. In: M.B. HOLNESS, ed, *Deformation enhanced Fluid Transport in the Earth’s Crust and Mantle: Mineralogical Society Series.* London: Chapman Hall, pp. 111-114.

Brown, M., Rushmer, T. and Sawyer, E.W., 1995. Special Section: Mechanisms and Consequences of Melt Segregation from Crustal Protoliths. *Journal of Geophysical Research,* **100**(B), pp. 15549-15808.

Brown, M., 2013. Granite: From genesis to emplacement. *Bulletin of the Geological Society of America,* **125**(7-8), pp. 1079-1113.

Brown, M., 2007. Crustal melting and melt extraction, ascent and emplacement in orogens: Mechanisms and consequences. *Journal of the Geological Society,* **164**(4), pp. 709-730.

Brown, M., 1994. The generation, segregation, ascent and emplacement of granite magma: the migmatite-to-crustally-derived granite connection in thickened orogens. *Earth-Science Reviews,* **36**(1–2), pp. 83-130.

Brown, M. and Solar, G.S., 1998. Granite ascent and emplacement during contractional deformation in convergent orogens. *Journal of Structural Geology,* **20**(9–10), pp. 1365-1393.

Brown, M. and Solar, G.S., 1998. Shear-zone systems and melts: feedback relations and self-organization in orogenic belts. *Journal of Structural Geology,* **20**(2–3), pp. 211-227.

Buick, I.S., Lana, C. and Gregory, C., 2011. A LA-ICP-MS and SHRIMP U/Pb age constraint on the timing of REE mineralisation associated with Bushveld granites, South Africa. *South African Journal of Geology,* **114**(1), pp. 1-14.

Byerlee, J.D. and Brace. W.F., 1968. Stick slip, stable sliding, and earthquakes. effect of rock type, pressure, strain rate, and stiffness. *J Geophysical Research,* **73**(18), pp. 6031-6037.

Cameron, E.N., 1936. Concepts of the internal structure of granitic pegmatites and their applications to certain peg of SW Africa. Transactions of Geological Society of South Africa.

Cameron, E.N., Jahns, R.H., Mcnair, A.H. and Page, L.R., 1949. Internal structure of granitic pegmatites. Economic Geology, **2,** pp. 1-115.

Carreras, J. and Druguet, E., 1994. Structural zonation as a result of inhomogeneous non-coaxial deformation and its control on syntectonic intrusions: an example from the Cap de Creus area, eastern-Pyrenees. *Journal of Structural Geology,* **16**(11), pp. 1525-1534.

Casas, A.M., Gapais, D., Nalpas, T., Besnard, K. and Román-berdiel, T., 2001. Analogue models of transpressive systems. *Journal of Structural Geology,* **23**(5), pp. 733-743.

Castro, A., 1987. On granitoid emplacement and related structures. A review. *Geologische Rundschau,* **76**(1), pp. 101-124.

Castro, A., 1986. Structural pattern and ascent model in the Central Extremadura batholith, Hercynian belt, Spain. *Journal of Structural Geology,* **8**(6), pp. 633-645.

Cawthorn, R.G. and Meyer, F.M., 1993. Petrochemistry of the Okiep copper district basic intrusive bodies, northwestern Cape Province, South Africa. *Economic Geology,* **88**(3), pp. 590-605.

Černý, P., 1991. Rare-element granitic pegmatites. Part I: anatomy and internal evolution of pegmatite deposits. *Geoscience Canada,* **18**(2), pp. 49-67.

Černý, P., 1991. Rare-element granitic pegmatites. Part II: regional to global environments and petrogenesis. *Geoscience Canada,* **18**(2), pp. 68-81.

Černý, P., 1992. Geochemical and petrogenetic features of mineralization in rare-element granitic pegmatites in the light of current research. *Applied Geochemistry,* **7**(5), pp. 393-416.

Černý, P. and ERCIT, T.S., 2005. The classification of granitic pegmatites revisited. *Canadian Mineralogist,* **43**(6), pp. 2005-2026.

Černý, P., London, D. and Novák, M., 2012. Granitic pegmatites as reflections of their sources.*Elements*,***8*** (4), pp. 289-294.

Černý, P., 2000. Constitution, petrology, affiliations and categories of miarolitic pegmatites. In: F. Pezzotta, ed, *Mineralogy and Petrology of Shallow Depth Pegmatites; Papers from the First International Workshop. Memorie della Societa´ di Scienze.* pp. 5-12.

Clemens, J.D., Petford, N. and Mawer, C.K., 1997. Ascent mechanisms of granitic magmas: causes and consequences. In: M.B. Holness, ed, *Deformation enhanced Fluid Transport in the Earth's Crust and Mantle.* London: Chapman and Hall, pp. 145-172.

Clemens, J.D. and Mawer, C.K., 1992. Granitic magma transport by fracture propagation. *Tectonophysics,* **204**(3–4), pp. 339-360.

Clemens, J.D. and Vielzeuf, D., 1987. Constraints on melting and magma production in the crust. *Earth and Planetary Science Letters,* **86**(2–4), pp. 287-306.

Clifford, T.N. and Barton, E.S., 2012. The O'okiep Copper District, Namaqualand, South Africa: A review of the geology with emphasis on the petrogenesis of the cupriferous Koperberg Suite. *Mineralium Deposita,* **47**(8), pp. 837-857.

Clifford, T.N., Barton, E.S., Stern, R.A. and Duchesne, J.-., 2004. U-Pb zircon calendar for Namaquan (Grenville) crustal events in the granulite-facies terrane of the O'okiep Copper District of South Africa. *Journal of Petrology,* **45**(4), pp. 669-691.

Collins, W.J. and Sawyer, E.W., 1996. Pervasive granitoid magma transfer through the lower-middle crust during non-coaxial compressional deformation. *Journal of Metamorphic Geology,* **14**(5), pp. 565-579.

Colliston, W.P., Praekelt, H.E. and Schoch, A.E., 1989. A broad perspective (Haramoep) of geological relations established by sequence mapping in the Proterozoic Aggeneys Terrane, Bushmanland, South Africa. *South African Journal of Geology,* **92**(1), pp. 42-48.

Colliston, W.P. and Schoch, A.E., 2000. Mid-Proterozoic tectonic evolution along the Orange River on the border between South Africa and Namibia. *Communications Geological Survey of Namibia*, **(12),** pp. 53-62.

Colliston, W.P. and Schoch, A.E., 2000. Tectonostratigraphic features along the Orange River in the western part of the Mesoproterozoic Namaqua mobile belt. *South African Journal of Geology,* **101**(2), pp. 91-100.

Colliston, W.P. and Schoch, A.E., 2006. The distribution and diagnostic features of deformed plutonic rocks in two terranes of the Namaque mobile belt along the Orange (Gariep) River, South Africa. *South African Journal of Geology,* **109**(3), pp. 369-392.

Colliston, W.P. and Schoch, A.E., 1998. Tectonostratigraphic features along the Orange River in the western part of the Mesoproterozoic Namaqua mobile belt. *South African Journal of Geology,* **101**(2), pp. 91-100.

Colliston, W.P., Praekelt, H.E. and Schoch, A.E., 1991. A progressive ductile shear model for the Proterozoic Aggeneys Terrane, Namaqua mobile belt, South Africa. *Precambrian Research,* **49**(3–4), pp. 205-215.

Cornell, D.H., Thomas, R.J., Moen, H.F.G., Reid, D.L., Moore, J.M. and Gibson, R.L., 2006. *The Namaqua-Natal Province*. In: M.R. Johnson, C.R. Anhaeusser and R.J. Thomas, (Eds.), *The Geology of South Africa.*

Geological Society of South Africa. Pretoria: Geological Society of South Africa/Council for Geoscience, pp. 395-420.

Cornell, D.H., Hawkesworth, C.J., Van Calstern, P. and Scott, W.D., 1990. Sm-Nd study of Precambrian crustal development in the Prieska-Copperton region, northern Cape Province. *Transactions of the Geological Society of South Africa*, **89**, pp. 17-28.

Cornell, D.H., Humphreys, H., Theart, H.F.J. and Scheepers, D.J., 1992. A collision-related pressure-temperature-time path for Prieska copper mine, namaqua-natal tectonic province, South Africa. *Precambrian Research,* **59**(1-2), pp. 43-71.

Cornell, D.H. and Pettersson, Å, 2007. Ion probe zircon dating of metasediments from the Areachap and Kakamas Terranes, Namaqua-Natal Province and the stratigraphic integrity of the Areachap Group. *South African Journal of Geology,* **110**(4), pp. 575-584.

Cornell, D.H., Pettersson, A., J., Whitehouse, M. and Scherstén, A., 2009. A new chronostratigraphic paradigm for the age and tectonic history of the Mesoproterozoic Bushmanland ore district, South Africa. *Economic Geology,* **104**(3), pp. 385-404.

Coward, M.P. and Potgieter, R., 1983. Thrust zones and shear-zones of the margin of the Namaqua and Kheis mobile belts, southern Africa. *Precambrian Research,* **21**(1-2), pp. 39-54.

Cox, S.F., 2010. The application of failure mode diagrams for exploring the roles of fluid pressure and stress states in controlling styles of fracture-controlled permeability enhancement in faults and shear-zones. *Geofluids,* **10**(1-2), pp. 217-233.

Davidson, C., Hollister, L.S. and Schmid, S.M., 1992. Role of melt in the formation of a deep-crustal compressive shear-zone: the Maclaren Glacier metamorphic belt, south central Alaska. *Tectonics,* **11**(2), pp. 348-359.

Davidson, C., Schmid, S.M. and Hollister, L.S., 1994. Role of melt during deformation in the deep crust. *Terra Nova,* **6**(2), pp. 133-142.

Davis, G.H., Bump, A.P., García, P.E. and Ahlgren, S.G., 2000. Conjugate Riedel deformation band shear-zones. *Journal of Structural Geology,* **22**(2), pp. 169-190.

De Beer, C.H., 2010. *The Geology of the Garies area.* Explanation sheet. 1:250 000 scale edn. Pretoria, South Africa: Council for Geoscience.

De Beer, C.H., Gresse, P.G., Theron, J.N. and Almond, J.E., 2002. The geology of the Calvinia area. *Explanation sheet.* 1: 250 000 scale edn. Pretoria, South Africa: Council for Geoscience.

De Beer, J.H. and Meyer, R., 1984. Geophysical characteristics of the Namaqua-Natal Belt and its boundaries, South Africa. *Journal of Geodynamics,* **1**(3–5), pp. 473-494.

De Beer, J.H. and Meyer, R., 1983. Geoelectrical and gravitational characteristics of the Namaqua Natal mobile belt and its boundaries. *Special publications of the Geological Society of South Africa,* **10**, pp. 91-100.

Demartis, M., PinottI, L.P., Coniglio, J.E., D'eramo, F.J., Tubía, J.M., Aragón, E. and Agulleiro Insúa, L.A., 2011. Ascent and emplacement of pegmatitic melts in a major reverse shear-zone (Sierras de Córdoba, Argentina). *Journal of Structural Geology,* **33**(9), pp. 1334-1346.

D'lemos, R.S., Brown, M. and Strachan, R.A., 1992. Granite magma generation, ascent and emplacement within a transpressional orogen. *Journal - Geological Society (London),* **149**(4), pp. 487-490.

Druguet, E. and Hutton, D.H.W., 1998. Syntectonic anatexis and magmatism in a mid-crustal transpressional shear-zone: an example from the Hercynian rocks of the eastern Pyrenees. *Journal of Structural Geology,* **20**(7), pp. 905-916.

Duchesne, J., Auwera, J.V., Liégeois, J., Barton, E.S. and Clifford, T.N., 2007. Geochemical constraints of the petrogenesis of the O'okiep Koperberg Suite and granitic plutons in Namaqualand, South Africa: A crustal source in Namaquan (Grenville) times. *Precambrian Research,* **153**(1-2), pp. 116-142.

Eglington, B.M. and Armstrong, R.A., 2000. SHRIMP dating of samples from the Loeriesfontein area, South Africa. *Open File Report (2000-0075-0)*. Pretoria, South Africa: Council for Geoscience.

Eglington, B.M., 2006. Evolution of the Namaqua-Natal Belt, southern Africa – A geochronological and isotope geochemical review. *Journal of African Earth Sciences,* **46**(1–2), pp. 93-111.

Eglington, B.M. and Armstrong, R.A., 2003. Geochronological and isotopic constraints on the Mesoproterozoic Namaqua-Natal Belt: Evidence from deep borehole intersections in South Africa. *Precambrian Research,* **125**(3-4), pp. 179-189.

Etheridge, M.A., 1983. Differential stress magnitudes during regional deformation and metamorphism: upper bound imposed by tensile fracturing. *Geology,* **11**(4), pp. 231-234.

Fleitout, L. and Froidevaux, C., 1980. Thermal and mechanical evolution of shear-zones. *Journal of Structural Geology,* **2**(1–2), pp. 159-164.

Friedman, M. and Logan, J.M., 1970. Microscopic feather fractures. *Bulletin of the Geological Society of America,* **81**(11), pp. 3417-3420.

Frimmel, H.E., Basei, M.S. and Gaucher, C., 2011. Neoproterozoic geodynamic evolution of SW-Gondwana: A southern African perspective. *International Journal of Earth Sciences,* **100**(2), pp. 323-354.

Frimmel, H.E., Hartnady, C.J.H. and Koller, F., 1996. Geochemistry and tectonic setting of magmatic units in the Pan-African Gariep Belt, Namibia. *Chemical Geology,* **130**(1-2), pp. 101-121.

Gamond, J.F., 1983. Displacement features associated with fault zones: a comparison between observed examples and experimental models. *Journal of Structural Geology,* **5**(1), pp. 33-45.

Geringer, G.J., Botha, B.J.V. and Slabbert, M.J., 1988. The Keimoes Suite -- a composite granitoid batholith along the eastern margin of the Namaqua mobile belt, South Africa. *South African Journal of Geology,* **91**, pp. 490-497.

Geringer, G.J., Botha, B.J.V., Pretorius, J.J. and Ludick, D.J., 1986. Calc-alkaline volcanism along the eastern margin of the namaqua mobile belt, south Africa - A possible middle proterozoic volcanic arc. *Precambrian Research,* **33**(1–3), pp. 139-170.

Geringer, G.J., Humphreys, H.C. and Scheepers, D.J., 1994. Lithostratigraphy, protolithology, and tectonic setting of the Areachap Group along the eastern margin of the Namaqua Mobile Belt, South Africa. *South African Journal of Geology,* **97**(1), pp. 78-100.

Geringer, G.J. and Ludick, D.J., 1990. Middle-Proterozoic calc-alkaline, shoshonitic volcanism along the eastern margin of the Namaqua Mobile Belt, South Africa - implications for tectonic evolution in the area. *South African Journal of Geology,* **93**(2), pp. 389-399.

Gevers, T.W., 1936. Phases of mineralization in Namaqualand Pegmatite. Trans. Geol. Soc. S. Afri. v 39, p 331-376. *Transactions of the Geological Society of South Africa,* **39**, pp. 331-376.

Gevers, T.W., Partridge, F.C. and Joubert, G.K., 1937. The Pegmatite area south of the Orange River in Namaqualand. Mem. Dept. Mines, Geol. Surv. No. 31. *Memoirs, Department of Mines, Geological Survey of South Africa,* **31**.

Ghosh, N. and Chattopadhyay, A., 2008. The initiation and linkage of surface fractures above a buried strike-slip fault: An experimental approach. *Journal of Earth System Science,* **117**(1), pp. 23-32.

Gibson, R.L., Robb, L.J., KIsters, A.F.M. and Cawthorn, R.G., 1996. Regional setting and geological evolution of the Okiep Copper District, Namaqualand, South Africa. *South African Journal of Geology,* **99**(2), pp. 107-120.

Gillespie, M.R. and Styles, M.T., 1999. *BGS Rock Classification Scheme, Volume 1: Classification of igneous rocks.* 1. Nottingham: British Geological Survey.

Goodwin, L.B. and Wenk, H.-., 1995. Development of phyllonite from granodiorite: Mechanisms of grain-size reduction in the Santa Rosa mylonite zone, California. *Journal of Structural Geology,* **17**(5), pp. 689-697,699-707.

Grantham, G.H., Eglington, B.M. and Armstrong, R.A., 2000. *The geochronology of some lithologies from sheet 3018AC Leliefontein, Namaqua Metamorphic Province.* Internal report edn. Pretoria: Council for Geoscience.

Grantham, G.H., Thomas, R.J., Eglington, B.M., De Bruin, D., Atanasov, A. and Evans, M.J., 1993. Corona textures in Proterozoic olivine melanorites of the Equeefa Suite, Natal Metamorphic Province, South Africa. *Mineralogy and Petrology,* **49**(1-2), pp. 91-102.

Gresse, P.G., Von Veh, M.W. and Frimmel, H.E., 2006. The Namibian (Neoproterozoic)**:** to early Cambrian successions. In: M.R. Johnson, C.R. Anhaeusser and R.J. Thomas, (Eds.) *The Geology of South Africa.* Second edn. Johannesburg and Pretoria: The Geological Society of South Africa and the Council for Geoscience, pp. 395-420.

Gretener, P.E., 1986. On the mechanics of the intrusion of sills. *Canadian Journal of Earth Sciences,* **6**, pp. 1415-1419.

Grujic, D. and Mancktelow, N.S., 1998. Melt-bearing shear-zones: analogue experiments and comparison with examples from southern Madagascar. *Journal of Structural Geology,* **20**(6), pp. 673-680.

Guineberteau, B., Bouchez, J.L. and Vigneresse, J.L., 1987. The Mortagne granite pluton (France) emplaced by pull-apart along a shear-zone: structural and gravimetric arguments and regional implication. *Bulletin Geological Society of America,* **99**, pp. 763-770.

Gutzmer, J., Beukes, N.J., Pickard, A. and Barley, M.E., 2000. 1170 Ma SHRIMP age for Koras Group bimodal volcanism, Northern Cape Province. *South African Journal of Geology,* **103**(1), pp. 32-37.

Hall, D. and Kisters, A., 2012. The stabilization of self-organised leucogranite networks-Implications for melt segregation and far-field melt transfer in the continental crust. *Earth and Planetary Science Letters,* **355-356**, pp. 1-12.

Hancock, P.L., 1985. Brittle microtectonics: principles and practice. *Journal of Structural Geology,* **7**(3-4), pp. 437-457.

Hand, M. and Dirks, P.H.G.M., 1992. The influence of deformation on the formation of axial-planar leucosomes and the segregation of small melt bodies within the migmatitic napperby gneiss, central Australia. *Journal of Structural Geology,* **14**(5), pp. 591-604.

Harris, R.W., 1992. *A structural analysis of the Hartbees River thrust belt, with special emphasis on the nature and origin of the change in structural patters across the boundary between the Bushmanland and Gordonia Subprovinces.* Cape Town: University of Cape Town.

Harris, R.W., 1988. Examination of dextral transpression as a model for the development of thrusts and late folds in eastern Namaqualand. *South African Journal of Geology,* **91**(3), pp. 329-336.

Hartnady, C.J., Joubert, P. and Stowe, C.W., 1985. Proterozoic crustal evolution in southwestern Africa. *Episodes,* **8**, pp. 236-244.

Henderson, I.H.C. and Ihlen, P.M., 2004. Emplacement of polygeneration pegmatites in relation to Sveco-Norwegian contractional tectonics: Examples from southern Norway. *Precambrian Research,* **133**(3-4), pp. 207-222.

Hoal, B.G., 1993. The Proterozoic Sinclair Sequence in southern Namibia: intracratonic rift or active continental margin setting? *Precambrian Research,* **63**(1-2), pp. 143-162.

Hoffman, P.F., 1992. *Global Grenvillian kinematics and fusion of the Neoproterozoic supercontinent, Rhodinia.*

Hoffman, P.F., 1991. Did the breakout of Laurentia turn Gondwanaland inside-out? *Science,* **252**(5011), pp. 1409-1412.

Hollister, L.S. and Crawford, M.L., 1986. Melt-enhanced deformation: a major tectonic process. *Geology,* **14**(7), pp. 558-561.

Holmes, A., 1950. The age of uraninite from Gordonia, Southern Africa. *American Journal of Science,* **248**, pp. 81-94.

Horstwood, M.S.A., Foster, G.L., Parrish, R.R., Noble, S.R. and Nowell, G.M., 2003. Common-Pb corrected in situ U-Pb accessory mineral geochronology by LA-MC-ICP-MS. *Journal of Analytical Atomic Spectrometry,* **18**(8), pp. 837-846.

Hugo, P.J., 1970. The pegmatites of the Kenhardt and Gordonia Districts. Cape Province. *Memoirs Geological Survey of South Africa,* **58**, pp. 1-94.

Humphreys, H.C. and Van Bever Donker, J.M., 1990. Early Namaqua low-pressure metamorphism: deformation and porphyroblast growth in the Zoovoorby staurolite schist, South Africa. *Journal of Metamorphic Geology,* **8**(2), pp. 159-170.

Humphreys, H.C. and Van Bever Donker, J.M., 1987. Aspects of deformation along the namaqua province eastern boundary, Kenhardt district, South Africa. *Precambrian Research,* **36**(1), pp. 39-63.

Hutton, D.H.W., 1997. Syntectonic granites and the principle of effective stress. A general solution to the space problem? In: J.L. Bouchez, D.H.W. Hutton and W.E. Stephens, (Eds.), *Granite: From Segregation of Melt to Emplacement Fabrics.* The Netherlands: Kluwer Academic Publishers, pp. 189-197.

Hutton, D.H.W., 1996. The 'space problem' in the emplacement of granite. *Episodes,* **19**(4), pp. 114-119.

Hutton, D.H.W., 1992. Granite sheeted complexes: evidence for the dyking ascent mechanism. *Transactions - Royal Society of Edinburgh: Earth Sciences,* **83**(1-2), pp. 377-382.

Hutton, D.H.W., 1988. Granite emplacement mechanisms and tectonic controls: inferences from deformation studies. *Transactions - Royal Society of Edinburgh: Earth Sciences,* **79**(2-3), pp. 245-255.

Hutton, D.H.W., 1988. Igneous emplacement in a shear-zone termination: the biotite granite at Strontian, Scotland. *Geological Society of America Bulletin,* **100**(9), pp. 1392-1399.

Hutton, D.H.W., DEMPSTER, T.J., BROWN, P.E. and BECKER, S.D., 1990. A new mechanism of granite emplacement: Intrusion in active extensional shear-zones. *Nature,* **343**(6257), pp. 452-455.

Hutton, D.H.W. and REAVY, R.J., 1992. Strike-slip tectonics and granite petrogenesis. *Tectonics,* **11**(5), pp. 960-967.

Jackson, M.P.A., 1976. *High grade metamorphism of the Namaqua Metamorphic Complex around Aus in the southern Namib Desert, South West Africa.* Cape Town, South Africa: University of Cape Town.

Jackson, S.E., PEARSON, N.J., GRIFFIN, W.L. and BELOUSOVA, E.A., 2004. The application of laser ablation-inductively coupled plasma-mass spectrometry to in situ U-Pb zircon geochronology. *Chemical Geology,* **211**(1-2), pp. 47-69.

Jacobs, J., Pisarevsky, S., Thomas, R.J. and Becker, T., 2008. The Kalahari Craton during the assembly and dispersal of Rodinia. *Precambrian Research,* **160**(1–2), pp. 142-158.

Jacobs, J. and Thomas, R.J., 1994. Oblique collision at about 1.1 Ga along the southern margin of the Kaapvaal continent, south-east Africa. *Geologische Rundschau,* **83**(2), pp. 322-333.

Jacobs, J., Thomas, R.J. and Weber, K., 1993. Accretion and indentation tectonics at the southern edge of the Kaapvaal Craton during the Kibaran (Grenville) orogeny. *Geology,* **21**(3), pp. 203-206.

Jahns, R.H., 1955. The study of pegmatites. *Economic Geology, 50th anniversary,* **2**, pp. 1025-1130.

Jahns, R.H. and Burnham, C.W., 1969. Experimental studies of pegmatite genesis: I. A model for the derivation and crystallization of granitic pegmatites. Econ. Geol. 64, 843– 864. *Economic Geology,* **64**(843), pp. 864.

Jefferies, S.P., Holdsworth, R.E., WIbberley, C.A.J., Shimamoto, T., Spiers, C.J., Niemeijer, A.R. and Lloyd, G.E., 2006. The nature and importance of phyllonite development in crustal-scale fault cores: an example from the Median Tectonic Line, Japan. *Journal of Structural Geology,* **28**(2), pp. 220-235.

Joubert, P., 1986. The Namaqua Complex, a model of Proterozoic accretion. *Transactions - Geological Society of South Africa,* **89**, pp. 79-96.

Joubert, P., 1975. The Vioolsdrif igneous and associated rocks and their relationship with the Namaqualand Metamorphic Complex. *Annual Report Pecambrian Research Unit University of Cape Town,* **13**, pp. 71-75.

Joubert, P., 1974. The gneisses of Namaqua and their deformation. Trans. Geol. Soc. S. Afr. v. 77, p. 339-345. *Transactions - Geological Society of South Africa,* **77**, pp. 339-345.

Joubert, P., 1971. *The regional tectonism of the gneisses of part of Namaqua Metamorphic Complex.* University of Cape Town.

Katz, Y., Weinberg, R. and Aydin, A., 2004. Geometry and kinematic evolution of Riedel shear structures, Capitol Reef National Park, Utah. *Journal of Structural Geology,* **26**(3), pp. 491-501.

Kisters, A.F.M., Charlesworth, E.G., Gibson, R.L. and Anhaeusser, C.R., 1996. The relationship between antiformal and monoclinal steep structures in the Okiep Copper District, Namaqualand: A case study. *South African Journal of Geology,* **99**(2), pp. 185-195.

Kisters, A.F.M., Charlesworth, E.G., Gibson, R.L. and Anhaeusser, C.R., 1996. Steep structure formation in the Okiep Copper District, South Africa: Bulk inhomogeneous shortening of a high-grade metamorphic granite-gneiss sequence. *Journal of Structural Geology,* **18**(6), pp. 735-751.

Kisters, A.F.M., Gibson, R.L., Charlesworth, E.G. and Anhaeusser, C.R., 1998. The role of strain localization in the segregation and ascent of anatectic melts, Namaqualand, South Africa. *Journal of Structural Geology,* **20**(2-3), pp. 229-242.

Kisters, A.F.M., Potgieter, J.E., Charlesworth, E.G., Anhaeusser, C.R., Gibson, R.L. and Watkeys, M.K., 1994. Emplacement features of cupriferous noritoids in the Okiep copper district, Namaqualand, South Africa. *Exploration & Mining Geology,* **3**(3), pp. 297-310.

Kisters, A.F.M., Vietze, M.E. and Buick, I., 2012. Deformation and age of the Stinkbank pluton and implications for the correlation of tectonometamorphic episodes in the Pan-African Damara Belt. *South African Journal of Geology,* **115**(3), pp. 309-326.

Kisters, A.F.M., Ward, R.A., Anthonissen, C.J. and Vietze, M.E., 2009. Melt segregation and far-field melt transfer in the mid-crust. *Journal of the Geological Society,* **166**(5), pp. 905-918.

Kretz, R., 1983. Symbols for rock-forming minerals. *American Mineralogist,* **68**(1-2), pp. 277-279.

Lee, P.E., Jessup, M.J., Shaw, C.A., Hicks III, G.L. and Allen, J.L., 2012. Strain partitioning in the mid-crust of a transpressional shear-zone system: Insights from the Homestake and Slide Lake shear-zones, central Colorado. *Journal of Structural Geology,* **39**(0), pp. 237-252.

Leloup, P.H., Ricard, Y., Battaglia, J. and Lacassin, R., 1999. Shear heating in continental strike-slip shear-zones: Model and field examples. *Geophysical Journal International,* **136**(1), pp. 19-40.

Liotta, D., Caggianelli, A., Kruhl, J.H., Festa, V., Prosser, G. and Langone, A., 2008. Multiple injections of magmas along a Hercynian mid-crustal shear-zone (Sila Massif, Calabria, Italy). *Journal of Structural Geology,* **30**(10), pp. 1202-1217.

Lister, J.R. and Kerr, R.C., 1991. Fluid-mechanical models of crack propagation and their application to magma transport in dykes. *Journal of Geophysical Research,* **96**(B6), pp. 10,049-10,077.

London, D., 2003, Pegmatopia: What are Pegmatites? Webpage: Available: http://pegmatopia.ou.edu/What%20are%20Pegmatites/what_are_pegmatites.htm, 2013], last update 2013.

London, D. and Kontak, D.J., 2012. Granitic pegmatites: Scientific wonders and economic bonanzas. *Elements,* **8**(4), pp. 257-261.

London, D. and Morgan, G.B., 2012. The pegmatite puzzle. *Elements,* **8**(4), pp. 263-268.

London, D., 2005. Granitic pegmatites: an assessment of current concepts and directions for the future. *Lithos,* **80**(1–4), pp. 281-303.

Lucas, S.B. and St-Onge, M.R., 1995. Syn-tectonic magmatism and the development of compositional layering, Ungava Orogen (northern Quebec, Canada). *Journal of Structural Geology,* **17**(4), pp. 475-491.

Ludwig, K.R., 2001. Isoplot/Ex, a geochronological toolkit for Microsoft Excel. *Special Publication 43, Berkely Geochronological Center* .

Macey, P.H., 2005. Dating Zircons - From ROCK to SHRIMP*:* An in-house manual for extracting minerals from rock samples and preparing them for analyses using the Sensitive High mass Resolution Ion Microprobe (SHRIMP), *Internal Report*, p40.

Macey, P.H., 2001. The geology of the region between Garies and Kliprand, southern Namaqualand*.*1:50 000 scale mapping of 3018CA, 3018CB, 3018DA, 3018DB*. Internal Report (unpubl)*, Pretoria, Council for Geoscience.

Macey, P.H., Siegfried, H.P., Minnaar, H., Almond, J.E. and Botha, P.M.W., 2011. The Geology of the Loeriesfontein Area. *Explanation sheet.* Scale: 1:250 000 edn. Pretoria, South Africa: Council for Geoscience.

Mahan, K.H., Bartley, J.M., Coleman, D.S., Glazner, A.F. and Carl, B.S., 2003. *Sheeted intrusion of the synkinematic McDoogle pluton, Sierra Nevada, California. Bulletin of the Geological Society of America*, **115** (12), pp. 1570-1582.

Mahan, K.H., Williams, M.L. and Baldwin, J.A., 2003. Contractional uplift of deep crustal rocks along the Legs Lake shear-zone, western Churchill Province, Canadian shield. *Canadian Journal of Earth Sciences,* **40**(8), pp. 1085-1110.

Mancktelow, N.S., 2006. How ductile are ductile shear-zones? *Geology,* **34**(5), pp. 345-348.

Martin, H., 1965. The Precambrian Geology of the South West Africa and Namaqualand. *Precambrian Research Unit University of Cape Town,* , pp. 145-147.

Martin, R.F. and DE VITO, C., 2005. The patterns of enrichment in felsic pegmatites ultimately depend on tectonic setting. *Canadian Mineralogist,* **43**(6), pp. 2027-2048.

McCaffrey, K.J.W., 1992. Igneous emplacement in a transpressive shear-zone: Ox Mountains igneous complex. *Journal - Geological Society (London),* **149**(2), pp. 221-235.

McLaren, A.H., 1988. McLaren, A.H. (1988): The geology of the area east of Pofadder with emphasis on the shearing associated with the Pofadder Lineament: *Bulletin Pecambrian Research Unit University of Cape Town,* **35**, pp. 1-123.

McIver, J.R., McCarthy, T.S. and Packham, B.D.V., 1983. The copper-bearing basic rocks of Namaqualand, South Africa. *Mineralium Deposita,* **18**(2), pp. 135-160.

McNulty, B.A., 1995. Shear-zone development during magmatic arc construction: the Bench Canyon shear-zone, central Sierra Nevada, California. *Geological Society of America Bulletin,* **107**(9), pp. 1094-1107.

Means, W.D., 1986. Retrodeformation of anisotropic rocks. 19 edn. Geological Society of America, Abstracts with Programs, 19, p 769.

Memeti, V., 2005. *Regional and emplacement-related tectonism during the intrusion of the Tuolume Batholith: Results from the Benson Lake and May Lake Pendants, Sierra Nevada, California.*

Miller, R.M., 2008. Miller, R. McG. (2008) : Namaqua Metamorphic Complex. In: R.M. MILLER, ed, *The Geology of Namibia: Archaean to Mesoproterozoic.* Namibia: Ministry of mines and Energy, Geological Survey Namibia, pp. 7.1-7.55.

Miller, R.B. and Paterson, S.R., 2001. Construction of mid-crustal sheeted plutons: Examples from the North Cascades, Washington. *Bulletin of the Geological Society of America,* **113**(11), pp. 1423-1442.

Minnaar, H. and Theart, H.F.J., 2006. The exploitability of pegmatite deposits in the lower Orange River area (Vioolsdrif - Henkries - Steinkopf). *South African Journal of Geology,* **109**(3), pp. 341-352.

Moen, H.F.G., 2001. *The geology of an area east of Onseepkans.* 2001-0233. Pretoria, South Africa: Council for Geoscience.

Moen, H.F.G., 1988. Petrology of the Wilgenhoutsdrif Group. *Bulletin Geological Survey of South Africa,* **89**, pp. 1-37.

Moen, H.F.G. and Toogood, D.J., 2007. *The geology of the Onseepkans area. Explanation sheet 2818.* Pretoria, South Africa: Council for Geoscience.

Moen, H.F.G., 1999. The Kheis Tectonic Subprovince, southern Africa: A lithostratigraphic perspective. *South African Journal of Geology,* **102**(1), pp. 27-42.

Moen, H.F.G. and ARMSTRONG, R.A., 2008. New age constraints on the tectogenesis of the Kheis Subprovince and the evolution of the eastern Namaqua Province. *South African Journal of Geology,* **111**(1), pp. 79-88.

Moore, A.C., 1975. The petrography and the regional setting of the Tantalite Valley Complex, South West Africa. *Transactions - the Geological Society of South Africa,* **78**, pp. 235-249.

Moore, A.C., 1981. The Tantalite Valley shear-zone — a major locus for igneous activity in Southern Namibia (South West Africa)? *Journal of Volcanology and Geothermal Research,* **10**(4), pp. 383-393.

Neves, S.P., Araújo, A.M.B., Correia, P.B. and Mariano, G., 2003. Magnetic fabrics in the Cabanas Granite (NE Brazil): Interplay between emplacement and regional fabrics in a dextral transpressive regime. *Journal of Structural Geology,* **25**(3), pp. 441-453.

Neves, S.P. and Vauchez, A., 1995. Magma emplacement and shear-zone nucleation and development in northeast Brazil (Fazenda Nova and Pernambuco shear-zones; State of Pernambuco). *Journal of South American Earth Sciences,* **8**(3–4), pp. 289-298.

Neves, S.P. and Vauchez, A., 1995. Successive mixing and mingling of magmas in a plutonic complex of Northeast Brazil. *Lithos,* **34**(4), pp. 275-299.

Neves, S.P., Vauchez, A. and Archanjo, C.J., 1996. Shear-zone-controlled magma emplacement or magma-assisted nucleation of shear-zones? Insights from northeast Brazil. *Tectonophysics,* **262**(1–4), pp. 349-364.

Neves, S.P. and Mariano, G., 1999. Assessing the tectonic significance of a large-scale transcurrent shear-zone system: the Pernambuco lineament, northeastern Brazil. *Journal of Structural Geology,* **21**(10), pp. 1369-1383.

Nicolaysen, L.O., 1962. Stratigraphic interpretation of age measurements in Southern Africa. In Engel et al., (Eds.).Petrologic Studies: A Volume of Honour of A.F. Buddington. *Geological Society of America.* pp. 569-598.

Nicolaysen, L.O. and Burger, A.J., 1965. An extensive zone of 1000 m.y. old metamorphic and igneous rocks in South Africa. *Proc. int. Colloq. Abs. Geochr., Nancy, France*.

Northrup, C.J. and Mawer, C.K., 1991. *Deformation and structural setting of the Harding Pegmatite, Picuris Mountains, New Mexico: evidence for late-Proterozoic NW-directed shortening in north-central New Mexico.* 23 edn.

Norton, J.J. and Redden, J.A., 1990. Relations of zoned pegmatites to other pegmatites, granite, and metamorphic rocks in the southern Black Hills, South Dakota. *American Mineralogist,* **75**(5-6), pp. 631-655.

Novák, M., Selway, J.B., Černý, P., Hawthorne, F.C. and Ottolini, L., 1999. Tourmaline of the elbaite-dravite series from an elbaite-subtype pegmatite at Blizna, southern Bohemia, Czech Republic. *European Journal of Mineralogy,* **11**(3), pp. 557-568.

O'Connor, P.J., Gallagher, V. and Kennan, P.S., 1991. Genesis of lithium pegmatites from the Leinster Granite margin, southeast Ireland: geochemical constraints. *Geological Journal,* **26**(4), pp. 295-305.

Paterson, S.R. and Miller, R.B., 1998. Mid-crustal magmatic sheets in the Cascades Mountains, Washington: Implications for magma ascent. *Journal of Structural Geology,* 20 (9-10), pp. 1345.

Paterson, S.R. and Schmidt, K.L., 1999. Is there a close spatial relationship between faults and plutons? *Journal of Structural Geology,* **21**(8–9), pp. 1131-1142.

Pawley, M.J., Collins, W.J. and Van Kranendonk, M.J., 2002. Origin of fine-scale sheeted granites by incremental injection of magma into active shear-zones: examples from the Pilbara Craton, NW Australia. *Lithos,* **61**(3–4), pp. 127-139.

Pearce, N.J.G., Perkins, W.T., Westgate, J.A., Gorton, M.P., Jackson, S.E., Neal, C.R. and Chenery, S.P., 1997. *A compilation of new and published major and trace element data for NIST SRM 610 and NIST SRM 612 glass reference materials.*

Pe-piper, G., Koukouvelas, I. and Piper, D.J.W., 1998. Synkinematic granite emplacement in a shear-zone: The Pleasant Hills pluton, Canadian Appalachians. *Bulletin of the Geological Society of America,* **110**(4), pp. 523-536.

Petford, N., Kerr, R.C. and Lister, J.R., 1993. Dike transport of granitoid magmas. *Geology,* **21**, pp. 845-848.

Petford, N., 1996. Dykes or diapirs? *Transactions of the Royal Society of Edinburgh, Earth Sciences,* **87**(1-2), pp. 105-114.

Petford, N. and Koenders, M.A., 1998. Self-organisation and fracture connectivity in rapidly heated continental crust. *Journal of Structural Geology,* **20**(9-10), pp. 1425-1434.

Petford, N., Lister, J.R. and Kerr, R.C., 1994. The ascent of felsic magmas in dykes. *Lithos,* **32**(1–2), pp. 161-168.

Pettersson, A., Cornell, D.H. and Yuhara, M., 2004. Evidence of an Archaean component in the Bushmanland terrane – Sm–Nd whole-rock model ages and U–Pb zircon dating. *Geoscience Africa, Conference with Abstracts, (CDROM),* Durban.

Pettersson, A., Cornell, D.H., Moen, H.F.G., Reddy, S. and Evans, D., 2007. Ion-probe dating of 1.2 Ga collision and crustal architecture in the Namaqua-Natal Province of southern Africa. *Precambrian Research,* **158**(1-2), pp. 79-92.

Raith, J.G., Cornell, D.H., Frimmel, H.E. and De Beer, C.H., 2003. New insights into the geology of the Namaqua Tectonic Province, South Africa, from ion probe dating of detrital and metamorphic zircon. *Journal of Geology,* **111**(3), pp. 347-366.

Raith, J.G. and Harley, S.L., 1998. Low-P/high-T metamorphism in the Okiep Copper District, western Namaqualand, South Africa. *Journal of Metamorphic Geology,* **16**(2), pp. 281-305.

Raith, J.G. and Cornell, D.H., 2000. The first U-Pb iron probe zircon ages from a migmatic metapelite, central zone, western Namaqualand, South Africa, Abstract: 18th Colloquium of African Geology, Graz. *Journal of African Earth Sciences,* **30**(4, Supplement 1), pp. 1-94.

Reichardt, H. and Weinberg, R.F., 2012. The dike swarm of the Karakoram shear-zone, Ladakh, NW India: Linking granite source to batholith. *Bulletin of the Geological Society of America,* **124**(1-2), pp. 89-103.

Reid, D.L. and Barton, E.S., 1983. Geochemical characterisation of granitoids in the Namaqualand geotraverse. Spec. Publ. Geol. Soc. S. Afri. 85, pp. 67-82. In: B.J.V. BOTHA, (Ed) *Namaqualand Metamorphic Complex.* Pretoria, South Africa: Geological Society of South Africa, pp. 67-82.

Reid, D.L., Erlank, A.J., Welke, H.J. and Moyes, A., 1987. The Orange River Group: A Major Proterozoic Calcalkaline Volcanic Belt in the Western Namaqua Province, Southern Africa. *Bulletin for Precambrian Research,*, **36**(2), pp. 99-126.

Reid, D.L., 1979. Total rock RbSr and UThPb isotopic study of Precambrian metavolcanic rocks in the lower Orange River region, southern Africa. *Earth and Planetary Science Letters,* **42**(3), pp. 368-378.

Robb, L.J., Armstrong, R.A. and Waters, D.J., 1999. The history of granulite-facies metamorphism and crustal growth from single zircon U-Pb geochronology: Namaqualand, South Africa. *Journal of Petrology,* **40**(12), pp. 1747-1770.

Robin, P..F. and Cruden, A.R., 1994. Strain and vorticity patterns in ideally ductile transpression zones. *Journal of Structural Geology,* **16**(4), pp. 447-466.

Rubin, A.M., 1998. Dike ascent in partially molten rock. *Journal of Geophysical Research B: Solid Earth,* **103**(9), pp. 20901-20919.

SACS (South African Committee for Stratigraphy), 1980. Stratigraphy of South Africa. Part 1 (Kent, L.E. comp). Lithostratigraphy of the Republic of South Africa, South West Africa/Namibia and the Republics of Bophuthatswana, Transkei and Venda. *Handbook, Geological Survey of South Africa,* Pretoria, South Africa, **8**, p690.

Sawyer, E.W. and Brown, M. 2008. In: Sawyer, E.W. and Brown, M (Eds.). Working with migmatites, *Mineral Association of Canada Short Course*, *series, 38*, Meeting, Quebec, Canada.

Sawyer, E.W., Dombrowski, C. and Collins, W.J., 2000. Movement of melt during synchronous regional deformation and granulite-facies anatexis, an example from the Wuluma Hills, central Australia. *Geological Society Special Publication*, **168**, pp. 221-237

Sawyer, E.W. and Robin, P.Y.F., 1986. The subsolidus segregation of layer-parallel quartz-feldspar veins in greenschist to upper amphibolite facies metasediments. *Journal of Metamorphic Geology,* **4**(3), pp. 237-260.

Schärer, U., Cosca, M., Steck, A. and Hunziker, J., 1996. Termination of major ductile strike-slip shear and differential cooling along the Insubric line (Central Alps): U-Pb, Rb-Sr and 40Ar/ 39Ar ages of cross-cutting pegmatites. *Earth and Planetary Science Letters*, **142** (3-4), pp. 331-351.

Schmidt, K.L. and Paterson, S.R., 2000. Analyses fail to find coupling between deformation and magmatism. *Transactions of the American Geophysical Union,* **81**, pp. 197-203.

Schmitz, M.D. and Bowring, S.A., 2003. Ultrahigh-temperature metamorphism in the lower crust during Neoarchean Ventersdorp rifting and magmatism, Kaapvaal craton, southern Africa. *Bulletin of the Geological Society of America,* **115**(5), pp. 533-548.

SCHUTTE, I.C., 1972. The main pegmatites of the area between Steinkopf, Vioolsdrif and Goodhouse, Namaqualand*. Memoirs Geological Survey of South Africa,* **60, p20.**

Sibson, R.H., 1996. Structural permeability of fluid-driven fault-fracture meshes. *Journal of Structural Geology,* **18**(8), pp. 1031-1042.

Sibson, R.H., 1992. Fault-valve behavior and the hydrostatic-lithostatic fluid pressure interface. *Earth Science Reviews,* **32**(1-2), pp. 141-144.

Sibson, R.H., 1990. Conditions for fault-valve behavior. *Deformation mechanisms, rheology and* tectonics, pp. 15-28.

Sibson, R.H., 1986. Brecciation processes in fault zones: Inferences from earthquake rupturing. *Pure and Applied Geophysics,* **124**(1-2), pp. 159-175.

Sibson, R.H., RH, 1975. Seismic pumping; a hydrothermal fluid transport mechanism. *Journal of the Geological Society,* **131, Part 6**(6), pp. 653-659.

Simmons, W.B., Foord, E.E., Falster, A.U. and King, V.T., 1995. Evidence for an anatectic origin of granitic pegmatites, western Maine, USA*.* 27 edn. Geological Society of America, Annual Meeting, Abstracts with Programs, **27**, (6)

Simmons, W.B., Foord, E.E. and Falster, A.U., 1996. Anatectic Origin of Granitic Pegmatites, Western Maine, USA*.* GAC-MAC Annual meeting, Winnipeg. Abstracts with Programs.

Sláma, J., Košler, J., Condon, D.J., Crowley, J.L., Gerdes, A., Hanchar, J.M., Horstwood, M.S.A., Morris, G.A., Nasdala, L., Norberg, N., Schaltegger, U., Schoene, B., Tubrett, M.N. and Whitehouse, M.J., 2008. Plešovice zircon - A new natural reference material for U-Pb and Hf isotopic microanalysis. *Chemical Geology,* **249**(1-2), pp. 1-35.

Stowe, C.W., 1983. The Upington geotraverse and its implications for craton-margin tectonics. *Special publications of the Geological Society of South Africa,* **10**, pp. 147-171.

Stowe, C.W., 1986. Synthesis and interpretation of structures along the north- eastern boundary of the Namaqua tectonic province, South Africa. *Transactions - Geological Society of South Africa,* **89**(2), pp. 185-198.

Stowe, C.W., 1986. Synthesis and interpretation of structures along the north- eastern boundary of the Namaqua tectonic province, South Africa. *Transactions - Geological Society of South Africa,* **89**(2), pp. 185-198.

Tack, L., Duchesne, J.P., Liegeois, J.P. and Deblond, A., 1993. Two successive mantle-derived A-type granitoids in Burundi: Kibaran late-orogenic extensional collapse and lateral shear along the edge of the Tanzanian Craton. *Extended Abstracts 16th Colloquium of African Geology,* pp. 353-355.

Tchalenko, J.S. and Ambraseys, N.N., 1970. Structural analysis of the Dasht-e Bayaz (Iran) earthquake fractures. *Bulletin of the Geological Society of America,* **81**(1), pp. 41-60.

Thomas, R.J., 1989. A tale of two tectonic terranes. *South African Journal of Geology,* **92**(4), pp. 306-321.

Thomas, R.J., Agenbacht, A.L.D., Cornell, D.H. and Moore, J.M., 1994. The Kibaran of southern Africa: Tectonic evolution and metallogeny. *Ore Geology Reviews,* **9**(2), pp. 131-160.

Thomas, R.J., CornelL, D.H., Moore, J.M. and Jacobs, J., 1994. Crustal evolution of the Namaqua-Natal metamorphic province, southern Africa. *South African Journal of Geology,* **97**(1), pp. 8-14.

Thomas, R.J., De Beer, C.H. and Bowring, S.A., 1996. A comparative study of the Mesoproterozoic late orogenic porphyritic granitoids of southwest Namaqualand and Natal, South Africa. *Journal of African Earth Sciences,* **23**(3), pp. 485-508.

Thomas, R.J., Eglington, B.M. and Bowring, S.A., 1993. Dating the cessation of Kibaran magmatism in Natal, South Africa. *Journal of African Earth Sciences (and the Middle East),* **16**(3), pp. 247-252.

Thomas, R.J., Von Veh, M.W. and McCourt, S., 1993. The tectonic evolution of southern Africa: an overview. *Journal of African Earth Sciences (and the Middle East),* **16**(1–2), pp. 5-24.

Tikoff, B. and Teyssier, C., 1994. Strain modeling of displacement-field partitioning in transpressional orogens. *Journal of Structural Geology,* **16**(11), pp. 1575-1588.

Tikoff, B. and Teyssier, C., 1992. Crustal-scale, en echelon "P-shear' tensional bridges: a possible solution to the batholithic room problem. *Geology,* **20**(10), pp. 927-930.

Tikoff, B., De Saint Blanquat, M. and Teyssier, C., 1999. Translation and the resolution of the pluton space problem. *Journal of Structural Geology,* **21**(8–9), pp. 1109-1117.

Tikoff, B. and Greene, D., 1997. Stretching lineations in transpressional shear-zones: an example from the Sierra Nevada Batholith, California. *Journal of Structural Geology,* **19**(1), pp. 29-39.

Tobisch, O.T. and Paterson, S.R., 1990. The Yarra granite: an intradeformational pluton associated with ductile thrusting, Lachlan Fold belt, southeastern Australia*. Bulletin Geological Society of America.* **102**. pp.693-703.

Tobisch, O.T. and Cruden, A.R., 1995. Fracture-controlled magma conduits in an obliquely convergent continental magmatic arc. *Geology,* **23**(10), pp. 941-944.

Tommasi, A., Vauchez, A., Fernandes, L.A.D. and Porcher, C.C., 1994. Magma-assisted strain localization in an orogen-parallel transcurrent shear-zone of southern Brazil. *Tectonics,* **13**(2), pp. 421-437.

Toogood, D.J., 1976. Structural and metamorphic evolution of a gneiss terrane in the Namaqua belt near Onseepkans, South West Africa. *Bulletin of the Precambrian Research Unit,* **19**, pp. 1-189.

Van Achterbergh, E., Ryan, C.G., Jackson, S.E. and Griffin, W., 2001. Data reduction software for LA-ICP-MS, Laser ablation-ICPMS in the Earth Sciences. Mineral Association of Canada, **29**, p239-243.

Van Bever Donker, J.M., 1991. A synthesis of the structural geology of a major tectonic boundary between a 1000 m.y. mobile belt and a 3000 m.y. craton. *Tectonophysics,* **196**(3–4), pp. 359-370.

Van Bever Donker, J.M., 1980. *Structural and metamorphic evolution of an area around Kakamas and Keimoes, Northern Cape Province.* Cape Town, South Africa: University of Cape Town.

Vauchez, A., Neves, S.P. and Tommasi, A., 1997. Transcurrent shear-zones and magma emplacement in Neoproterozoic belts of Brazil. In: J.L. Bouchez, D.H.W. Hutton and W.E. Stephens, (Eds.) *Granite: From Segregation of Melt to Emplacement of Fabrics.* Dordrecht, Boston, London: Kluwer Publishers, pp. 275-294.

Vernon, R.H. and Paterson, S.R., 2001. Axial-surface leucosomes in anatectic migmatites. *Tectonophysics,* **335**(1–2), pp. 183-192.

Vigneresse, J.L. and TIKOFF, B., 1999. Strain partitioning during partial melting and crystallizing felsic magmas. *Tectonophysics,* **312**(2-4), pp. 117-132.

Vigneresse, J.L., 1995. Control of granite emplacement by regional deformation. *Tectonophysics,* **249**(3–4), pp. 173-186.

Waters, D.J., 1990. Thermal history and tectonic setting of the Namaqualand granulites, southern Africa: clues to Proterozoic crustal development. *Granulites and crustal evolution*, pp. 243-256.

Waters, D.J., 1989. *Metamorphic evidence for the heating and cooling path of Namaqualand granulites.*

Waters, D.J., 1988. Partial melting and the formation of granulite facies assemblages in Namaqualand, South Africa. *Journal of Metamorphic Geology,* **6**(4), pp. 387-404.

Waters, D.J., 1986. Metamorphic zonation and thermal history of pelitic gneisses from western Namaqualand, South Africa. *Transactions - Geological Society of South Africa,* **89**(2), pp. 97-102.

Weinberg, R.F., 1999. Mesoscale pervasive felsic magma migration: Alternatives to dyking. *Lithos,* **46**(3), pp. 393-410.

Weinberg, R.F. and GEORDIE, M., 2008. Magma migration, folding, and disaggregation of migmatites in the Karakoram Shear-zone, Ladakh, NW India. *Bulletin of the Geological Society of America,* **120**(7-8), pp. 994-1009.

Weinberg, R.F., MARK, G. and REICHARDT, H., 2009. Magma ponding in the Karakoram shear-zone, Ladakh, NW India. *Bulletin of the Geological Society of America,* **121**(1-2), pp. 278-285.

Weinberg, R.F. and REGENAUER-LIEB, K., 2010. Ductile fractures and magma migration from source. *Geology,* **38**(4), pp. 363-366.

Weinberg, R.F., SIAL, A.N. and MARIANO, G., 2004. Close spatial relationship between plutons and shear-zones. *Geology,* **32**(5), pp. 377-380.

Welke, H.J., Burger, A.J., Corner, B., Kroner, A. and Blignault, H.J., 1979. U-Pb and Rb-Sr age determinations on Middle Proterozoic rocks from the Lower Orange river area, south-western Africa. *Transactions, Geological Society of South Africa,* **82**(2), pp. 205-214.

Wenk, H. and Pannetier, J., 1990. Texture development in deformed granodiorites from the Santa Rosa mylonite zone, southern California. *Journal of Structural Geology*, **12** (2), pp. 177-184.

Westraat, J.D., Kisters, A.F.M., Poujol, M. and Stevens, G., 2005. Transcurrent shearing, granite sheeting and the incremental construction of the tabular 3.1 Ga Mpuluzi batholith, Barberton granite-greenstone terrane, South Africa. *Journal of the Geological Society,* **162**(2), pp. 373-388.

Williams, I.S., Buick, I.S. and Cartwright, I., 1996. An extended episode of early Mesoproterozoic metamorphic fluid flow in the Reynolds Range, central Australia. *Journal of Metamorphic Geology,* **14**(1), pp. 29-47.

Xu, S., Nieto-Samaniego, A.F. and Alaniz-Álvarez, S.A., 2013. Emplacement of pyroclastic dykes in Riedel shear fractures: An example from the Sierra de San Miguelito, central Mexico. *Journal of Volcanology and Geothermal Research,* **250**(0), pp. 1-8.

Zegers, T.E., De Keijzer, M., Passchier, C.W. and White, S.H., 1998. The Mulgandinnah Shear-zone; an Archaean crustal scale strike-slip zone, eastern Pilbara, Western Australia. *Precambrian Research,* **88**(1-4), pp. 233-247.

Zelt, G.A.D., 1980. Granulite-facies metamorphism in Namaqualand, South Africa. *Precambrian Research,* **13**, pp. 253-274.

Appendices

Appendix A: Geological Map, 1: 50 000 scale.

Appendix B: List of samples used for geochronology and petrography

Appendix C: Summery table of structural features and comparison to other work

Appendix D: Data tables of from geochronology analysis of selected samples

- **D1**: Sample CP32 (Zircon analysis and secondary standard)
- **D2**: Sample CM38-A (Monazite)
- **D3**: Sample CM13-B (Monazite)
- **D4**: Sample CM15-B (Monazite)
- **D5**: Sample CP31-C (Monazite)
- **D6**: Sample KG36-A (Monazite)

The Pofadder Shear Zone, Namibia and South Africa

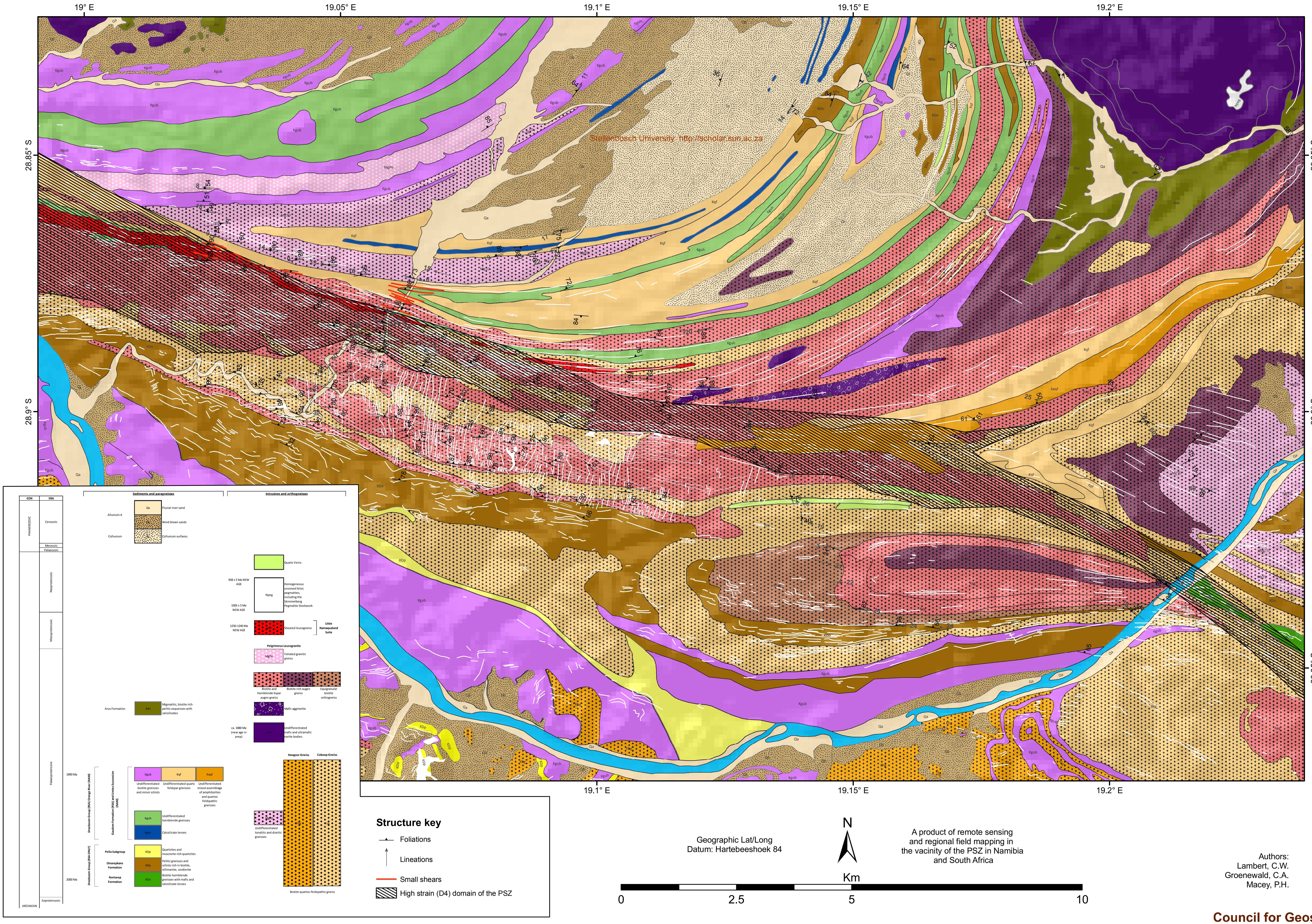

Authors:
Lambert, C.W.
Groenewald, C.A.
Macey, P.H.

Council for Geoscience

Appendix B

Sample ID	Latitude	Longitude	Brief description	Purpose
CM13B	-28.894743	19.054510	Pegmatite dyke from SPS (quartz+feldspar+muscovite with minor muscovite and garnet)	Geochron (monazite)
CM15B	-28.895856	19.060787	Pegmatite dyke from SPS (quartz+feldspar+muscovite with minor muscovite and garnet)	Geochron (monazite)
CM38A	-28.892872	19.048872	Undeformed pegmatite sill from SPS	Geochron (monazite)
CP31C	-28.878131	19.062107	Deformed pegmatite axial planar to parasitic F4 folds	Geochron (monazite)
CP32	-28.881166	19.059121	Deformed leucogranite. Quartz ribbons with rotated feldspar	Geochron (zircon)
KG36	-28.909050	19.216200	Pegmatite sill from outside the SPS, axial planar to F3/F4 fold axis	Geochron (monazite)
CM17C	-28.882640	19.058787	Phyllonite	Thin section
CM20B	-28.885164	19.058602	Mylonite-phyllonite (hornblende+biotite+quartz+feldspar)	Thin section
CM21C	-28.886926	19.059020	Mylonite-protomylonite (quartz, feldspar, biotite)	Thin section
CM38B	-28.892872	19.048872	Noudap K-feldspar-quartz-but gneiss in SPS	Thin section
CMAK1	-28.892718	19.068003	Quartz-feldspar ultramylonite in PSZ-core (previously NS pegmatite dyke from SPS)	Thin section
MN11	-28.885183	19.058600	Mafic mylonite (hornblende)	Thin section
MN13	-28.8846670	19.0586170	Mylonite to cataclasite (biotite + chlorite matrix)	Thin section
MN18	-28.883667	19.059150	Mafic mylonite (hornblende)	Thin section
MN54	-28.883100	19.058717	Mafic mylonite (hornblende)	Thin section
MN65	-28.881867	19.058783	Mafic mylonite (hornblende)	Thin section
MN71	-28.880517	19.059600	Weakly deformed to mylonitic amphibolite	Thin section

Appendix C

Generally accepted deformation phases and those derived from this study		Age	Fabric	Description	Associated pegmatite geometry	Structural event
D4	D4b	ca. 960-980 Ma (this study)	L4b	Moderate to steeply dipping stretching lineation primarily developed on the S4b, defined by stretched biotite and chlorite assemblages	Wedge shaped pegmatite dykes emplaced in Mode I opening fractures	PSZ formation
			S4b	Greenschist grade metamorphism defined by the progressive retrogression of amphibolite mineral assemblages to biotite/chlorite and the extensive development of thick phyllonite successions.	Z-like pegmatites developed in dilatant jogs.	
	D4a	ca. 1005 Ma (this study)	S4a	Amphibolite grade planar fabric defined by the preferred alignment of hornblende and biotite. S4a is developed either as a weak axial planar foliation to F4 folds or as pervasive, subvertical mylonitic domains of variable thickness	Tabular-sheeted pegmatites cross cutting the mylonitic foliation orientated as synthetic Riedel shears	
			L4a	Sub-horizontal mineral stretching lineations defined by streaked hornblende, biotite and quartz aggregates on S4a surfaces or developed as fold-rodding lineations in F2/F4 fold hinges.	Subvertical tabular-sheeted pegmatite sills parallel to mylonitic S4a	
			F4	Tight to isoclinal, upright to south verging high grade folds.	Subvertical tabular-sheeted pegmatite sills axial planar to F4.	
			F2/F4	Intensification and tightening of shallow SW verging F2 / F3 folds to form subvertical to upright folds adjacent to the PSZ. Developed primarily along the northern margin of the PSZ.	Subvertical tabular-sheeted pegmatite sills concentrated within the hinge zone of F2/F4 folds.	
D3		ca. 1030 Ma	NA			Peak metamorphism in NMC
			L3	Not well developed within the NMC	Migmatitic leucosomes (including those axial planar to small scale F3 folds) and steep structures	
			S3	Subvertical, non-penetrative planar cleavage developed by dextral and sinistral shearing along F3 parasitic folds		
			F3	Kilometre-scale to parasitic, originally W-E trending, upright- to inclined, shallow-plunging, open folds		
D2		ca. 1120-1086 Ma	L2	Strong NE-trending stretching lineation defined by amphibolite grade assemblages	Migmatitic leucosomes	Main deformation of NMC
			S2	Regionally consistent across the NMC as a sub-horizontal to NE dipping high-grade (amphibolite-granulite) fabric occurring axial planar to F2 folds. With the study area S2 is completely re-orientated by the PSZ		
			F2	Large, W-E trending isoclinal folds formed during the Namaqua Orogeny		
D1		> 1800 Ma	S1	Not observed in the study area. Regarded as an axial planar fabric to intrafolial F1 folds.	NA	Pre-NMC fabric
			F1	Intrafolial folding in supracrustal rocks in other parts of the NMC		

Deformation phases according to Toogood (1976)	Fabric	Description	Structural event
D6	L6	A mineral stretching lineation in the mylonites defined by stretched quartz and feldspar, orientation varies	PSZ formation
	S6	S6 fabric restricted to rocks adjacent to the shear. Defined by mylonitic foliation parallel to PSZ as an axial planar foliation to F6	
	L6	A mineral stretching lineation in the mylonites defined by stretched quartz and feldspar, orientation varies	
	F6	F6 antiforms with trace parallel to PSZ, deforming earlier F5 folds to display interference fold patterns.	
D5	S5	S5 fabric and mylonites form parallel to the axial plane in the hinge zones of F5 folds.	
	F5	Open, elongate NE trending doubly plunging folds with axial trace originally perpendicular to PSZ.	
D4	L4	Extensively developed parallel to fold axial planes	Described only as predating PSZ
	S4	Weak axial planar foliation to F4 folds	
	F4	Tight to isoclinal macroscopic, mesoscopic and intrafolial folds where in places folds are highly asymmetric and have variable orientations	
D3	L3	Strong L3 lineation defined by mineral and boudin alignment parallel to axial trace of F3 fold generations	Third metamorphic Event in Gordonia
	S3	Weak axial planar S3 foliation, locally developed in the hinge zones of some folds . Orientation varies	
	F3	The majority of the folds are open to closed trending NE with minor parasitic folds. Exceptions show isoclinal NE trends with northerly plunge	
D2	L2	Strong L2 lineation defined by mineral and boudin alignment	Second metamorphic event due to extensive igneous intrusions in Gordonia
	S2	Regional penetrative foliation leading to the formation of banded gneisses and augen gneisses in the NMC	
	F2	Highly refolded to intrafolial folds	
D1	S1	Foliation observed in xenoliths of Beenbreeek Granite	First Metamorphic event in Gordonia
	F1	Refolded folds observed in F2 hinge zones gneisses (Miller, 2008)	

Appendix D-1

	CP32			CONCENTRATIONS				RATIOS							AGES [Ma]						
	Spot Number	Comment	cPb	^{207}Pb (cps)	U (ppm)	Pb (ppm)	Th/U Measurement	$^{207}Pb/^{235}U^b$	2 σ	$^{206}Pb/^{238}U$	2 σ	rho	$^{207}Pb/^{206}Pb$	2 σ	$^{207}Pb/^{235}U$	2 σ	$^{206}Pb/^{238}U$	2 σ	$^{207}Pb/^{206}Pb$	2 σ	Conf (%)
Analyses used	1	Rim	n	14838	134	32	0.81	2.3883	4.0	0.2113	3.7	0.93	0.0820	1.5	1239	50	1236	46	1245	15	100
	2	Core	n	33696	304	70	1.04	2.1249	4.2	0.1889	3.3	0.78	0.0816	2.6	1157	49	1115	36	1236	26	96
	3	Rim	n	19653	180	42	0.77	2.3432	4.5	0.2075	2.9	0.63	0.0819	3.5	1225	56	1216	35	1243	34	99
	4	Core	y	7354	32	10	1.29	2.3824	6.0	0.2122	2.6	0.44	0.0814	5.4	1237	74	1240	33	1232	53	100
	5	Core	n	102485	874	194	0.56	2.1961	3.2	0.1951	2.6	0.81	0.0816	1.9	1180	38	1149	30	1236	18	97
	6	Rim	y	49473	384	63	0.60	1.2944	4.7	0.1161	4.0	0.84	0.0809	2.5	843	40	708	28	1218	25	84
	7	Xen Core	y	311072	1358	291	0.61	1.6780	5.0	0.1445	2.7	0.54	0.0842	4.3	1000	50	870	24	1297	41	87
	8	Rim	y	52020	324	85	0.78	2.4056	3.8	0.2132	2.7	0.70	0.0818	2.7	1244	48	1246	33	1242	27	100
	10	Rim	y	134083	878	195	0.69	2.0312	4.6	0.1801	3.2	0.69	0.0818	3.3	1126	52	1068	34	1240	32	95
	11	Core	y	24148	199	53	1.25	2.3843	3.1	0.2135	2.5	0.82	0.0810	1.8	1238	38	1247	31	1222	17	101
	12	Rim	y	96675	1286	159	0.47	1.1310	3.7	0.1096	2.9	0.77	0.0748	2.4	768	29	670	19	1064	24	87
	13	Rim	y	53681	1111	87	0.19	0.5849	6.5	0.0548	4.8	0.75	0.0774	4.3	468	30	344	17	1132	43	74
	14	Xen Core	n	54256	289	77	0.72	3.4295	4.2	0.2231	3.7	0.88	0.1115	2.0	1511	63	1298	48	1824	18	86
	15	Rim	n	39274	344	88	1.16	2.2858	3.1	0.2040	2.9	0.94	0.0813	1.1	1208	38	1197	35	1228	11	99
	16	Rim	n	26268	230	51	0.56	2.2893	3.4	0.2032	2.7	0.81	0.0817	2.0	1209	41	1193	32	1238	19	99
	17	Core	y	28641	240	60	0.87	2.4019	3.8	0.2128	3.2	0.84	0.0819	2.0	1243	47	1244	39	1242	20	100
	18	Rim	n	32190	284	73	1.09	2.3660	3.0	0.2126	2.8	0.95	0.0807	0.9	1232	37	1243	35	1215	9	101
	19	Rim	n	5040	45	12	1.25	2.3615	5.3	0.2110	3.4	0.65	0.0812	4.1	1231	65	1234	42	1225	40	100
	20	Rim	n	4717	43	11	1.28	2.3525	4.3	0.2105	3.4	0.78	0.0811	2.6	1228	52	1232	41	1223	26	100
	21	Xen Core	y	80725	480	123	1.09	2.0260	4.5	0.1800	4.0	0.89	0.0817	2.0	1124	51	1067	43	1237	20	95
	22	Rim	n	103147	1427	168	0.28	1.1313	3.1	0.1098	2.5	0.79	0.0747	1.9	768	24	672	17	1060	19	87
	23	Core	n	17654	156	41	1.25	2.3734	4.0	0.2112	3.3	0.82	0.0815	2.3	1235	49	1235	40	1234	22	100
	24	Rim	n	76291	674	153	0.55	2.3575	3.0	0.2091	2.8	0.93	0.0818	1.1	1230	37	1224	35	1240	11	100
	25	Xen Core	y	79916	805	163	0.68	2.0179	3.6	0.1802	3.0	0.83	0.0812	2.0	1122	40	1068	32	1227	20	95
	26	Rim	y	60437	692	103	0.78	1.3758	4.6	0.1251	4.5	0.97	0.0797	1.0	879	41	760	34	1191	10	87
	27	Core	n	4222	36	10	1.72	2.3654	4.0	0.2097	3.1	0.78	0.0818	2.5	1232	49	1227	38	1241	24	100
	29	Rim	n	1569	14	4	1.19	2.3924	5.0	0.2126	3.0	0.60	0.0816	4.0	1240	62	1243	37	1236	39	100
	30	Core	n	56959	702	103	0.44	1.4925	3.7	0.1324	3.4	0.90	0.0817	1.6	927	35	802	27	1239	16	86
	31	Core	n	12783	114	31	1.30	2.3903	3.1	0.2124	2.4	0.77	0.0816	2.0	1240	39	1242	30	1236	20	100
	32	Core	n	10427	91	23	0.95	2.3831	3.9	0.2118	3.0	0.78	0.0816	2.4	1238	48	1238	37	1236	24	100
	33	Xen Core	y	118597	705	160	0.69	1.9294	3.7	0.1715	2.8	0.76	0.0816	2.4	1091	41	1020	29	1236	24	83
	34	Rim	n	25515	238	58	0.97	2.3130	2.8	0.2061	2.5	0.89	0.0814	1.3	1216	34	1208	30	1231	12	98
	35	Core	y	35560	452	78	1.01	1.5877	4.9	0.1418	3.1	0.64	0.0812	3.8	965	47	855	27	1227	37	70
	36	Rim	y	101222	907	144	0.54	1.4253	3.4	0.1340	3.0	0.88	0.0771	1.7	900	31	811	24	1125	17	72
	37	Core	y	50030	435	95	0.53	2.1910	4.1	0.1957	3.7	0.89	0.0812	1.8	1178	48	1152	42	1226	18	94
	39	Core	n	12088	105	27	1.06	2.3860	4.3	0.2118	3.5	0.81	0.0817	2.5	1238	54	1239	44	1238	25	100
Analyses not used	9	metamict	n	3215	29	7	1.24	2.2162	4.9	0.1992	3.1	0.63	0.0807	3.8	1186	59	1171	36	1214	38	99
	28	rev discordant	n	5838	45	11	0.53	2.5923	4.3	0.2312	3.1	0.72	0.0813	3.0	1298	56	1341	41	1229	29	103
	38	mechan mal	y	105022	881	123	0.98	1.2717	6.8	0.1031	6.5	0.95	0.0895	2.1	833	57	632	41	1415	20	45
	40	mechan mal	y	83062	1352	96	0.25	0.5857	24.3	0.0565	24.0	0.99	0.0752	3.9	468	114	354	85	1074	40	33
Plešovice secondary standard	PL		n	12427	716	36	0.11	0.3885	3.4	0.0528	3.2	0.94	0.0534	1.2	333	11	332	11	344	13	97
	PL		n	10032	561	28	0.11	0.3960	3.9	0.0539	3.2	0.83	0.0533	2.1	339	13	338	11	343	24	99
	PL		y	18862	561	32	0.11	0.3943	9.2	0.0536	3.3	0.36	0.0534	8.5	338	31	336	11	346	96	97
	PL		y	10508	560	28	0.10	0.3854	4.9	0.0529	2.9	0.59	0.0529	3.9	331	16	332	10	324	44	103
	PL		y	13719	726	37	0.13	0.3911	6.3	0.0531	3.5	0.55	0.0534	5.3	335	21	333	12	348	60	96
	PL		n	10781	517	27	0.11	0.3942	5.0	0.0537	3.4	0.67	0.0533	3.7	337	17	337	11	341	42	99
	PL		n	12591	739	37	0.10	0.3894	3.5	0.0529	3.2	0.91	0.0533	1.5	334	12	333	11	344	17	97
	PL		n	12694	751	38	0.11	0.3907	3.8	0.0532	3.3	0.88	0.0532	1.8	335	13	334	11	338	20	99
	PL		n	12752	750	37	0.10	0.3900	3.6	0.0532	3.2	0.87	0.0532	1.8	334	12	334	11	335	20	100
	PL		n	13330	779	39	0.10	0.3898	3.8	0.0529	3.2	0.83	0.0534	2.1	334	13	332	10	347	24	96
	PL		n	13831	810	40	0.10	0.3901	3.7	0.0530	3.1	0.83	0.0534	2.0	334	12	333	10	347	23	96

Appendix D-2

	CM38-A		CONCENTRATIONS				RATIOS							AGES [Ma]						
	Spot Number	Comment	U (ppm)	Pb (ppm)	Th (ppm)	Th/U Measurement	$^{207}Pb/^{235}U$	2 σ	$^{206}Pb/^{238}U$	2 σ	rho	$^{207}Pb/^{206}Pb$	2 σ	$^{207}Pb/^{235}U$	2 σ	$^{206}Pb/^{238}U$	2 σ	$^{207}Pb/^{206}Pb$	2 σ	Conf (%)
Analyses used	1	NA	1511	250	67930	44.96	1.65	0.04	0.165	0.003	0.88	0.0725	0.0008	991	22	987	18	999	21	99
	2	NA	917	141	41308	45.05	1.55	0.04	0.154	0.003	0.85	0.0727	0.0009	949	22	924	17	1007	25	92
	3	Rim	1638	271	93814	57.27	1.65	0.04	0.165	0.003	0.88	0.0722	0.0008	988	22	987	18	991	22	100
	4	Rim	1799	298	99329	55.22	1.66	0.04	0.166	0.003	0.88	0.0727	0.0008	993	22	987	18	1007	21	98
	5	Rim	2408	401	97897	40.66	1.65	0.04	0.166	0.003	0.88	0.0721	0.0008	991	22	992	18	988	21	100
	10	Rim	4651	756	5670	1.22	1.62	0.04	0.162	0.003	0.88	0.0723	0.0008	977	22	970	18	993	21	98
	11	Core	1634	275	77221	47.26	1.68	0.04	0.168	0.003	0.88	0.0726	0.0008	1003	22	1003	18	1002	21	100
	12	Rim	1730	290	92664	53.57	1.66	0.04	0.168	0.003	0.88	0.0720	0.0008	995	22	999	18	986	22	101
	13	Rim	1922	321	101300	52.70	1.67	0.04	0.167	0.003	0.88	0.0724	0.0008	996	22	995	18	998	21	100
	14	Core	1399	234	78794	56.31	1.67	0.04	0.167	0.003	0.87	0.0727	0.0008	998	22	995	18	1004	22	99
	15	Rim	2058	342	119033	57.83	1.65	0.04	0.166	0.003	0.88	0.0718	0.0008	988	22	991	18	981	22	101
	16	Rim	2182	363	120986	55.44	1.64	0.04	0.166	0.003	0.88	0.0715	0.0008	986	22	992	18	972	22	102
	17	Na	1909	316	54306	28.45	1.66	0.04	0.166	0.003	0.86	0.0728	0.0008	994	23	988	18	1007	23	98
	18	Core	1592	267	45394	28.52	1.68	0.04	0.168	0.003	0.87	0.0727	0.0008	1002	22	1001	18	1007	22	99
	19	Rim	1598	268	94563	59.17	1.68	0.04	0.167	0.003	0.87	0.0726	0.0008	1000	22	998	18	1004	22	99
	20	Rim	2387	399	89008	37.28	1.66	0.04	0.167	0.003	0.87	0.0721	0.0008	994	22	996	18	990	22	101
	21	NA	1653	277	67038	40.55	1.68	0.04	0.167	0.003	0.87	0.0727	0.0008	1000	22	998	18	1005	22	99
	22	Core	896	150	31011	34.61	1.69	0.04	0.168	0.003	0.77	0.0729	0.0012	1003	25	1000	18	1011	32	99
	23	Rim	1205	201	73593	61.07	1.65	0.04	0.167	0.003	0.86	0.0720	0.0008	991	22	994	18	985	23	101
	24	Rim	1910	316	88180	46.17	1.64	0.04	0.166	0.003	0.86	0.0720	0.0008	988	22	988	18	986	23	100
Analyses not used	6	mechanical mal	2637	224	57736	21.89	1.17	0.03	0.085	0.002	0.88	0.0994	0.0011	785	18	527	10	1613	20	33
	7	detector tripped	6209	650	5912	0.95	1.74	0.04	0.105	0.002	0.88	0.1207	0.0013	1024	23	642	12	1967	18	33
	8	detector tripped	6036	578	7775	1.29	1.87	0.04	0.096	0.002	0.88	0.1417	0.0015	1071	24	590	11	2248	18	26
	9	detector tripped	8171	320	9498	1.16	1.76	0.04	0.039	0.001	0.88	0.3265	0.0034	1031	23	247	5	3601	16	7
Thomson Mine secondary sample	TM		1161	366	112931	97.26	4.66	0.10	0.315	0.006	0.89	0.1073	0.0011	1760	39	1765	31	1754	19	101
	TM		1149	360	112727	98.11	4.67	0.10	0.314	0.006	0.89	0.1080	0.0011	1761	39	1758	31	1765	19	100
	TM		1042	329	112928	108.40	4.73	0.11	0.316	0.006	0.89	0.1085	0.0011	1773	40	1771	31	1775	19	100
	TM		793	252	127791	161.16	4.69	0.10	0.317	0.006	0.88	0.1072	0.0011	1766	39	1777	31	1753	19	101
	TM		788	252	127352	161.59	4.75	0.11	0.319	0.006	0.88	0.1078	0.0011	1776	40	1787	31	1763	19	101
	TM		791	250	127025	160.64	4.70	0.10	0.316	0.006	0.88	0.1079	0.0011	1766	39	1769	31	1764	19	100
	TM		1004	314	124034	123.54	4.64	0.10	0.313	0.006	0.88	0.1075	0.0011	1757	39	1757	30	1758	19	100
	TM		1687	528	132393	78.47	4.61	0.10	0.313	0.006	0.88	0.1068	0.0011	1751	39	1756	30	1745	19	101

Appendix D-3

	CM13-B		CONCENTRATIONS				RATIOS							AGES [Ma]						
	Spot Number	Comment	U (ppm)	Pb (ppm)	Th (ppm)	Th/U Measurement	$^{207}Pb/^{235}U$	2 σ	$^{206}Pb/^{238}U$	2 σ	rho	$^{207}Pb/^{206}Pb$	2 σ	$^{207}Pb/^{235}U$	2 σ	$^{206}Pb/^{238}U$	2 σ	$^{207}Pb/^{206}Pb$	2 σ	Conf (%)
Analyses used	1		4984	799	198940	39.92	1.56	0.04	0.160	0.003	0.88	0.0705	0.0008	954	22	959	18	942	21	102
	3		4446	714	171194	38.50	1.57	0.04	0.161	0.003	0.88	0.0708	0.0008	958	22	961	18	953	21	101
	5		5236	845	192411	36.75	1.58	0.04	0.161	0.003	0.88	0.0710	0.0008	963	22	965	18	958	22	101
	7		3998	644	142981	35.76	1.57	0.04	0.161	0.003	0.88	0.0709	0.0008	960	22	963	18	954	21	101
	8	Pb loss	5088	708	90039	17.70	1.37	0.03	0.139	0.003	0.83	0.0713	0.0010	876	21	840	16	967	22	87
	9	Pb loss	4642	513	95700	20.62	1.09	0.03	0.110	0.002	0.74	0.0716	0.0013	749	20	675	13	975	22	69
	12		4062	651	186974	46.03	1.56	0.04	0.160	0.003	0.88	0.0703	0.0008	953	22	959	18	938	22	102
	13		3754	607	177983	47.41	1.60	0.04	0.162	0.003	0.88	0.0716	0.0008	969	22	966	18	975	22	99
	14		4329	690	198769	45.91	1.55	0.04	0.159	0.003	0.88	0.0705	0.0008	950	22	954	18	942	22	101
	15		3951	633	206984	52.39	1.57	0.04	0.160	0.003	0.87	0.0709	0.0008	957	22	958	18	955	22	100
	16		4205	681	163807	38.95	1.58	0.04	0.162	0.003	0.88	0.0710	0.0008	964	22	967	18	957	22	101
Analyses not used	2	Pb loss	6859	988	182382	26.59	1.41	0.03	0.144	0.003	0.88	0.0711	0.0008	894	20	867	16	961	21	90
	4	mixed signal across zonation	6080	798	164124	26.99	1.42	0.03	0.131	0.003	0.89	0.0787	0.0008	899	20	795	15	1165	20	68
	6	short signal	3095	579	137532	44.43	1.91	0.04	0.187	0.004	0.89	0.0742	0.0008	1085	24	1105	20	1047	21	106
	10	detector tripped	7864	470	120113	15.27	1.77	0.04	0.060	0.001	0.90	0.2147	0.0021	1034	23	374	7	2941	17	13
	11	detector tripped	6439	291	95603	14.85	2.30	0.05	0.045	0.001	0.88	0.3699	0.0040	1213	27	285	6	3791	16	8
Thomson Mine secondary sample	TM		809	256	184642	228.22	4.70	0.11	0.316	0.006	0.89	0.1079	0.0011	1767	40	1770	31	1763	19	100
	TM		829	261	159858	192.89	4.68	0.11	0.315	0.006	0.89	0.1077	0.0011	1764	40	1767	31	1760	19	100
	TM		991	312	188966	190.69	4.68	0.11	0.315	0.006	0.89	0.1078	0.0011	1763	40	1765	31	1762	19	100
	TM		1395	442	237462	170.25	4.70	0.11	0.317	0.006	0.88	0.1076	0.0011	1767	40	1774	31	1759	19	101
	TM		1171	367	200558	171.27	4.66	0.11	0.313	0.006	0.88	0.1079	0.0012	1759	40	1756	31	1764	19	100
	TM		969	307	182760	188.59	4.70	0.11	0.317	0.006	0.88	0.1076	0.0012	1767	40	1773	31	1759	19	101

Stellenbosch University http://scholar.sun.ac.za

Appendix D-4

	CM15-B		CONCENTRATIONS				RATIOS							AGES [Ma]						
	Spot Number	Comment	U (ppm)	Pb (ppm)	Th (ppm)	Th/U Measurement	$^{207}Pb/^{235}U$	2 σ	$^{206}Pb/^{238}U$	2 σ	rho	$^{207}Pb/^{206}Pb$	2 σ	$^{207}Pb/^{235}U$	2 σ	$^{206}Pb/^{238}U$	2 σ	$^{207}Pb/^{206}Pb$	2 σ	Conf (%)
Analyses used	2		2590	420	104231	40.24	1.59	0.04	0.162	0.004	0.91	0.0714	0.0008	968	24	968	20	969	21	100
	3		2365	382	95659	40.45	1.58	0.04	0.162	0.004	0.91	0.0711	0.0008	964	24	965	20	960	21	101
	4		2650	430	86231	32.54	1.59	0.04	0.162	0.004	0.90	0.0710	0.0008	966	24	970	20	958	21	101
	5		3499	569	98004	28.01	1.60	0.04	0.163	0.004	0.90	0.0715	0.0008	972	24	971	20	973	21	100
	6		3613	582	126575	35.03	1.58	0.04	0.161	0.004	0.90	0.0710	0.0008	961	24	963	20	957	21	101
	7		3335	544	97369	29.20	1.60	0.04	0.163	0.004	0.90	0.0710	0.0008	968	24	974	20	956	21	102
	8		3256	520	109366	33.59	1.56	0.04	0.160	0.004	0.90	0.0707	0.0008	953	23	955	20	949	21	101
	9		2427	394	105774	43.58	1.59	0.04	0.162	0.004	0.90	0.0711	0.0008	968	24	971	20	961	22	101
	10		3969	645	101901	25.67	1.60	0.04	0.163	0.004	0.90	0.0713	0.0008	970	24	971	20	966	21	100
	11		3150	507	106029	33.66	1.57	0.04	0.161	0.003	0.89	0.0708	0.0008	959	23	962	19	952	22	101
	12		2515	405	100611	40.00	1.58	0.04	0.161	0.003	0.89	0.0711	0.0008	962	23	963	19	960	22	100
	13		2769	443	85223	30.78	1.57	0.04	0.160	0.003	0.89	0.0712	0.0008	959	23	957	19	964	22	99
	14		2829	460	86058	30.42	1.60	0.04	0.163	0.003	0.89	0.0711	0.0008	969	23	972	19	960	22	101
	15		2824	454	106504	37.72	1.57	0.04	0.161	0.003	0.89	0.0710	0.0008	960	23	961	19	958	22	100
	16		3011	487	99285	32.97	1.59	0.04	0.162	0.003	0.88	0.0713	0.0008	966	23	966	19	966	22	100
	17		2917	467	91447	31.35	1.57	0.04	0.160	0.003	0.88	0.0712	0.0008	959	22	957	18	963	22	99
	18		3134	505	97895	31.23	1.58	0.04	0.161	0.003	0.88	0.0711	0.0008	961	22	962	18	959	22	100
	19		3009	479	107429	35.70	1.56	0.04	0.159	0.003	0.88	0.0712	0.0008	955	22	952	18	962	22	99
	20		3551	572	103920	29.27	1.57	0.04	0.161	0.003	0.88	0.0710	0.0008	960	22	962	18	956	22	101
Analyses not used	1	scattered signal	2013	339	80530	40.00	1.83	0.05	0.168	0.004	0.91	0.0789	0.0008	1057	26	1003	21	1169	21	86
Thomson Mine secondary sample	TM		1303	409	78033	59.87	4.64	0.12	0.314	0.007	0.91	0.1072	0.0012	1757	44	1761	35	1753	19	100
	TM		1200	380	132021	110.05	4.70	0.12	0.316	0.007	0.90	0.1078	0.0012	1768	45	1773	36	1762	20	101
	TM		2092	660	121710	58.18	4.63	0.12	0.316	0.007	0.90	0.1064	0.0012	1754	44	1768	35	1738	20	102
	TM		1238	389	75357	60.88	4.66	0.11	0.314	0.007	0.89	0.1075	0.0012	1760	42	1763	33	1758	20	100
	TM		1535	488	93099	60.67	4.70	0.11	0.318	0.007	0.89	0.1072	0.0012	1768	42	1781	33	1752	20	102
	TM		1243	393	82689	66.53	4.68	0.11	0.316	0.007	0.89	0.1073	0.0012	1763	42	1770	33	1755	20	101

Appendix D-5

	CP31-C		CONCENTRATIONS				RATIOS							AGES [Ma]						
	Spot Number	Comment	U (ppm)	Pb (ppm)	Th (ppm)	Th/U Measurement	$^{207}Pb/^{235}U$	2 σ	$^{206}Pb/^{238}U$	2 σ	rho	$^{207}Pb/^{206}Pb$	2 σ	$^{207}Pb/^{235}U$	2 σ	$^{206}Pb/^{238}U$	2 σ	$^{207}Pb/^{206}Pb$	2 σ	Conf (%)
Analyses used	1		2524	424	113592	45.00	1.69	0.04	0.168	0.003	0.88	0.0728	0.0008	1004	22	1002	18	1008	21	99
	2		1937	325	84940	43.85	1.69	0.04	0.168	0.003	0.87	0.0732	0.0008	1006	22	1001	18	1018	22	98
	3		3113	518	129800	41.69	1.65	0.04	0.166	0.003	0.88	0.0721	0.0008	991	22	992	18	989	21	100
	4		1756	297	79423	45.22	1.70	0.04	0.169	0.003	0.86	0.0729	0.0008	1008	23	1007	18	1011	23	100
	8		2333	394	104168	44.65	1.70	0.04	0.169	0.003	0.87	0.0729	0.0008	1008	22	1006	18	1011	22	100
	9		2654	444	94874	35.75	1.68	0.04	0.167	0.003	0.87	0.0730	0.0008	1002	22	997	18	1014	22	98
	10		3015	506	137708	45.67	1.71	0.04	0.168	0.003	0.86	0.0741	0.0009	1013	23	1000	18	1043	23	96
Analyses not used	5	detector tripped	2503	574	117364	46.90	6.72	0.15	0.229	0.004	0.88	0.2125	0.0022	2075	45	1331	23	2925	17	46
	6	detector tripped	2532	601	169272	66.85	9.53	0.21	0.237	0.005	0.88	0.2913	0.0031	2391	52	1373	24	3425	16	40
	7	no signal	0	0	1	error	-2.11	-15.71	-0.011	0.072	-0.87	1.3776	4.9884	error	error	-72	471	5684	2053	-1
	11	irregular signal	2624	472	107142	40.84	2.07	0.05	0.180	0.003	0.86	0.0834	0.0010	1137	25	1066	19	1277	22	83
	12	irregular signal	1418	312	73473	51.81	7.32	0.16	0.220	0.004	0.86	0.2409	0.0028	2151	48	1284	22	3126	18	41
Thomson Mine secondary sample	TM		969	306	109941	113.41	4.69	0.10	0.315	0.006	0.88	0.1080	0.0011	1766	39	1766	30	1766	19	100
	TM		819	257	108781	132.87	4.65	0.10	0.314	0.006	0.88	0.1075	0.0011	1758	39	1759	30	1757	19	100
	TM		788	249	104694	132.89	4.67	0.10	0.316	0.006	0.88	0.1072	0.0011	1761	39	1768	30	1753	19	101
	TM		807	254	108664	134.67	4.66	0.10	0.315	0.006	0.86	0.1073	0.0012	1759	39	1764	30	1754	20	101
	TM		800	249	107542	134.37	4.64	0.10	0.312	0.006	0.86	0.1079	0.0012	1756	39	1749	29	1764	20	99
	TM		787	250	106898	135.77	4.68	0.10	0.317	0.006	0.86	0.1071	0.0012	1764	39	1775	30	1751	21	101

Appendix D-6

	KG36		CONCENTRATIONS				RATIOS							AGES [Ma]						
	Spot Number	Comment	U (ppm)	Pb (ppm)	Th (ppm)	Th/U Measurement	$^{207}Pb/^{235}U$	2 σ	$^{206}Pb/^{238}U$	2 σ	rho	$^{207}Pb/^{206}Pb$	2 σ	$^{207}Pb/^{235}U$	2 σ	$^{206}Pb/^{238}U$	2 σ	$^{207}Pb/^{206}Pb$	2 σ	Conf (%)
Analyses used	1		1747	294	128361	73.46	1.69	0.04	0.168	0.003	0.87	0.0728	0.0008	1004	23	1002	19	1008	23	99
	2		1553	259	122276	78.72	1.65	0.04	0.167	0.003	0.88	0.0717	0.0008	989	23	994	19	978	22	102
	3		1205	200	123023	102.08	1.65	0.04	0.166	0.003	0.88	0.0721	0.0008	989	23	990	19	989	23	100
	4		1496	247	135027	90.26	1.63	0.04	0.165	0.003	0.88	0.0716	0.0008	981	23	983	19	975	22	101
	5		1437	235	133181	92.70	1.61	0.04	0.164	0.003	0.88	0.0714	0.0008	974	23	978	18	967	23	101
	6		1932	322	152167	78.75	1.66	0.04	0.167	0.003	0.88	0.0723	0.0008	994	23	994	19	994	23	100
	7		1371	229	136923	99.86	1.66	0.04	0.167	0.003	0.87	0.0722	0.0008	994	23	994	19	992	23	100
	8		1531	253	146061	95.38	1.64	0.04	0.165	0.003	0.87	0.0719	0.0008	984	23	985	19	982	23	100
	9		2579	432	132369	51.33	1.67	0.04	0.168	0.003	0.86	0.0724	0.0009	998	23	999	19	996	24	100
	10		3541	589	170947	48.28	1.66	0.04	0.166	0.003	0.87	0.0722	0.0008	992	23	993	19	992	23	100
	12		2410	403	138712	57.55	1.67	0.04	0.167	0.003	0.86	0.0722	0.0009	995	23	997	19	992	24	101
	14		1387	231	136684	98.55	1.66	0.04	0.167	0.003	0.86	0.0721	0.0009	992	23	994	19	988	24	101
Analyses not used	11	irregular signal	5255	254	152658	29.05	2.29	0.05	0.048	0.001	0.87	0.3442	0.0039	1211	28	305	6	3681	17	8
	13	irregular signal	1576	259	78674	49.93	2.17	0.05	0.164	0.003	0.87	0.0957	0.0011	1171	27	981	18	1541	22	64
Thomson Mine secondary sample	TM		787	248	114309	145.21	4.68	0.11	0.315	0.006	0.87	0.1078	0.0012	1763	41	1764	31	1763	20	100
	TM		810	255	117213	144.75	4.68	0.11	0.314	0.006	0.87	0.1079	0.0012	1763	41	1762	31	1765	20	100
	TM		892	283	123244	138.10	4.69	0.11	0.317	0.006	0.87	0.1073	0.0012	1766	41	1776	31	1754	21	101
	TM		893	280	124327	139.27	4.68	0.11	0.314	0.006	0.85	0.1082	0.0013	1764	42	1759	31	1770	23	99
	TM		898	283	125492	139.68	4.69	0.11	0.315	0.006	0.85	0.1078	0.0014	1765	42	1767	31	1763	23	100
	TM		902	283	125736	139.47	4.65	0.11	0.314	0.006	0.85	0.1075	0.0014	1758	42	1759	31	1757	23	100